The Effects of Machine Parameters on the Integrity of WC-Ni Coatings Deposited onto Titanium Parts with Laser Additive Manufacturing

.

by
Marius Cornelius van Coller

Thesis presented in fulfilment of the requirements for the degree of Master of Engineering (Industrial Engineering) in the Faculty of Engineering at Stellenbosch University

Supervisor: Prof. G.A. Oosthuizen
Co-Supervisor: Prof. N. Sacks.

April 2019

DECLARATION

By submitting this thesis electronically, I declare that the entirety of the work contained therein is my own, original work, that I am the sole author thereof (save to the extent explicitly otherwise stated), that reproduction and publication thereof by Stellenbosch University will not infringe any third party rights and that I have not previously in its entirety or in part submitted it for obtaining any qualification.

April 2019

ABSTRACT

Part quality specifications are of the utmost importance within industries that include specialized applications, for instance the medical, aerospace, nautical and mining industries. Attributable to the high costs of specialized parts and the risks involved in operation, such as the loss of human lives and company integrity. Parts are expected to showcase consistent properties throughout their life cycle as catastrophic consequences may ensue if they do not align with industry specifications. The goal of today's part manufacturers is to extend part lifecycles and mitigate unwanted occurrences like crack formation, deformation or creep in the material. To maintain the highest achievable production rate and most efficient use of resources, consistent material homogeneity of components within stark operating conditions is a crucial pursuit.

Titanium and its alloys have become popular contributors within these industries due to their advantageous material properties, e.g. biocompatibility, corrosion resistance and high strength. This said, titanium has poor tribological properties, which restricts its range of applications in environments where friction and wear is prevalent. Titanium's high temperature wear and oxidation resistance is poor and to solve these inefficiencies, surface treatments have been applied to titanium and its alloys. These modifications largely incorporate the use of hardened coatings, like carbide composites, and employ laser beam technologies for application because of its high energy density, coherence and good directionality.

Little research exists on the application of laser additive manufacturing technologies for production of carbide coated parts. In the pursuit to improve the current supply chain capabilities for carbide strengthening and refurbishment, this study investigated the feasibility of depositing tungsten carbide onto titanium parts using laser melting technology. Nickel was employed for the binder material in the cermet as an alternative to cobalt, which is conventionally used for additive manufacturing of hardened carbides. The research study was aimed at designing an experiment to determine which machine parameters result in the optimal adhesion characteristics between titanium alloy Ti-6Al-4V and tungsten carbide in a 10% nickel binder (WC-Ni).

The machine parameters evaluated were the laser power, scanning speed and hatch spacing. The experimentation consisted of both a single-track screening experiment and single layer depositions. From the screening, suitable hatch spacings and a process window for scanning speed and laser power was deduced. These results were incorporated into further experimentation that evaluated layered depositions by varying the three parameters under study. The parameter combinations were tailored to maintain a consistent volumetric energy density range between 28.85 J/mm^3 and 88.33 J/mm^3 to test the individual effects of input parameters at a constant energy input. The evaluated responses were: 1) the surface quality of coatings, 2) penetration and diffusion of the deposition into the substrate, and 3) the consistency of coating material at the substrate interface.

Optimal quality coatings yielded between 20wt.% and 40wt.% tungsten carbide at layer surfaces, while maintaining a layer thickness between 30µm and 60µm; diffusion depths of up to 50µm were also achieved. Higher energy densities resulted in deeper penetration and good diffusion of the coating into the substrate but lacked sufficient presence of the coating material at the substrate surface. It was concluded that higher laser powers and high hatch spacings combined with intermediate scan speeds produced the most desirable coatings. This corresponded to depositions in the energy density range of 28 J/mm^3 and 58 J/mm^3. Furthermore, the validity of the volumetric energy density equation as a predictive metric in laser additive manufacturing was addressed, as significant differences in layer quality were achievable by varying parameter values at identical energy densities.

OPSOMMING

Die kwaliteit spesifikasies van onderdele is van uiterste belang in nywerhede wat hoogs gespesialiseerde toepassings insluit, byvoorbeeld die mediese, lugvaart-, seevaart- en mynbedrywe. Laasgenoemde word toegeskryf aan die hoë koste van die gespesialiseerde onderdele en die risiko's van operasie, soos die verlies van menselewens en maatskappy integriteit, sou die onderdele nie die mas op kom nie. Daar word van die onderdele verwag om konsekwente eienskappe gedurende hul lewensiklus te vertoon, aangesien dit katastrofiese gevolge kan meebring indien hulle nie in lyn is met bedryf spesifikasies nie. Die doelwitte van vandag se onderdeel vervaardigers is, onder andere, om ongewenste gebeurtenisse soos kraak vorming, vervorming of die kruip in die materiaal te versag, om die hoogste haalbare produksie snelheid en die mees doeltreffendste gebruik van hulpbronne te handhaaf. Die konsekwente materiële homogeniteit van die vervaardigde komponente/onderdele in moeilike bedryfstoestande is 'n belangrike strewe in die hedendaagse tyd.

Titaan en sy legerings het gewilde bydraers geword in hierdie nywerhede as gevolg van titaan se voordelige eienskappe, bv. Bio-verenigbaarheid, korrosie weerstand en hoë sterkte. Dit gesê, moet mens titaan het swak tri-bologiese eienskappe ook in ag neem, welke eienskappe sy toepasbaarheid beperk in omgewings waar wrywing en slytasie algemeen voorkom. Titaan se slytasie in hoë temperature en oksidasie weerstand is baie swak en om hierdie tekortkoming op te los, word oppervlak behandeling op titaan en sy legerings toegepas. Hierdie oppervlak behandelinge van titaan en sy legerings bestaan grotendeels uit die gebruik van verharde bedekkings, soos metaal komposiete, en gebruik word dikwels gemaak van laserstraal tegnologie vir die toepassing daarvan as gevolg van die hoë energie digtheid en kleefbaarheid.

Daar is min navorsing oor die toepassing van laser toevoegings produksie tegnologie by die vervaardiging van metaal-bedekte onderdele. In die strewe om die huidige verskaffings ketting vermoëns vir die versterking en opknapping van metaal te verbeter, het hierdie studie ondersoek ingestel na die uitvoerbaarheid van die toevoeging van wolfram karbied op titaan-dele met behulp van lasersmelt tegnologie. Nikkel was gebruik as die bindings materiaal in die struktuur as 'n alternatief vir kobalt, wat normaalweg gebruik word vir toevoegings vervaardiging van verharde karbied. Die studie is hoofsaaklik daarop gemik om 'n eksperiment te ontwerp wat bepaal watter masjien parameters die optimale kleefbaarheid eienskappe tussen titaan legering Ti-6Al-4V en wolfram karbied sou bied in ‘n 10% nikkel binder (WC-Ni).

Die masjien parameters wat geëvalueer was is die laser krag, skandeer spoed en luik spasiëring. Die eksperimente het bestaan uit beide 'n enkelspoor siftings-eksperiment en enkellaag stortings. Uit die sifting is geskikte luik spasies en 'n proses vensterd vir skandeer spoed en laser krag afgelei. Hierdie resultate is geïnkorporeer in verdere eksperimente wat lae steekproef afsettings geëvalueer het deur die drie parameters onder die studie te verander. Die parameter kombinasies is aangepas om 'n konstante volumetriese energie digtheid tussen 28,85 J / mm3 en 88,33J / mm3 te handhaaf om die individuele effekte van inset parameters te toets teen 'n konstante energie-inset. Die geëvalueerde antwoorde was: 1) die oppervlak kwaliteit van lae, 2) penetrasie en diffusie van die afsetting in die substraat, en 3) die konsekwentheid van die laagmateriaal by die substraat-koppelvlak.

Optimale kwaliteit van lae het tussen 20wt. En 40wt.% Wolfram karbied by laag oppervlaktes gelewer, terwyl 'n laagdikte van tussen 30µm en 60µm behou word; diffusie dieptes van tot 50µm is ook behaal. Hoër energie digthede het dunner penetrasie en goeie diffusie van die laag in die basis tot gevolg gehad, maar het nie genoegsame teenwoordigheid van die laagmateriaal op die basis materiaal gehad nie. Daar is bevind dat hoër laserkragte en hoë luik spasiëring gekombineer met intermediêre skandeer snelhede die mees wenslike oppervlakbedekking geproduseer het. Dit stem ooreen met afsettings in die energie digtheid berekening. Verder is die geldigheid van die volumetriese energie-digtheid vergelyking as 'n voorspelling metriek in die vervaardiging van laseradditiewe aangespreek, aangesien beduidende verskille in laagkwaliteit bereikbaar is deur verskillende parameterwaardes by identiese energiedigtheid.

ACKNOWLEDGEMENTS

First and foremost, I would like to thank the financial support received from the Department of Science and Technology in partnership with the National Research Foundation. Furthermore, the Industrial Engineering Department of Stellenbosch University, the Centre of Excellence in Strong materials at Wits University, and the Centre for Rapid Prototyping and Manufacturing at the Central University of Technology for their support in providing equipment and expert knowledge.

I would also like to express my sincere gratitude to for the following individuals who have supported me throughout the past two years and put up with my stress induced antics.

My supervisors, Professor G. A. Oosthuizen and Professor N. Sacks, for their valuable insights, guidance and aid in securing funding to make this project a reality.

Martin Bezuidenhout, Devon Hagedorn-Hansen, Carlo Olivier, Emad Uheida and De Wet du Toit for their constructive support and aid on both an academic and personal level. Their insights and ability to play the devil's advocate helped me to iteratively conceptualise my ideas into a practical research effort.

The Stellenbosch Technology Centre (STC-LAM) and its staff for the use of their facilities and help in producing crucial experimental components.

My friends and family for their undying support and, specifically my parents and my sister Claudia, whom have loved, encouraged and believed in me throughout each endeavour I choose to pursue.

CONTENTS

LIST OF FIGURES

LIST OF TABLES

GLOSSARY

3DP	Three-Dimensional Printing
AM	Additive Manufacturing
AMTS	Advanced Manufacturing Technology Strategy
BCC	Body Centred Cubic
BIS	Beam Interference Solidification
BPM	Ballistic Particle Manufacturing
CAD	Computer Aided Design
CAF	Central Analytical Facilities
CCC	Circumscribed Central Composite
CCD	Central Composite Design
CCF	Face Centred Central Composite
CCI	Inscribed Central Composite
CMC	Ceramic Matrix Composite
CP	Commercially Pure
CRPM	Centre for Rapid Prototyping and Manufacturing.
CSIR	Council for Scientific and Industrial Research
CUT	Central University of Technology
CV	Clad Zone
DMLS	Direct Metal Laser Sintering
DoB	Drop-on-Bed
DoD	Drop-on-Drop
DOE	Design of Experiments
DP	Dual Property
EDS	Energy-dispersive X-ray spectroscopy
ELI	Extra Low Interstitial
ES	Electrosetting
FCC	Face Centred Cubic
FDM	Fused Deposition Modelling
GARPA	Global Alliance of Rapid Prototyping Associations
GDP	Gross Domestic Product
GPD	Gas Phase Deposition
HAZ	Heat Affected Zones
HC	Hybrid Composite
HCP	Hexagonal Close Packed
HE	Higher Education
HIS	Holographic Interference Solidification
HV	Hardness Vickers
IZ	Interfusion Zone
LC	Laser Cladding
LENS	Laser Engineered Net Shaping
LM	Laser Melting
LMD	Laser Metal Deposition

LOM	Laminated Object Modelling
LTP	Liquid Thermal Polymerisation
MAZ	Machining Affected Zones
MMC	Metal Matrix Composite
MS	Mean Squared
MSE	Mean Squared Error
NC	Numerical Control
NDP	National Development Plan
OEM	Original Equipment Manufacturer
PDS	Product Design Specifications
PH	Potential of Hydrogen
PM	Powder Metallurgy
PMC	Polymer Matrix Composite
PSD	Particle Size Distribution
R&D	Research and Development
RAPDASA	Rapid Product Development Association of South Africa
RP	Rapid Prototyping
RP	Rapid Prototyping
RPD	Rapid Product Development
RSA	Republic of South Africa
SDM	Shape Deposition Modelling
SED	Specific Energy Density
SEM	Scanning Electron Microscopy
SGC	Solid Ground Curing
SL	Stereolithography
SLM	Selective Laser Melting
SLS	Selective Laser Sintering
SMS	Selective Metal Powder Sintering
SS	Sum of Squares
STL	Solid to Layer
TD	Total Depth
TGM	Thermal Gradient Mechanisms
TRS	Transverse Rupture Strength
TS	Tensile Strength
TV	Toevoeging vervaardigingstegnologië
UC	Ultrasonic Consolidation
USA	United States of America
UTS	Ultimate Tensile Strength
UV	Ultra Violet
VED	Volumetric Energy Density
WIP	Work in Progress
YS	Yield Strength
Nd:YAG	Neodymium-Doped Yttrium Aluminium Garnet

NOMENCLATURE

Symbol	Description	Units
A	Area	mm^2, m^2, μm^2
A	Powder Material Absorptivity	-
C	Specific Heat	J/Kg·K
d	Coating layer thickness	mm^2
E	Material Influence on Energy Balance	W/m·K
E_d	Specific Energy Density	J/mm^2
ε_{pl}	Expansion due to plastic strain	-
ε_{th}	Expansion due to thermal strain	-
h	Hatch Spacing	mm^2
k	Number of input factors to experiment	-
k	Thermal Conductivity	W/m·K
L	Number of levels an experimental factor is evaluated at	-
N	Number of experimental trials	-
σ'_{comp}	Compression due to tensile stress	Pa
σ'_{tens}	Compression due to tensile stress	Pa
P	Laser Power	W
T	Temperature	°C
v	Laser Scanning Velocity	mm/s
$\mathbf{W_H}$	Island Scan Strategy Height	mm
$\mathbf{W_V}$	Island Scan Strategy Width	mm
α	Significance level upon determining confidence interval	-
α	Distance of star points from centre point in CCD	-
ε	Heat accumulation factor due to track overlapping	-
λ	Laser Wave Length	µm
ρ	Density	Kg/cm^2
φ	Energy input per unit time	W/s
ϕ	Scan track overlapping rate	%

CHAPTER 1

1. INTRODUCTION

This chapter identifies the problems addressed throughout the research project, along with appropriate opportunities that may be exploited by the final concept. A clear framework of realistic objectives is also included to aid in tracking progress throughout the limited research time frame provided.

1.1 BACKGROUND & MOTIVATION

In modern industries, continuous product and process innovation is necessary to stay relevant in competitive environments. As product designs evolve so does the need for the new materials and manufacturing techniques to bring them to life [1]. There is a continuous pursuit for improved performance, specified by criteria like higher strength to weight ratios, cost effectiveness, and multiplicity of applications. Composite materials are a promising solution to this cycle, and it's diversity of material combinations adds to its adaptability in varying environments [2]. Today a variety of constituent combinations may be utilized to create composites that can cater to distinct design requirements. Predictions suggest that the demand for such materials will increase consistently as designs become more daring and complex, with emphasis on those useful in hostile environments or in highly specialized fields [2].

In the same manner that requirements for specialized materials have shaped the composite industry, the need for innovative production techniques to accommodate them has led to the rise of additive manufacturing (AM). AM has garnered remarkable praise from both industry and academia for the mass of applications it can cater to in a variety of fields. It includes a collective of flexible, resource-efficient and cost-effective technologies that facilitate the fabrication of multifaceted parts that range in size from sub-micrometre to several meters [3]. AM technology is easy to use, reliable, and can produce parts from a multitude of materials. In combination with composite technology, new research avenues are exposed relating to 3D engineered materials that display multi functionality and superior mechanical properties [3].

Cemented tungsten carbide parts have a range of applications; the material is extremely hard which makes it popular in applications that require good wear resistance. Consistent innovation in fields such as manufacturing, agriculture, and mining is present as companies aim to improve their manufacturing technologies and gain a competitive advantage. The South African mining sector contributes to 18% of the GDP and over 50% in foreign exchange earnings [4]. This sector alone contains a wealth of opportunities for organizations with the upper hand in research and development (R&D) departments to acquire larger market shares. Compared to conventional manufacturing techniques, additive manufacturing, is characterized by superior process flexibility and the ability to produce complex geometries with relative ease. These capabilities represent a powerful advantage in R&D and present the opportunity to decrease the lead time for new concepts to transition from the prototyping phase to full product rollout.

Little research has been conducted concerning the application of laser melting (LM) additive manufacturing technologies for production of carbide coated parts. This branch of AM includes powder-based processes such as selective laser melting (SLM), selective laser sintering (SLS), liquid

phase sintering (LPS) and laser cladding, which all utilize high powered laser energy to consolidate powder materials into final geometric parts. This study investigates the possibility of manufacturing tungsten carbide nickel (WC-Ni) reinforced titanium parts with laser additive manufacturing.

Titanium is utilized in a variety of industries due to its corrosion resistance, high strength to weight ratio, high temperature load bearing capabilities and elasticity compared to tool steels. Though during operation in stark environments titanium parts are prone to inhomogeneous heat dissipation. This results in heat affected zones where microstructural differences create nucleation sites from which cracks propagate. These effects are accelerated if parts are constantly subjected such conditions and limits the extent to which titanium's high temperature strength may be exploited.

To increase part reliability in hostile conditions, titanium is often combined with composite carbide coatings comprised of hard carbide particles bonded together by a metallic binder. In the most common structure of cemented carbides currently in vogue, there is a hard phase of tungsten carbide (WC) held together by a metallic matrix phase of cobalt (Co). Current research ventures in this field are aimed at finding alternative constituents to the conventional WC-Co system, by either the partial or complete replacement of the cobalt binder or the replacement of WC by more durable Titanium derivatives. Initial research efforts were aimed at finding loopholes for patent restriction, yet more recently to accommodate material scarcity or developmental efforts. Binder alternatives include metals such as iron (Fe), chromium (Cr), nickel (Ni), molybdenum (Mo), or combinations thereof. Hardened phase replacements generally consist of tantalum carbide (TaC), titanium carbide (TiC), or niobium carbide (NbC) derivatives. [5].

The cermet material in the proposed study is comprised of Tungsten Carbide within a Nickel binder phase (WC-Ni). This alloy is dense, hard, well bonded and suitable for use in high stress environments. Compared to popular Tungsten carbide alternatives such as those within a cobalt binder, WC-Ni is more ductile and less prone to chipping. It also boasts with both a higher resistance to saltwater and higher fatigue strength than traditional chrome protective layers [5].

Due to consistent innovation in industries that frequently use titanium parts, companies with superior research and development efforts often have the upper hand. Production of specialized parts with AM has received widespread attention as of late. It's superior flexibility and supply chain capabilities can accommodate rapid levels of innovation and prototype generation. This research venture will investigate the feasibility of reinforcing a Titanium substrate with a Tungsten Carbide – Nickel alloy, utilizing laser additive manufacturing technology (AM).

1.2 PROBLEM STATEMENT

Titanium's resistance to oxidation and corrosion significantly decreases at higher temperatures. Poor tribological properties further hinder the extent of its applications in high temperature wear environments. A popular surface modification method to improve these qualities in titanium and its alloys is laser cladding. Laser cladding is an additive manufacturing process and popular coating solution, capable of producing dense microstructures and strong metallurgical bonds with the substrate material. It is often used to improve the high temperature oxidation resistance and wear resistance of parts. Though, laser cladding lacks the surface quality and dimensional accuracy for smaller parts of complex geometrical shape. The novel technology of selective laser melting has been proposed for coating and reinforcement on smaller scale. The SLM process is based on similar laser physics as laser cladding but allows for processing with greater dimensional accuracy and geometrical complexity [6].

Novel materials have recently been investigated to replace the conventional hard carbide system. In the WC-Ni system, good solubility of tungsten in nickel, its potential for corrosion resistance and improved ductility compared to WC-Co has popularised its use in new alloys. Processing windows have been established for various materials in laser additive manufacturing, yet little research exists on WC-Ni and the deposition of coatings [7].

Preliminary investigations suggest the possibility of producing tungsten carbide layers on tool steel parts utilizing selective laser melting, proven in a prior study conducted by van Staden [8]. Additionally, a study involving the selective laser melting of tungsten nickel (WNi) hard metals have indicated favourable microstructural developments during processing of the material combination [9].

Despite confirmation that SLM has this capability, there is still much left to be researched regarding the process' feasibility and the integrity of titanium parts reinforced in this manner.

The effects of processing parameter combinations on important part properties of the parts are unknown, such as the surface quality of coatings, the coating composition and adhesion between the substrate and reinforcement layer. The bonding mechanisms between the deposit and substrate materials require investigation to determine whether post processing operations are required to achieve standardized specifications for coated parts.

1.3 RESEARCH METHODOLOGY AND OBJECTIVES

The objective of this paper was to utilise laser powder bed fusion to evaluate the effects of process parameters on single layer WC-Ni coatings on wrought Ti6Al4V. Commercial WC powder containing 10% Nickel binder was used as the coating material. Primary process parameters evaluated were laser power, scanning speed, and hatch spacing. Ranges of process parameters investigated for single layer coatings were identified through single-track screening experiments.

Ti-Al6-V4 was chosen due to its good coating adhesion, availability and widespread industry applications. By conducting a thorough literature study pertaining to powder metallurgy, laser technology and various strengthening techniques already employed within industry, a suitable powder grading of WC-Ni was selected for the experiment. Knowledge gathered from further literature review and expert insight were translated into an experiment, designed to determine a response surface that characterises coating quality when using the selected powder.

A single-track screening was first conducted to identify a parameter window suitable for layered depositions. The tracks were analysed qualitatively based on criteria specified throughout literature and quantitatively in terms of track width and penetration depth into the substrate. Layered depositions were then produced within this parameter window by varying critical machine parameters proven to have a significant influence on the quality of final layers, namely, 1) scanning speed, 2) laser power and 3) hatch spacing.

Hereafter the bond ability, and phase representations were analysed, these characteristics were utilized to identify the cause and effect relationship between set machine parameters and the quality of diffusion between the carbide layer and substrate. These findings may be extrapolated to make informed assumptions of the carbide layer's fitness for use as a protective coating material.

The following are research objectives the study aimed to achieve throughout its major assessment areas. Figure 1-1 integrates the methodology and objective phases into a visual representation of the study.

- Phase 1: Understand
    - Identify and evaluate conventional Ti-6Al-4V surface treatments.
    - Investigate the advantages of utilizing a Nickel binder matrix instead of Cobalt.
    - Identify primary SLM parameters that will affect substrate adhesion.
- Phase 2: Experiment
    - Investigating how varying SLM parameters affect part integrity with regards to:
        - Coating surface quality
        - Coating diffusion
- Phase 3: Analysis
    - Measure the surface composition of coatings
    - Measure surface quality of deposited coatings i.t.o cracking and geometric integrity.
    - Study the diffusion of materials surrounding the interface and look for correlation with the parameters utilized throughout the process

- Phase 4: Conclusion
    - Conclusions will be drawn by integrating the knowledge from prior research and the experimental findings from the project at hand.
    - Findings will be translated into a framework for depositing WC-Ni onto Ti-6Al-4V with laser additive manufacturing, based on the material grading and machine parameters evaluated.
    - Recommendations and areas for future investigation will be highlighted.

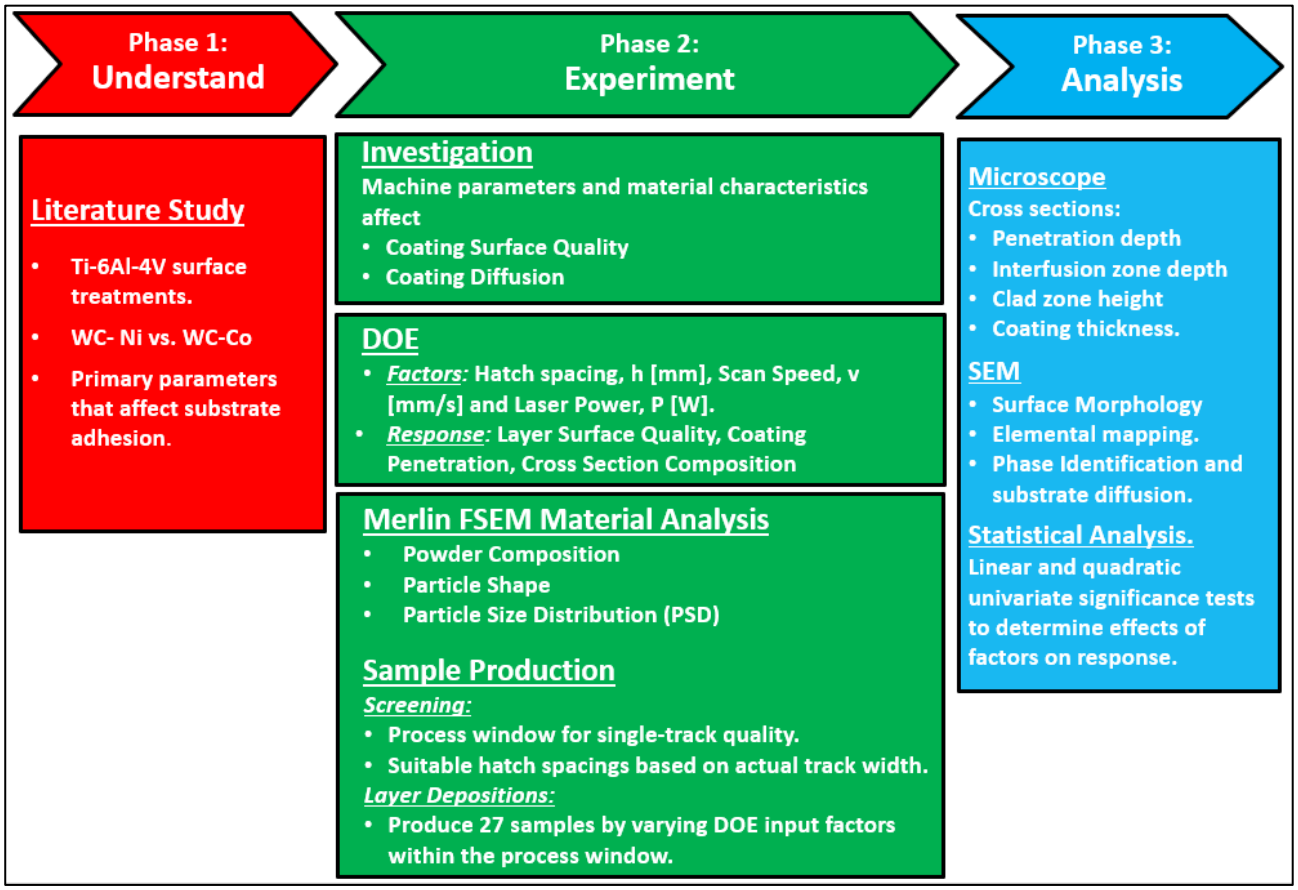

FIGURE 1-1: METHODOLOGY OF THE RESEARCH STUDY

CHAPTER 2

2. ADDITIVE MANUFACTURING

This chapter reviews the background of the additive manufacturing industry, both locally and globally. It also provides an overview of popular AM technologies and the processes they are comprised of. In combination with the literature on composite materials throughout Chapter 3, a research article was composed and submitted for the annual Rapid Product Development Association of South Africa (RAPDASA) conference proceedings. The article, *A Review of Composite Materials Produced with Additive Manufacturing,* is attached in Appendix M.

AM technology is a disruptive manufacturing enterprise that is shaping the future of customizable products, available on demand with unique and instantaneous design distribution. The technology was originally invented in the early 1980s and developed into a niche market for mock-up and rapid prototyping (RP) manufacturing purposes. According to Pham and Gault [10], RP technologies gave birth to the concept of additive manufacturing, originally described by two classes, i.e. processes that entail the removal of material (subtractive manufacturing) and those concerned with material addition (additive manufacturing).

Material removal processes start with a bulk amount of input material which is worked and machined to remove the excess, and ultimately leaves the desired geometrical part intact [11]. On the contrary, AM is based on the exact opposite principle, wherein the required geometrical shape is built from the bottom up by the layered addition of consecutive material deposits in precise geometries. Theoretically, any conceivable shape could be manufactured with meticulously precise tolerances using material addition technologies [8]. Figure 2-1 includes a classification of rapid prototyping methods adapted from [10].

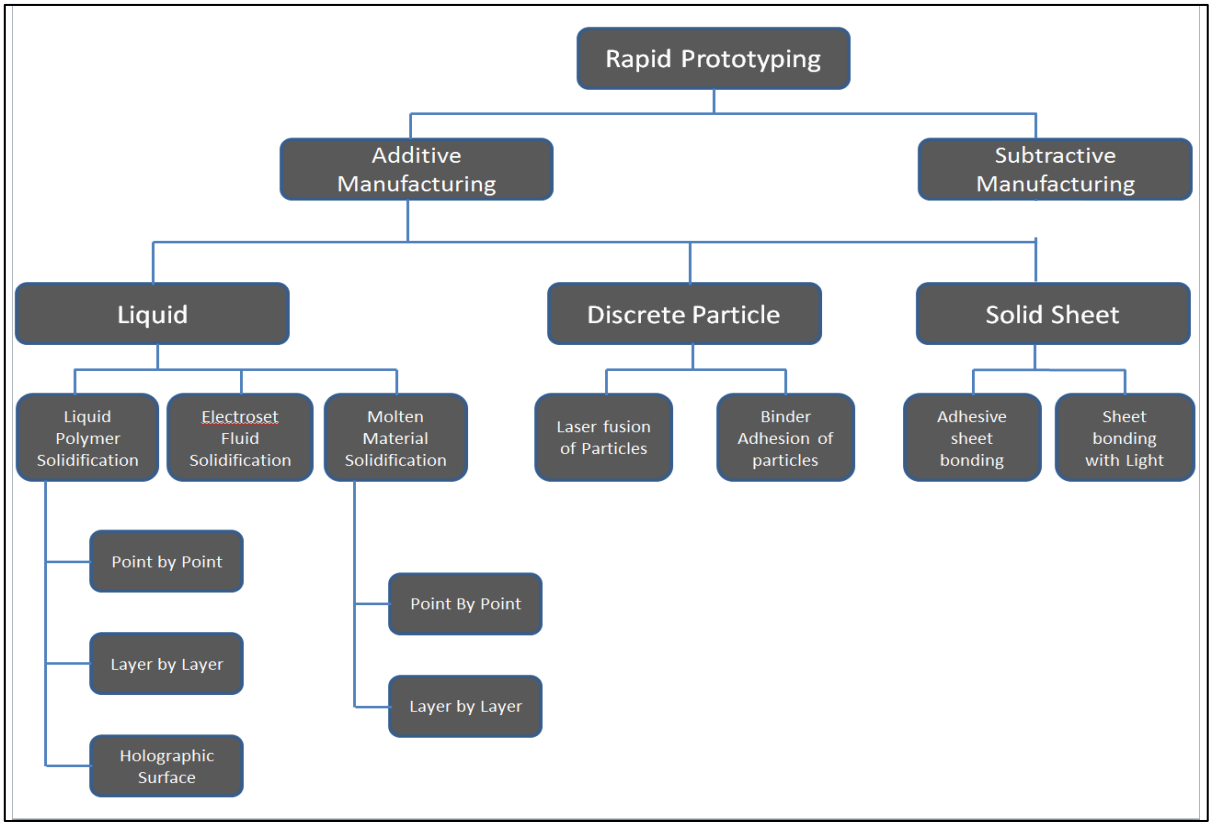

FIGURE 2-1: CLASSIFICATION OF RAPID PROTOTYPING METHODS ADAPTED FROM [10].

Prior to the popularization of AM, design concepts were iteratively produced by hand with engineering drawings and conventional machining procedures such as turning, grinding and milling. This meant that even prototyping phases of new concepts were time consuming and skilled labour intensive [12]. AM quickly replaced such prototyping activities due to its capability to produce accurate models with minimal resource requirements [8].

Although the technology does not yet have a disruptive impact on the South African (SA) economy, its global influence is clear. It has established itself as an alternate to many conventional manufacturing processes, capable of supplementing or replacing existing process chains to improve efficiency [13]. It is also no longer limited exclusively to prototyping. New 3D printing applications and materials have developed, expanding the opportunities available for appropriate manufacturing systems within the global manufacturing market, adding to their popularity and demand throughout industries like medical, tool-and-die, aerospace and automotive production [14].

In 2009 the expiration of key patents concerning the technology allowed several start-ups to surface, offering affordable consumer-oriented AM services. A media craze surrounding 3D printing in 2012, propelled it into the limelight and stimulated rapid growth in the industry. Growth of the worldwide 3D printing market is estimated to escalate from a $1.71 billion industry in 2011, to upwards from $ 10.8 billion in 2021 [15].

Swift industry growth occurred primarily for smaller companies requiring in house Rapid Prototyping (RP) capabilities. This can be attributed to two major factors, namely: the improved purchase cost of machines, and notably lower annual maintenance costs (AM machinery maintenance costs being only 20% - 50% of that of high-end machinery). Better part quality and more precise material handling capabilities were also significant contributors [16].

Even though machine costs are improving as the technology matures, the initial investment costs associated with 3D machines and their materials remain relatively high when compared to subtractive manufacturing (SM). To wholly reap the benefits of their effectiveness, while keeping costs at a minimum, integration frameworks have been developed to inspire collaboration between subtractive manufacturing and additive manufacturing. [13].

2.1 ADDITIVE MANUFACTURING IN A SOUTH AFRICAN CONTEXT

The Republic of South Africa (RSA) has a peculiar set of socio-economic circumstances. Due to its recent emergence from economic isolation, it is subject to considerable wealth inequalities between class boundaries. It boasts with developed regions focused on consistent innovation, but this is contrasted by regions with poorly developed infrastructures. Despite these contrasts, South African industries have been focused on modernization in an effort to contribute to The National Development Plan's (NDP) objectives of increased growth, employment, exports and government revenue [17].

In 1991 the very first rapid prototyping (RP) system was introduced in South Africa, owned by the Council for Scientific and Industrial Research (CSIR). The CSIR is a government supported organization responsible for innovation in various scientific fields. Over the following years as the number of AM machines steadily increased, the majority were owned by academic institutions with the aim of inspiring cooperation with industry. Research concerning AM in South Africa started approximately a decade behind the rest of the world [17].

In 1998 the National Research and Technology Foresight Project's Manufacturing Report implored manufacturers to focus on rapid prototyping and tooling as key technologies. They would reportedly assist international competition by speeding up production time. This suggests that the pursuit of innovations in RP technology has been part of the government's developmental strategy for nearly two decades, although the efforts have only become fruitful in recent years [4].

Albeit slightly delayed, In 2004 the Department of Science and Technology developed an additive manufacturing technology road map, working alongside the CSIR, the manufacturing industry, - and academia; plotting the course for South African companies and manufacturers in this “revolution” [18]. Since its implementation, the amount of AM machines in South Africa has increased significantly. In 2009 the totality of machines in ownership already reached an approximate value of US $ 9.25 million [16]. Research in the field has been backed by institutions of higher education in tandem with the CSIR, emphasising application based research to meet industrial needs [19].

New machines are typically funded through government support and a key condition of grants are to inspire industry collaboration. For example, machines are purchased for a specific application whilst being made available to research wider applications that may be transferred to commercial operations. RP research and implementation opportunities have been firmly supported by central government be it via direct funding of RP systems, or through developmental initiatives wherein RP plays a fundamental role. The National Product Development Centre at the CSIR is the central node in a network of initiatives aimed at supporting the manufacturing industry and ultimately benefitting South African product developers [19].

RAPDASA has singlehandedly made the most significant contributions in raising awareness for rapid prototyping technologies, these include annual conferences to inspire progress from both industry and academia and links with the Global Alliance of Rapid Prototyping Associations (GARPA) [14]. The organization was formed in 1999 to act as a representative for those involved in all aspects of the b local rapid product development (RPD) community. Members hail from both academic organizations and industrial companies and RAPDASA promotes this diversity in its core governance [20].

2.2 AM TECHNOLOGY OVERVIEW

The technology includes several novel processes for printing three-dimensional objects from computer aided design (CAD) - files, 3D model or other electronic data source. Objects can be of almost any geometry and designs distributed online with ease. The process builds objects layer by layer from thousands of cross-sectional fillets measured from a CAD-file. AM machines compile fine layers of molten material in a precise pattern, which hardens and allows for successive layers to be deposited onto each other and built into specific three-dimensional geometries. Once an entire object has been manufactured, excess material is removed via a chemical bath or specific post processing techniques [21].

Advantages of AM are that it enables the production of low cost, highly customizable goods, while integrating with CAD software with ease. After an object has been created with commercial design software like SolidWorks or Autodesk, an STL (industry-standard solid to layer format) file of the design can be generated. This enables the user to simply print the part in the same manner as using a desktop printer [21]. This simplicity has propagated successful attempts to integrate AM into conventional process chains, with continuous development of frameworks that facilitate the incorporation of the technology to improve production [13].

The technology is considered to be the pinnacle of integration between material sciences, laser technology, and mechanical engineering [8]. Addition processes occur in one of three material states, namely: 1) Powder, 2) liquid, or 3) solid [10]. The technology has been further classified in relation to three material deposition techniques: Continuous printing, Drop-on-Drop (DoD), and drop-on-Bed (DoB) printing. The latter two are collectively referred to as Drop-on-Demand Printing. The relationships between classifications is illustrated in Figure 2-2 [22].

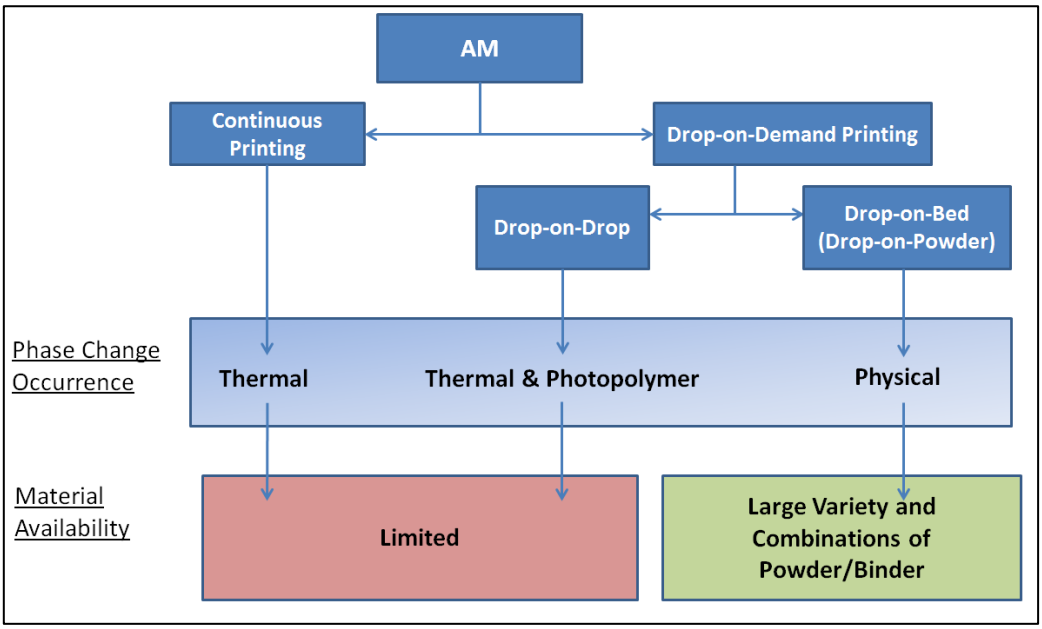

FIGURE 2-2: A SUMMARY OF ADDITIVE MANUFACTURING TECHNOLOGIES [22].

In Drop-on-Drop and continuous printing, the range of manufacturing materials is limited by their fluid printability and intended application. Drop-on-Bed printing offers an extensive range of printable materials. (nearly any material that can be transformed into a powder state). Drop-on-Bed printing may be used to transforms the powder into a solid by melting it together in pure form or utilizing a binder material which provides an adhesive matrix for materials that are difficult to melt without excessive energy input [22]. This shifts the burden to finding an appropriate binder material, in contrast to finding specific materials that corresponds to the limitations of the technology itself.

AM offers specific competitive advantages over standard manufacturing technologies, such as improved material flexibility and geometrical freedom, but it is no way intended to replace these well-established processes. Variable wall thicknesses., zero draft and other geometrical capabilities not tolerated by conventional manufacturing processes can be achieved with relative ease utilizing AM technology [8].

From a financial outlook, costs throughout the manufacturing supply chain may be reduced by 70% with the use of AM technologies. In addition, the total time to market may be reduced by up to 90%. This is due to minimal levels of waste generated by AM processes. By only using the exact amount of material required to produce a part, the total mass of materials required for production is minimized, and waste disposal costs are eliminated almost entirely. Should manufacturers decide to recycle scrap materials by recovery, processing and reuse, cost reductions may be increased even further [23].

These revolutionary technologies are reshaping entire manufacturing supply chains, but there are always issues associated with emerging technologies. Drawbacks include material limitations, economic feasibility and technology adoption by the public [8]. Base materials and their processing parameters still leave much to be desired for application purposes. Process accuracy can also be improved along with part design methods. Lastly in order for AM technology to be accepted into mainstream manufacturing culture the cost effectiveness of materials and machinery need to be addressed [8].

AM operations improve the responsiveness and reliability of an agile supply chain. Not only is tool changing is eliminated, but the number of assemblies and the time required for setup and changeovers are reduced. Complex part production only requires 3D data and raw material input. These simplifications reduce the need for warehousing, transportation and packaging operations [24]. AM is a highly standardized production activity and does not require a precision skillset, but only knowledge of how to operate machinery, which reduces labour costs significantly. Additionally, its multi-platform design sharing capabilities reduces design phase expenses.

The conventional manufacturing supply chain requires inputs from various industries to deliver products to customers. This includes retailers, logistics services, distributors, component procurement, raw material suppliers and equipment manufacturers; AM technology has the capacity to limit the number of phases present in the traditional supply chain and their associated costs [25]. This simplification reduces material distribution of work-in-progress (WIP) inventory, lowering inventory-holding costs. Additionally, both component parts and products required can be stored in stock as reduced value raw materials, which also eliminates the risk of obsolescence in part or product designs.

The popular consensus regarding AM technology is that it has more beneficial environmental characteristics than standard manufacturing methods as most only utilize the amount of material needed for production, reducing energy consumption and lifecycle material mass drastically when compared to conventional subtractive manufacturing. AM eliminates the main sources of hazardous pollution in the subtractive manufacturing waste stream; engineered scrap materials and harmful ancillary process inputs, such as cutting fluids. In addition, its use releases limited aerosol or liquid residues and material can be melted and reused minimizing pollution in terrestrial, aquatic, and atmospheric systems [26].

AM systems have a unique operating style and system complexity compared to that of conventional production. The ATKINS project [27]. conducted a widespread comparison of AM with alternate manufacturing processes concerning virgin material use, landfill usage, energy usage, and water usage. The study concluded that AM has distinct advantages in terms of environmental impact, although it indicated higher levels of energy consumption compared to conventional processes. Results are summarized in Table 2-1.

TABLE 2-1: A SUMMARY OF ENERGY USE AND ENVIRONMENTAL IMPACT COMPARISON BETWEEN ADDITIVE MANUFACTURING AND FLEXLINE MACHINING PROCESSES. INFORMATION SOURCED FROM [27].

Environmental Impact areas (kg per component)	AM impact	Conventional machining (Flexline)
Energy use (kg CO_2)	13.15	2.4
Water usage	0	0.08
Landfill waste	0	1.512 (Recyclable wastes)
Virgin Material	0.65	2
Hazardous waste	0	0.0064

There are clear environmental advantages associated with AM, however, these new processes may result in alternate health problems. Little research has been conducted on the environmental and toxicological hazards associated with additive manufacturing. Such investigations could possibly be a catalyst for research and development in the industry, which would lead to acceptance from the general public [25].

Numerous studies conducted on AM processes and their associated materials conclude that operators are at moderate risk when meeting the chemicals, either by vapour inhalation or material spillage on the skin. Side effects include soft tissue irritation and allergic skin reactions. No evidence indicates that prolonged exposure could be fatal, but it may induce chronic allergies. Production also releases noxious gasses; carbon dioxide (CO_2), carbon monoxide (CO), and nitrogen oxides emanate from processes after the breakdown of AM materials [28], although the effects of these emissions may be mitigated via proper operator training, safety masks and gloves.

Despite remarkable recycling capabilities, the biodegradability of AM materials is poor, causing non-recyclable materials to stay in the environment for lengthy periods. There is still much room for research regarding the environmental impact and toxicity of raw materials, and the chemical degradability of solvents utilized for post processing [28].

The following sections aim to further describe AM processes according to the input material phase utilized to produce final parts. Several examples of processes that relate to each classification are mentioned throughout. Emphasis will be placed on powder material addition processes, specifically SLM, as the research specimens will be produced with this technology.

2.2.1 Solid Material Addition Processes

Solid material additive manufacturing processes are the most limited of the three variations and are largely restricted to prototyping and modelling purposes. The most popular technology within this classification is laminated object manufacturing (LOM), a process where thin layers of plastic, paper, or metal materials are laminated with an adhesive coating. A hot roller is used to activate a heat-sensitive adhesive which glues the layers in place. The laminates are layered on top of each other and each layer is cut into a specified shape by a programmable laser cutter or knife. Objects produced may be additionally modified post production and part resolution depends on the thickness of the material feedstock [10].

The second, less popular variation of solid material addition is Solid Foil Polymerization, which binds semi-polarized foil sheets together by curing them with Ultra Violet light. Though with the recent developmental trends in advanced AM technologies, LOM processes have become obsolete and are rarely used for its originally intended purposes [10]. Lastly, a more novel technology within the field of solid material addition is Ultrasonic Consolidation (UC). This entails the fabrication of metallic parts from various foils and allows for multi material structures. A source of high frequency ultrasonic energy induces static and oscillating shear forces within metal foils. Solid state bonds are then formed and a near net shape part is built and machined to meet its final dimensional requirements [29].

2.2.2 Liquid Material Addition Processes

There are two key classifications of liquid based additive manufacturing. The first involves the solidification of liquid polymers by light, laser impact or heating, and the second involves the deposition of molten material that re-solidifies into a desired geometry. This second involves a variety of usable materials, including metals, plastics and resins [10]. Table 2-2 summarizes popular liquid-based AM processes.

Table 2-2: A summary of popular Liquid based AM materials [10].

Name	Description.
Stereolithography (SL)	Layers of liquid polymer are additively solidified upon exposure to UV light.
Liquid Thermal polymerization (LTP)	Like SL, except infrared light is used instead of UV light.
Beam Interference Solidification (BIS)	Resin Polymerization is induced by two differing frequency lasers which first excite the liquid before it is polymerized.
Solid Ground Curing (SGC)	Layered masks are created from a CAD-file. The masks are placed over photopolymer resin and exposed to light, causing the exposed resin to solidify.
Holographic Interference Solidification (HIS)	A 3D holographic image is projected into a photosensitive monomer which then solidifies the entire model instead of building it layer by layer.
Electrosetting (ES)	Entails the printing of electrodes onto a conductive base material which is submerged in an ES fluid. Complete layers produced from the object's CAD-file are then placed onto the electrodes and energised. This causes the liquid between layers to solidify.
Ballistic Particle manufacturing (BPM)	Molten droplets of material are applied onto each other. As the droplets contact the substrate material, they are cold welded onto it.
Fused Deposition Modelling (FDM)	Parts are produced via the deposition of molten resin materials that immediately cold weld to the applied surface.
Shape Deposition Modelling (SDM)	Molten material is sprayed onto a substrate base in near net shape, thereafter numerical control (NC) is used to remove excess material.

2.2.3 POWDER MATERIAL ADDITION PROCESSES

The primary principle of powder material addition is the joining of discrete particles utilizing a laser, either melting the powder together, or solidifying it in a binder material [10]. It is considered by many to be the most important branch of AM technology, which is evident due to widespread research efforts aimed at developing innovative, more cost effective alternatives to standard production processes [12]

There are seven popular powder-based manufacturing processes wherein ample research has been conducted; these are included in Table 2-3 below, along with their acronyms and a brief description. This research study is predominantly concerned with selective laser sintering, selective laser melting and laser cladding, which will be discussed in depth in further sections.

TABLE 2-3: SIX PRIMARY POWDER-BASED MANUFACTURING PROCESSES.

Name	Description.
Selective Laser Sintering (SLS)	In this process a guided high-power laser beam selectively scans successive layers of powdered material that has been preheated to a temperature just below its melting point. The bed is scanned where solid material is required; according to the geometric information sourced from the 3D object model. The process can be further classified as either direct metal laser sintering (DMLS) or indirect SLS. It produces porous green parts due to only partial melting of the powder mixture, using either a binding phase (indirect SLS) or an adhesion coating (direct metal laser sintering) to conjoin the hardened particle phase [30].
Selective Laser Melting (SLM)	SLM was developed as an adapted SLS procedure and thus requires similar processing procedures and apparatus to SLS [31]. A laser beam is used to bring a binder-less metallic powder to its melting temperature and the material is fully melted on the laser's entire contact area. SLM operates by delivering a higher incident energy density, resulting in less porous final parts when compared to SLS [12].
Selective Metal Powder Sintering (SMS)	Defined as a subclass of Stereo-lithography, SMS produces porous green parts by focusing an energy source onto an unbound metal powder to melt them together layer by layer. Parts normally require post processing to increase density and strength [31].
Three-Dimensional Printing (3DP)	This Machine utilizes a powder bed and printing head. The head dispenses adhesive polymer resin, binding to the powder and solidifying it. Each successive layer requires another spread of powder. Its defining characteristic is the ability to change the colour of the print during manufacturing, resulting in any combination of colours. Additionally, it can also print movable parts similar to FDM technologies [11].
Gas Phase Deposition (GPD)	Reliant on the solidification of reactive gas particles. The gas molecules decompose into a solid when exposed to either heat or light. The solidified particles then adhere to a substrate material to form the final part [10].
Laser Engineered Net Shaping (LENS)	The LENS process utilizes metal or ceramic powders to produce functional parts with a focused Nd–YAG laser beam. CAD data is translated into a laser scanning path for each layer. The cross sections are created by first melting a pool of substrate material. The powder is injected into the pool as the substrate moves in the X-Y plane. The layers are created by producing an outline of each feature and then filling its cross section with a rastering technique. The process is repeated for each layer until the part is complete [32].
Laser Cladding	A stream of powder material is fed into a high-power laser beam which is scanned across a substrate surface, leaving a coating of the powder material deposited onto the substrate. The laser cladding process provides good bonding between the coating and substrate without inducing high thermal gradients. The process is commonly employed for coating applications, though it is capable of building parts layer by layer [33].

2.3 LASER ADDITIVE MANUFACTURING

Many powder-based AM technologies popularized in recent years are based on laser melting of powder particles. This brought about an array of novel research avenues for materials that are yet to be investigated in this domain. Figure 2-3 below includes a categorization of laser additive manufacturing technologies suitable for producing metallic components. The experimentation in this study is primarily concerned with technologies that incorporate pre-production powder application.

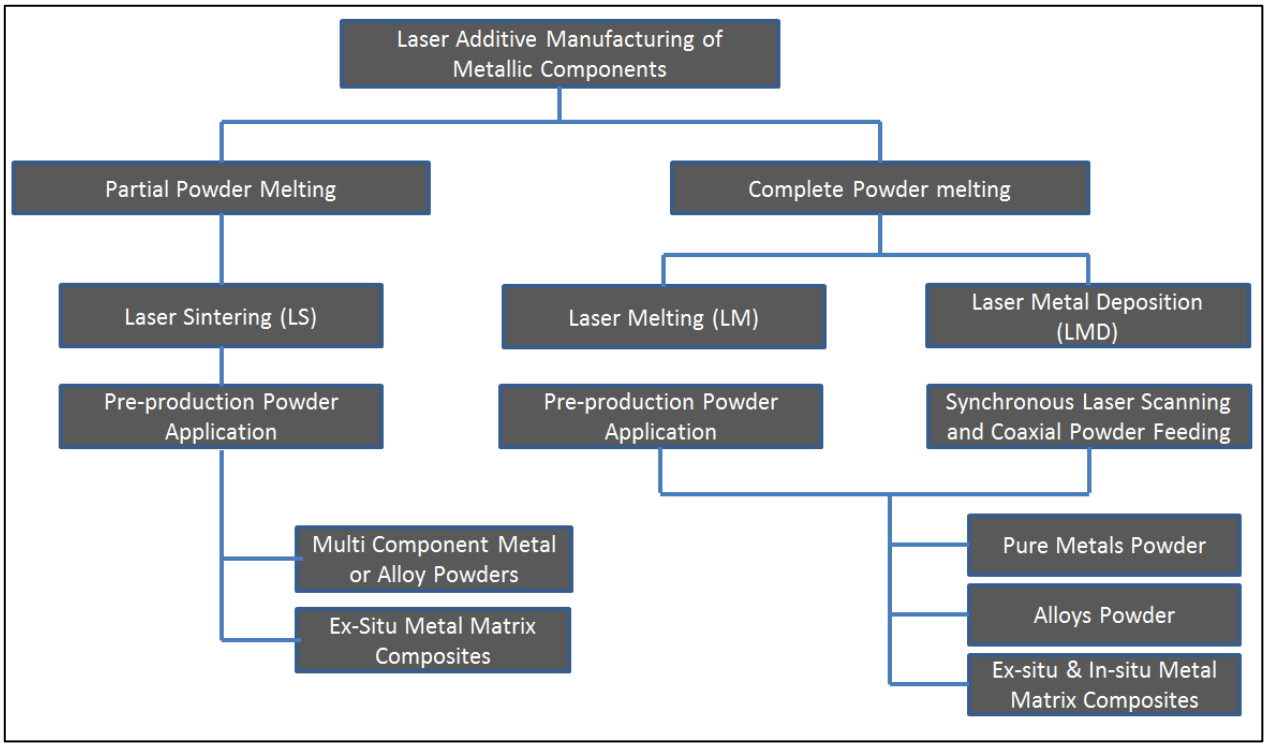

FIGURE 2-3: CATEGORIZATION OF LASER ADDITIVE MANUFACTURING OF METALLIC COMPONENTS

2.3.1 THE DEVELOPMENT OF SLS/SLM

The widespread success of laser sintering (LS) may be attributed to its capability of processing nearly any material type; accommodating various applications. Though, as the material selection progressed to include metals, higher energy density inputs were required to ensure functional parts of adequate densities [30]. This lead to the development of SLM [30]. The core differences between SLM and SLS is that SLM involves the complete melting and solidification of the powder material without the use of a polymer coating or binder to improve adhesion. It is also capable of higher final part densities due to a higher instance energy density [31]. The physics of SLM is similar to that of laser cladding or laser metal deposition technologies. However, these technologies are largely utilised for coating applications where powder is fed into the laser beam path during processing instead of being applied prior.

SLS was developed to promote a more adaptable product cycle that decreases the time and cost associated with prototyping. It entails building layers of a three-dimensional object successively by selectively sintering or partially melting a powder bed using precision laser radiation. The process is further classified into either direct or indirect SLS. The latter of the two utilizes metal grains that have been coated with a polymer, which is melted during the process and acts as an adhesive to fuse the metal grains together. Post-sintering treatments such as furnace treatments are required to eliminate the polymers and create metal-metal bonds between contiguous powder grains. Direct metal laser sintering (DMLS) utilizes no polymer coating, but rather a low melting point metal binder that envelops the high melting point particulate phase in a metal matrix [30].

Both processing variations of SLS produce parts with mechanical properties akin to their weakest constituent phase. Parts produced by these processes often emerge as porous and rigid due to shrinking of the powder mixture after transitioning from a molten liquid to a solidified layer. Temperature variations induce mechanical stresses in final parts, and the density of materials produced with SLS is highly dependent on how the temperature evolves throughout the process. Densities may be improved significantly by adjusting specific process parameters and powder characteristics, or with the addition of post-treatments. Alternatively, SLM accommodates the fabrication of high-density parts without post-processing operations. These parts possess likened material characteristics compared to those produced with conventional machining [30].

SLM manufacturing enlists an array of compatible materials, which has resulted in multiple new metallic powders being developed for use in SLM machinery. The technology is currently regarded as the most versatile of all AM processes with the capability of processing a range of metals, alloys, metal matrix composites, and ceramics. Furthermore, SLM allows for increased process flexibility and production of geometrically complex parts without any tools, whereas conventional manufacturing methods require dedicated tools such as moulds and dies. The technology may open up new avenues for creating innovative new material types to satisfy niche requirements in emerging markets such as hybrid parts [34].

Even so, the process is not yet capable of competing with large lot production of slightly complex parts, as modernized manufacturing techniques have been perfected to be far more cost – and – time efficient. SLM also tends to be more energy intensive, as high laser powers are required to completely melt all phases within the powder material. Most SLM parts are produced directly as final parts or functional prototypes, and commercial applications of the technology are often limited to single part and small batch manufacturing. Despite higher costs for batch production, SLM offers large savings in terms of costs and labour and improved functionality due to infinite geometrical variability [35].

2.3.2 Laser Sintering/Melting Process

The core components in a SLM/SLS machine setup includes a laser system and optical beam focusing set, a powder feed system (comprising of a loader and layer coater), and a central control panel. Many patented machines that have recently emerged essentially serve the same purpose as SLM and SLS, yet they have alternate nomenclature due to legal reasons. For example, LaserCusing ®, direct metal laser sintering, selective laser melting etc. are all distinguishable based on their laser scanning strategies and material selection, yet the core principle of the technologies are very similar [12]. The conventional SLS/SLM machine layout is included in figure 2-4.

The desired geometry is first designed on computer aided design software to produce a file format compatible with the designated machine. The standard graphic file currently used among commercial manufacturers is the STL (solid to layer) format, which provides a meshed map of the external and internal surfaces of the part. Hereafter the system software processes the STL – file to specify the build's orientation and slicing layers. The part is orientated, and a growth direction is selected that will be most beneficial in terms of production time and dimensional accuracy. The step size of each sliced layer governs the smoothness of the final part and breaks it down into orthogonal planes built upon each other in the direction of the build. The contour of each section defines a scanning path for the laser beam and the thickness of the layers [30].

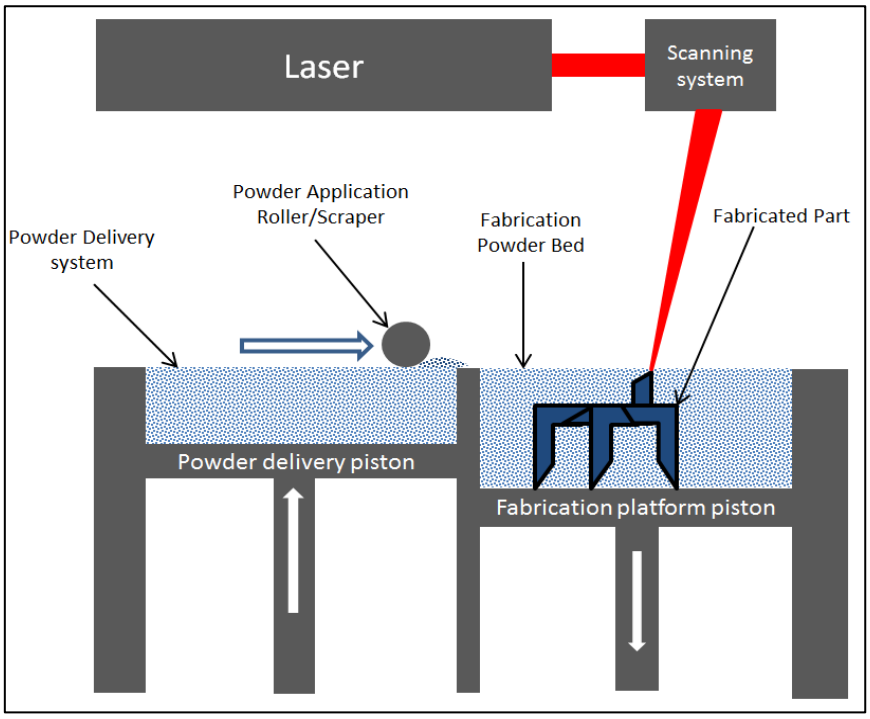

FIGURE 2-4: A TYPICAL SLM MACHINE LAYOUT. ADAPTED FROM [36].

Under an inert atmosphere of argon or nitrogen, the chamber temperature is increased and kept constant close to the powder's melting temperature. This prevents uneven thermal expansion, distortions, residual stresses and unwanted porosity. The pre-heating process is also useful in minimizing laser power requirements. It improves the absorption of the beam and prevents warping during production caused by variable thermal expansions. Better absorption improves the wetting properties of the melt and reduces temperature gradients. The laser induced heat at the surface of the powder causes the binder particles to fuse together and forms a molten pool. This results in a metal matrix composite material layer where the hard particles are entrenched in a binder matrix. The substrate is lowered by a single layer thickness and the powder roller distributes a layer of equal thickness onto the build. The process is then reiterated until the full geometry has been produced [36].

Powder surrounding the part is left in place to support the structure, which eliminates the necessity for support material reinforcement during printing as is required with several AM processes [35]. After printing is completed, a cooling period is essential within the contained environment. If the part is prematurely exposed to an external atmosphere, oxidation may occur, degrading the parts beyond usefulness. Once the specimens are cooled and ready to be handled, excess powder is cleaned off and necessary post-processing operations may be initiated [37].

The process may be tailored to modify microstructural features including texture, grain shape and grain size, however, the machine settings to achieve this vary based on the selected powders and may result in inconsistent mechanical properties for each specific material [37]. As metallic particles are molten entirely, elevated thermal gradients within the material induces residual stresses that lead to part distortion, cracking and delamination [30]. Temperatures often close to double that of the powder material's melting point are required during the SLM process. This results in evaporation of the powder material (commonly the binder phase). Rapid expansion of evaporated particles brings about the ejection of material from the melted zone, due to overpressurization [38].

Isolated spheres similar in diameter to that of the lazer beam's focus may form within the powder material. This is commonly referred to as spheroidization or "Balling". It occurs when surface tention inhibits the the molten material from fully wetting the substrate. It is the result of excessive energy input, that makes the powder low in viscocity.

2.3.3 Laser Metal Deposition

In this AM process, powder is fed into a melt pool formed by a laser aimed at a substrate's surface. The powder and substrate are fusion-bonded together by a high-powered laser, which is shielded by argon gas, and translated across the material surface by a robotic arm or X-Y gantry system. The most popular variant of LMD is Laser Cladding, a technology regularly used for deposition of protective coatings, hard facing, refurbishing and in some cases layered manufacturing of parts [39]. It is capable of coating with a broad array of materials when powder injection technologies are employed and include a number of advantages compared to conventional coating technologies. Figure 2-5 presents a schematic of the laser cladding mechanisms.

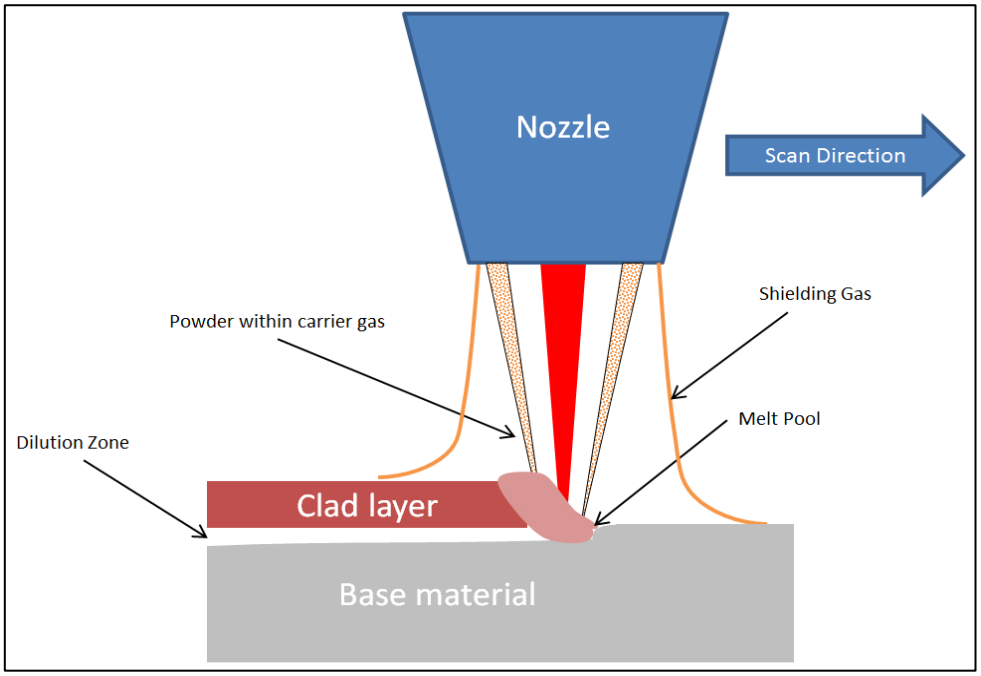

Figure 2-5: A schematic elaborating the laser cladding process [39].

The laser cladding process is favoured over conventional cladding/coating processes such as arc plasma spraying or arc welding. It produces more dense coatings with good metallurgical bonds to the substrate, has improved surface quality, minimal dilution and less distortion. Prominent benefits of the technology include: 1) Reduced production time, especially with regards to prototyping, 2) superior thermal control, 3) tool refurbishment and repair without destructive processes, and 4) functionally graded parts possible by switching the materials injected during processing [39].

However beneficial the technology may be, it is still plagued by certain drawbacks. Such as: poor reproducibility due to sensitivity and lack of shielding during processing, high energy requirements, and poor printing resolution. Compared to laser technologies like SLS/SLM that are based on similar consolidation phenomena, laser cladding is less effective on smaller scale. This renders its extraordinary capabilities to be less effective on beam focus diameters typically less than 0.5mm [40].

2.3.4 Laser Metal Deposition & Laser Melting Comparison

There are several prominent similarities between LM and LMD technologies, especially in terms of the build process, powder requirements and material consolidation phenomena. Though, when energy input, and dimensional capabilities come into play there are clear advantages toward the use of laser melting. On the other hand, LMD shows superiority with regards to processing time and cost. Research by Leyens et al. [41], presented at the annual laser additive manufacturing (LAM) conference, conducted a thorough comparison of SLM and LMD throughout all aspects of the process chain. The conclusion of their research was qualitatively summarised in the radar graph in figure 2-6 below, adapted from [41].

This research is aimed at investigating the capabilities of laser additive technology for surface modifications and coatings. Laser melting and laser sintering have proven to be capable of excellent near net shape production and geometric complexity. These benefits may be exploited to produce coatings on sub millimetre parts with complex structures. There are, however, various aspects of SLS and SLM technology that need to be improved, such as the ability to conduct free form printing on non-conformal surfaces and the elimination of material wastes due to underutilization.

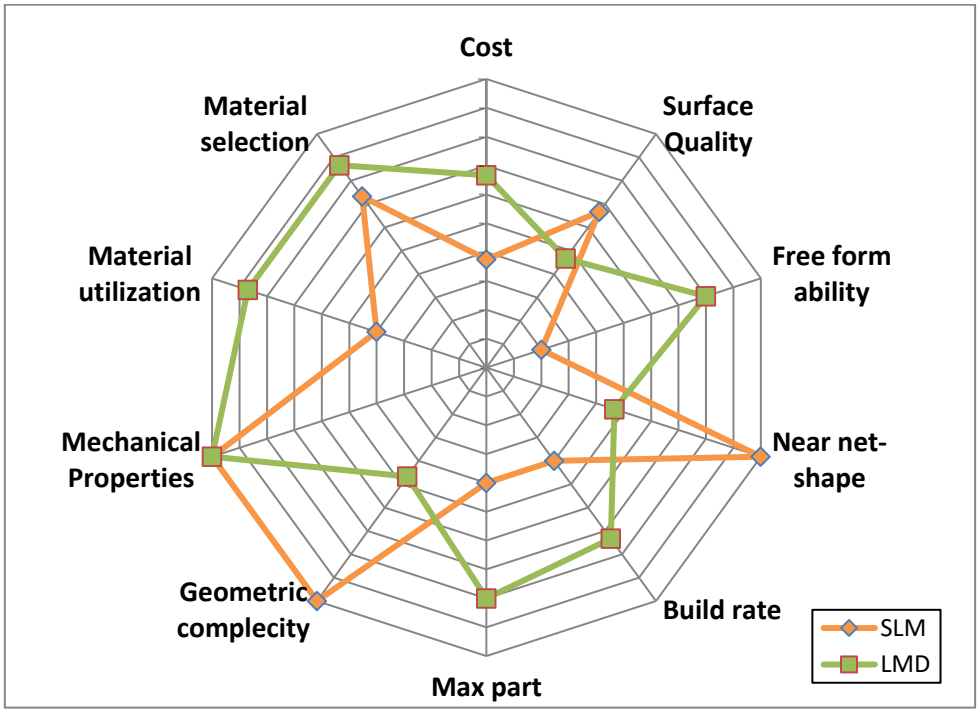

FIGURE 2-6: COMPARISON OF SLM/SLS AND LMD THROUGHOUT ALL ASPECTS OF THE PROCESS CHAIN [41].

CHAPTER 3

3. MATERIAL STUDY

3.1 TITANIUM

Titanium is the fourth most abundant structural metal available, after aluminium, magnesium and iron; accounting for 0.6% of the earth's crust. It was first discovered in 1791 by William Gregor, a British mineralogist, within minerals now recognized as rutile [6]. Commercial production of titanium alloys only kicked off well into the 20th century and has been increasing in popularity since the early 1950's. Its popularity is largely because of its exceptional material characteristics, such as a high strength-to-density ratio, high corrosion resistance and the ability to withstand relatively high temperatures without creeping. Titanium has been the preferred metal for specialised applications in various industries. It is used extensively in the aerospace, biomedical and chemical fields, with new areas of implementation continuously researched and developed [42].

3.1.1 COMMERCIALLY PURE TITANIUM

Also referred to as unalloyed titanium, commercially pure (CP) titanium is comparable to low grade steels in terms of its mechanical properties, but it is only 60 % as dense. CP titanium is rarely used to substitute tool steels due to its lesser availability and cost-effectiveness compared to alternatives with similar characteristics. Unalloyed titanium's exceptional corrosion resistance, non-magnetic properties and biocompatibility has proven its utility in more niche applications [43]. Conditional to the concentration of residual interstitial elements within the material such as O_2, N_2, H_2 and C; unalloyed titanium is divided into four divergent grades. Generally, an oxygen content of 500 ppm or less is present, although advanced electrolytic methods have been used to yield high-purity titanium sponge material. Each grade possesses varying hardness, formability, corrosion resistance or biocompatibility characteristics that prove to be beneficial for different applications [6].

CP titanium is an allotropic element, which means it is capable of existing in multiple forms or structures within the same physical state. These states are known as allotropes of the element. Depending on its surrounding temperature, unalloyed titanium may consist of one of two crystalline structures, namely an alpha (α) – phase and beta (β) – phase. At room temperature (20°C), the α-phase is present, and atoms are arranged in a hexagonal close-packed (HCP) crystal structure. In this state the material density is roughly 4.51 g/cm^3. At temperatures exceeding 882 ± 2°C unalloyed titanium transitions to its β – phase. In this state the crystalline structure rearranges to a body centred cubic (BCC) structure with a lower density of ± 4.35 g/cm^3. [6].

3.1.2 TI-6AL-4V ALLOYS

In 1932 a method for extraction of titanium was discovered in Luxembourg by Wilhelm Justin Kroll. Still known today as the Kroll process, it employs a magnesium reducing agent to facilitate extraction of titanium from unprocessed minerals. The element is commonly alloyed in order to optimize required material properties. Good corrosion resistance, biocompatibility and a high specific strength are key characteristics of titanium alloys, which is why they are often utilized in the medical, aerospace and chemical industries [44]. Of all titanium alloys, Ti-6Al-4V is the most commonly utilized variation. It accounts for more than half of all titanium alloys produced worldwide, attributable to its great popularity within the aerospace industry. An estimated 80% of all Ti-6Al-4V production is dedicated to aerospace uses,

overshadowing other prominent applications in the medical prostheses, chemical, marine and automotive industries [6].

By altering the contents of impurities or interstitial particles such as aluminium, vanadium, carbon, iron, hydrogen, nitrogen and oxygen within the alloy, certain characteristics of the material may be tailored. Table 3-1 indicates common compositional ranges of Ti-6Al-4V by weight percentage. Increasing the presence of these elements coincides with an increase in the alloy's strength but leaves it more vulnerable to corrosion. Alternatively, when decreasing the concentration of interstitial particles, the material becomes tougher, more ductile, and resistant to stress corrosion and crack propagation. Extra low interstitial (ELI) grades of Ti-6Al-4V are commercially available, wherein reduced levels of oxygen and iron induce higher damage tolerance in the alloy, especially beneficial at cryogenic operating temperatures. Furthermore, to enhance corrosion resistance, palladium may be added to the alloy to form Ti-6Al-4V-Pd.

TABLE 3-1: COMPOSITION % BY WEIGHT OF INTERSTITIAL ELEMENTS IN TI-6AL-4V [43].

Compositional elements	% Range (By Weight)
Aluminium (Al)	≤ 6.75
Vanadium (V)	≤ 4.5
Iron (Fe)	≤ 0.4
Oxygen (O)	0.08 – 0.25
Carbon (C)	≤ 0.08
Nitrogen (N)	≤ 0.05
Hydrogen (H)	≤ 0.015

Ti-6Al-4V is produced in several forms, conventionally available as powder metallurgy (PM), cast, or wrought products. Depending on the interstitial contents and thermal processing of the alloys, the properties of each form may vary widely. Wrought Ti-6Al-4V samples will be used within this study as a substrate material to be reinforced with a tungsten carbide nickel layer.

TI-6AL-4V MICROSTRUCTURE DURING SINTERING

It is crucial to study the microstructures of materials in order to define their mechanical properties and predict behaviour during working conditions. This enables the capability of tailoring materials to fit specific product design specifications (PDS). These PDS are used as a guideline to determine which production parameters and post processing techniques will achieve a microstructure with properties that fit the desired application. Whilst avoiding properties that may reduce the product's operating lifetime [45].

Due to Ti-6Al-4V being an alpha beta alloy, specimens may have differing volume contents of alpha and beta phases depending on prior treatments and interstitial particle contents (primarily oxygen content). Ti-6Al-4V is available in an assortment of microstructures, comprised of various geometrical alpha and beta phase morphologies, which are strongly dependant on the thermo mechanical treatments the material undergoes. The various microstructural arrangements may be summarized into three categories, namely, equiaxed, lamellar, or bimodal (hybrid), however various complex variations occur as hybrids of these categories. Microstructural examples of each are indicated in figure 3-2 [46].

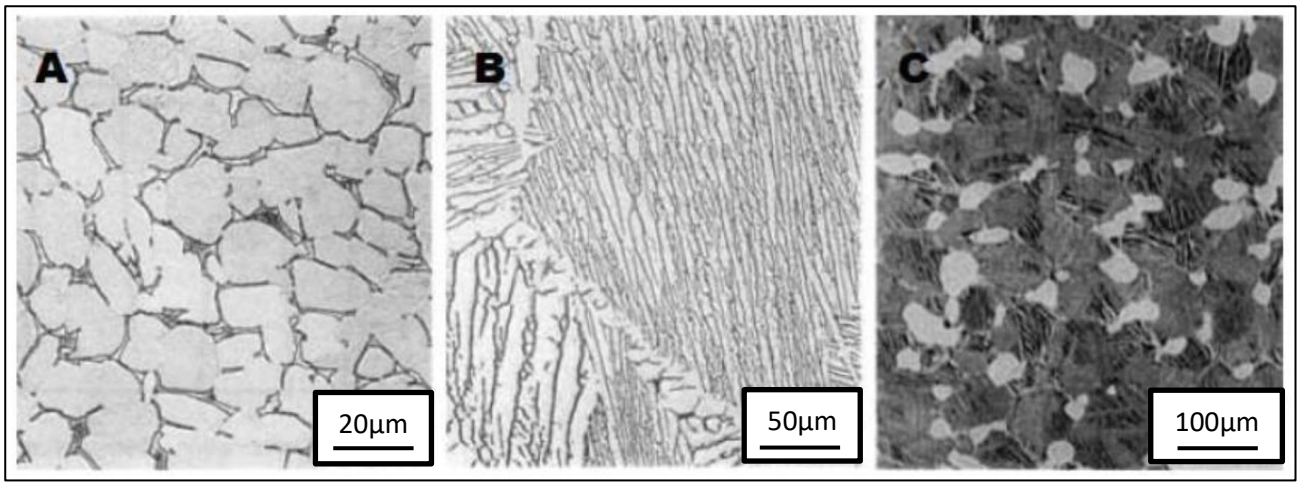

FIGURE 3-1: TI-6AL-4V PRIMARY MICROSTRUCTURES A) EQUIAXED, B) LAMELLAR, C) BIMODAL (HYBRID), SOURCED FROM [44].

By applying thorough heat treatments, lamellar microstructures may be freely controlled. During SLM processing, operating temperatures exceed the β – phase transitional temperature. Cooling from such conditions induces grain growth and nucleation of α-phase plates surrounding β – phase boundaries. Quenching the material from greater than 900°C results in a needle shaped HCP martensite lamellar structure [6]. Figure 3-2 indicates the phase diagram of Ti-6Al-4V.

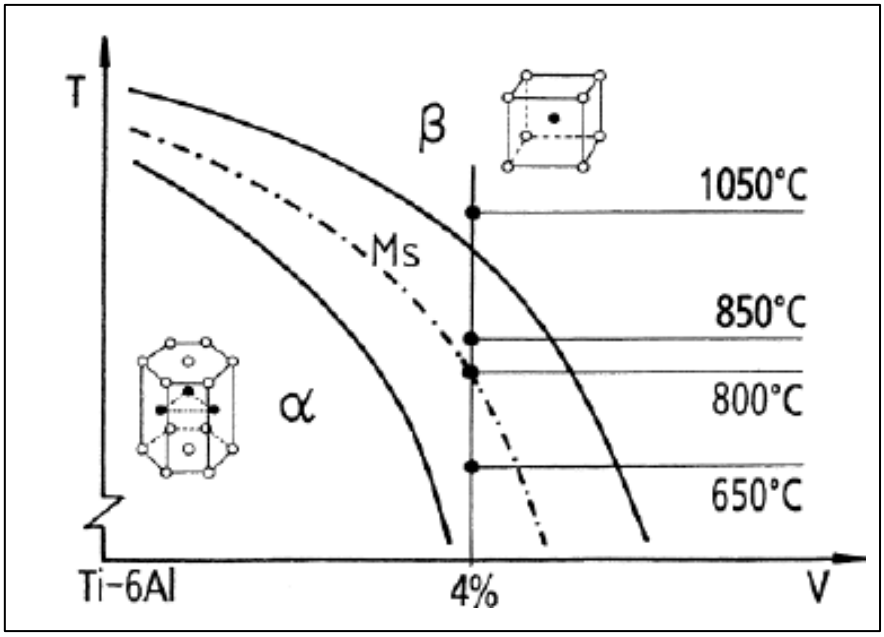

FIGURE 3-2: TI-6AL-4V PHASE DIAGRAM SOURCED FROM [46]

Equiaxed microstructures occur after intensive mechanical working, during processing in the α+β region on the phase diagram, resulting in up to a 75% material volume reduction. Subsequent annealing procedures at temperatures less than 950°C, followed by slow cooling may be employed to achieve coarser grain structures. Lastly, bimodal structures are obtained when isolated primary α-grains are encapsulated into a transformed β-matrix. These structures occur by quenching the sample after annealing at approximately 950°C. Table 3-2 includes a summary of specific microstructural morphologies and their effects on the mechanical properties of Ti-6Al-4V alloys. A '+' - symbol indicates a positive influence, while '-' indicates a negative influence.

TABLE 3-2: MICROSTRUCTURAL INFLUENCE ON THE MECHANICAL PROPERTIES OF TI-6AL-4V ALLOYS [44].

Microstructure morphology	Crack propagation (high and low cycle fatigue)	Crack initiation (High cycle fatigue)	Fracture toughness (KIC tests)	Ductility (ϵ frac)	Strength (UTS)
Coarse	+	-	-	-	-
Fine	-	+	-	+	+
Equiaxed	-	+	-	+	+
Lamellar	+	-	+	-	-
Widmanstätten α – pattern	+	-	+	-	-
α Colonies	+	-	+	-	-
Secondary α	-	+	-	+	+
GB α	+	-	+	-	

TI-6AL-4V MATERIAL PROPERTIES

Titanium is renowned for its unique mechanical and chemical material properties. The Ti-6Al-4V alloy has been tailored to accommodate a wide variety of applications, Table 3-3 includes a summary of its mechanical and physical properties.

TABLE 3-3: MECHANICAL PROPERTIES [44].

Properties	Metric Value	Range
Shear Strength	760 MPa	-
Poisson Ratio	0.342	-
K_{IC} Fracture Toughness	75 MPa $m^{1/2}$	33 – 110 MPa $m^{1/2}$
% Elongation	14%	13-16%
Tensile Strength (TS)	950 MPa	900 – 1200 MPa
Yield Strength (YS)	880 MPa	800 – 1100 MPa
Young's Stiffness Modulus	113.8 GPa	110 – 140 GPa
Vickers Hardness	349 HV	300 – 400 HV
Density	4.43 g/cm	-

The thermal properties of Ti-6Al-4V are a primary point of interest due to the nature of the LM procedure. It will be necessary to study the material's reaction when exposed to focused laser energy and extrapolate these findings to form logical conclusions on how the part may be affected during operating conditions. The thermal properties of Ti-6Al-4V are listed in Table 3-4 below.

TABLE 3-4: THERMAL PROPERTIES [44].

Thermal Properties	Metric Value
Transus Temperature (T_B)	980 °C
Liquidus	1660 °C
Solidus	1604 °C
Melting Temperature	1604 – 1660 °C
Thermal Conductivity	6.7 W/m K
Specific Heat Capacity	0.5263 J/g °C
Coefficient of thermal expansion (Linear 500°C)	9.7 µm/m °C
Coefficient of thermal expansion (Linear 250°C)	9.2 µm/m °C
Coefficient of thermal expansion (Linear 20°C)	8.6 µm/m °C
Annealing Temperature	700-785 °C

3.1.3 Heat Affected Zones in Ti-6Al-4V

In specifically technical applications, as those notable in the aerospace, nautical and mining industries, high operating standards are expected due to critical risks associated with losses of human lives and monetary investments when component failure arises. Parts are expected to display consistent properties throughout their entire life cycle; unexpected events such as deformation, creep, or sudden crack formation may result in failures of catastrophic proportions. It is therefore of critical concern to maintain microstructural homogeneity of materials to ensure consistent performance in high temperature load-bearing environments.

Machining procedures conventionally induce a sharp increase in the surface temperature of the contact areas, whether it is wire-cutting, grinding or high-speed machining. This localized temperature increase leads to transformations in the material microstructure and may induce phase changes should the temperature exceed a specific threshold for extended periods. The material then consists of localised variations in material properties [47]. These areas are referred to as heat affected zones (HAZ), or in the case of machining applications, machining affected zones (MAZ). These zones display completely foreign material behaviour compared to that of the inner region unaffected during operation. The phenomenon of differing microstructural compositions and material properties within the same part is denoted as inhomogeneity. Its main origin stems from phase differences which may be summarized as varying compositions of the alloy's constituent materials throughout different zones [48].

Titanium and its alloys are characterized by reduced capabilities of thermal conductivity. This means that heat applied to the material does not dissipate well throughout the bulk thereof, but rather becomes trapped in the MAZ. In applications related to tooling and machining, the heat induced by the cutting tool only intensifies. The temperature at the MAZ could exceed 1100℃ [49]. At such temperatures, a phase transformation process occurs at the surface of the alloy that is not experienced by the inner regions of the alloy.

Unexpected variations in the surface microstructure of titanium alloys may induce weakened areas that become nucleation sites for cracking to originate and develop from. Even microscopic cracks could propagate promptly should the area be applied to high stresses and extended cyclic loadings. It is for this reason that homogeneity is maintained in the microstructure throughout the part's life cycle or restored by repairing treatments before they are rejected by stringent quality control procedures. Several innovative methods of reducing microstructural changes on titanium alloys are applied in practice, one solution being the application of protective layers to the part surface [50].

Prior studies concluded that titanium provides strong composite coating adherence, although differing material properties between the reinforcement and substrate may cause cracking and exfoliation under severe conditions, which in turn affects part performance at high temperatures [50].

3.1.4 Surface Treatments of Ti-6Al-4V

Ti-6Al-4V is already one of the most utilised materials in high temperature applications, a prominent failure mode in such conditions is wear. This limits the extent to which titanium and its alloys can be employed due to poor tribological properties [51]. This shortcoming can be overcome by modifying the surface of the material to improve wear resistance.

Various conventional surface treatments methods can be applied to achieve improved erosion/wear resistance of titanium. Such treatments include, but are not limited to, surface hardening and surface cladding. This represents techniques like nitriding, arc welding, plasma spraying, thermal spraying and focused energy technology (electron beam or laser). Welding processes tend to be too energy intensive, resulting in unwanted distortions, thermal stresses and localised inhomogeneity where cracks may propagate from. The rapid heating and cooling nature of laser surfacing make it a suitable method for treating titanium alloys.

Laser surface modification induces less stresses in the material and facilitates the tailoring of specific microstructures to achieve material properties that traditional processing cannot produce. These microstructures are heavily dependent on the heating and cooling cycles throughout the process and the machine parameters selected. Further benefits of laser surface processing include the production of a hardened surface layer with low levels of dilution between the substrate and coating, mitigated deformation due to residual stresses, minimal grain growth and elimination of the need for a quenching medium [52].

Laser cladding has received considerable interest for the treatment of titanium alloys. It can produce quality hard-particle reinforced layers onto titanium substrates, typically comprised of carbides, borides or nitrides. These treatments improve the wear properties of the material significantly by both the hard particle reinforcement at the surface and the laser heat treatment which induces a hard matrix at the surface of the material. The most common carbide reinforcement phases are Vanadium carbide (VC) and titanium carbide(TiC) [51].

Little research has been conducted regarding the laser surface treatment of Ti-6Al-4V with tungsten carbide coatings, let alone the use of tungsten carbide nickel (WC-Ni).

3.2 COMPOSITE MATERIALS

According to Callister et al. [45], composites may be defined as multiphase materials that can be artificially produced, resulting in a combination of desirable properties from its constituent base phases. Conventionally two phases are present within the material, 1) a dispersed phase of reinforcement particles, and 2) the matrix phase which surrounds the dispersed particles. Composites are conventionally referred to according to 4 classifications, namely, particle-reinforced, fibre-reinforced, structural, and nanocomposite. These classifications are included in Figure 3-4.

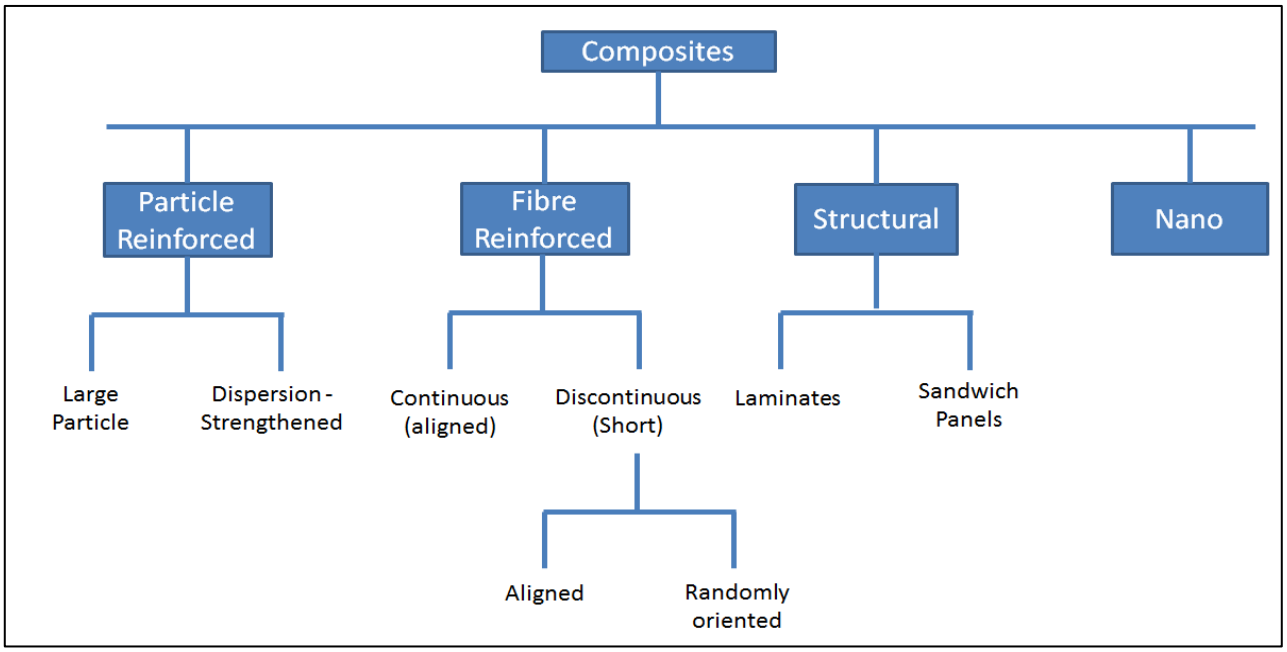

FIGURE 3-3: CLASSIFICATIONS OF COMPOSITE MATERIALS [45].

3.2.1 Particle Reinforced Composites

Particle reinforced composites consist of a hard-particulate phase that is engulfed in a binding matrix phase. The particulate phase reinforces the material by restricting movement of the matrix phase within their vicinity, thereby hindering the motion of dislocations. This restricts plastic deformation and increases tensile strength and hardness of the material. These materials are capable of high strength compared to their weight. An applied load is transmitted through the more ductile matrix phase to the reinforcement particles. At the particle extremities reinforcement discontinues, thus the efficiency thereof depends on the size of the particles and the strength of the bonds between the matrix and particulate phases [45].

The binding phase that surrounds the fibres or particles is categorized by the matrix type, which entails metal-, ceramic-, and polymer-matrix composites, though they are conventionally made of polymers or metals. This phase serves to perform three functions, namely, 1) bind together the reinforcement and diffuse externally applied loads onto them, 2) Shield particles from surface damage, and 3) prevent crack propagation between reinforcement particles. Table 3-5 includes a briefing of the different matrix combinations that are popular in composite materials [45].

Table 3-5: Descriptions And Acronyms Of Popular Fibre Reinforced And Particle Reinforced Composites Within Binder Matrices Sourced From [1].

Matrix material	Description
Polymer-Matrix Composite (PMC)	These composites are the most popular and diverse due to easy fabrication and low cost for their desirable properties. A polymer resin (high-molecular-weight plastic reinforcement) represents the matrix phase which is reinforced with fibres or particles intended for use at room temperatures.
Metal-Matrix Composite (MMC)	In these materials, the matrix phase consists of ductile metals and the reinforcement either continuous or discontinuous fibres or particulates. MMCs can withstand higher working temperatures than PMCs and have improved stiffness, abrasion resistance, creep resistance, specific strength, dimensional stability, and thermal conductivity.
Ceramic- Matrix Composite (CMC)	Ceramic materials are often praised due to their resistance to oxidation and weakening in high temperature environments, but these properties are countered by the material's affinity to brittle fracture. CMCs improve the brittle nature of ceramics by embedding ceramic particulates and fibres into a ceramic matrix material. The improved fracture toughness is due to dispersed phase particles that interact with advancing cracks through various toughening techniques.
Hybrid Composite (HC)	Hybrid composites may be obtained by combining two different fibre materials within a matrix, which comply with the principle of combined action in producing a part that has superior properties compared to the constituent materials. The most common variety contains carbon and glass fibre reinforcements. Where the carbon provides stiffness and strength, and the glass is utilized as a more cost-effective reinforcement.

Within powder-based AM techniques, it is especially difficult to produce fibre-reinforced composite parts due to the inability to draw smooth layers of the powder-fibre mixture. These AM methods work better with shorter reinforcement fibres, whereas solid material addition processes such as LOM and SL can produce materials with long or continuous fibre reinforcements. Powder-based AM composites consist almost exclusively of particulate reinforcements to ease processing and prevent defects [53].

3.3 CEMENTED CARBIDES

Tungsten is customarily present in naturally occurring tungstates, the most important variations being scheelite ($CaWO_4$) and wolframite ($(Fe,Mn)WO_4$). The element was a critical input for the production of wolfram within the armaments industry throughout World War II, and played a prominent role in diplomatic and trade relations [54].

In 1914, to improve applications for drawing dies and rock drilling, the first sintered tungsten carbide material was developed. This paved the way for the creation of the first carbide tool in 1923 by Karl Schröter at the OSRAM studiengesellschaft [55]. Schröter applied for a patent in 1926, claiming the invention of both the unique new carbide alloy and the manufacturing thereof by Powder Metallurgy (PM) processes that press or sinter WC and binder particles together. The patented alloy comprised of hard tungsten carbide (WC) and smaller concentrations (10–20 wt.%) of iron-group binder metals [55].

Cemented carbides consist of a range of material composites. The carbide phase commonly makes up between 70-97 % of the composite's net weight with a grain size averaging between 0.4 – 10 µm [56]. In the most common structure of cemented carbides, the hard phase is comprised of tungsten carbide (WC) held together by a cobalt (Co) binder. The cobalt has a melting point of 1495°C and acts as an adhesive binder to join the WC-particles which melt at a considerably higher temperature of 2800°C. Cobalt has excellent wettability and is used as a binder due to the solubility of WC therein [56]. Cobalt's effective wetting properties contributes to eliminating residual porosity and increases the strength and toughness of sintered parts [54].

A defining characteristic of cemented carbide is its outstanding reliability. Reliability is a problem often associated with tool wear and cemented carbides offer excellent wear resistance. Additionally, these hard metals can withstand intensive of deformation, are impact and heavy load resistant, and it can withstand high pressures, temperatures, thermal shock and corrosion. In tooling industries such as rock drilling and metal cutting these characteristics provide optimal solutions to various problems that have long plagued the industry [56].

Various industry sectors today utilize the versatility and reliability associated with cemented carbides. The most prominent global contributors being the tooling, mining, wood working and construction industries, indicated in figure 3-5. WC-based tools are the top choice world-wide, with 95% of all cutting tools consisting of WC cermets. A consistent growth has been noted in the global consumption of cemented carbides, from a humble 10 tons annually in 1930 to a staggering 30 000 ton at present day. World-wide production of tungsten exclusively for the use in tungsten carbide was estimated at 62 000 tons in 2007, and in 2011 the global carbide industry production was worth more than 10 billion € [54].

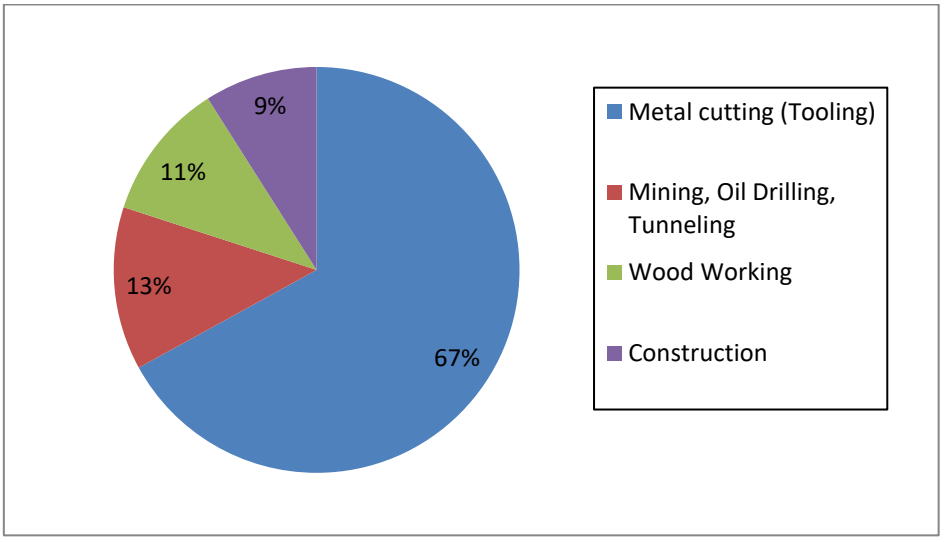

FIGURE 3-4: SECTORS CONTRIBUTING TO GLOBAL CEMENTED CARBIDE USAGE [54]

3.3.1 Developments in Cemented Carbides

Due to the widespread appeal of WC-Co since its inception, it is not surprising that the bulk of research regarding cemented carbides was aimed almost exclusively at improving WC-Co. Whether by means of studying failure mechanisms, hot deformation or crack formation, a concerted research effort was made to improve and diversify knowledge of the material. Different types of cemented carbides have been developed from this structure, which may contain varying proportions of tantalum carbide (TaC), titanium carbide (TiC), and niobium carbide (NbC). These are mutually soluble carbides, capable of dissolving high proportions of tungsten carbide.

In metal cutting industries, breakthroughs involving the reinforcement of WC-Co with TiC and TaC were crucial as it brought about the improvement of high temperature wear and crater resistance in components. TiC was proven to reduce crater formation by restricting diffusion between WC and the steel swarf. Additionally, TaC additions of up to 2% promote grain refinement of the crystal structure, and levels greater than 4% are added to improve the material's hot strength [5].

In addition to varying hard phases, the binder phase may also be replaced by, or alloyed with, different binding metals such as iron (Fe), chromium (Cr), nickel (Ni), molybdenum (Mo), or different combinations of these metals.

3.3.2 Requirements for Quality Hard Metal Carbides

In metallurgical terms, cemented carbides are comprised of three individual phases. The tungsten carbide (WC) phase is commonly referred to as the alpha phase (α-phase), the binder as the beta phase (β-phase), and additional singular or combination carbide phases, such as TiC and Ta/NbC, are the gamma phases (γ-phase) [56]. No internationally accredited grouping of cemented carbides is currently in existence, although Swedish engineering company, Sandvik, has outlined a grouping of four main categories to better describe cemented carbide grades. These groups are outlined briefly in Table 3-6 [56].

Table 3-6: Grouping of the four main categories to better describe cemented carbide grading sourced from [56]

Grades	Description
Corrosion resistant	To achieve corrosion resistance, the cobalt binder phase is alloyed with, or replaced by metals like nickel and chromium, or completely replaced by materials less prone to oxidation.
Dual property (DP)	In these grades, the binder phase is modified to achieve zones with microstructural differences, altering the material properties on the surface compared to the centre of the object.
Cubic Carbide content	Large γ-phase carbide quantities are included to improve thermal stability, lower grain growth and provide resistance to oxidation.
Straight WC-Co	These materials contain WC and Co exclusively and are classified according to their Co – content and the size of its WC grains.

For carbides to be effective, the hard phases must be sintered together to yield a strong carbide/binder interface devoid of anomalous carbide growth. To achieve a dense composition, melting must occur at the lowest possible temperature while easily wetting carbide surfaces in order to develop an uninterrupted binder distribution. Carbide on carbide interfaces should be minimized for optimal properties [57].

Low interfacial energies related to drop contact angles of 90 degrees or less (preferably zero) facilitate enough wetting of the non-liquid constituents. Should the contact angles of the hardened phases be high, surface tension forces will be more prominent, pushing grains together and inducing recrystallization into coarser grain sizes. To facilitate good wetting of the hardened particle phase, 'absorption' at the grain interfaces is necessary. A diffusion gradient must also be established, which describes the solution of solid phase particulates into the binder phase. To warrant good bonding, the work of adhesion must be maximised and requires low contact angles between grains [5].

The WC-Co system is a good example of ideal features required to produce an effective hard metal composite. Indicated in figure 3-6, a eutectic occurs at 1275°C far enough below the melting point of cobalt at 1495°C, thus at sintering temperatures the solubility of WC in the cobalt phase is high. However, solubility declines as the melt cools and existing carbide grains undergo re-precipitation, establishing a low-stress interface between the binder and carbide that mitigates crack initiation [5]. Other features that grant the WC-Co system its favourable properties include: 1) the good thermal conductivity, elastic modulus and toughness of the WC hard phase, 2) cobalt's variety of powder specifications, which include extra fine powders (1-2um) that improves mixing and spreading of the binder. 3) Lastly cobalt's magnetic properties facilitate non-destructive production control techniques. These properties provide a benchmark for future developments and alternatives to WC-Co [57].

3.4 TUNGSTEN CARBIDE – NICKEL & COBALT

A prominent topic in research regarding cemented carbides is the development of new composite combinations. This entails the partial or complete replacement of conventional cobalt binders with more economically feasible. Substitution of cobalt with iron or nickel binders in composite parts has recently been introduced into industrial manufacturing. Several other replacement alloys such as Ni-Fe or Ni-Fe-Cr have also been considered [54].

From an economic standpoint, should the raw material supply for cermets be limited to specific regions (such as with cobalt's lesser accessibility in developed countries), scarcity of ore deposits may result in price fluctuations. Cemented carbides are required in various fields globally. By diversifying the material combinations that result in similar product functionality, risks associated with material scarcity and global demand patterns could be mitigated [54].

The chief ore deposits for constituents of hard metals are found in less accessible countries, which is problematic due to the primary production facilities being located in the 'Industrialized World' [5]. A 1990 survey concluded that 58% of cobalt utilized for global production was sourced from Central Africa and a further 21% from Eastern Europe. Furthermore, comparable statistics for global tungsten deposits estimated that 38% is sourced from China and 31% from Eastern Europe. The drivers for development of WC cermets have been directed towards: 1) the partial or complete replacement of the cobalt binder and 2) the replacement of WC by more durable Titanium derivatives

Early research pertaining to nickel rich iron indeswrs indicated that an increase in nickel content convoys with a widened two-phase field in the phase diagram. Also, the equilibrium carbon level required to elude graphite and eta-phase development decreased with an increase in nickel content. The two-phase regions where almost doubled by increasing binder contents and substituting the Fe:Ni ratio of 3:1 to 1:3. Nickel has received positive reviews when considered for a binder alternative to cobalt and has been used nearly exclusively in die and wears part production for its excellent corrosion resistance. It has a similar lattice structure and material properties to cobalt. Fcc nickel's lattice parameter is (0.352 nm) only slightly less than that of cobalt (0.354), resulting in two principle differences: 1) fcc cobalt can transform to hcp due to its metastability, 2) Cobalt is far more magnetic than nickel [58].

3.4.1 MATERIAL PROPERTIES OF NICKEL AND COBALT

In order to conduct a thorough comparison between WC-Ni and WC-Co, each individual binder material's properties should be investigated. Once a systematic understanding of these constituents has been gained, then their combined properties within a WC-system can be addressed. Tables 3-7 and 3-8 compares the thermal and mechanical properties of cobalt and nickel, respectively

TABLE 3-7 : THERMAL PROPERTIES OF COBALT AND NICKEL [59].

Thermal Properties	Cobalt	Nickel
Melting Temperature	1495 °C	1455 °C
Boiling Temperature	2870 °C	2913 °C
Specific Heat (J/kg·K)	0.52	0.44
Thermal Conductivity (W/m·K	21.90	90.90
Thermal Expansion (µm/m·K)	8.60	13.40
Latent heat of fusion (kJ/mol)	15.48	17.57
Enthalpy of vaporization (kJ/mol)	429	371.8

TABLE 3-8: MECHANICAL PROPERTIES OF COBALT AND NICKEL [59].

Properties	Cobalt	Nickel
Shear Modulus (GPa)	44	76
Poisson Ratio	0.31	0.32
Bulk Modulus (GPa)	110	180
Tensile Strength (MPa)	434	345
Young's Stiffness Modulus (GPa)	116	200
Vickers Hardness (MPa)	1043	638
Density (g/cm^3)	4.51	8.91
Liquid Density (g/cm^3)	4.11	7.81

3.4.2 WC-NI & WC-CO PHASE RELATIONSHIPS

Since 1936 after a study by Takeda et al. in a scientific report to Tōhoku Imperial University [58], data on Ni-W-C and Co-W-C phase diagrams have been available, which indicated similarities between the systems. The only differences being eutectic temperatures, phase field widths, and solubility. The phase diagrams of both W-C-Ni and W-C-Co are indicated for comparison in figure 3-6. Both diagrams were developed with a 10 wt. % binder material. The (●) - symbol indicates the stoichiometric composition at 5.5% wt. % C. Respectively, points a and b represent the minimum and maximum carbon contents for alloys in a two-phase (fcc + WC) – state, immediately after equilibrium solidification.

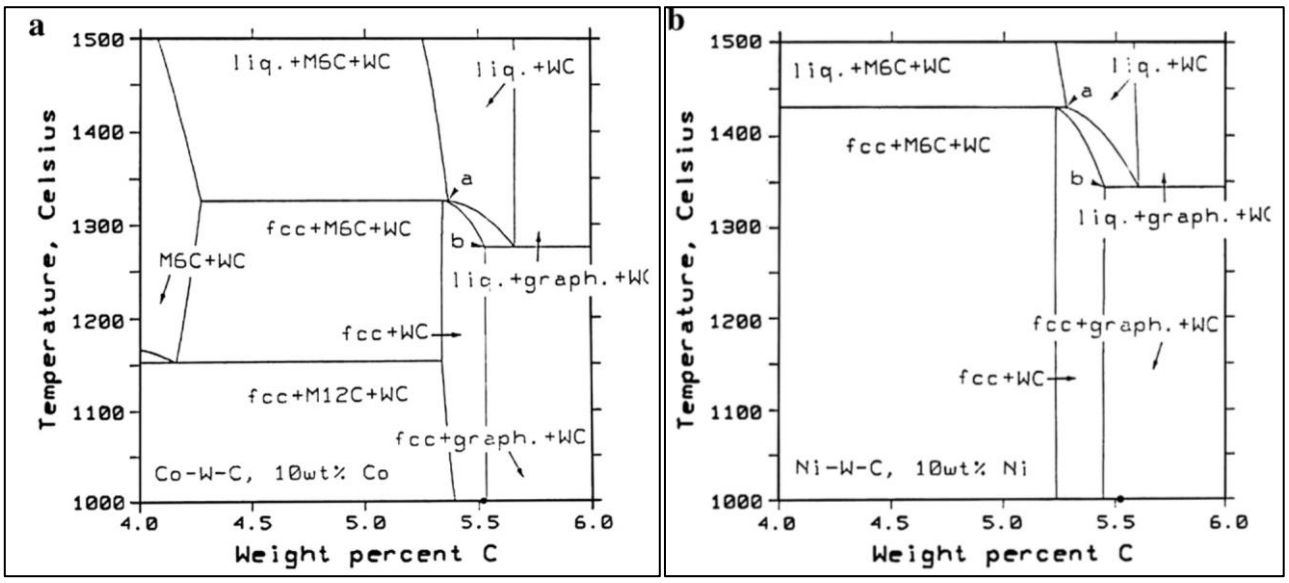

FIGURE 3-5: PHASE DIAGRAMS FOR W-C-CO (A), AND W-C-NI (B) [54].

Of all WC-Co binder alternatives, nickel has drawn the most consideration. Computer modelling simulations confirmed that Ni has a greater solubility for tungsten, and that WC-Ni has a wider two-phase region than WC-Co. When comparing the phase diagrams, it is possible to predict the consequences of substituting Co-binder entirely with a Ni-binder phase. The regions indicating the fcc/WC phases are similar for both diagrams, however upon inspecting the stoichiometric compositions, regions indicating favourable carbon content change to lower values [54].

Changing to a nickel binder substitute brings about a beneficial increase in eutectic and peritectic equilibrium temperature points. The partial substitution of Co with Ni also brings an increase in these temperature points; however, the difference is reliant on the Co:Ni ratio. As per Guillermet's findings [60], pending full substitution with Ni, the effects of partial Co/Ni mixture on the solid/liquid equilibrium temperatures are close to negligent. Tungsten has a favourable solubility in nickel, estimated to be equal or more than that of cobalt [61]. In the ternary W-C-Ni system's liquid state, the solubility of C and W was reportedly 2.0 and 5.0 wt. % at 1350 °C. While a solubility of 5.4 wt. % has been reported for tungsten in nickel at room temperature.

3.4.3 Sintering Characteristics

Appreciably, the melting point of nickel (1455 °C) is less than that of cobalt (1495°C), though cobalt has a ternary eutectic with tungsten and carbon melting at a mere 1275 °C. Even if nickel's melting temperature is less; its ternary eutectic occurs at 1342°C, 70°C higher. Temperatures for sintering the two different systems may vary due to the laser source and constituent content %. Sintering temperatures were found to be 100°C - 120°C above the eutectic temperatures for powders with 10% binder content. When binder contents increased to 20%, the sintering temperature decreases by 80°C, and alternatively increased by approximately 70°C in cases where 6 % binder contents where used [5]. Cobalt and Nickel are both capable of producing full density parts by conventional sintering processes, void of anomalous grain growth, which is indicative of good wetting characteristics. Anomalous grain growth has often been associated with poor material mixing, if this can be avoided grain sizes ought to be similar.

During the sintering of WC-Ni powders, it is necessary to increase the sintering temperature and time to ensure proper densification of the melt while cooling [54]. Nickel has a vapour pressure tenfold that of cobalt that causes considerably more binder material loss during sintering. It is thus important that the working pressure be monitored closely. In practical applications at least a 10% loss of nickel binder was described. Thus dedicated equipment is an necessity to avoid cross contamination when switching materials, which may cause the formation of graphite or eta-phases [54].

3.4.4 Solubility and Microstructural Evolution During Sintering

While sintered, nickel particles must be melted to form a liquid phase wherein the hard WC grains should be soluble, meaning that the liquid phase should fully wet the solid and provide capillary forces to pull the grains together upon solidification. Good solubility of the hardened phase within the binder accommodates lower sintering temperatures and a shorter processing time [62]. The reigning consensus throughout several investigations reads that tungsten has similar solubility in nickel and cobalt. For both binders, the solubility just underneath their eutectic temperature is threefold the solubility at room temperature. In cobalt binder solubility is affected by the carbon content of the system, and reportedly reaches up to 15% at temperatures surrounding 1250°C. However, solubility in a nickel binder alternative is reported to be of the same magnitude with an inclination to be higher[58], measuring at 5.4% solubility in nickel binders and 3.4% in cobalt at ambient temperature.

Detailed analyses on WC-15.6Ni indicated that the high solubility levels of Tungsten in Nickel may increase the binder matrix volume significantly. Results included an increase in tungsten from the WC-Ni-C boundary where it measured merely 2.3% to 7.8% in the two-phase region, after an increase up to 11.5% was noted at the eta-phase boundary. For the WC-Co system, carbon's solubility in the binder phase at elevated temperatures ranges from 0 - 0.2%, reaching higher levels when less tungsten is present. An interesting note is that in cobalt binders, tungsten and carbon have an inverse relationship, however in nickel they

seem to diverge independently. Lower equilibrium carbon contents in the WC-Ni system has been characterised by higher levels of tungsten throughout the solution [62].

In a study by Zhang et al. [62] the effects of nickel content on the microstructure of W-Ni alloys during SLM were investigated. A similar forming mechanism to traditional liquid phase sintering was utilized and indicated that the process favoured higher binder contents. In LPS the driver for sintering relies on the reduction of surface energy by minimization of surface area. The study utilized three specimens with varying binder contents of 10%, 20% and 40%. At temperatures exceeding 1455 °C this resulted in approximate liquid phases of 26, 44% and 67%, respectively. Furthermore, the microstructures observed at each respective Ni-content progressed from, bar shaped, to dendrites, to honeycomb structures.

After the SLM process a spectrum of elements was compiled by X-ray diffraction. The primary peaks were comprised of W, Ni, and Ni_4W. The latter being an intermetallic compound phase which formed during sintering. A decrease in Ni peaks was also observed, which may be attributed to a loss of material due to the high vapour pressure of Ni. At temperatures above 970°C, the W-phase reacts to form Ni_4W, consistent with the W-Ni phase diagram in figure 3-6.

As the Ni content in the alloy increases, the presence of this Ni_4W compound also increases accordingly. It was observed that during the LPS process only Ni_4W phase was observed and no W-Ni phase. In its place tungsten dendrites were detected that formed during solidification, which evidently points to the partial melting of some W-particles [63].

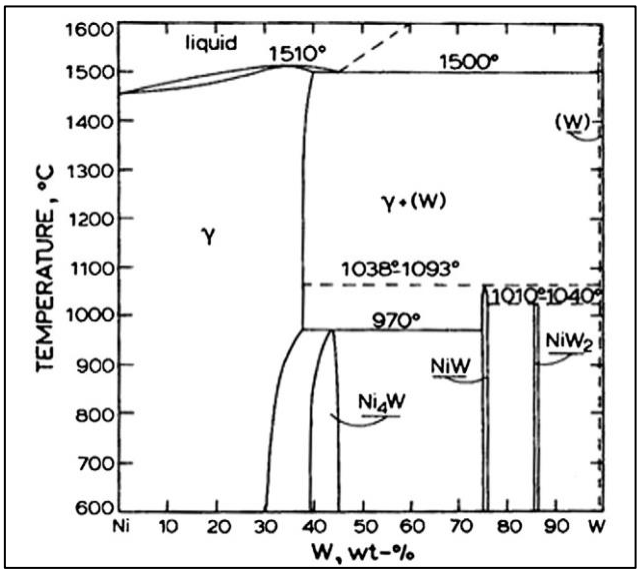

FIGURE 3-6: W-NI PHASE DIAGRAM [54]

In Zhang et al. 's research it was elaborated that according to dendritic growth theory [64], nickel's lower melting point induces a lower temperature gradient over the powder bed, which would affect the growth of dendritic microstructures. The increasing binder content and lower temperature gradients are therefore consistent with the microstructural development from bars, to dendrites, to honeycomb. Furthermore, in line with metal solidification theory [65], with an increase in binder content, the powder system was exposed to rapid melting-solidification conditions. These conditions are governed primarily by constitutional undercooling that arise due to supercooling of the molten material prior to the solid-liquid interface.

Constitutional undercooling induces the segregation of alloying elements prior to their solid-liquid front and entails the rejection of a solute (Ni) by the solid phase (W) into the melt. At this phase interface boundary, the melting point is lower and widens the freezing range of the alloy. Across a positive thermal gradient, depending on the constitutional undercooling of the powder system, the dendritic structural features varied. As indicated in Figure 3-7 the level of undercooling increased the microstructure evolved throughout cellular crystals, columnar crystals and, finally, free dendrites.

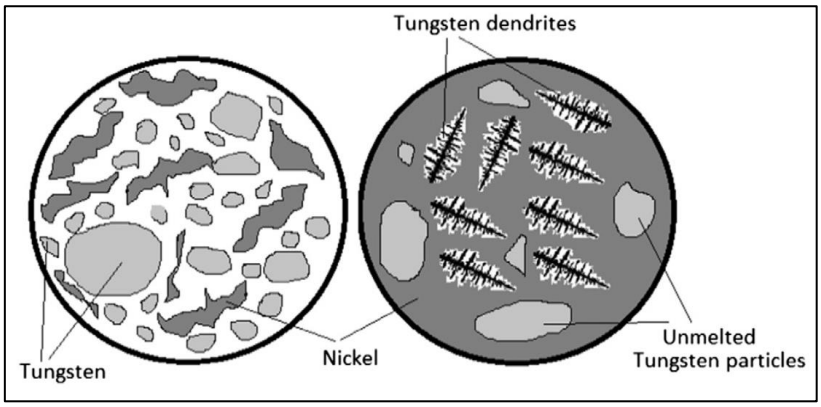

FIGURE 3-7: FORMING MECHANISM FOR W-NI POWDER SYSTEM THROUGHOUT SLM PROCESSING, SOURCED FROM [63]

3.4.5 MECHANICAL PROPERTIES & DEFORMATION CHARACTERISTICS

In WC-cermets, the two primary factors that directly influence the mechanical properties are the WC grain sizes and the binder content. Increased levels of binder convoy with a decrease in hardness, and the finer the grains the material is comprised of the more hardness increases. Transverse rupture strength (TRS) increases with an increase in binder content and decreases with an increase in hardness (and grain refinement). A trade-off occurs between finer grains that produce better TRS values and higher binder contents that reduce hardness (and TRS) [5].

The tailoring of parts' structural characteristics is heavily dependent on tungsten's solubility in the binder material, along with how this affects the carbon balance. The WC-Co system requires a carbon level at the stoichiometric composition for WC (6.12%) in order to achieve optimal TRS values. In the WC-Ni system, however, this value is lower at 6.05% [7].

Hard metal grades meant for steel cutting employ materials with lower binder contents, these grades commonly have roughly 6% binder content, and have far lower TRS values. 6% - 15% binder content materials are utilized for wear parts and dies, 9% - 15% for tooling in mining applications, and high levels of binder between 20% and 30% for high impact uses where greater TRS values are critical such as extrusion dies, cold forming and heading [58]. Various commercial material grades are available from an extensive array of hard metal manufacturers, most of which have focused research and development programs aimed at customising the performance of materials in unique environments.

The gradual replacement of cobalt binder matrix with that of nickel alternatives showed a consistent drop in hardness by roughly 100 HV from 300 HV. A conclusive study indicated that cobalt binder systems produce harder materials on average. Similarly, the ultimate compressive strength of the material also declined with a graduated increase in the nickel content, scoring better for WC-Co dominant systems when compared to WC-Ni alternatives [58]. Figure 3-8 indicates the effects of binder content on material hardness for various WC systems.

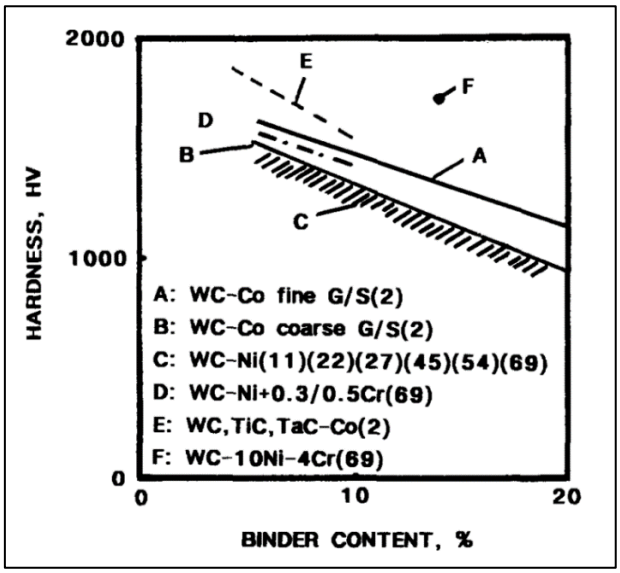

FIGURE 3-8: EFFECTS OF BINDER CONTENT ON MATERIAL HARDNESS (HV) [54].

Regarding failure strain characteristics, similar values were recorded for both systems. During tensile testing, superior elongations were noted for nickel alloys of 20 – 40%, compared to mere 2-12% elongations for cobalt alloys. TRS values were mostly unaffected after binder replacement, though minor chromium additions to the nickel binder were necessary to obtain matching values [66].

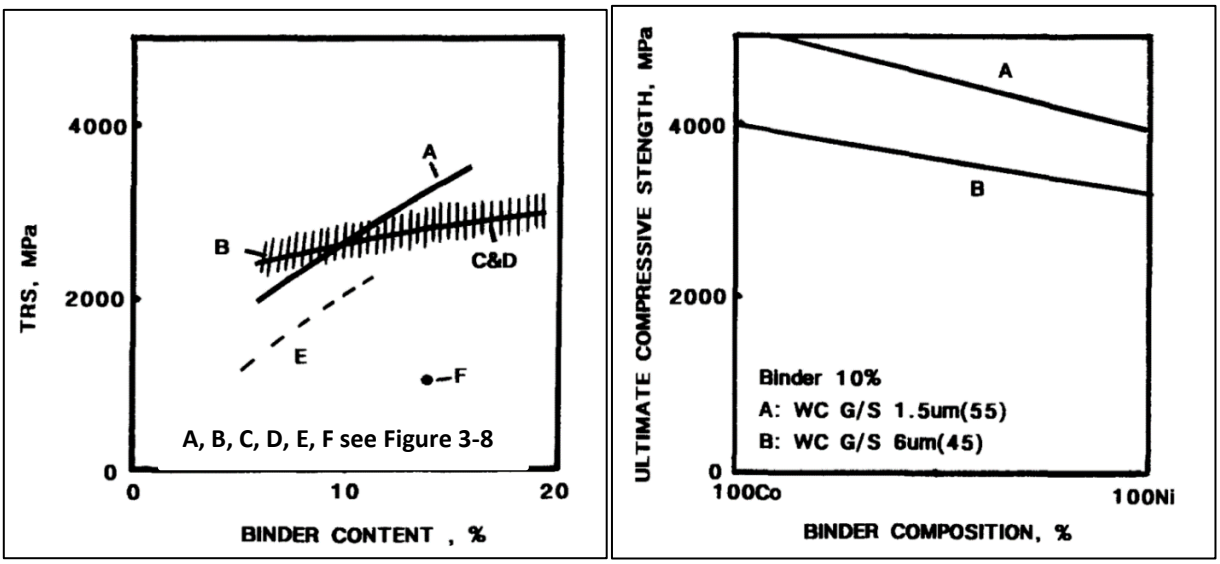

FIGURE 3-9: (LEFT) EFFECTS OF BINDER CONTENT ON TRANSVERSE RUPTURE STRENGTH (TRS). (RIGHT) EFFECTS OF BINDER CONTENT ON ULTIMATE COMPRESSIVE STRENGTH [54]

Compared to their nickel binder equivalents, superior work-hardening rates are present in compressed WC-Co systems. This phenomenon is related to its metastable fcc to hcp transformation. The fcc transformation has reportedly been as little 10% in WC-Co systems with both 6% and 15% binder content. Fcc to hcp transformations reduced significantly after the substitution of cobalt with nickel. At 15% binder content, transformations dropped from 44% with cobalt binders to 32%, and 30% binder content yielded as low as 11 % transformation [67].

The failure strain for partially replaced binders in a WC-(Co+Ni) system was significantly greater than both individual systems, suggesting fracture toughness may be improved with partial replacement of cobalt by nickel. The binders' stress-strain characteristics were used to extrapolate the fracture toughness values of materials. Higher fracture toughness normally coincides with increased carbon levels (and therefore less tungsten) closer to the WC-Ni/WC-Ni-C boundary. Although findings throughout research have indicated that carbon contents just under stoichiometric levels have produced higher fracture toughness values [67].

3.4.6 Oxidation & Corrosion Resistance

Primary applications for hard metals that require oxidation resistance is in rolling mills and hot rolls. Rolls manufactured from WC-Co develop cracks quickly in the stark operating environment, which rapidly increase in size and deteriorate parts. In comparison to WC-Ni, WC-Co materials require a far shorter incubation period below 700°C, before oxidation commences. A Nickel binder substitute will thus incite a notable improvement in performance. However, the material can be enriched even further by adding traces of chromium to the binder alloy[54].

Both WC-Co and WC-Ni are corrosion resistant in basic solutions above pH 7, though in acidic solutions WC-Ni performs far better than WC-Co. The material may be further improved by alloying the nickel binder with traces of chromium, and molybdenum is often added to improve resistance to chlorides. Studies on the material characteristics of WC-6Ni and WC-10Ni indicated that when alloyed with 0.5% chromium, hardness values reaching 1550 HV and 1375 HV were obtainable, respectively. In the same analysis TRS values of 2100 MPa and 2700 MPa were noted for the respective materials. These values are comparable to that of WC-Co alternatives. A common composition of corrosion-resistant hard metal that includes nickel is WC-8Ni-0.7Cr-0.3Mo [5]. Table 3-9 includes a qualitative comparison of the corrosion resistant properties of WC-Ni and WC-Co at various pH-levels. It was compiled by the Federal Carbide Company, an international distributor of tungsten carbide die and wear parts situated in Pennsylvania, USA [67].

Table 3-9: Qualitative comparison of WC-Ni and WC-Co corrosion resistance at various PH levels [67].

<table>
<tr><th>PH Level</th><th>WC-Co</th><th>WC-Ni</th></tr>
<tr><td>12</td><td rowspan="3">Very Good</td><td rowspan="6">Excellent</td></tr>
<tr><td>11</td></tr>
<tr><td>10</td></tr>
<tr><td>9</td><td rowspan="2">Good</td></tr>
<tr><td>8</td></tr>
<tr><td>7</td><td>Fair</td></tr>
<tr><td>6</td><td>Poor</td></tr>
<tr><td>5</td><td rowspan="6">Very poor resistance to none</td><td rowspan="2">Good</td></tr>
<tr><td>4</td></tr>
<tr><td>3</td><td rowspan="2">Fair</td></tr>
<tr><td>2</td></tr>
<tr><td>1</td><td rowspan="2">Poor</td></tr>
<tr><td>0</td></tr>
</table>

WC-Co cermets provide reasonable resistance to corrosive wear by organic solvents like gasoline, ethanol and acetone, in addition to most bases, weak acids, ammonia and tap water. Cobalt's tendency to react with corrosive agents is a major cause of cemented carbide failure in such environments. In a phenomenon referred to as cobalt "leaching", the cobalt binder dissolves at exposed surfaces leaving behind a brittle skeleton of loosely knit WC-grains, which results in the flaking of carbide grains on the affected area [67].

The cobalt binder phase is especially vulnerable to stronger acids such as sulfuric, phosphoric, nitric, hydrochloric, hydrofluoric and formic acids. The material's affinity to corrosion may be affected by environmental factors and the specific properties of the corrosive agent, like the temperature, electric conductivity and concentration. To remedy this, binder is often alloyed with nickel, chromium and/or molybdenum. The addition of these constituents improves the corrosion resistance, but is not as effective at extending part lifecycles as the complete substitution of cobalt with nickel and its alloys [5].

WC-Ni cermets and further specialized formulations such as carbides that utilize a nickel, chromium, and molybdenum alloy binder (WC-Ni-Cr-Mo) are developed to resist corrosion without mitigating the material's strength or reliability attributes. These materials are valuable in various applications including: seal rings, bearings, fluid control components, nozzles and choke valves [67].

3.5 WC-NI APPLICATIONS

As discussed in section 3.4, nickel has been increasingly popular as a binder alternative in hard metals due to the need for alternative material combinations that may result in similar properties to WC-Co cermets. Scarcity of WC-Co constituents in developed countries incurs higher production costs should they have to be imported. Furthermore, cermets with capabilities for specialized applications are in high demand such as improved corrosion resistance, or the substitution of the WC phase with TiC and TaC to improve operation in high temperature environments. Additionally, the toxicity of WC-Co has recently sparked controversy as industries are becoming more focused on environmental impact [5].

In the material catalogue for Federal Carbide Company [67] an array of corrosion resistant carbide materials are listed that employ nickel rich alloys. Harder WC-Ni grades with 6% nickel binder content are recommended for components in corrosive environments intended to control fluid throughput, such as nozzles and seal rings. Tougher variations with binder contents of 10% or higher are applied in cases where higher impact strength is necessary.

WC-Ni is currently used in specialized compact dies intended for processing rare earth magnets, in the nuclear industry, and in applications that require good corrosion and oxidation resistance. These applications commonly involve additions of chromium and molybdenum to the binder alloy, or a hybrid of both nickel and cobalt. These materials are put to work in hot rolls, wood and hard plastic machining, pump parts and oil well seals. Therefore, nickel has been identified as a suitable replacement for cobalt in hard metal composites, though to avoid cross contamination and the formation of eta phases, dedicated equipment should be utilized for each material within industry [5].

3.5.1 WC-NI COATINGS

WC coatings are popular in applications plagued by incessant wear, whether by high temperatures, chemical corrosion or abrasion. Recent research has identified WC coatings as a suitable replacement for hard chrome plating. Showing process chain advantages in terms of cost wear resistance and environmental impact [68]. The outstanding wear resistance of WC is an especially important improvement as coating failure induces crack initiation of the substrate and decreases its fatigue lifetime. In addition, WC coatings indicate superior corrosion resistance to hard chrome plating, especially with regards to nickel alloy-based coatings. These not only showcase improved corrosion resistance, but also excel at abrasive and adhesive wear resistance with good bonding strength. Due to superficial substrate melting during coating with laser technologies, strong metallurgical bonds occur between the coating and substrate material, rendering it as a popular selection in composite materials [69]. WC-Ni coatings may be used to produce parts intended for various components, such as roller extruders, turbines, plungers, wearing plates and rolling mill rollers [7].

A study by Guest et. al [70] investigated the utility of wear resistant WC-Ni coatings for components employed in the mining of oil sand deposits. The protection of equipment against the corrosive and erosive environment is a prominent issue that must be addressed to increase operating efficiency and cut production costs. For such a demanding environment, several overlay material compositions have been investigated, though none have proven to be as effective as nickel matrix WC cermets. The coatings are most prominently used for digging wheels, shovel teeth, sieves and crusher teeth. The overlays are conventionally comprised of nickel matrices that are hardened with chromium, silicon or boron additions and reinforced by monocrystalline tungsten carbide or eutectoid W_2C/WC carbides.

Verwimp et. al [69], investigated the integrity of Ni-based laser clad wear resistant coatings in various applications. The evaluated applications included asphalt cutting, shape forming of glass vessels, and high temperature pressing tools. The study concluded that for all applications, crack free coatings could be generated with wear resistance improved by at least a factor 3 to the conventional processing techniques.

A large variety of techniques are available to coat parts with nickel-based coatings, these include, but are not limited to thermal spraying, electrodeposition, laser cladding, plasma transferred arc welding and hot

wire assisted gas tungsten arc welding GTAW. Research in the field of WC coatings is concurrently testing novel production techniques, such as the application of coatings using AM technologies. In many cases, the production of customized WC-Ni and W-Ni alloy parts possess limitations that are difficult to overcome [69].

Kim et al. [71] noted a detrimental effect on the mechanical properties of Ni-activated sintered tungsten compact, due to a brittle, nickel-rich network forming along tungsten grain boundaries. Further, in electrodeposition of W-Ni or WC-Ni alloys, failings lie in the process' inability to accommodate a tungsten content higher than 76 wt. % [72]. Supplementary production techniques such as metal injection moulding require pre-alloyed materials, and traditional powder metallurgy (PM) suffers geometrical constraints on complex designs. This calls on dedicated tooling and custom moulds which can be expensive. There is thus a need for the research of new forming and coating techniques for W-Ni and WC-Ni alloys.

CHAPTER 4

4 LASER ADDITIVE MANUFACTURING OF CEMENTED CARBIDES

The following chapter will identify the system of interactions that influence the quality of laser AM parts. These interactions have a defining effect on the internal forces that directly influences the mechanical properties, integrity and working life of final parts. The section will aim to group effects that stem from the material type, processing parameters, and energy source. Furthermore, phenomena that occur due to compounding factors will be described.

4.1 PRINTING MATERIALS

According to Li et al. [73], the appropriate mixture of metal powder is crucial in building parts with acceptable properties. Homogeneous powder mixtures improve particle rearrangement and wetting within the melt pool which limits porosity in final parts. Effective heating by laser irradiation of metal powders differs significantly from solid, non-transparent bodies. For solid metallic parts, the material properties' influence on the energy balance may be described by the relationship between the heat conductivity k [W/cm·K] and absorptivity A of the material (seen in equation 4.1).

$$E = \frac{k}{A} \tag{4.1}$$

When the powder particles are still in their solid state, before melting has commenced, the process is principally influenced by thermal conductivity properties. This said, when the process commences, and layers are subject to re-melting, the $\mathrm{k/A}$ ratio must be considered. During laser processing the radiation is only partially absorbed by the surface particles of the powder layer. The remaining radiation pierces gaseous pores between particles and interacts with underlying powder and the substrate. The distribution of heat to the rest of the powder layer and the laser intensity dissipation with deeper penetration into the layer may then be modelled with conventional mechanisms [74].

A prominent obstacle in laser AM is the occurrence of porous parts. Lower part densities result in weakened mechanical properties and lower part quality overall. This has led to part porosity being a primary research focus in SLM/SLS technology [75]. Pore formation in parts has been related to two core causes: 1) the presence of bubble motions in the material melt pool, and 2) coalescence of pores due to bubble movement. Open air contents in uncompressed powders prior to manufacturing have a significant effect on the porosity of final parts. Powder mixtures must be compacted to improve density by exerting a greater pressure on the powder rake when feeding material onto successive layers, though this is dependent on the capabilities of the machine in use [76]. By compacting powders before processing, final part density is improved, and the material heating process can be controlled more precisely. The reduction of air cavities in the material results in more consistent absorption and dissipation of laser energy, which in turn supports a stable material melt pool [77].

There are various material specific factors that influence attainable final part properties in LM, these include: composition, material type, particle size, particle distribution and particle shape [78]. Research conducted by Murr et al. (2012), indicates that the uniformity of the melt, material flow ability, and layer packing are all optimized by the selection of powder particles that tend towards seamless spherical shape [79].

When conducting sintering procedures on sub-micron WC composite materials, the principal mechanism that affects large carbide constituents is particle rearrangement, whereas for finer carbide particles dissolution precipitation is the core sintering mechanism [80]. Attainable properties of parts in laser sintering/melting processes may be optimized by meticulous investigation of process parameters such as particle size and shape, ratio of constituent powders, laser power, scan intervals and scan speed.

Upon limiting the experiment's independent variables to scan speed and laser power while printing with tungsten powders, Zhang et al. [81], noted that when optimising the compounding effects of these two parameters, a smooth and uniform surface finish was obtainable on the part. Another noteworthy observation was regarding particle shape; during SLM, higher particle rearrangement and coordination numbers occurred with the use of polygonal shaped particle powders. Finer powders facilitate higher laser energy absorption which result in even melting throughout the material due to a larger specific contact area.

An additional aspect of the process that influences final part porosity is the surface quality of completed layers. Should they have a rough surface quality, air pockets may decrease the compaction of successive powder layers, inducing pores and increased porosity. Lastly, should the powder layers be spread unevenly, increased thicknesses in specific areas could create cavities throughout parts where powders remain unmelted. The unconsolidated powder cavities are far less dense than the bulk of the surrounding material, which increases the overall porosity of the part and diminishes its mechanical properties [82].

4.2 MACHINE CONTROL PROCESS

To achieve specific mechanical and microstructural requirements in SLM parts, the part design and printing control should be kept in consideration. The printing setup and process may be scrutinized in such a way that it affects final part mechanical and microstructural features as much as material selection or laser parameters would. These parameters include the scanning strategy, single layer thickness, hatch spacing and scan velocity.

It is evident that an inclusive evaluation of material specific parameters and process controls is required for SLM, SLS and laser metal deposition technologies. The goal of such studies is to pinpoint material specific approaches that result in high density parts with enough integrity for their intended applications. Though each evaluation is heavily dependent on the specified machine and laser system in use, it still provides a baseline to streamline future research endeavours [83].

There are two parameters in laser melting technology that have a crucial effect on the quality of the laser scan tracks: 1) laser power and 2) scan speed. Scan track formation is often the first qualitative screening conducted before printing to establish an initial parameter range for experimentation. The process should provide enough energy for full absorption to melt the powder thoroughly, while remaining conservative enough to avoid balling effects and impurities. The laser power affects the thickness and depth of scan tracks given a custom scan speed, whereas scan speed determines the width of the scan track [11].

As stated by Li et al [73] to outline material specific processing parameters, it is important to first study the effects of track formation on a single powder layer. These findings may then be extrapolated to make assumptions on how well successive layers will adhere to each other [84]. To distinguish the relationship between the abovementioned processing parameters, the Specific energy density characteristic is utilized, which is represented by the equation [30]:

$$E_d = \frac{P}{vd} \tag{4.2}$$

The variables in equation 4.2 are the specific energy density E_d [J.mm^{-2}], the layer thickness *d* [mm], laser power *P* [W], and scanning speed *v* [mm/s]. However, for a more thorough estimate of the absorbed energy within the powder melt, the volumetric energy density (*VED*) may be calculated. This adapts the specific energy density equation in 4.2 by accounting for the hatch spacing of the laser pattern *h* [mm] [33, 60, 61].

$$VED = \frac{P}{vdh} \tag{4.3}$$

An elevated volumetric energy density is necessary when producing high net density parts with LM technologies especially in the case of SLM. Using unalloyed metal powders, densities of up to 99% or greater are achievable. Favourable results call for the appropriate combination of optimised process parameters such as elevated laser power, lesser diameter spot sizes, good beam quality, and thin powder layers. However, these parameter arrangements often result in a more energy intensive and time consuming process [37].

Before processing an unfamiliar material, an experimental process window must first be determined based on scan track quality. This aims to avoid volatilities including spheroidisation (also referred to as "balling") and partial melting of the powder that lead to increased porosity levels [36]. Li et. al [73] classified four common melting states that help pinpoint the desired process window for the material under study. This was achieved by altering the laser power and scan speed during single layer experimentation with tungsten cobalt powders (W-Cu). The four states are 1) appropriate melting, 2) Balling, 3) partial melting, and 4) no melting.

To overcome the occurrence of balling during processing, overheating should be avoided. a processing window must be outlined based on the material specific powder deposition and laser parameters that facilitate an adequate temperature [83]. Another temperature dependant obstacle during processing is the vaporisation of binder material. The vaporisation temperature of binder particles must be accounted for to ensure that the laser temperature does not exceed this temperature, which may lead to overpressure in the melted area due to the hastened expansion of binder particles. This phenomenon ejects material from the powder bed. In processes such as SLM where complete melting of the hardened phase in the alloy is required, material ejection phenomena may be a prevailing obstacle.

The metallurgical features that come to be during processing of metal powders is highly dependent both material and process specific parameters. The compounding effects of these parameters should be studied to outline a process window which will result in the optimal scan track quality. Scan track improvement will in turn improve the adhesion of layers and the mechanical integrity of the entire part geometry.

4.2.1 Scanning Strategies

There are a multitude of scan strategies that have been developed over the years since laser melting technology was popularised. Each strategy possesses unique advantages and disadvantages and has been tailored to accommodate specific material properties. For instance, the evolution of the grain structure in SLM/SLS parts is highly dependent on the scanning strategy that is employed. It dictates the microstructural texture of the grains, as well as their orientation [44]. Currently there is no universal terminology for scanning strategies, as many authors tend to define strategies based on technology utilised in their research through analogies that are familiar to them, but there are recurring scan strategies popular throughout literature. Scan strategies may be further classified into either vector or layer strategies. Vector scan strategies relate to the individual scan tracks, whereas layer strategies describe the combination of vector strategies used to create successive layers and how they fit onto each other. The following section includes a summary of some popular vector scan strategies. Figure 4-1 showcases common features and terminology used to describe laser melting scan strategies.

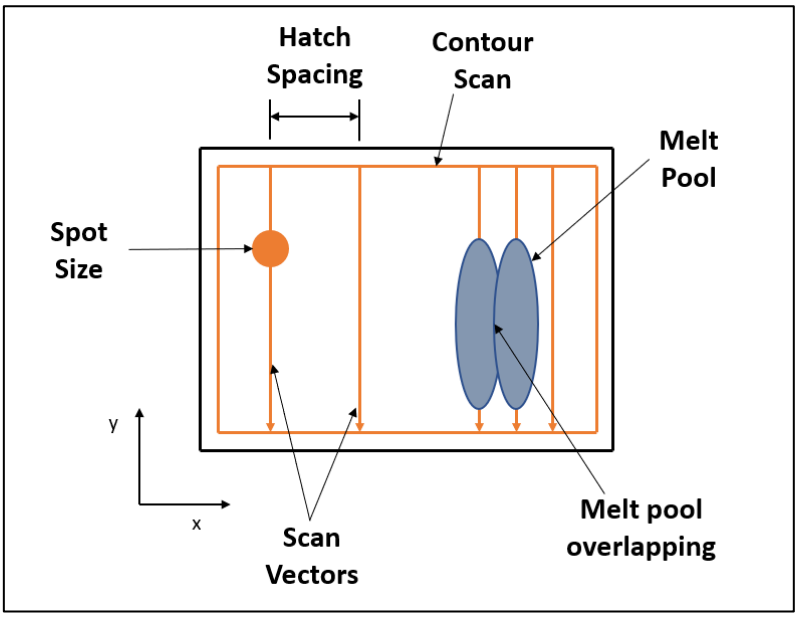

FIGURE 4-1: COMMON FEATURES AND TERMINOLOGY IN SLM/SLS SCAN STRATEGIES [44].

PARALLEL SCANS

This includes simple universal strategies that are easily executable. Vectors are all orientated parallel to one another in the same direction or alternating directions. For unidirectional, the laser scans from the origin (tail) to the end (head), and then returns to the origin to initiate each subsequent track. In alternating scans, the direction of each subsequent scan is alternated. The tail of each scan originates from the same side of the previous' head [44]. Lastly, there is the progressive scan strategy, a versatile pattern based on a similar concept to the alternating scan strategy. Tracks flow continuously without any intermission from the laser source.

At low speeds, these strategies often result in large temperature gradients, thermal stresses and increased porosity levels. At higher speeds temperature gradients are decreased, however, to maintain consistent energy input, the laser power must be increased proportionally. The aptly named, multiple scan strategy is a remedy employed to decrease the effects of thermal tresses. Here the laser power is kept constant and the scan is multiplied by an integer factor n (n = 1,2,3,4 …); the laser beam then re-scans the same path n times instead of once [87]. Figures 4-2 and 4-3 illustrate examples of these strategies.

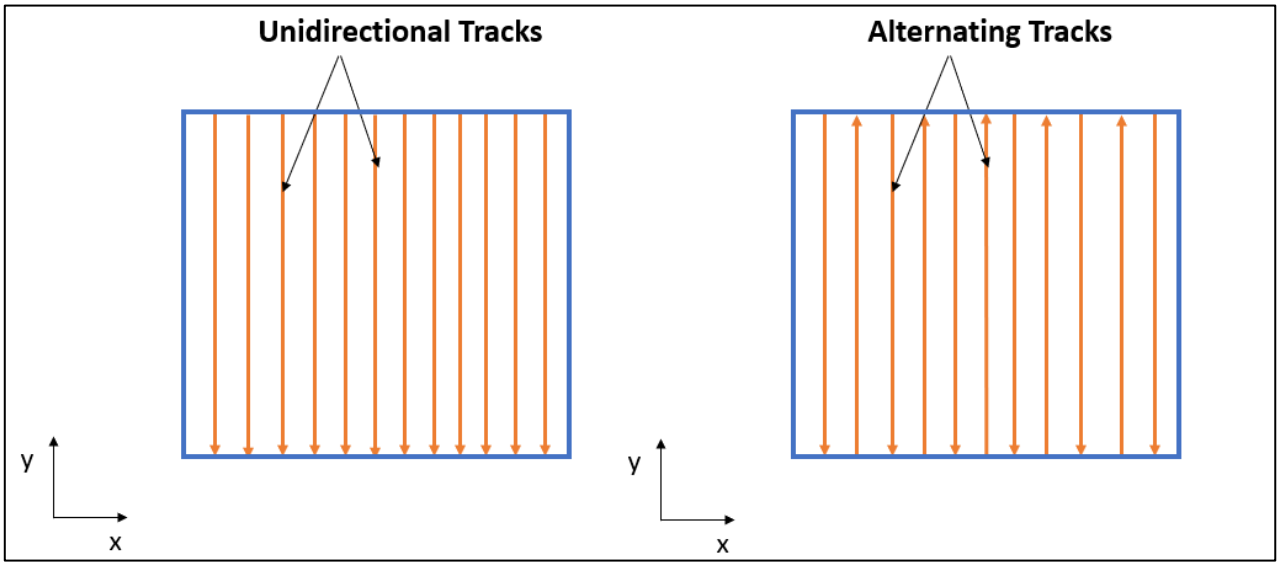

FIGURE 4-2: (LEFT) UNIDIRECTIONAL AND (RIGHT) ALTERNATING PARALLEL SCAN TRACKS [44].

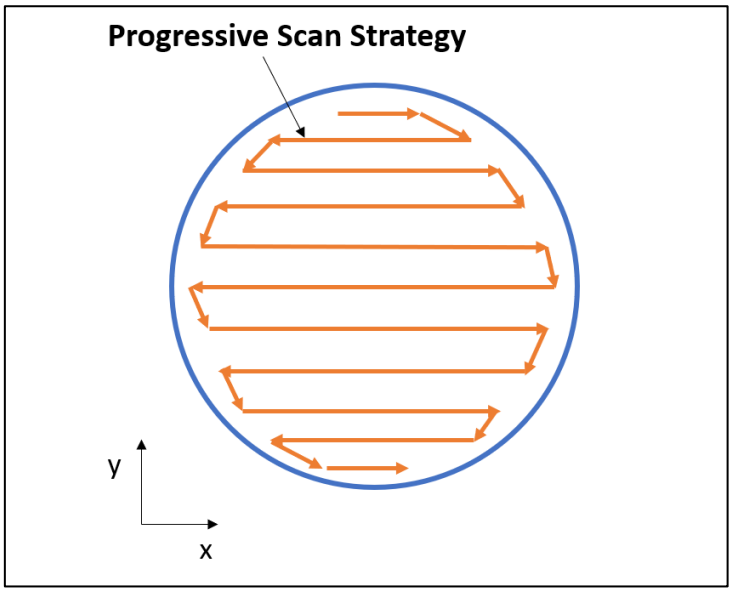

FIGURE 4-3: THE PROGRESSIVE PARALLEL SCANNING STRATEGY [44].

HELIX SCANS AND SPIRAL SCANS

Helix scan strategies are suitable for complex part production and were established with the aim to reduce steep thermal gradients and their associated deformations. The strategy operates with varying paths by compiling a Voronoi diagram of the individual layers and improves material bonding between layers [44]. The helix pattern may be exploited in several ways, vectors may be designed to change directions after each subsequent scan, or the origin could be set at the outer rim progressing inward, or at the centre of the part progressing outward. This pattern generally results in rougher surface finishes and is not suitable for production of cylindrical parts [87].

The spiral strategy is very similar to the helix, the difference being that the scan consists of a single continuous spiral vector for each layer [44]. Spiral scanning was proposed as a possible remedy for overheating and to equilibrate the thermal gradient. The strategy works best with high scanning speeds and may yield better results than parallel scanning strategies. Multiple spiral scanning of the same layer is often used to increase the density of parts; the main condition for multiple scans to be effective is that heat losses between scans must be minimal when compared to the deposited energy. In the case of very conductive powders, multiple scans can create exceptionally strong bonds between layers, but only small surfaces may be treated at high scan speeds and laser power. It is critical to acknowledge that spiral strategies incur severe overheating at the centre of the part [87]

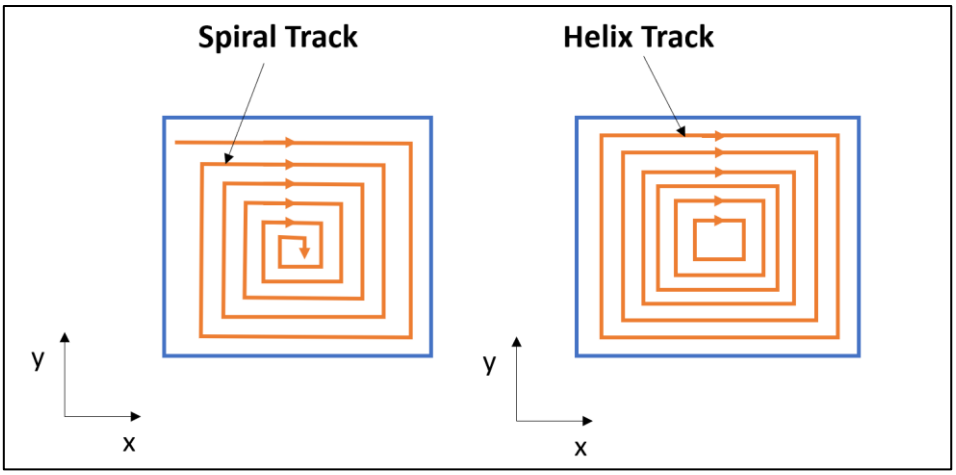

FIGURE 4-4: (LEFT) SPIRAL TRACK AND (RIGHT) HELIX TRACK SCANNING STRATEGIES [44].

ISLAND SCANS

Also known as the Chess board strategy, it divides the subjected area into smaller sections (islands). These sections are then scanned in a random order with shorter tracks, which reduces localised heating. To further reduce localised thermal stress and contribute to a smooth surface finish, each section is comprised of alternating tracks of a different orientation [44]. The sections consist of widths (W_H & W_v) and may be described by a repetition of small-scale parallel scan strategies. The randomisation of printing islands is crucial as it adapts thermal dynamics in the powder bed as to mitigate temperature inhomogeneities [87].

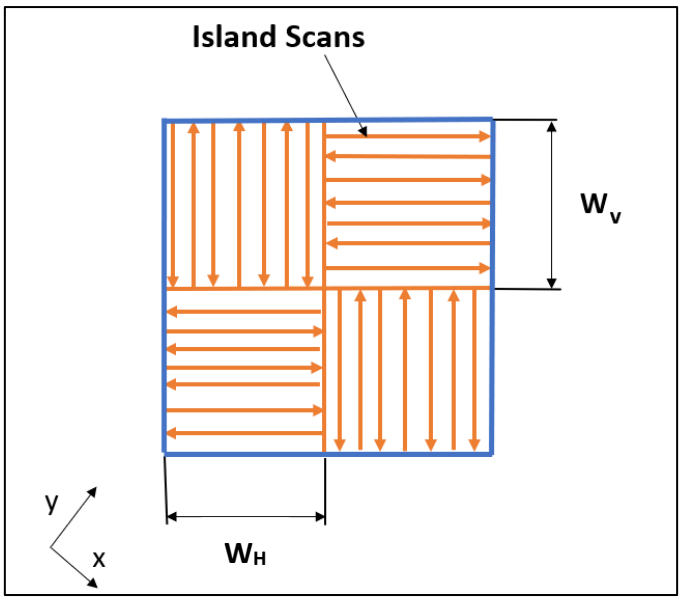

FIGURE 4-5: SCHEMATIC INDICATING THE FEATURES OF ISLAND SCANS [44]

4.3 LASER ENERGY SOURCE

As the laser power is reduced, the peak temperature and size of the powder melt pool is also reduced. This induces an increased rate of cooling and ultimately higher levels of deformation. Therefore, higher laser power levels result in less final part deformation, at the cost of increased energy usage [88]. In addition to mitigating the effects of deformation, increased laser power also improves final part porosity. Though porosity is heavily dependent on the scanning strategy employed, higher laser power has been proven to increase the density of parts [89]. In all additive manufacturing processes that deal with powder-based materials, a multitude of elements can influence proper particle amalgamation; a prominent factor being laser specific parameters such as the energy per laser pulse, wavelength, laser power and spot diameter.

A common problem associated with the laser focal point of SLS and SLM machinery is the uniformity of heat distribution as the laser angle varies across the surface of the material. Should the laser be completely perpendicular to the surface, optimal energy absorption will occur on a perfectly round focal point. Though as the laser contact angle varies when the laser travels across the surface, the laser's penetration angle changes accordingly. The spot focal point transforms into a more oval shape at the edge of the powder bed and energy absorption becomes less effective throughout the entire contact area. This brings about complications associated with part density and deformation [90].

In 2012, Zhang et al. [81] confirmed that increased laser energy absorption is possible if a smaller laser beam focus was combined with greater laser power. A smaller diameter laser beam may overcome the detrimental effects of the elliptically deformed contact area at the powder bed edges. As the nominal size of part features approach the spot size diameter of the beam their overall accuracy falters [30]. It is apparent that in laser sintering operations the laser beam selection plays a prominent role in how well powder particles consolidate during processing.

Both the energy absorptivity of the material and densification of the powder are dependent on laser specific parameters. For instance, the absorptivity is heavily reliant on the wavelength of the laser source, and densification of amalgamated particles on the incident laser energy applied to the powder bed. The amount of energy transferred to the powder bed is directly proportional to the duration of exposure per spot diameter area. The average contact time ranges between 0.5ms and 25ms, derived from the spot size diameter and scan speed [30]. Within powder bed technology the material absorptivity characteristic is dependent on the apparent density, granulomorphometry and physicochemical properties of the powder. This results in far higher absorptivity for powders compared to bulk materials. For example: $A_{Fe\ bulk} = 0.36$ $A_{Cu\ bulk} = 0.02$, and $A_{Fe\ powder} = 0.7$, $A_{Cu\ powder} = 0.6$ for laser wavelengths $\lambda = 1.06\ \mu m$ [91].

To achieve favourable particle consolidation, three popular high energy density laser variants are used in LS/LM applications, namely: 1) neodymium-doped yttrium aluminium garnet lasers (Nd:YAG), 2) high powered CO_2 lasers, or 3) Fibre lasers [92]. When operating with such laser technologies, the reflectivity of the processed material must be considered. Reflective properties are unique for each material, which may each react differently depending on the wavelength of the applied laser during the process. For example, Copper (Cu) portrays high reflectivity for wavelengths around 1064nm, which causes poor energy absorption into the material and subpar particle sintering [78]. In extreme cases the laser may be reflected in a mirror like fashion which could damage the interior of the machines processing chamber. Proper surface treatment before laser processing is thus of the utmost importance.

4.4 OBSTACLES IN POWDER BED TECHNOLOGY

In the early 1990s when additive manufacturing was still a novel research concept, warping and residual stresses within parts was predicted to become one of the field's supreme obstacles. The following sections aim to identify how these phenomena may be quantified, while highlighting the mechanisms that result in warping and deviation of part geometry during the laser melting process.

There are several phenomena that affect additively manufactured parts, particularly when powder bed technologies are employed. These impede the machines capability of producing parts according to desired specifications. The process specific phenomena & their solutions were summarised by Kumar [93] into five difficulties faced by SLS and SLM technologies.

(1) **Uprooting** occurs when the sample surface is uneven or slanted and the laser is incapable of reaching the necessary sections. Usually, this is due to insufficient bonding between the substrate and prior layers from surface imperfections or protrusions on the sample. (2) **Displacement** often occurs due to the same causes as uprooting. When samples are shifted on the base plate during processing, offsetting the planned geometry. (3) **Warping** happens when the edges of the layer remain attached to the underlying surface while the centre of the layer protrudes outward. (4) **Delamination** is the Fractional undoing of a processed layer or multiple layers from an adjacent layer or the substrate surface. It often follows an abrupt change in process parameters that affect the adhesion of certain layers compared to others. Lastly, (5) **Curling**, involves the upward bending at the edges of a sintered part despite the centre remaining attached to underlying layers.

The abovementioned shortcomings are predominantly process specific and may be remedied by adjusting machine parameters during production. A study by Kumar in 2009 [93] stated that curling and warping may be mitigated by supplying a lower incident laser energy. Furthermore, delamination may be avoided by keeping the process parameters constant throughout production to guarantee that stresses and inter layer bonding forces are equally distributed throughout. There are three converging factors that may be adjusted to reduce displacement and uprooting, namely, 1) scan the initial layers with higher laser power, or re-scan it to ensure consolidation and part adhesion to the substrate throughout processing. 2) Should protrusions or sharp edges occur, laser power must be lowered as they hinder layer adhesion and risk catching onto the powder distributor and dislodging the part from its fixture. 3) To ensure sufficient adhesion of layers, laser power should be increased if the occurrence of only partial sintering is noted [93].

An additional remedy to uprooting and displacement of the part involves increasing the laser pulse frequency. This brings about anxcv increased energy density per unit length and a molten pool that persists for longer [94]. In experiments with WC-Co, this resulted in better wetting characteristics and the formation of an improved metal matrix. On the downside, large increments in the laser pulse frequency may incur overheating of tungsten carbide particles, which leads to graphite precipitation and undesirable phenomena such as build-up of carbon monoxide (CO) or carbon dioxide (CO_2) or the formation of hardened W_2C and W_6C phases.

4.4.1 RESIDUAL STRESS

Several ways exist to classify the residual stresses in materials. A popular variant concerns three types of stresses based on the length scale (l_0) over which they autonomously come into equilibrium [95]. ***Type I*** residual stresses influence the entirety of the part body, are macroscopic in nature and equilibrate across the entire length of the subject structure $l_{0,\,I.}$ The second variation, **Type *II*** stresses, consist of residual stresses originating from localized, intergranular occurrences that commonly occur over a range of multiple grains $l_{0,\,II.}$ Type II stress has a consistent presence in polycrystalline materials due to their innate anisotropic crystal structure and multitude of grain orientations [95]. Lastly, ***Type III*** residual stresses are caused by intra-granular defects in the crystal structure on a far smaller scale than the prior types $l_{0,\,III}$. These defects distort the crystal lattice and include dislocations, alien atoms and vacancies. Types II and III stresses are considered microscopic in nature.

A multitude of phenomena result in residual stresses, which all typically bring about inhomogeneous plastic deformations. Temperature gradients induce thermal residual stresses and may even be prompted by local differences in thermal expansion during equilibrium cooling. Induction of this nature convoy with non-uniform cooling of the material melt pool and is a common occurrence in SLM or welding processes. Non-uniform cooling causes colder zones in the bulk material to contract and more malleable hot zones to give way under the contraction. If the part is free to move, these interactions may result in warping and deformities on a greater scale [95].

RESIDUAL STRESSES IN SLM/SLS AND THEIR INFLUENCE ON MECHANICAL BEHAVIOUR

SLM has the capability to produce parts with close to zero porosity; residual stresses are still induced during the process due to high thermal gradients. Residual stresses result in distorted part features, delamination of layers, or cracking. These defects occur when there is inadequate stress relief between formed layers. In SLM/SLS parts' residual stresses are less prominent in the scan direction than its perpendicular[78].

Part deformation is the most taxing consequence of residual stresses, especially since laser AM processes have received praise for dimensional accuracy in producing complex geometries. Parts curl upwards or warp due to bending moments induced by the distribution of stresses, this is largely dependent on the orientation and size of the part, regardless of its geometry. This warping has often been seen as an opportunity to study the residual stresses within AM parts and their effects during production [96]. Residual thermal stresses that originate from temperature gradients within materials are discussed thoroughly within the following sections. The effects of these stresses on mechanical behaviour may be concisely classified into three occurrences [95]:

- Unexpected part failure due to compounding effects of residual stresses and applied mechanical stresses
- When Type I or Type II tensile stresses are present at unprotected surfaces, stress-corrosion cracking often occurs.
- Undesirable component deformation induced by residual stresses due to thermal gradients.

PREVENTION AND TREATMENT OF RESIDUAL STRESSES

In conventional powder metallurgy residual stresses may be controlled by prolonging the sintering process. In AM, however, several techniques exist, one being the preference of sintering procedures instead of full melting. Lower sintering temperatures limit thermal stress formation, and ultimately mitigates deformation, cracks and delamination [37]. In SLM grain growth can be controlled by re-melting layers before advancing to successive scans to reduces residual stresses. Furthermore, laser beam parameters and other processing settings may be tailored to anneal processed layers [79]. Re-heating of layers may bring about comparable results to stress relief efforts in prolonged sintering in PM.

An additional method of reducing residual stresses and limiting distortions in parts would be to heat the build platform prior to processing. Once the platform reaches temperatures just below the material melting point the powder is sufficiently pre heated. This is advantageous for sintering and final part quality and has been reported to improve the process in the following ways: [30]

- Reduced temperature gradients
- Better metal matrix wetting properties
- Enhanced absorption of laser energy
- Inhibition of non-uniform thermal contraction and expansions that result in part warping
- Reduced laser power requirements during processing.

Upon analysing laser sintered and laser melted parts, it was observed that the residual stress profile was comprised of considerable tensile stresses at both the top and bottom sides. Compressive stresses were noted throughout the bulk between the part [83]. The characteristics of the stress profile are affected by the following:

- The laser scanning strategy and process parameters
- Height of the part
- Properties of the substrate and printing materials.

According to Wang et al. [97], a functional composite gradient may potentially induce compressive surface stresses in the material, which could benefit its structural integrity. Crack initiation may be hindered, or its propagation halted by compressive stresses that either mitigate WC surface grain pull-out, or closed crack tips.

4.4.2 SCAN TRACK STABILITY

During operation, a laser scans the surface of the powder bed line after line, melting the material into an elongated spherical pool. The pool may be circular or a segmental cylinder depending on the surface tension of the liquid. After scanning, molten tracks can become fragmented instead of continuous, which is referred to as the “balling” effect. This track instability is a well-known phenomenon in SLM/SLS and is affected by process characteristics such as laser power, layer thickness, scanning speed, granulomorphometry of the powder, substrate materials and the physical properties of the subject material. The quality of the final parts is heavily dependent on the properties of single tracks and single layers [91]. Track stability and instability zones must be identified. Stable tracks have continuous and uninterrupted melt pools, while unstable tracks are characterized by non-continuous tracks and the formation of scattered droplets[98].

The occurrence of spheroidisation and other surface defects often sprout from the presence of oxides between layers of powder particles. To ensure smooth layer formation, appropriate wetting within the powder system, and consistent metal to metal bonding without cavities, the prevalence of surface oxides must be addressed [83]. An inert operating environment of argon or nitrogen gas has proven to reduce oxidation, however at their corresponding melting temperatures, most metals form oxides regardless of the presence of low oxygen partial pressures in the environment [83].

In a study conducted by Rombouts et al. [99] dense iron-based parts were manufactured with SLM technology in an N_2 atmosphere of less than or equal to 0.05% residual oxygen content ($\%O_{atm}$). It was found that a higher percentage of atmospheric oxygen content ($\%O_{atm}$) was directly related to an increase in balling effects. Oxygen is present in most metals as an impurity element, but may be collected from the atmosphere to satisfy the equilibrium concentration at each respective metal's melting temperature [99].

The experiments concluded that lower scan speeds resulted in no balling effects and smooth scan tracks, which lead to smooth layer formation. At intermediary scanning speeds, perpendicular to the scan direction convex cylindrical sectors formed resulting from the overlapping effects of successive scan tracks. At high scan velocities, lower heat absorption resulted in layers covered with smaller discrete droplets.

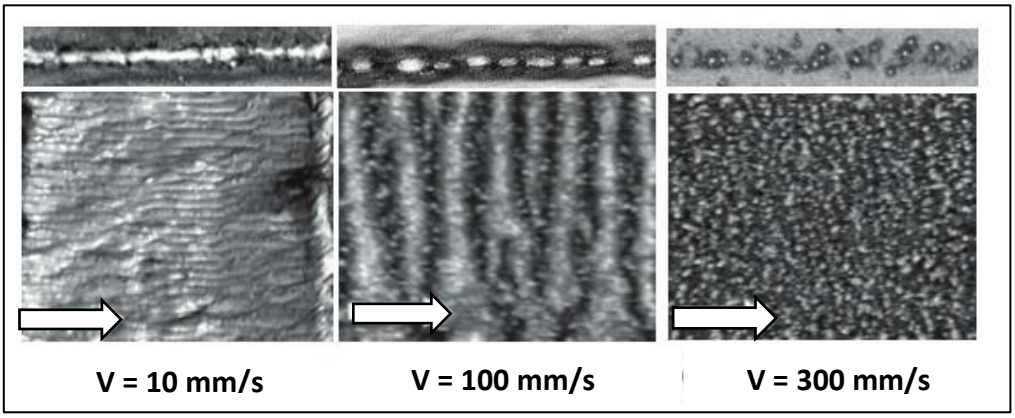

FIGURE 4-6: SCAN TRACK QUALITY MEASURED AT VARIOUS VELOCITIES UTILIZING 95W LAZER, 0.14MM LAYER THICKNESS AND 3% OXYGEN CONTENT SOURCED FROM DONG DONG ET AL. [78].

A study by Manvatkar et al. [88] scanned loose Fe powder with varying speeds of single laser tracks. His work validated that the occurrence of spheroidisation is directly influenced by the oxygen content of the work chamber and scan speed of the laser. The melt pool area increased within an O_2 atmosphere compared that of an inert N_2 atmosphere. This area increase was also noted when increasing the laser scan speed. The width of the melt pool remained relatively constant and when an area increase occurred it was likely due to an increase in melt pool length. This initiated Rayleigh instability, which occurs when a liquid cylinder breaks up to decrease its surface energy due to a high aspect ratio and contributes to balling effects.

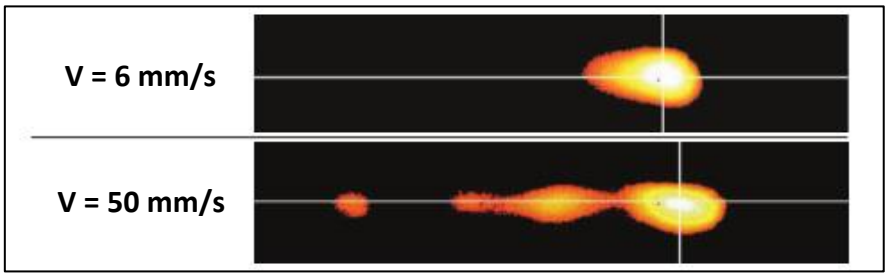

FIGURE 4-7: MELT POOL QUALITY OF SINGLE TRACKS CONDUCTED IN AN INERT ATMOSPHERE WITH FE POWDER. SOURCED FROM DONG DONG ET AL. [78]

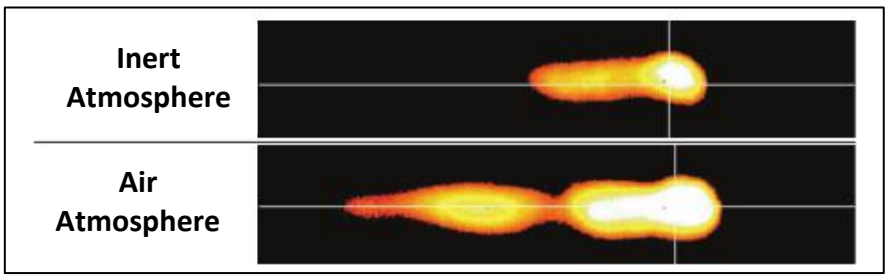

FIGURE 4-8: THERMAL IMAGES OF MELT POOLS FOR FE POWDER AT V =16 MM/S IN VARING ATMOSPHERIC CONDITIONS. SOURCED FROM DONG DONG ET AL. [78].

As a result of the substantial difference in melting temperatures between the reinforcement phase and the binder phase, intercrystallite weaknesses occur as solid particles de-bond alongside their boundaries [37]. This de-bonding has a notable detrimental influence on the mechanical properties of parts produced by partial melting, specifically the tensile strength. The manifestation of surface oxides on the powder particles yields a decarburisation process during sintering of WC. This decarburisation results in the formation of a W_2C phase, that critically affects the final density of parts [100]. Upon excessive heating of WC-alloys, the precipitation of carbon produces graphite phases and an overall carbon deficiency. As stated by Anderen et al. [101],the following equation illustrates the chemical reaction that takes place in such cases.

$$2WC \rightarrow W2C \rightarrow W2C + C \tag{4.4}$$

Graphite interacts with the oxygen and forms carbon dioxide (CO_2) and carbon monoxide (CO) in gaseous cavities between layers that cause parts to become porous and brittle. By adding excess carbon into the powder mixture the formation of gaseous phases may be mitigate, however, throughout processing this ultimately increases grain growth [101].

Often when the input energy density is insufficient, a cylindrical free surface forms with a small contact area onto the substrate. There is a diminished level of heat conductivity and minimal penetration of the powder into the substrate which mitigates adhesion of the track to the surface. In a study by Yadroitsev et al [91], the single track properties of various grades of tool steels were observed. It was noted that given a specific laser power input, lower scan speeds resulted in high energy input per unit length and higher temperature melt pool volumes. At low scan speeds and laser power, there was not enough energy transmitted into the powder bed to melt the substrate material, which negated the stabilizing effect of powder penetration into the substrate.

The layer thickness of the deposited powder layer is another prime determinant scan quality; its selection should be based on thorough consideration of shrinkage characteristics and powder particle size. The aim is to achieve an effective energy balance wherein all the powder particles interact with laser radiation and bond with the substrate, while avoiding extreme energy levels that may distort tracks. As the maximum energy input into the material increases, so should the thickness of layers that will result in desirable scan tracks. [102].

Yadroitsev et. al [103] concluded that the SLM/SLS process is subject to two threshold phenomena: stability and instability zones. The prior is identifiable by continuous tracks, and the latter by inconsistent or broken tracks. At lower scanning speeds instability zones occur as irregularities and distortions, while at higher speeds it leads to balling. At higher laser powers, the formation of desirable scan tracks was achievable at a wider range of scanning speeds. Which suggests that a process window less prone to sensitive variation is achievable at higher laser powers.

In a study by Wang et al. [98], when evaluating single scan tracks they were divided into four groupings; it was apparent that track types were related to specific energy input ranges. The energy input per unit volume is denoted by equation 4.5. Layer thickness is not included in this formula, as it should be set to the lowest possible value permissible by the particle size for the calculation to be sound.

$$\psi_1 = \frac{4P}{\pi d^2.v} \tag{4.5}$$

The four scan track groupings were: 1) regular and thick tracks, 2) regular and thin tracks, 3) regular but broken tracks, 4) and irregular pre-balling tracks. A range of energy input per unit volume (ψ) was attributed to each grouping, which gave a level of predictability to the outcome of different parameter combinations. The tracks deemed to be suitable for part fabrication were regular to thin continuous tracks and regular to thick continuous tracks.

In the same study multi-track layers were also investigated, specifically the effects of heat accumulation from track overlapping. In order to yield dense parts with desirable surface quality, suitable hatch spacing should be utilized. Wang et al. concluded that thinner tracks required smaller hatch spacing to ensure more overlapping while thicker tracks produced better parts at lower hatch spacing.

4.4.3 LASER PENETRATION MODES

Keyhole formation is a definitive characteristic of high-powered laser processing. If the laser beam is focused at high enough energy densities, the temperature at the material's surface may be enough to melt the powder layer and extend the molten pool through to the substrate material. In this case intensive evaporation induces a recoil momentum, which creates a narrow vapour cavity in the molten material and improves laser absorption, allowing the laser to penetrate deeper into the substrate. This phenomenon is useful for creating a strong bond between the deposited layers and the substrate and can produce a dense microstructure along the surface of the treated part. Although, upon the collapse of the cavity, voids are often left behind that contribute to unwanted porosity [104].

Three primary variations of keyhole formation were first identified in research pertaining to high power laser welding; referred to as weld modes. These include 1) conduction mode, 2) transitional mode, and 3) keyhole penetration mode. These modes are indicated in figure 4-9 below.

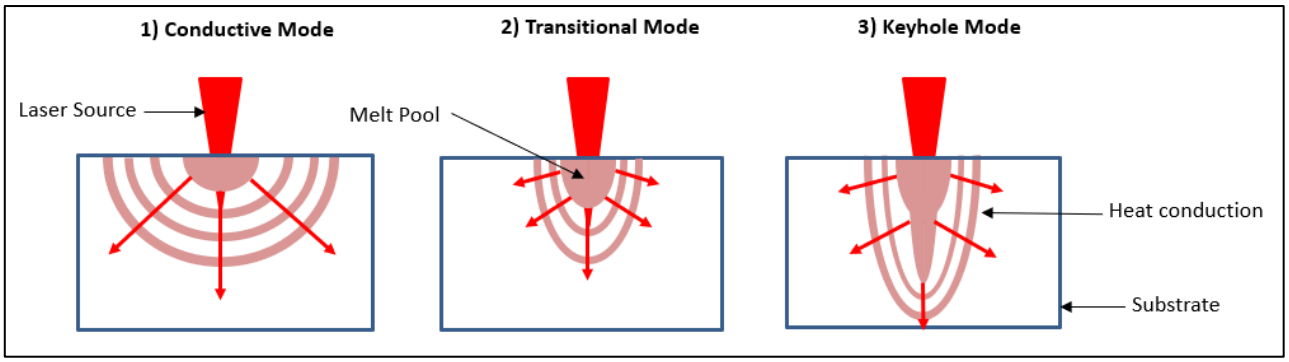

FIGURE 4-9: COMMON MELT POOL MODES [104].

Due to the similarity of laser welding and laser additive manufacturing processes, these phenomena may be transferred to describe laser penetration characteristics in laser melting and cladding processes [103]. The understanding and regulation of keyhole formation is an important endeavour to improve quality control in laser fusion technologies.

In a study on laser cladding technology by Locs et al [105], it was found that first layer application of coatings with keyhole mode penetration may ensure a gradual distribution of internal stresses near the surface and provide additional resistance to external cyclic loading. By controlling the size and shape of the keyhole penetration, a smooth internal stress distribution was achievable at the coating substrate interface. Furthermore, by manipulating processing parameters such as the scanning speed and hatch spacing, the microstructure of the material may be tailored to refine grains at the substrate surface. These findings may be applied to exclude the need for a buffer layer during common surface modification techniques.

4.4.4 LAYERED DEPOSITIONS

Track width is a major influence on surface quality, density and dimensional accuracy of parts and is a crucial factor in laser manufacturing. As stated in the research by Wang et. al [98], due to the occurrence of overlapping and re-melting during scanning of successive tracks, inevitable heat effects from prior scans occur. Following this assumption, the energy density formula (4.5) discussed prior must be augmented to account for heat accumulation. Here, ε represents heat accumulation due to multi track deposition, it accounts for the wetting matrix provided by prior tracks for each new scan.

$$\psi_2 = \frac{4P}{\pi d^2 . v} (1 + \varepsilon) \tag{4.6}$$

To ensure dense and smooth surface quality during sintering an overlapping rate must be chosen and is closely relatable to the heat accumulation due to successive scans. Conventionally, the hatch spacing, h [mm] and beam diameter, d [mm] is used to determine multi track overlapping according to the formula:

$$\phi = \left(\frac{d-h}{d}\right) 100\% \tag{4.7}$$

However, the practical track width obtained is not considered in this estimate, which is a function of the laser processing parameters employed to produce each track. Intuitively, the spot diameter is replaced by the practical track width 't'. The formula is now rewritten as:

$$\phi = \left(\frac{t-h}{t}\right) 100\% \tag{4.8}$$

Figure 4-10 below describes this relationship between hatch spacing, practical track width and overlapping rate as per equations 4.7 and 4.8. Despite the logical reasoning behind 4.6, it is still difficult to apply practically due to the inherent complexity of the heat accumulation represented by the ε - term and its interactions during processing. In a study by Prashanth et. al [106], the reliability of energy density equations were evaluated for laser AM applications. The research concluded that conventional energy density measurements only provided approximate estimations, and it was recommended that material properties and hatch parameters be included into a more robust model to correctly estimate energy density.

Therefore, analyses throughout this research will rely on the conventional energy density models, described in equations 4.2 and 4.3; yet the use of equations 4.7 and 4.8 will also be employed to determine reasonable hatch spacing and overlapping parameters for the layered deposition phase of experimentation.

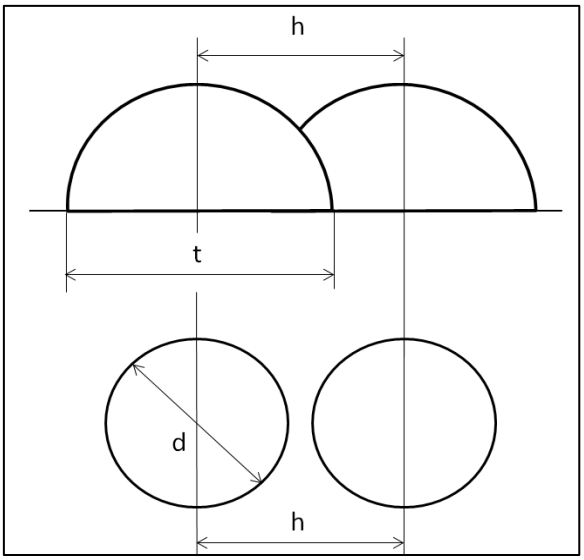

FIGURE 4-10: SECTIONAL VIEW (TOP) AND TOP VIEW (BOTTOM) OF SCAN TRACKS IN FORMATION OF LAYERS.

4.4.5 GRAIN GROWTH DURING SINTERING

For LM technology, the grain growth phenomenon is different to that of conventional casting. As a laser beam scans across the surface, heat is conducted perpendicular to the scanning direction wherein the material solidifies into prior layers and yields multidirectional grain growth. Concurrently, LM entails a high-speed solidification process that results in the simultaneous formation of various multi-directional grains. Neighbouring grains quickly come in contact with each other before they can propagate far and the material thus consists of various small grains with a very fine microstructure [98].

Grain growth is a prominent obstacle in the AM of carbide powders. This phenomenon may be controlled by tailoring the consolidation parameters such as laser temperature and sintering duration in the printing process. The solidification microstructures and the respective grain sizes that accompany them determine the mechanical properties of parts produced with AM [107]. For instance, when employing functionally graded carbide composites (FGCs), which include WC-Ni, WC-Co and other alloy variations, a gradient in the size of WC grains and distribution of binder material is exhibited.

The effects of these gradients converge, ultimately producing components with varying microstructural features due to fluctuating gradients of their constituent materials. This impedes thorough classification of the part's material and mechanical characteristics [107].

In sintering processes, rapid solidification microstructures are moulded by prompt conduction through the substrate [83]. Such microstructural phases are characterised by unique mechanical properties that rely on the composition of the material. According to studies on WC-Co by Allibert et al. [108] the two phase WC-Co region is only attainable within a precise powder composition range. The slightest variation in the constituent concentrations of carbon or tungsten will likely result in formation of carbon or eta (M_6C) phases, which cause undesirable material and mechanical properties in finished components [94].

In a study on the influence of laser scanning strategies on grain structure development during SLM. Carter et al. [109] reported a tendency for epitaxial grain growth from one layer to the next due to consistent re-melting. Additionally, the heat conduction between layers in the z-direction resulted in largely elongated columnar grains and fine-grained regions that formed due to the laser scan spacing. The scanning pattern has a critical influence on the grain structure of parts produced. Prominent trends exist when considering both the grain structure and scanning pattern, however, the results are also largely dependent on the material's heat specific characteristics.

4.4.6 Cracking & Shrinkage

Cracking of samples produced in powder metallurgy-based AM systems is a major obstacle that may occur due to both process inadequacies and treatment post-production. During processing, crack formation is commonly ascribed to thermal gradient mechanisms (TGM) which induce residual stresses throughout the part. Post-production, parts with rough surfaces and irregularly shaped pores are more likely to crack due to stress concentrations at sharp edges throughout the material [83]. Crack formation can be further classified into macroscopic or microscopic variations. Macroscopic cracking, also referred to as "cold cracking", is prevalent after the melt has solidified into its final geometry, owing to insufficient material ductility and deformation due to stresses induced during cooling. Microscopic cracks, or "hot cracking", occurs on a far smaller scale and may be attributed to rapid cooling or solidification of the powder melt. Pent up residual stresses throughout the material layers present the opportunity for cracks to originate, and particle bonds following grain boundaries to be broken [8].

Crack formation may be further attributed to TGM such as a rapid temperature increase on the uppermost layer by the incident laser energy and the slow conduction of heat to prior layers. [37] This temperature surge reduces the yield stress of the material, and upon reaching this stress threshold the upper layers of the print are plastically compressed. Hereafter, the upper layers will cool and shrink again, while the lower layers are warmer due to the slow conduction of heat into the bulk of the material.

The uppermost layers become shorter and an upward bending moment is generated towards the laser beam. With each consecutive powder layer consolidated onto the top of the sample, the underlying layers experience a similar recurring temperature gradient. This induces distortion and failure of working parts through delamination and cracking as the TGM forces the underlying layers to bend the amalgamated layers towards the laser beam [110]. Figure 4-11 indicates the abovementioned TGM process and introduces the continuous sequence of thermal expansion and shrinkage, resulting in cracking of the produced parts.

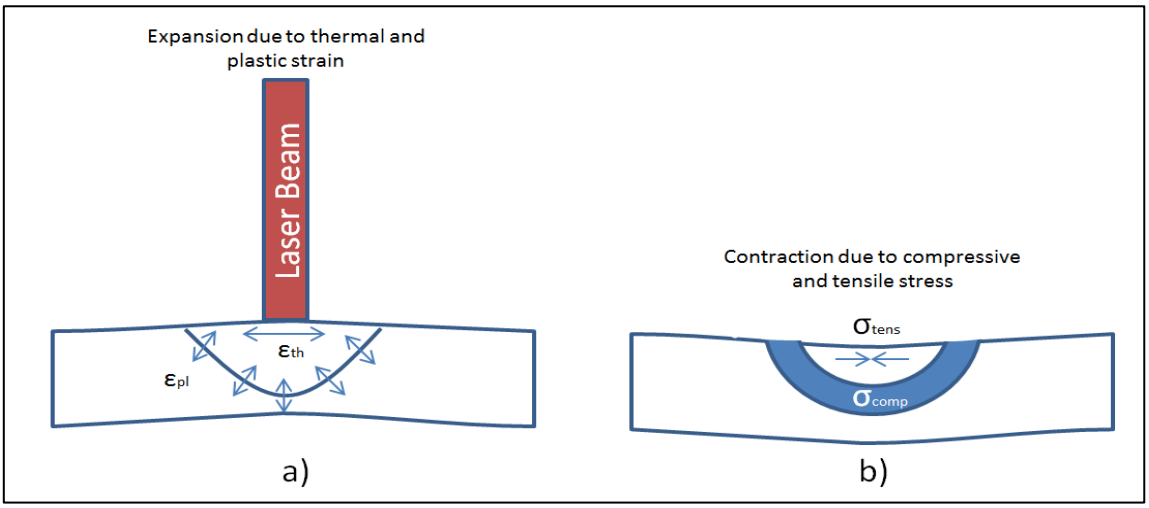

FIGURE 4-11: TGM DUE TO A) THERMAL EXPANSION AND B) CONTRACTION. SOURCED FROM [84] & [110]

4.5 PRIOR RESEARCH

The following section aims to highlight the current state of research pertaining to AM techniques that produce novel cemented tungsten carbide materials. The research encompasses a variety of processes and materials that may aid in providing process recommendations in the experimental phase of this study.

Many prior studies have been conducted concerning the effects of various process parameters on the properties of final parts. As AM is still an emerging field, an urgent need has arisen to decipher which parameter combinations will result in optimal outcomes for each new material in the wide array of novel materials that the technology is capable of processing. Critical properties include high density, desirable toughness to hardness ratio & capability to resist wear.

Research ventures such as Yadroitsev and Smurov [74], Gu and Shen [86], Agarwala et al. [111] and Yadroitsev et al. [102], honed their studies on SLS and SLM process parameters and their effects on multi-layer, single layer, and single scan track properties. Specifically scan speed, laser power and layer thickness parameters. Authors like Hauser et al. [38], Mumtaz et al [112], Yadroitsev et al. [74] and Simchi [85], focused on the achievable properties of single scans, layers and amalgamated layers that may result from novel materials types and compositions. Further research supplementary to this thesis includes the analysis of detailed forming mechanisms during sintering such as residual stresses and balling effects by Shiomi et al. [113] and Tolochko et al. [103].

These works provide a broad base of knowledge from which laser melting technologies can expand to various other novel materials and applications. For example, when experimenting with new materials such as WC-Ni, prior research on the effects of laser power and scan speed on WC-Co part quality provides a level of predictability from which conclusions can be drawn when designing an experiment. This is advantageous when time and resources are scarce, and the number of experimental iterations should be kept low.

According to work conducted by Zaeh and Ott [75] in a study on tungsten carbides in particular, it was discovered that heating the build platform prior to production resulted in superior part porosity, and improved handling of materials that are difficult to fuse i.e. cemented carbides. Critical boundary conditions were recognized throughout their experiments which include: 1) An invariant laser source, 2) open loop control of the build platform heating, 3) Consistent powder with the same configuration throughout the entire build is required.

In a study by Sinirlioglu [114], wherein dental bridges were manufactured utilising an M1-Cusing machine, a wide range of laser scan strategies and parameters were considered. While there are over 100 parameters at play during scanning, those with the greatest notable effects were determined to be:

- Layer thickness, d [mm]
- hatch spacing, h [mm]
- Spot size diameter [mm],
- Scan speed, v [mm/s], and
- Laser power, P [W].

Yasa and Kruth [82], delved further into these results by varying laser power, scan speed and hatch spacing. Their findings concluded that an optimal arrangement of these parameters may lead to desirable surface features and high-density final parts. This said, there may be critical influences on final part properties in the parameter ranges not yet considered. The rationale behind experimentation by Zaeh and Ott [75], is that by evaluating the volumetric energy density (VED) at several configurations of its constituent parameters (i.e. layer thickness, hatch spacing, scan speed and laser power) the study would conclude and optimal parameter combination.

Yasa and Kruth [82], outlined in their investigations that the conventional layer thickness for laser processing technologies varies between 30 – 70 µm however these values are dependent on the mean particle diameter of the powder and the machine's OEM (original equipment manufacturer) specifications. For instance when utilizing LaserCusing® the recommended layer thickness is shifted to between 20 – 50 µm [114]. In the research by Yasa and Kruth [110] on AISI 316 stainless steel powders, the following combination yielded parts with the best porosity: scan speed (380 mm/s), laser power (105W) and hatch spacing (125 µm). It was noted that higher energy input was directly related to drastic increase in part porosity, while decreasing porosity was seen between scan speeds of 50 – 200 mm/s.

Since they are the primary drivers for material melting during sintering, Campanelli et al. [30], experimented exclusively with varying scan speed and laser power while producing 18-Ni-Marage-30 steel samples. The material is comparable to conventional maraging steels reinforced with a cobalt or nickel binder and the powder particles had an average size below 40µm. Layer thickness was kept at a consistent height of 30 µm and unchanged oxygen content within the build chamber at 0.08%. Hereafter 15x15x10mm^3 samples were produced and their density, hardness and microstructural features were further analysed. The results of this study indicated that part density increases while high energy densities are applied. Applying a scan speed of 180mm/s and laser power of 100W returned samples with excellent approximate porosities at 0.01%.

Paul and Khajepour [94] looked into component level fabrication with laser melting technology, however, before commencing with the full scale prints several single tracks were produced to inspect the parameter combinations that produce uniform, fully melted and continuous tracks. The authors discovered that higher laser pulse frequencies produced increased energy densities for each unit length. This permitted the melt pool to stay in liquid phase for a longer period and resulted in a more desirable WC-Co matrix. In contrast, it was observed that increasing the laser pulse frequency too far overheated the samples and induced graphite precipitation and the formation of eta-phases.

In an attempt to mitigate the current limitations of SLM technology Yasa and Kruth [82] verified that re-melting each built layer after solidification lead to released stresses, decreased trace porosities and a smoother surface quality of samples. Their study proved that the re-melting technique (when applied with a suitable parameter set) can improve the density and microstructural features of final parts. However, this is at the cost of additional processing time and power input to produce the same number of samples as with conventional procedures.

Zhang et al. [115] inspected the microstructure evolution, processing behaviour and phase transformation of tungsten-nickel-iron (W-Ni-Fe) parts produced by SLM. The study aimed at manufacturing functional components that display wide-ranging material properties, improved corrosion resistance and high

densities. Further conclusions by Kim et al. [71] while experimenting with grain sizes as low as 0.4 µm read that finer WC powders resulted in higher part densities and improved mechanical properties.

Additionally, in an alternate study, Zhang et al. [63] observed the application of nickel as binder material in the SLM production of tungsten based parts. The forming mechanism closely resembled that of LPS in conventional PM, wherein the molten liquid nickel phase encompassed the solid tungsten particles and drew them together with capillary forces. However, some W particles experienced partial melting, which resulted in the formation of a compound Ni_4W phase. Here the addition of nickel binder for the sintering of tungsten alloys proved to be a promising endeavour as it reduces the viscosity of the melt and promotes the diffusion of particles, improving the overall sintering process. The study concluded that the microstructure evolved from bar shaped to dendritic to honeycomb at 10, 20 and 40 wt.% tungsten respectively, indicating that higher binder content promoted melt uniformity and decreased melt viscosity. The inc4rease in nickel content also convoys with better molten track quality and improved the stability of scan tracks at higher speeds. Lastly, hardness decreased along the build direction, which occurred because of powder bed shrinking.

4.6 EXPERIMENTAL HYPOTHESIS

This section will condense the acquired literature throughout the study and translate it into an experimental plan. This will aid in determining boundary conditions for the experiments and formulating a reasonable hypothesis for what is to be expected therefrom.

As mentioned in prior research by Sinirlioglu et al. [114], despite the broad array of possible input factors for laser additive manufacturing, there are roughly 5 with undeniably more significant contributions to scan quality (listed in section 4.5). These parameters are all contributors to the VED & SED-equations, which is a popular metric utilised throughout most research on laser melting technology. Based on the availability of literature and professional experience, three factors were chosen for further study in the deposition of WC-Ni onto Ti-6Al-4V by laser melting.

- Laser power, P [W]
- Scan speed, v [mm/s], and
- Hatch Spacing, h [mm]

For proper resistance against adhesive and abrasive failure of coatings, both a strong bond with the substrate and dense surface presence of the deposited material is required. Improved bonding may be achieved by deeper interfacial penetration into the surface. Therefore, the noteworthy effects of laser power on the melt pool depth merits further investigation [116]. In addition, scan speed and hatch spacing both affect the surface quality of coatings and contribute to the accumulation of heat in the melt pool, which is proportional to the diffusion capability of the coating into the substrate [98].

Decreased penetration occurs at higher speeds, and larger contents of the material is present at the surface of the substrate, however at speeds that are too high depositions are prone to adhesive failure and macro cracking. Whereas other prominent defects are related to overheating of the melt pool, such as material evaporation and ejection, or spheroidisation.

The outstanding variables (spot size diameter and layer thickness) are heavily dependent on the powder composition and machine capabilities and will be kept constant. A screening experiment focused on scan speed and laser power will first be conducted to determine a specific energy density (SED) range with good track quality. From these results, a hatch spacing range may be tailored, and a volumetric energy density window calculated wherein an experiment can be designed using the Design of Experiments (DoE) methodology. All possible parameter combinations will be conducted within the specified VED-range, in order to better quantify the individual and compounding effects of factors.

Based on the available literature, it is apparent that optimal intersection points will have to be found between the 3 response variables, the depth of diffusion into the substrate, presence of the WC-Ni material at the surface, and the occurrence of defects (layer quality).

$$VED = \frac{P}{vdh} \tag{4.3}$$

Melt pool depth increases with a VED increase, and thus according to equation 4.3, it corresponds with an increase in laser power, P [W] and a decrease in speed, v [mm/s] and hatch spacing, h [mm]. The inverse relationship is true for the presence of deposited material at the substrate surface. Lastly, the presence of surface defects has several causes, that may not be rooted in the machine parameters alone. Yet, when inspecting only the effects of VED values on the presence of defects, their occurrence increases when the VED is either exceptionally high or too low. Figure 4-12 includes a qualitative conceptualization of the hypothesised interactions between each factor and the VED.

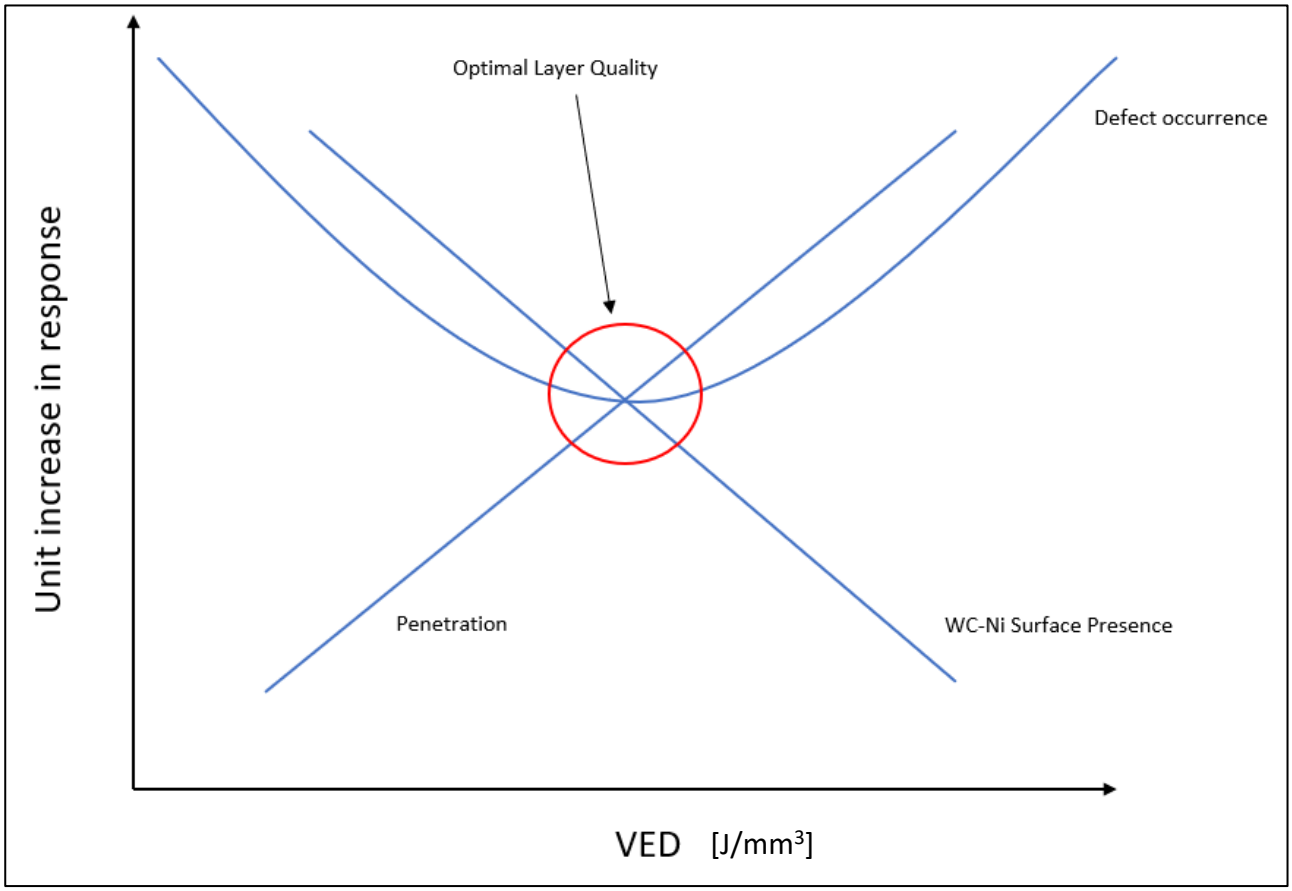

FIGURE 4-12: CONCEPTUAL INTERACTIONS BETWEEN VED AND RESPECTIVE RESPONSE VARIABLES (FOR ILLUSTRATIVE PURPOSES ONLY – NOT TO SCALE)

CHAPTER 5

5 EXPERIMENTAL METHODOLOGY

This section of the research report outlines the methodology for experimentation. The various phases leading to the experiment will be discussed, throughout the equipment and materials employed to substrate production and the statistical models used to design the experiment.

5.1 EOSINT M 280 MACHINE SPECIFICATIONS

The EOSINT M 280 (depicted in figure 5-1) is a laser-sintering machine that accommodates the direct production of metallic prototype parts, final parts and tooling inserts directly from CAD data. It is a prominent system in the e-Manufacturing movement currently in vogue within the industrial sector. It employs the Direct Metal Laser-Sintering (DMLS) process. The forming mechanism present in DMLS is similar to liquid phase sintering in conventional powder metallurgy processes. Parts are built layer by layer with a high-powered Ytterbium fibre laser beam, melting fine particle metal powders into geometries specified within the object CAD-file. The process is capable of creating highly complicated geometries seen in parts with free form surfaces and 3D cooling channels [117].

FIGURE 5-1: THE EOSINT M 280 DMLS MACHINE [118]

Key features of this technology include: 1) a solid-state laser capable powers up to 400 watts. Its laser power monitoring (LPM) system permits the fine tuning of laser parameters during processing. 2) An optimized gas management system, capable of processing with both argon and nitrogen atmospheres to warrant material specific processing conditions. 3) A researched assortment of parameter sets for production of specific materials; providing a foundation from which to customize parameters based on the part application. 4) A modular build capacity that may be tailored for processing from batch manufacturing, to smaller samples for experimentation.

The system utilizes the EOSTATE software, which can integrate with several software suites and process a range of CAD data files. Additionally, it provides users with an extensive overview of all production data at any given points during processing. Table 5-1 includes a summary of the relevant specifications of the EOSINT M 280 device as stated in the OEM system technical data [119]. The full technical data sheet is included in Appendix B.

TABLE 5-1: RELEVANT TECHNICAL SPECIFICATIONS OF EOSINT M 280 [118]

Technical Data	
Build volume (platform included)	250mm x 250mm x 325mm
Laser	400W Yb-fibre laser
Scan Speed	0 – 7000 mm/s
Layer Thickness	Variable 30µm- 50µm
Focus diameter	Variable 70µm – 500 µm
Software	Eos RP Tools; Eostate Magics RP (Materialise)
CAD Interface	STL. (Optional converters for all standard formats available)

The machine used at the CRPM institute for experimentation has specific limitations compared to that of the machine specifications. The spot size has been fixed at 70µm and the reduced build volume only accommodates substrates 50x50x5mm in size. This limits the amount single track scans per plate to roughly 50 samples.

5.2 POWDER ANALYSIS

This section will provide a brief overview of the technology and processes employed to analyse the chosen WC-Ni powder. The material was sourced from Weartech (Pty limited), a company that specialises in the sourcing and supply of welding, thermal spray and specialty technology products. The powder is a product of Praxair Surface Technologies (PST). This section highlights the specifications provided from the original equipment manufacturer (OEM) catalogue (included in Appendix C) and its correlation with the analysed composition under scanning electron microscope (SEM) at Stellenbosch University's central analytical facilities (CAF).

5.2.1 PRAXAIR POWDER SPECIFICATIONS

Praxair Surface Technologies, Inc. offers an extensive catalogue of ceramic and metallic powdered materials for use in additive manufacturing, thermal spray and other specialised technologies. According to their product catalogue, the powder (WC-724-1 / 1310 VM) is tungsten carbide based, containing 10% Nickel (Ni), 5.5 % Carbon (C) and is further balanced by Tungsten (W). The particles are agglomerated and sintered spherical particles, suitable for laser manufacturing technologies. It displays improved corrosion protection compared to standard WC-Co powders, and notably superior low- temperature wear resistance properties up to 482°C. It also showcased superior deposition efficiency, which refers to the relationship between the weights of the deposited melt compared to that of the applied powder. Furthermore, the powder density is 4.4 g/cm, and the particle size reportedly varies between 16µm and 53µm [120].

5.2.2 SEM ANALYSIS

Scanning Electron Microscopy (SEM) utilises high-energy focused electron beam which emits various signals at the sample surface. The interactions of the sample with these signals provide analysts with data that characterises the external surface morphology of the sample, as well as the internal chemical composition and orientation of its crystalline structure. Information from a specific section of the sample surface is then generated into a 2-dimensional image showcasing the various microstructural properties and spatial variations.

The powder characteristics and composition are important sources of information to predict its melting behaviour during processing. For example, high binder metal contents will often result higher part densities and tougher parts [121]. Whereas with lower binder contents the structural reinforcement phase makes up a larger percentage of the bulk material, and brings about greater hardness at the expense of a lowered fracture toughness [93]. Compositional analysis of the powdered material is critical to ensure proper replication of findings. Mixed crystals of other elements are frequently added to the powdered material in

minute contents in order to augment final part characteristics such as wear resistance or improve grain growth throughout sintering.

Upon analysing the WC-Ni powder sample at Stellenbosch university's central analytics facilities (CAF), utilizing a MERLIN field emission scanning electron microscope, the particle size, shape and material composition was inspected. The powder material was adhered to a strip of double-sided carbon tape to eliminate blurring of the images due to particle movement. The tape was then placed onto an aluminium substrate (although carbon or epoxy are also common in practice), and scanned at 200X, 500X, 1000X, and 4000X magnifications. The figure 5-2 below indicate the powder at the lowest and highest magnifications.

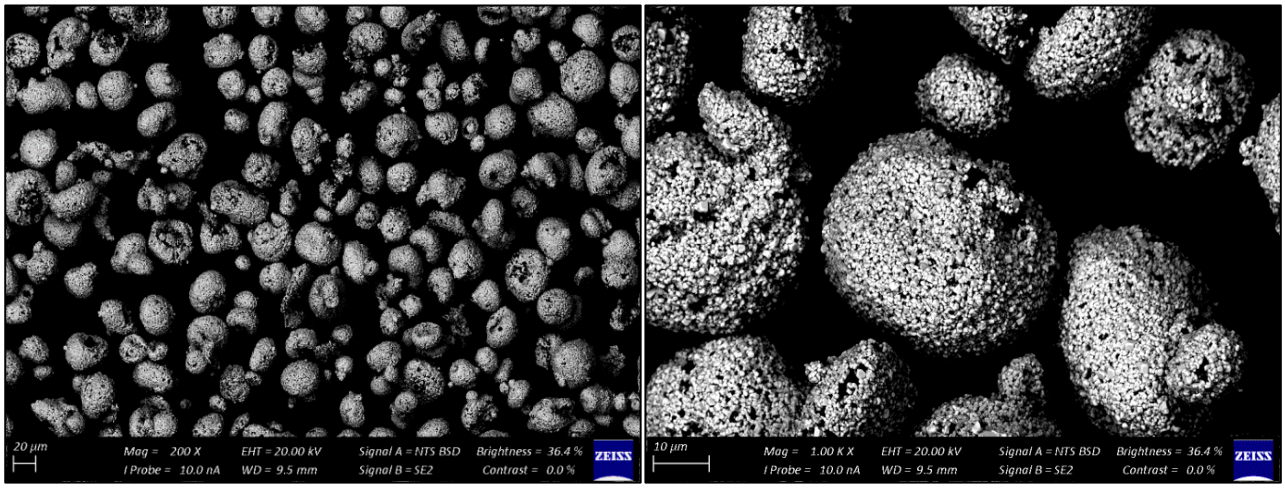

FIGURE 5-2: (LEFT) 200X AND (RIGHT) 1000X MAGNIFICATION IMAGES OF WC-NI (10%) POWDER ANALYSED UNDER SEM.

To inspect the composition of the particles, a spectrum analysis is conducted at several positions throughout the sample where particles are oriented according to scanning requirements (with a broad side perpendicular to the scanner). The average of all the spectrums is then calculated across the collection of positions to estimate a compositional spectrum. It is necessary to note that the composition specified in the OEM catalogue is a generalised measurement of the overall constituent composition for the entire volume of a batch, across numerous production batches. Therefore, scanning individual points on crystals scattered throughout a minute sample will most likely yield varying results. Though it is still a good indication of the elements present in the material, and aids in identifying possible contaminant elements. Appendix C includes a summary of the data extracted from the SEM analysis [12].

PARTICLE CHARACTERISTICS

From Figure 5-2 the powder particles tend towards a spherical geometry. As stated in Murr et al. [79], powders consisting of spherical (or nearly spherical) particles with a broad distribution of particle sizes improves flow-ability and uniformity of the melt, and aids in effective layer packing. The particle shape is also an important factor in determining the viability of the powder. Characteristics such as satellite particles and particle cavities should be avoided as they contribute to porous parts. A specific concern regarding the WC-Ni powder is that although the particles are satisfactorily spherical, some indicate hollow cavities and satellite particles.

A limitation of laser melting AM technologies with autonomous powder deposition systems is the minimum layer thickness. This is often taken as the maximum particle size of the powder in use to mitigate the possibility of surface irregularities that may lead to cavities between layers. The particle size distribution (PSD) is a probability distribution which includes the minimum, maximum and mean particle sizes. The particle size range has been specified between 16µm and 53µm by the OEM [120], however the mean particle size is not indicated and was calculated by a analysing the 200X magnification SEM image in Figure 5-2 with the ImageJ public domain image processing software, which enables users to solve intricate image processing problems.

The ImageJ software was used to find the ratio between the scale of the image in Figure 5-2 and its pixel resolution, which enables accurate measurement of sample features without the need for operating on the SEM software. Figure 5-2 was converted to a binary black and white image consisting of black particles and white background. The software identified 184 discreet particles in the image with a diameter greater than 5µm^2 and calculated the area of each respectively. This created 184 data points which were exported to an Excel spreadsheet where the mean particle diameter was determined by employing the following equation.

$$Avg.Diameter = \frac{\left(\sum_{i=1}^{184} 2\left(\frac{A}{\pi}\right)^{\frac{1}{2}}\right)}{184} \quad (5.1)$$

This approximation assumes spherical geometry for all particles. By equation 5.1 the PSD was approximated by writing simple excel code to identify the frequency of each particle size (in increments of 2µm) between 5 to 60µm. The distribution encompass a wide range of particle sizes, which tends to produce higher density parts with a smoother surface finish due to the higher probability of cavities being filled with smaller particles [122].

TABLE 5-2: PSD ANALYSIS RESULTS

Particle size distribution analysis	
Sample Size	184
Average Particle Diameter (µm)	28.23
Maximum bound (µm)	51
Minimum bound (µm)	7

5.3 SUBSTRATE MANUFACTURING

Ti-6Al-4V substrates were produced according to the specifications of the reduction unit in the EOSINT M 280 used for experimentation at the CRPM institute (shown below in Figure 5-3). The platelets were cut from a 200mm long cylindrical billet with a diameter of 75mm. The billet was cut by a horizontal bunt saw into ten slices roughly 8mm thick. The slices were then modified in a 3-axis milling machined to fit the specifications of the reduction unit, with 4 holes in the corners of each platelet where they will be fixed onto the platform.

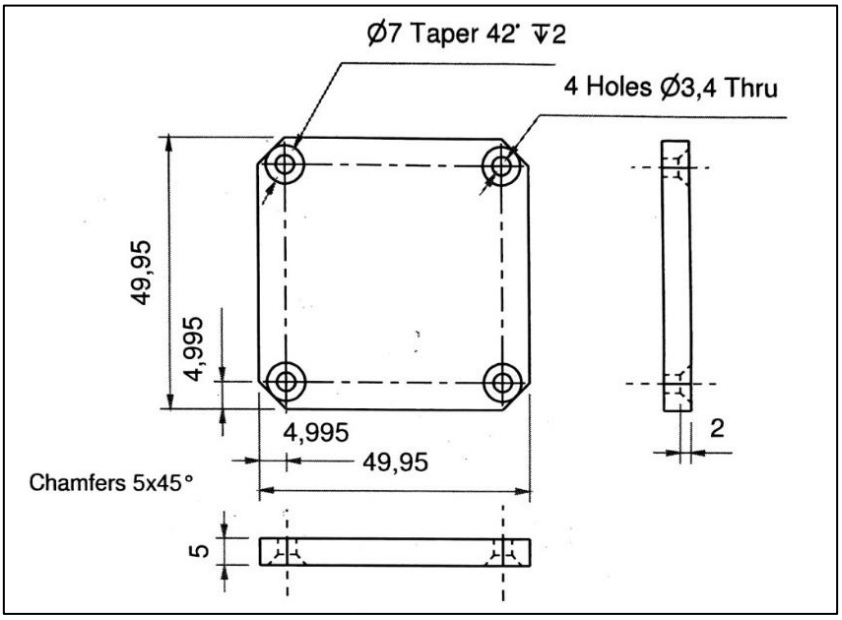

FIGURE 5-3: TECHNICAL DRAWINGS OF BASEPLATES FOR USE IN EOSINT M 280 REDUCTION CHAMBER.

Prior to production the baseplates are prepared by shot peening the surface to reduce reflectivity and thereby optimise laser absorption while mitigating the chances of laser beam reflection. Additionally, the dulled surface provides better circumstances for adhesion of the molten powder onto the substrate. Lastly, the substrate must be analysed with a magnetometer to determine if de-magnetization is required before processing to ensure that the powder distribution is not affected. Due to the low magnetism of Titanium, Nickel and Tungsten the odds of de-magnetism is low risk, but still necessary [8]. Further documentation of the substrate manufacturing phase is indicated in Appendix D, which includes photographs of the plates at each stage of production.

5.4 DESIGN OF EXPERIMENTS

This section describes some of the Design of Experiments (DOE) methods that may be applicable for this research venture. DOE is implemented to specify the ideal methodology for the design, implementation and analysis of an experimental procedure. It ensures the ability to achieve trustworthy results and draw comprehensive conclusions therefrom.

Different DOE types are employed for different purposes. For example, screening experiments is a branch thereof used to identify the factors with the most significant effects on the response and their processing ranges. In a nutshell, a screening experiment may be seen as an economical experimental plan, designed to first determine the interactions of factors, and their relative significance, before more comprehensive experiments are applied [123].

After pinpointing the significant factors, experiments are carried out to determine which combinations thereof result in an optimal response. The input values are evaluated at different levels to measure their interactions and ultimate effects. Although, there is no perfect solution to any experimental approach, the models can be selected to fit the scope and constraints of each individual study. Some popular DOE methods include: Full and Fractional factorial experiments, Central composite designs, Latin Squares, and Taguchi experimental designs.

5.4.1 STATISTICAL METHODS

To draw objective conclusions from the experiments, the designs must integrate statistical methods with experimentation. Three critical components of the design must be considered in order to effectively and efficiently conduct experiments and avoid bias, namely replication, randomisation and blocking [124].

Replication entails the randomised repetition of experimental trials to obtain statistically sound outcomes. The number of replications must be tailored in such a way to ensure a realistic sample mean and factor/response interactions. Which in turn improves the capability of error estimations. With enough replications statistical inference on the cause-and-effect relationship of factors and interactions becomes clearer. **Randomisation** is implemented to mitigate experimental bias and its effects on outcomes. It refers to the randomized order in which runs are performed to ensure that prior trial conditions do not have significant effects on the current measurement [124]. It thereby filters statistical “noise” that may be generated by interacting factors. Lastly, **blocking** is relied on to improve the efficiency of the design by reducing overbearing variation. When blocking, known systematic biases are isolated and kept from concealing the primary interaction effects. It entails the arrangement of samples in groups (blocks) that have similar characteristics. The variability of factors for subsequent runs is limited and precision is improved [125].

The following experimental features are useful in identifying the DOE method that best fits the study at hand: 1) the number of experimental runs (M) which is dependent on the cost and time each individual run. 2) The amount of input parameters, or factors (k), that will be the adjusted and analysed for their compounding response, and 3) the levels (L), denoting the number of intensities/stages at which each factor will be evaluated. [125]. The Table 5-3 below includes several popular DOE methods highlighted by Cavazzuti et. Al [125], the formula for calculating a suitable number of experimental trials, and a summary of the suitable applications for each.

TABLE 5-3: SEVERAL POPULAR DOE METHODS, THEIR FORMULA FOR COMPUTING THE REQUIRED NUMBER OF TRIALS, AND COMMON APPLICATIONS OF EACH.

DOE	Number of Trials	Application
Latin Squares	$N(L) = L^2$	Resource efficient evaluation of a single factor at several levels
Full Factorial	$N(L,k) = L^k$	Aimed at generating a response of primary interactions for factors evaluated at various levels.
Fractional Factorial	$N(L,k,p) = L^{k-p}$	When the experiment is too large or resource intensive to implement a full factorial, this method is Used to estimate the effects of factor interactions by utilizing a resolution (R), where R = k-p
Central Composite	$N(k) = 2^k + 2k + 1$	Investigate a sample space (without the need for three-level analysis) to generate a quadratic response surface.

An increase in factors (k) commonly results in an exponential increase in the number of trials. Thus, the input parameters are best to be limited to those which have a known significant effect on the response. Like factors, incrementing the number of levels in an experiment also convoys with a significant increase in experimental trials. In contrast, less levels makes for difficult interpolation of the response in the design space. Therefore, a trade-off should be considered between lowering the number of levels to save resources and increasing them should the designer expect uncertainty in the response. The shape of the response surface relies on the number of levels in the DOE. For instance, a two -level design will result in a linear/bi-linear response surface, and a three-level DOE yields a response surface that is roughly quadratic/bi-quadratic in nature. The models in Table 5-3 were all considered for this study.

5.4.2 CENTRAL COMPOSITE DESIGN

Also referred to as a Box-Wilson Central Composite Design (CCD), this design incorporates fractional factorial or full factorial designs with specified centre points, to which "star" points are added to augment the design space and estimate curvature. This design is a popular selection when a quadratic response surface is required, but resources are too constricted to conduct a three-level analysis. If the distance from the design space centre point to either factorial point equals +/- 1 unit for either factor, the distance, α, from the centre to any star point proves |α| > 1. However, the precise value of α is dependent on the properties and constraints of the design as well as the number of factors. This is also the case for the amount of centre points required [123].

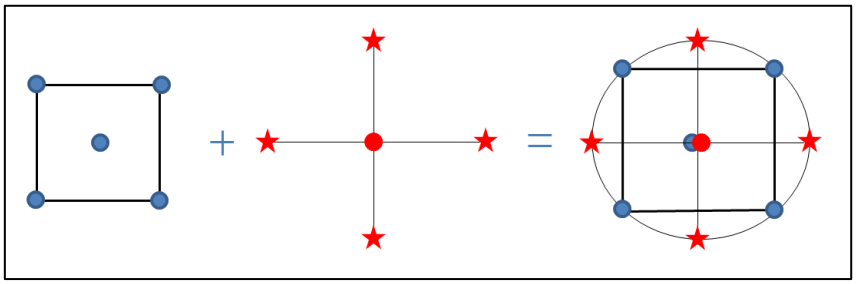

FIGURE 5-4: THE GENERATION OF A TWO FACTOR CCD [123].

A CCD should always contain at least twice as many star points as the number of factors evaluated in the design illustrated by Figure 5-4. Star points represent low and high external extremes to be evaluated outside of the proposed design window. Three variations exist for the placement of star points regarding two factor designs, which corresponds to the three primary CCD types, namely: 1) circumscribed (CCC), 2) inscribed (CCI) and 3) face centred (CCF)[123]. These variations are indicated in Figure 5-5.

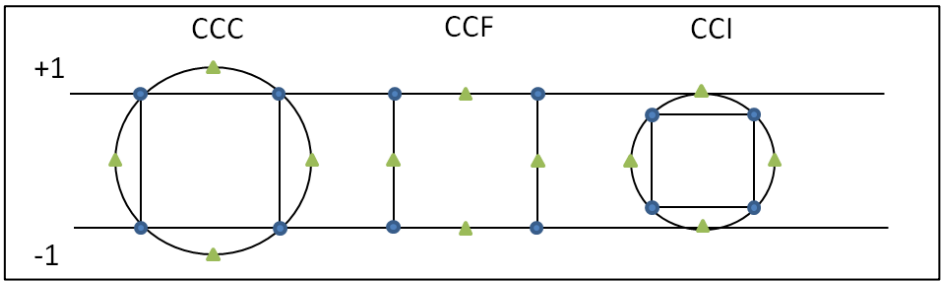

FIGURE 5-5: GRAPHIC REPRESENTATION OF STAR POINT PLACEMENT IN EACH CCD VARIATION [123].

The **CCC** is the original design; here star points are located at a distance α around the central point and correspond to the high and low extreme values included in the search space. CCC designs require that each factor be evaluated at 5 levels and possess hyper spherical, circular and spherical symmetry. In **CCF** designs the centre of each face in the factorial space contains a star point, thus $\alpha = \pm 1$. Face centred (CCF) designs require at least 3 levels per factor and is not a rotatable design. Lastly, **CCI** designs are intended for design spaces where the extremes are the actual limitations of the design space. These factor settings are applied as the star points and a fractional factorial or factorial design is created within these limits. It resembles a scaled down version of a CCC design, and consequentially also requires each factor to be evaluated at 5 levels and is also rotatable. The CCI is generated by taking a CCC design and dividing each factor level by α [123].

The value of α is chosen to maintain relatability and depends on the amount of experimental trials within the central composited design's factorial portion [123]. Following the equation:

$$\alpha = (factorial\ runs)^{\frac{1}{4}} \tag{5.2}$$

Thus, if it is a full factorial the equation yields:

$$\alpha = \left(2^k\right)^{\frac{1}{4}} \tag{5.3}$$

5.4.3 FULL FACTORIAL DESIGN

The three-level full factorial may also be expressed as a 3^k design and are often proposed because of the need to model curvature within the response surface function. Whilst simplifying the process using a common factorial model merely evaluated at an additional level, it facilitates an investigation of quadratic interactions between individual factors and their response variables [123]. An unfortunate drawback of the three-level design is that it is limiting due to the number of experimental trials required with increasing levels, and therefore effort and costs may quickly become taxing.

THE 3^3 DESIGN

This design's statistical model and number of runs are determined by evaluating three factors (k) at three levels (L) each. For simplification the levels are expressed as 2, 1, and 0 respectively. The number of runs (N) may then be denoted as 3x3x3 = 3^3, and requires minimum of 27 treatment combinations, shown graphically below in Figure 5-6. Here, Layer thickness, Laser Power and Scan Speed are each evaluated at low (0), intermediate (1), and high (2) levels; illustrating the interactions for all combinations and outlining the sample space wherein a response will be generated [123].

The centre point of the design is shown at (1,1,1) in red, the 8 orange points are the factorial points or design extremes, and the green points are the facial points. These all represent valuable trials that may be repeated to increase the robustness of the data. The experimental interactions illustrated in Figure 5-6 will result in a response surface which may be modelled by the second order transfer function in equation 5.4.

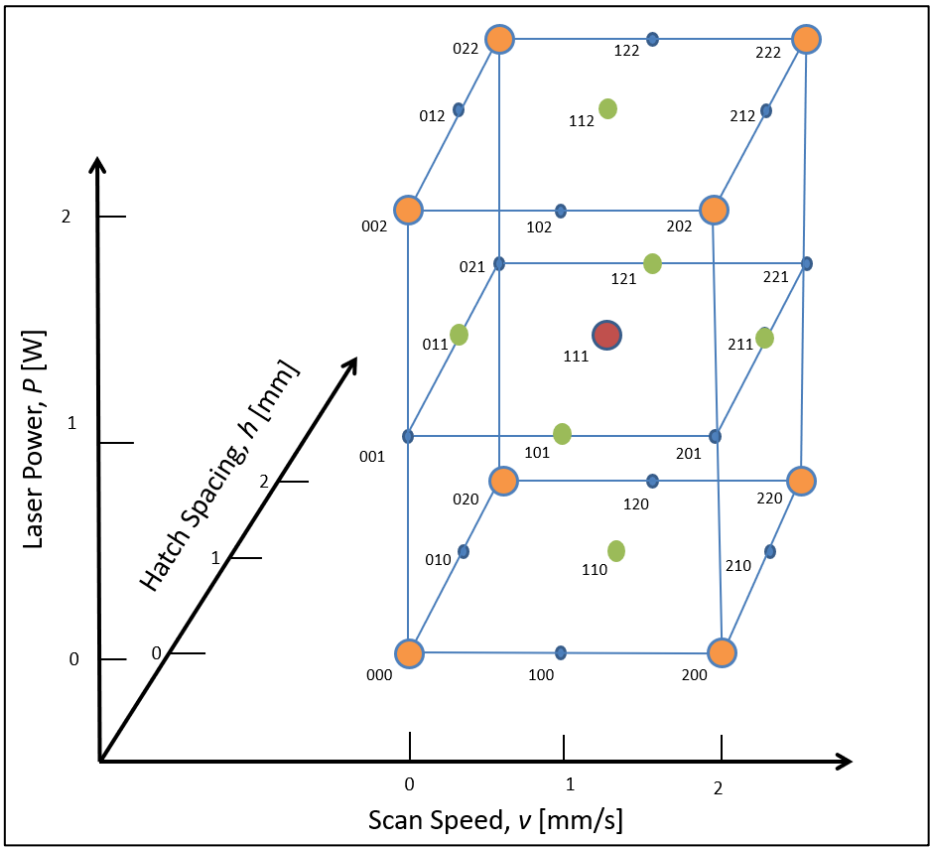

FIGURE 5-6: ALL PARAMETER COMBINATIONS OF LASER POWER, P [W], SCAN SPEED, V [M/S], AND HATCH SPACING, H [MM] AT LOW, INTERMEDIATE AND HIGH LEVELS WITHIN THE 3^3 DESIGN SPACE [123].

$$Y = f(x_1, x_2, x_3) = \quad B_0 + B_1x_1 + B_2x_2 + B_3x_3 \qquad \text{_____ (5.4.1)}$$

$$+ B_{12}x_1x_2 + B_{13}x_1x_3 + B_{23}x_2x_3 + B_{123}x_1x_2x_3 \qquad \text{_____ (5.4.2)}$$

$$+B_{11}x_1^2 + B_{22}x_2^2 + B_{33}x_3^2 + \varepsilon_{ijk} \qquad \text{_____ (5.4.3)}$$

Here 'Y' represents the response surface, which is a function of the response variables: x_1, x_2 and x_3. The 'B_0' -term is the intercept, or simply where all response variables equal zero and all subsequent B_{ijk} – terms denote the transfer function coefficients which produce the quantified effects for the investigated x – parameters. Epsilon 'ε' characterises random variability in the design and represents the error between measured and predicted responses, with a mean value of zero and variance of σ^2. Furthermore, the equation may be divided into 1) linear terms responsible for the main effects of each variable, 2) interaction terms, and 3) quadratic terms. These correspond to the terms in the first, second, and third lines of the equation, excluding B_0 and ε [126].

In de Baun's research [127], the 3^3 sample space in Figure 5-6 is evaluated for its utility in exploring a second order response surface. To implement these designs the following subsets of the 27 points of the sample space may be considered, each consisting of a subset that is symmetrical about the origin.

1. The entire 3^3 factorial, consisting of all points.
2. The cube or factorial points indicated by the orange dots.
3. The Centre point, illustrated by the red point at (1, 1, 1).
4. The Octahedron or facial points indicated by the green dots.
5. The cuboctahedron which is a combination of the green dots on the central horizontal plane, and the blue dots on the top and bottom planes.

To increase robustness and limit uncertainty in the data, it is recommended to evaluate second order models with a combination of the designs listed above.

CHAPTER 6

6. SINGLE TRACK EXPERIMENTATION

The following section highlights all the relevant reasoning throughout the initial screening on single track stability to define a suitable parameter range for production of clad layers. This phase is necessary to streamline the production of said layers and the analysis of their features in order to generate a meaningful response.

6.1 EXPERIMENTAL OUTLINE

In order to first estimate a suitable parameter window that will result in high quality layered samples, 48 single tracks were printed onto Ti-6Al-4V substrate. The 48 tracks consisted of two 24-track screening repetitions, wherein three different laser power settings (50W, 150W and 300W) are each evaluated at eight different speeds. The parameter sets were proposed by Dr. Igor Yadroitsev, a specialist in the field of SLM/SLS at CUT. They are specifically tailored to investigate a wide range of energy densities to extrapolate a fitting process window. The parameter combinations are indicated in Table 6-1, along with their resulting specific energy density values.

Due to the novelty of the WC-Ni powders in SLS, and the similarity of nickel and Cobalt's heat specific characteristics, the experiment was based on common screening experiments for WC-Co with the same binder content (10%). The parameter sets proposed by Dr Yadroitsev are indicated in Table 6-1 and were all executed with a constant layer thickness of 50µm. Figure 6-1 provides a representation of the energy densities investigated for each laser power.

TABLE 6-1: SCREENING PARAMETER COMBINATIONS AND RESULTING SPECIFIC ENERGY DENSITIES

Parameter set	Power [W]	Speed [mm/s]	SED [J/mm^2]
1	**P1** [50W]	60	16.67
2		80	12.5
3		100	10
4		120	8.33
5		140	7.14
6		160	6.25
7		180	5.56
8		200	5
9	**P2** [150W]	400	7.5
10		600	5
11		800	3.75
12		1000	3
13		1200	2.5
14		1400	2.14
15		1600	1.88
16		1800	1.67
17	**P3** [300W]	1000	6
18		1200	5
19		1400	4.29
20		1600	3.75
21		1800	3.33
22		2000	3
23		2200	2.73
24		2400	2.5

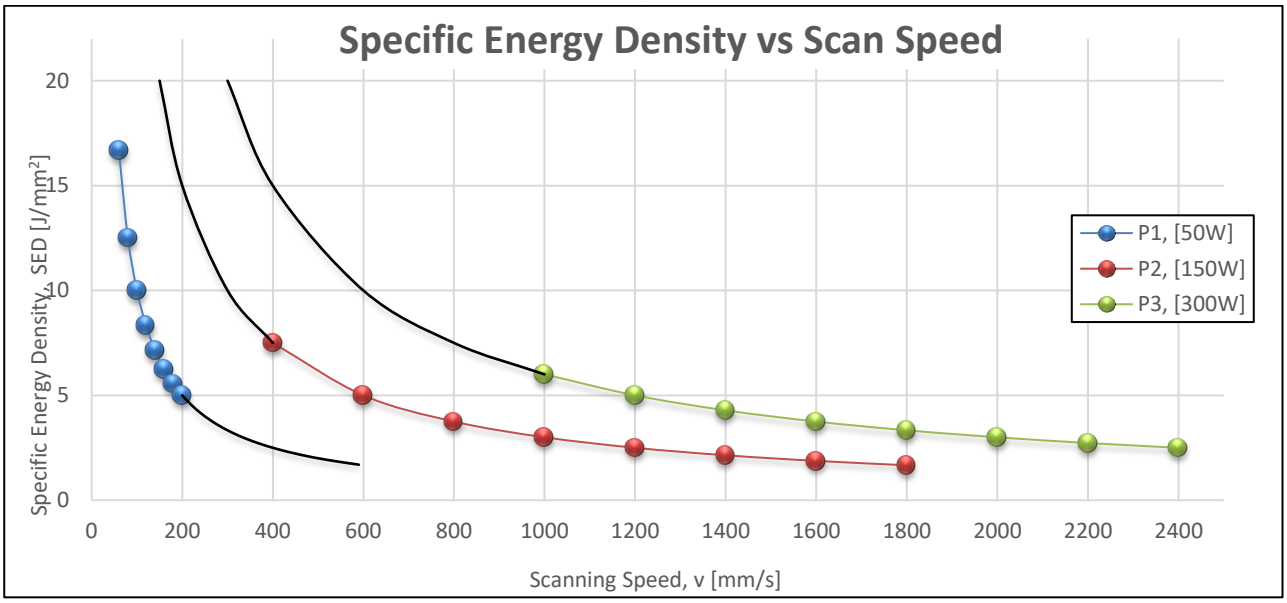

FIGURE 6-1: ENERGY DENSITY RANGES EVALUATED FOR EACH LASER POWER

The EOSINT M280 build chamber was fitted with a reduction unit to accommodate the experimental setup. Powder was deposited onto the unit before being manually spread onto the substrate in the required layer thickness of 50µm. The machine setup is specified in Figure 6-2. The build chamber was filled with inert nitrogen gas, and the oxygen content was reduced to below 0.01% to mitigate the effects of oxidation. The plate was scanned according to the experimental layout indicated in Figure 6-3, each scan track is approximately 20mm in length and 2mm apart. Figure 6-4 showcases the plate after laser exposure.

The SEM images in Appendix E were utilised to determine which tracks had the best qualities for layered depositions. The images were once again processed with the ImageJ software suite to enhance their contrast and ease edge detection while measuring the width. The plate was then sectioned according to Figure 6-3, grinded, polished and etched with a hydrofluoric acid solution in preparation for microscope analysis. Track width and depth measurements were conducted at 3 different points (top, middle and bottom) for each track. The measured data can be found in tables throughout Appendix G.

The etchant selected is a solution commonly used for pickling and chemical milling, consisting of 2 wt.% hydrofluoric acid (HF) and 20 wt.% nitric acid (HNO_3). This 10:1 ratio is useful in reducing H^+ uptake in Ti-6Al4V extra low interstitial (ELI) crystal structures. This process is known as hydrogen embrittlement [128]. After etching, the laser penetration depth into the substrate was determined by optical microscopy.

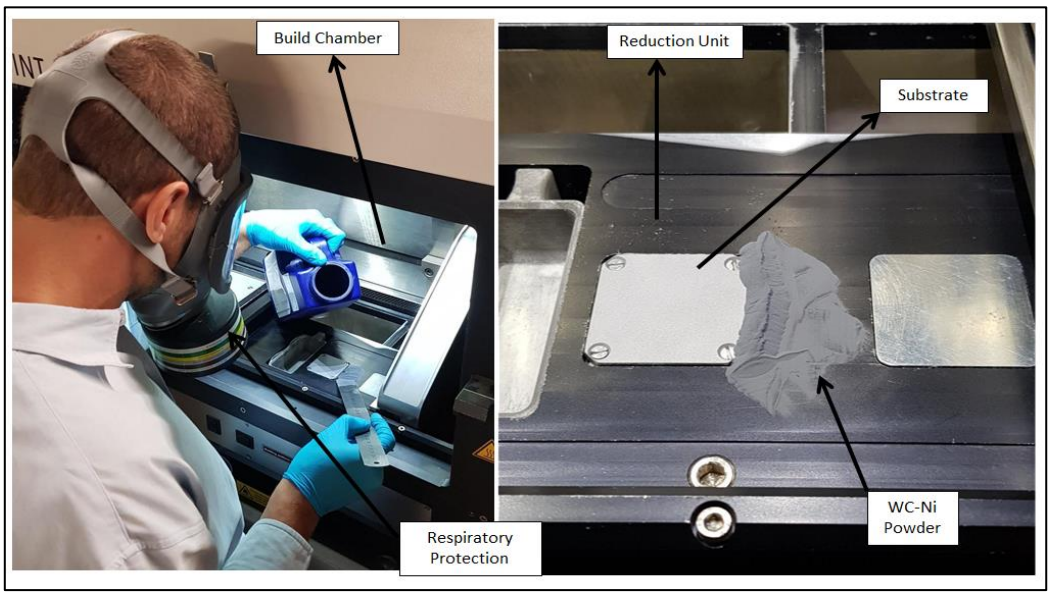

FIGURE 6-2: EOSITNT M280 MACHINE SETUP.

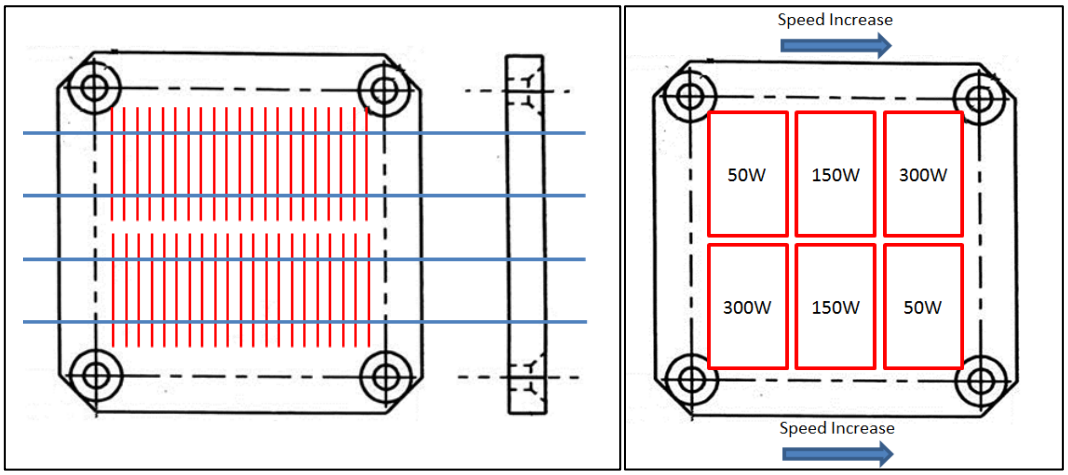

FIGURE 6-3: REPRESENTATION OF THE SECTIONS CUT THROUGH THE TI64 BASE PLATE (LEFT), AND THE LAYOUT OF THE SCANS ON THE BASE PLATE (RIGHT).

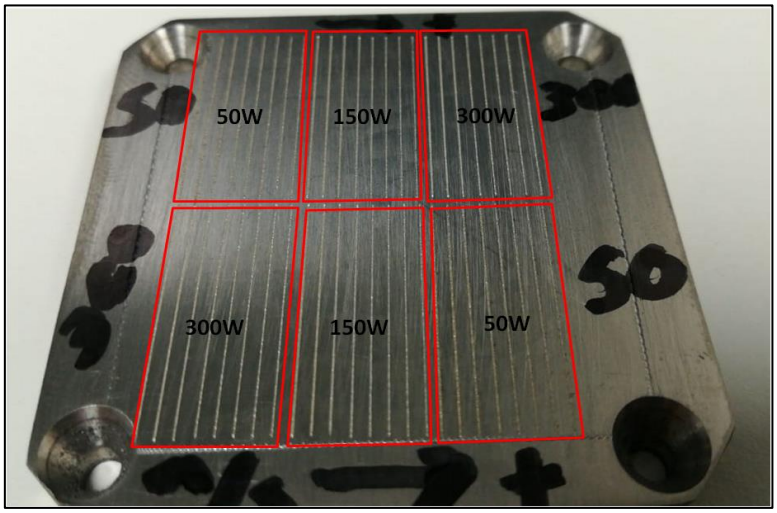

FIGURE 6-4: IMAGE OF THE SUBSTRATE AFTER SCREENING EXPERIMENT HAS BEEN CONDUCTED

6.2 TRACK CATEGORIZATION

Single-track characteristics were evaluated at each parameter combination to identify energy density ranges with optimal track quality. Ideally tracks would require good penetration, a continuous track without cracking or splattering and consistent width. Tracks were divided into 4 categories similar to the research on energy input during SLM by Wang et al. [98]. The 4 categories included 1) irregular “splattered” tracks subject to spheroidisation, 2) straight, continuous tracks, 3) continuous tracks with irregular width, and 4) irregular and partially melted or broken tracks. These categories are qualitatively described in Figure 6-5 with images included of tracks at high, mid and low energy input within each inspected range.

Upon inspecting the top view of the tracks, all parameter combinations at P1 (50W laser power) produced significant amounts of splattering. This is an undesirable characteristic as it leads to irregular surface qualities, cavities and reduction in the density of layers. Cases with excessive splattering may be attributed to high energy density ranges, which induce temperatures above the evaporation point of nickel. Rapid expansion of particles produces an overpressure in the melt pool and ejects material from the powder bed. As stated, prior, nickel has a vapour pressure twice that of cobalt and ejects material from the melt pool at a greater rate once evaporation ensues, which in turn increases the level of contamination in the build chamber. Good quality continuous tracks were achieved at 150W and 300W between the energy density ranges of 3.5 J/mm^3 to 7.5 J/mm^3. The quality of tracks in this range could be attributed to partial melting of WC particles, which improves diffusion into the substrate.

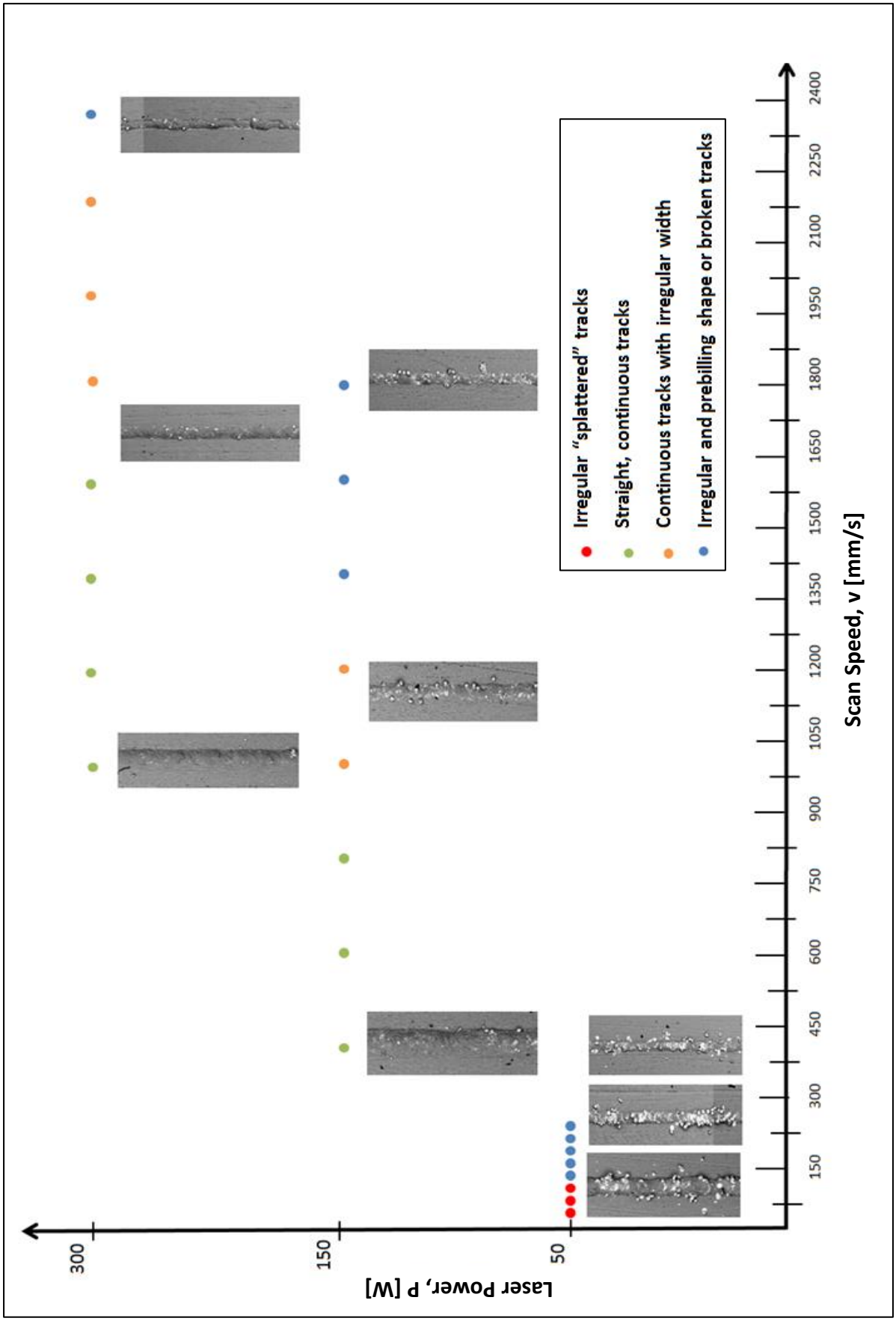

FIGURE 6-5: QUALITATIVE CATEGORIZATION OF SINGLE-TRACK QUALITY

6.3 TRACK WIDTH

Estimation of track width and geometrical shape is an important step in determining working parameters for layered production. The dimensional accuracy of parts and the resolution of surface qualities are dependent on consistent track width. The primary goal of this phase is to establish process parameters that permit well melted tracks while preserving the carbide phase and not exceeding the boiling point of the binder. Two main input factors contribute to single track quality, namely scan speed and laser power. Kruth et. al indicated that scan speed has a greater effect on track width, whereas laser power had a noticeably larger effect on track thickness and penetration depth [129].

3 width measurements of each track (6 per parameter combination) were taken at its top middle and bottom. The average track width at 50W, 150W and 300W measured 131µm, 124µm and 125µm respectively. Tracks were thicker on average at 50W, it should be considered that this experimental space covered a far higher energy density range as indicated in Table 6-1. In these ranges excessive levels of splattering occurred and at lower scan speeds, partial melting was prevalent.

The 300W tracks had the most consistent widths and the lowest variability (standard deviation ± 18.32µm). This was also the range with the largest number of good quality tracks (good melting) despite exploring the lowest energy density window. The best tracks within this range were achieved between 1000 mm/s and 1600 mm/s. At 150W the width variability was the highest (standard deviation ±26.68µm), however good tracks with consistent width were noted in the range of 400mm/s to 800 mm/s. The graph in Figure 6-6 indicates the track width for each observed laser power.

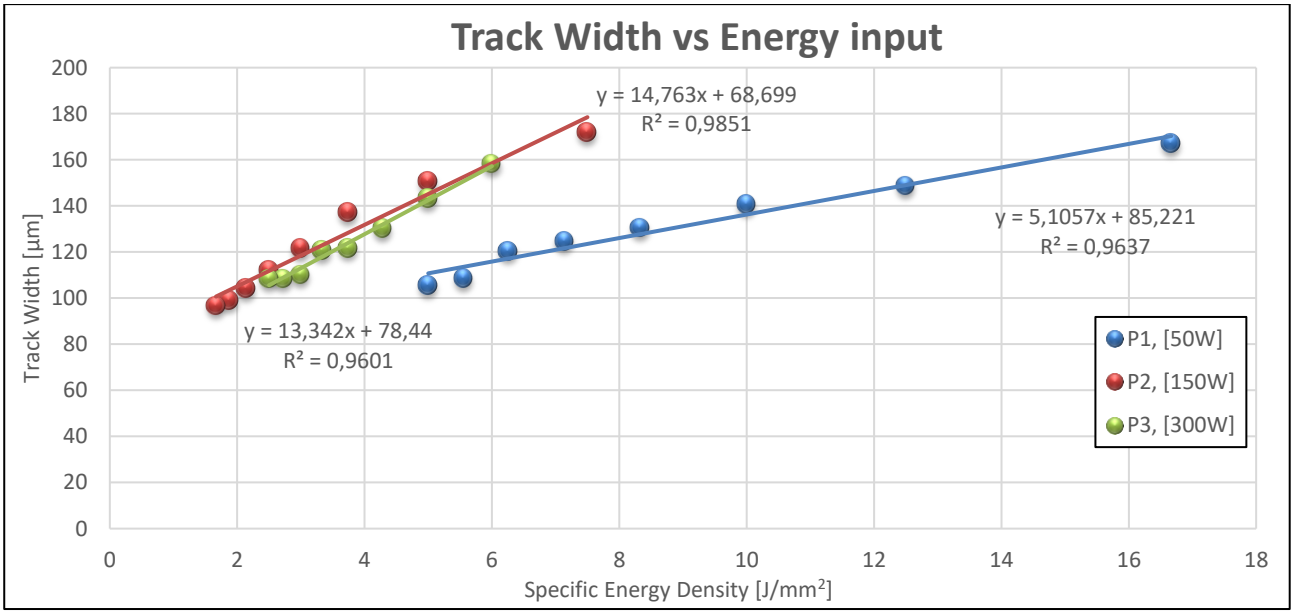

FIGURE 6-6: TRACK WIDTH VS ENERGY DENSITY AT 50W (BLUE), 150W (RED) AND 300W (GREEN)

From Figure 6-6 it is apparent that at the lower laser powers thinner tracks are achieved for the same energy input as at higher power. Furthermore, as the laser power increases, the track width also follows a more conformal trend, seen by the similarity in data points at 150W and 300W. All three trends have high R-squared values (R^2), which indicate that the plot follows a linear trend. Better track quality and consistent track width occur at lower energy densities in the 150W and 300W process window. Though more intensive power requirements are present due to higher laser wattage, scans are performed at up to 10 times faster.

In Figure 6-7 clear linear trend is exhibited between scan speed and track width. The graph also represents an example of how the process window becomes less sensitive at higher laser powers as noted by Yadroitsev et al. [102]. The gradient of the trend line at 50W is far steeper than those at 150W and 300W. For example, a reduction of 20mm/s in the scanning speed induces approximately a 20µm variation in the track width at 50W, whereas for the same difference to occur at 150W and 300W the speed should be reduced by nearly 200 mm/s.

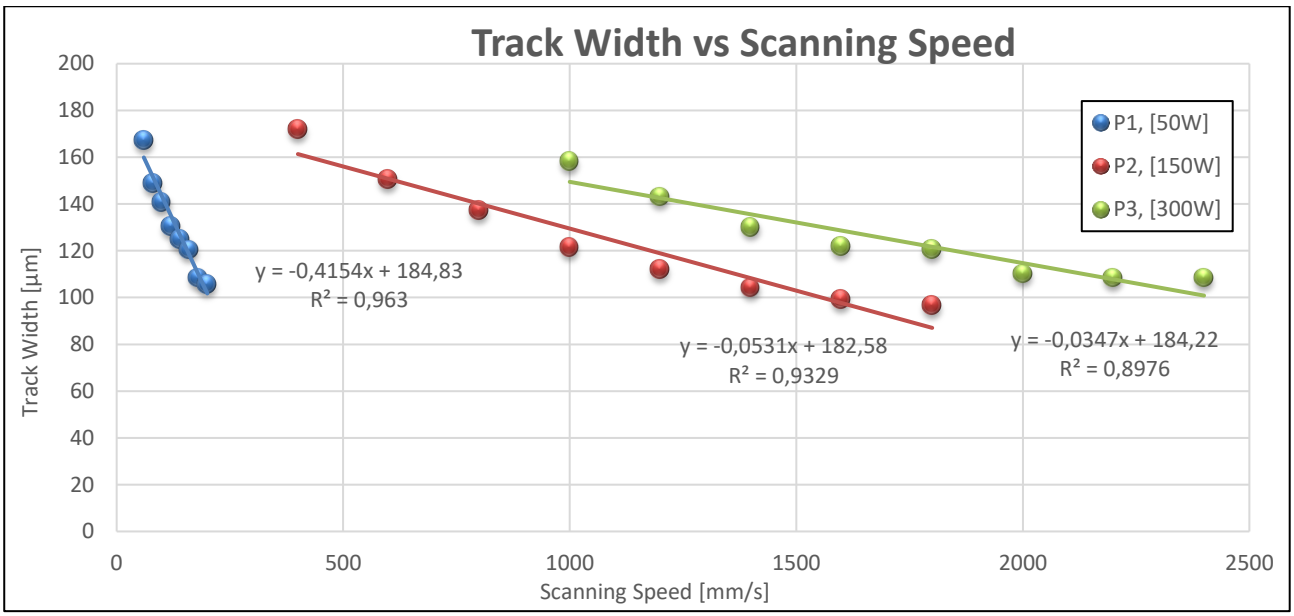

FIGURE 6-7: TRACK WIDTH VS SCANNING SPEED AT 50W (BLUE), 150W (RED) AND 300W (GREEN)

A quadratic regression analysis was also conducted using the Statistica software suite. Table 6-2 provides a summary of the results, which are available in full throughout Appendix G. The model's F-value of 18.83 and p-value below 0.05 implies that the model is significant, and R^2 values above 0.79 infer that predictions have good accuracy. Furthermore, the model's terms for laser power (A) and scanning speed (B) both have p-values less than 0.05, which suggests that they both have significant effects on the response. Speed is more significant in this model than power, in the case of both linear and quadratic terms, which correlates with findings throughout literature.

TABLE 6-2: UNIVARIATE TESTS OF SIGNIFICANCE FOR SINGLE-TRACK WIDTH.

	Univariate Tests of Significance for Track Width - Std. Error of Estimate: 9.6984				
Effect	**SS**	**Degr. Of Freedom**	**MS**	**F**	**p**
Intercept	9840.87	1	9840.9	104.62	0
Laser Power	2774.25	1	2774.3	29.495	4E-05
Laser Power²	581.989	1	581.99	6.1875	0.0229
Speed	3477.5	1	3477.5	36.971	1E-05
Speed²	958.486	1	958.49	10.19	0.005
Laser Power*Speed	139.767	1	139.77	1.4859	0.2386
Error	1693.06	18	94.059		

The significance of quadratic terms for power (A^2) and speed (B^2) means it is likely that a local maximum or minimum is present in the investigated response range. Additionally, it describes the quadratic increase in response for fixed successive increments of factors. For example, as scan speed increases in fixed increments, it's effect on the track width becomes exponentially larger. The interaction of laser power and scan speed indicate no significant effect on the track width. The estimated coefficients for the model equation are indicated in equation 6.1. This enables the prediction of the track width given the levels of each input factor.

$$Track\ Width = 93.82 + 1.16(\mathrm{A}) - 0.13(\mathrm{B}) - 0.0002(\mathrm{AB}) - 0.002\ (\mathrm{A}^2) + 0.0004\ (\mathrm{B}^2) \quad (6.1)$$

6.4 PENETRATION DEPTH

Like track width, penetration depth was measured at three points on each track according to the sections indicated in Figure 6-3 (top, middle and bottom). These measurements contributed to six data points per parameter set.

As the intensity of laser radiation decreases with penetration into the powder layer, higher laser powers will result in better penetration into the substrate. A study on laser cladding by Locs and Boiko [105], investigated the hypothesis that keyhole formation achieved at higher laser powers may be exploited to mitigate residual stresses at the coating substrate interface. To investigate the same principle in laser melting for coating and strengthening applications, cross sections of quality tracks with good penetration depth will be considered for further analysis.

The average penetration depths at 50W, 150W and 300W were recorded as 48µm, 75µm and 78µm respectively. The greatest penetration depth (205µm) was achieved at 150W and 400mm/s scan speed. This trial, indicated in Figure 6-9, is the only iteration that indicated a fully formed keyhole mode, and reached a depth almost double that of the following iteration at 600mm/s.

It is hypothesised that at 400mm/s and 150W (and a corresponding SED of 7.5 J/mm^2) a larger binder gas phase is present on the melt pool surface, allowing the laser to penetrate deeper and form a keyhole mode. This energy density combination will be investigated at different power levels in further experimentation to look for correlation with this hypothesis.

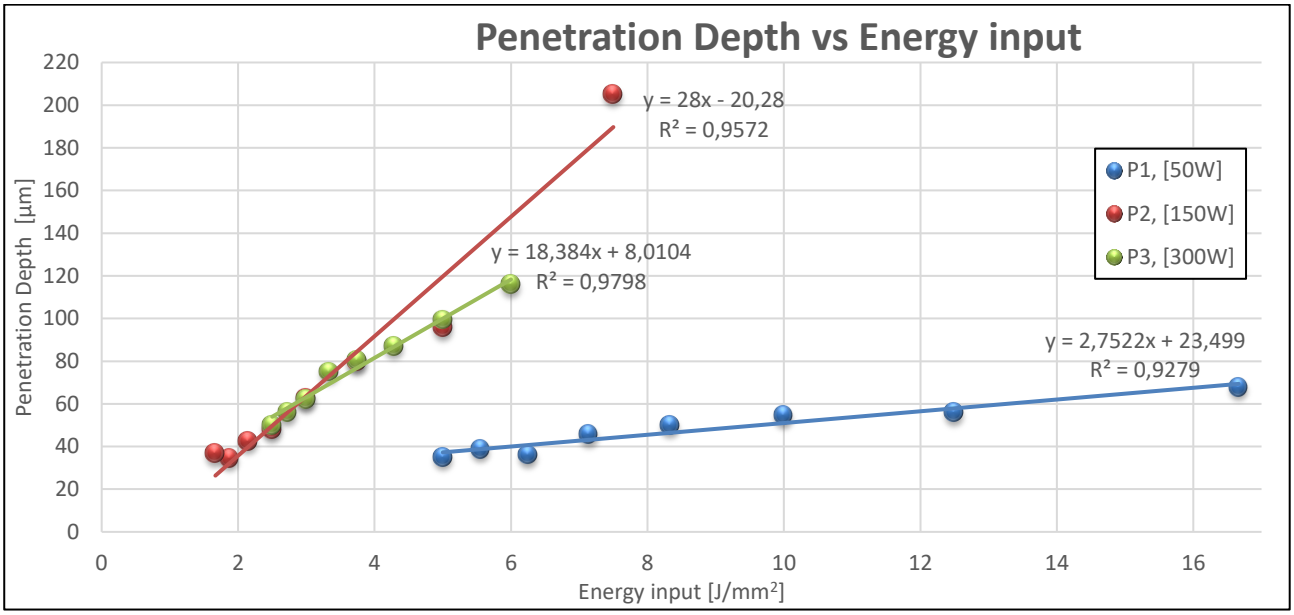

FIGURE 6-8: SINGLE-TRACK PENETRATION DEPTH VS ENERGY DENSITY AT 50W (BLUE), 150W (RED) AND 300W (GREEN)

The most consistent penetration depth throughout occurred at 150W on iterations between 400mm/s and 800mm/s. These were the only iterations with VED values above 3.5 J/mm^2 that had low variability (standard deviation ±10µm), good surface quality and consistent width. Another window where good penetration occurred and tended toward keyhole formation, was at 300W between 1000mm/s and 1400mm/s. This range also corresponded to consistent track widths and good scan track quality. Cross sections of these tracks are included in Appendix F.

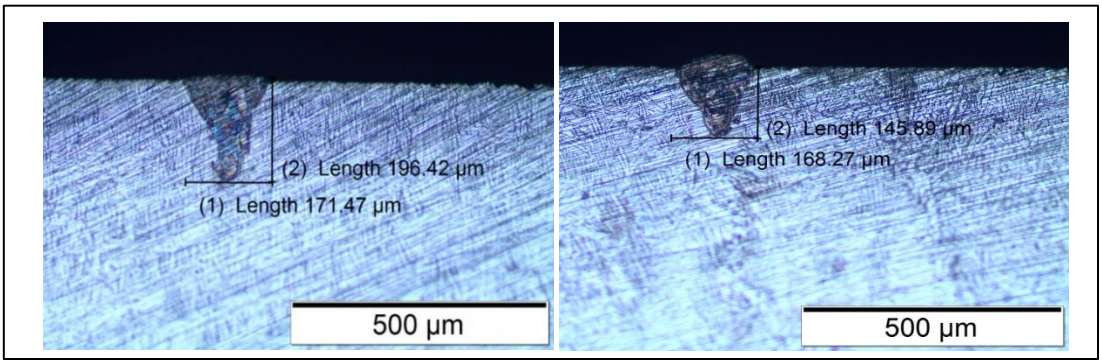

FIGURE 6-9: CROSS SECTIONS OF THE SINGLE TRACKS WHERE KEYHOLE MODES WERE ACHIEVED. AT PARAMETER COMBINATIONS 9 AT 150-WATT (LEFT), AND 17 AT 300-WATT (RIGHT).

For all tracks, a trend of conductive mode melt pools was seen, with a tendency to converge toward a keyhole shape at higher energy densities. Figure 6-9 indicates the two iterations where keyhole modes were achieved. In Figure 6-8 the penetration depth is shown at each parameter set's corresponding energy input, for the evaluated power levels, plots reveal a linear increase in penetration depth as energy input is increased. Furthermore, in literature the consensus is that laser power has a significant effect on penetration depth, which is reinforced by the fact that data at 50W the penetration depth shows a very gradual incline despite being subjected to energy densities more than double those at 150W and 300W.

Figure 6-10 reinforces the same observation made in the track width analysis; that the process window becomes less sensitive at higher laser powers. Though to a lesser extent than track width, the trend at 50W is still far steeper than at 150W and 300W. The extreme leap in the penetration depth due to keyhole formation at parameter set 9 was ignored in this representation to ease the comparison of the datasets.

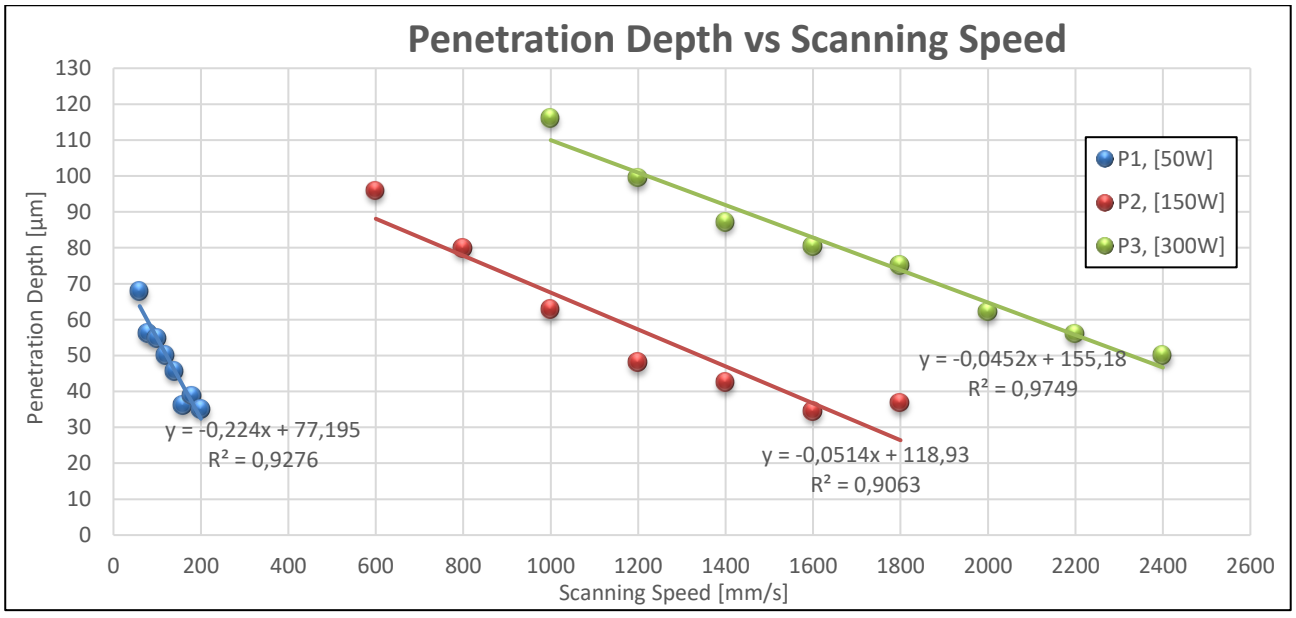

FIGURE 6-10: SPECIFIC ENERGY DENSITY VS SCAN SPEED AT 50W (BLUE), 150W (RED) AND 300W (GREEN)

A summary of the results from the regression analysis on the penetration depth response is included in Table 6-3, with detailed results available in Appendix G. Once again, the model's F-value of 23.61 and borderline zero p-value implies that it is significant, and exceptional R^2 values all exceeding 0.83 signify good reliability of the model's predictions. Inspecting the p-values of input factors, both terms for laser power (A) and scanning speed (B) have high significance.

Laser power has the greatest effect on penetration depth, which is consistent with prior literature on single track analyses. The model further concluded that the interaction between laser power and speed (AB) has no significant effect on the depth, but the significance of compounding effects of laser power (A^2) and scanning speed (B^2) provide evidence for an exponential increase in the response as the individual factors are incremented, and point towards a local maximum or minimum in the response within the investigated range. The estimated coefficients for the model equation are indicated in equation 6.2. This enables the prediction of the penetration depth given various levels of each input factor.

TABLE 6-3: UNIVARIATE TESTS OF SIGNIFICANCE FOR SINGLE-TRACK DEPTH.

Effect	Univariate Tests of Significance for Track Depth- Std. Error of Estimate: 9.6984				
	SS	Degr. Of Freedom	MS	F	p
Intercept	2424.43	1	2424.43	10.52472	0.004503
Laser Power	15248.06	1	15248.06	66.1936	0
Laser Power^2	4505.78	1	4505.78	19.56012	0.000329
Speed	11003.43	1	11003.43	47.76718	0.000002
Speed^2	3038.48	1	3038.48	13.19041	0.001907
Laser Power*Speed	316.79	1	316.79	1.3752	0.256206
Error	4146.4	18	230.36		

$$Penetration\ Depth = -46.56 + 2.71(\mathrm{A}) - 0.226(\mathrm{B}) - 0.0002(\mathrm{AB}) \\ -0.005\ (A^2) + 0.0001(B^2) \quad (6.2)$$

6.5 HATCH SPACING

An array of hatch spacing values was identified based on the track width of the highest quality line scans and prior research conducted by Wang et. al [98]. Wang reported that, depending on material specific parameters, good layer quality predominantly occurs at hatch spacings that result in between 10% to 40 % track overlap. To calculate overlapping rate, the average width of the optimal tracks achieved at 150W and 300W in the screening experiment were plugged into equation 4.8. The track width highlighted in red, was estimated using equation 6.1 by substituting the values for 300-Watt laser power and 800 mm/s scan speed.

The predicted percentage overlap per track width was determined at 7 different hatch spacing values. Hatch spacings that investigate a broad range of volumetric energy densities, while keeping the overlapping rates below 50%, were identified. Table 6-4 indicates the percentage overlap of each track at hatch spacing values between 80µm to 140µm. The cells with a green infill highlight the ranges included for further investigation.

TABLE 6-4: OVERLAPPING RATE DETERMINED FROM ACTUAL TRACK WIDTHS IDENTIFIED IN THE SINGLE-TRACK SCREENING.

Laser power [W]	Scan Speed [mm/s]	Avg. Track Width [µm]	Percentage overlap at each hatch spacing						
			80µm	90 µm	100µm	110µm	120µm	130µm	140µm
150	400	171.888	53.46%	47.64%	41.82%	36.00%	30.19%	24.37%	18.55%
	600	150.555	46.86%	40.22%	33.58%	26.94%	20.29%	13.65%	7.01%
	800	137.335	41.75%	34.47%	27.18%	19.90%	12.62%	5.34%	-1.94%
300	800	178.82	55.26%	49.67%	44.08%	38.49%	32.89%	27.30%	21.71%
	1000	158.222	49.44%	43.12%	36.80%	30.48%	24.16%	17.84%	11.52%
	1200	143.22	44.14%	37.16%	30.18%	23.20%	16.21%	9.23%	2.25%
	1400	130.222	38.57%	30.89%	23.21%	15.53%	7.85%	0.17%	-7.51%
	1600	121.77	34.31%	26.09%	17.88%	9.67%	1.46%	-6.75%	-14.96%

To better investigate the interactive effects between input parameters, experiments would have to be conducted at consistent energy densities. Hatch spacing values were thus chosen based on two key characteristics, 1) the overlapping rate and its effects on surface quality found throughout literature, 2) hatch spacings that investigate a wide VED range. Table 6-5 includes the VED values that correspond to the selected hatch spacings.

TABLE 6-5: VOLUMETRIC ENERGY DENSITY VALUES FOR INVESTIGATED HATCH SPACING PARAMETERS.

Laser power [W]	Scan Speed [mm/s]	Avg. Track Width [µm]	VED at each hatch spacing [J/mm³]						
			80µm	90 µm	100µm	110µm	120µm	130µm	140µm
150	400	171.888	93.75	83.33	75.00	68.18	62.50	57.69	53.57
	600	150.555	62.50	55.56	50.00	45.45	41.67	38.46	35.71
	800	137.335	46.88	41.67	37.50	34.09	31.25	28.85	26.79
300	800	178.82	93.75	83.33	75.00	68.18	62.50	57.69	53.57
	1000	158.222	75.00	66.67	60.00	54.55	50.00	46.15	42.86
	1200	143.22	62.50	55.56	50.00	45.45	41.67	38.46	35.71
	1400	130.222	53.57	47.62	42.86	38.96	35.71	32.97	30.61
	1600	121.77	46.88	41.67	37.50	34.09	31.25	28.85	26.79

6.6 SCREENING RESULTS

In summation, the screening experiment provided insights on workable parameter ranges that may be employed for processing WC-Ni (10%) powder. The iterations that resulted in optimal scan track quality occurred at parameter sets 9, 10, 11, 17, 18, 19 and 20 in Table 6-6. These parameter combinations fall within the specific energy density ranges of 3.5 J/mm^2 to 7.5 J/mm^2. Furthermore, the screening experiment proved that at lower laser powers no good quality tracks were achieved due to excessive splattering, inconsistent penetration depth throughout and the sensitivity of the response at 50W laser power. Further experimentation will focus on higher laser powers.

Due to different machine characteristics on various laser melting devices, it would be beneficial to specify a less sensitive processing window for novel materials to ensure that the experimental conditions are easily transferrable. It is for this reason that the 50W range was excluded from further study. Instead, an additional parameter set was introduced at 225W by interpolating between the optimal values at both 150W and 300W. The speeds at each laser power were adjusted to achieve the same specific energy density as the optimal scan tracks identified in the screening experiment. The tracks at 7.5 J/mm^2 will be inspected during further experimentation to determine if keyhole formation would occur as in parameter set 9 at 150W.

TABLE 6-6: REFINED PARAMETER WINDOW VALUES, LASER POWER, SCANNING SPEED AND SPECIFIC ENERGY DENSITY

Laser Power [W]	Speed [mm/s]	Specific Energy Density [J/mm^2]
150	400	7.5
	600	5
	800	3.75
225	600	7.5
	900	5
	1200	3.75
300	800	7.5
	1200	5
	1600	3.75

CHAPTER 7

7. LAYERED SAMPLE PRODUCTION.

The findings from the single-track screening experiment was analysed and used to determine a process window that will result in the best quality layered depositions. A second Ti-6Al-4V platelet was utilised to investigate key points in the new parameter ranges to estimate the response at various levels.

7.1 EXPERIMENTAL PROCEDURE

The final experiment resembles a hybrid of both the 3-factor full factorial design and the face centred central composite design (CCF) discussed in section 5.4. The design consists of 3 CCF-type experiments that are performed at each laser power (150W, 225W and 300W), evaluated at proportionately higher speed ranges to achieve consistent energy densities. Furthermore, each laser power and speed combination are evaluated at the three hatch spacing values specified in Table 6-4 to estimate a VED range that will result in optimal layer quality; void of surface defects such as cracking and irregularities. Due to constraints on time and resources available, no design points could be repeated. A graphic representation of the experiment's design space is included in Figure 7-1 below.

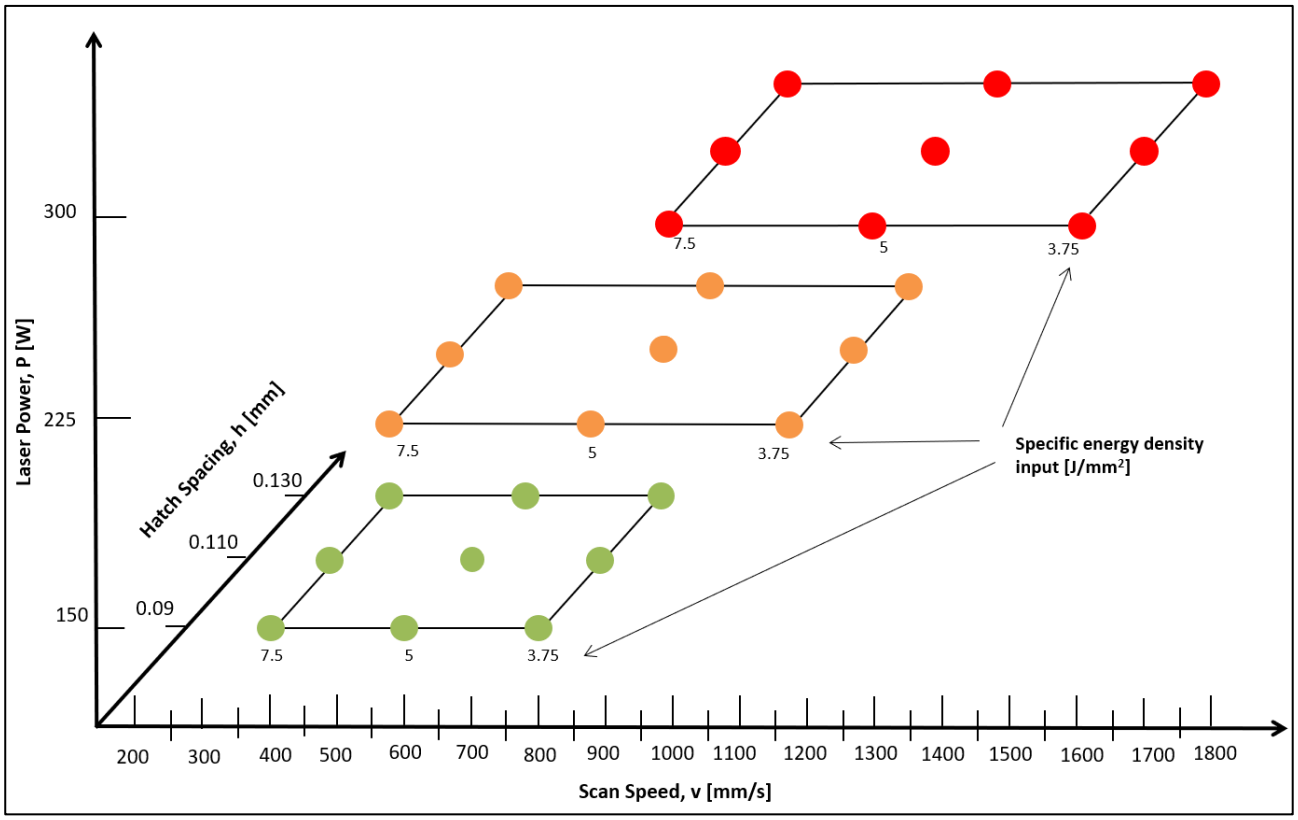

FIGURE 7-1: REPRESENTATION OF THE DESIGN SPACE FOR THE LAYERED DEPOSITION EXPERIMENT

Table 7-1 indicates the build parameters for each specimen according to the design. The samples are thus grouped into blocks that correspond to the laser power and hatch spacing being evaluated. The volumetric energy densities cover a range from 28.58 J/mm^3 to 83.33 J/mm^3 in each laser power block. The consistency of the VED throughout each power level provides a constant reference point from which the interaction effects of its constituent factors may be determined.

TABLE 7-1: PARAMETER SPECIFICATIONS FOR THE FINAL LAYER DEPOSITION, LASER POWER, SCAN SPEED, HATCH SPACING, AND VOLUMETRIC ENERGY DENSITY IS INDICATED FOR EACH RUN, ALL PERFORMED AT A CONSTANT 50µM LAYER THICKNESS

Iteration Number	Experimental block	Power, P [W]	Speed, v [mm/s]	Hatch Spacing, h [mm]	Layer Thickness, d [mm]	VED [J/mm^3]
1		150	400	0.09	0.05	83.33
2		150	600	0.09	0.05	55.56
3		150	800	0.09	0.05	41.67
4	1	150	400	0.11	0.05	68.18
5		150	600	0.11	0.05	45.45
6		150	800	0.11	0.05	34.09
7		150	400	0.13	0.05	57.69
8		150	600	0.13	0.05	38.46
9		150	800	0.13	0.05	28.85
10		225	600	0.09	0.05	83.33
11		225	900	0.09	0.05	55.56
12		225	1200	0.09	0.05	41.67
13		225	600	0.11	0.05	68.18
14	2	225	900	0.11	0.05	45.45
15		225	1200	0.11	0.05	34.09
16		225	600	0.13	0.05	57.69
17		225	900	0.13	0.05	38.46
18		225	1200	0.13	0.05	28.85
19		300	800	0.09	0.05	83.33
20		300	1200	0.09	0.05	55.56
21		300	1600	0.09	0.05	41.67
22		300	800	0.11	0.05	68.18
23	3	300	1200	0.11	0.05	45.45
24		300	1600	0.11	0.05	34.09
25		300	800	0.13	0.05	57.69
26		300	1200	0.13	0.05	38.46
27		300	1600	0.13	0.05	28.85

The experimental layout on the platelet is comprised of 27 3mmx10mm layers, arranged in 3 blocks of 9 samples, corresponding to each laser power. This design was sent to the CRPM where, using the EOSTATE Magics RP (Materialise) software, a build environment was simulated, and the layers positioned on the substrate according to the design. After the build parameters for each are specified, a slicing algorithm then processes the 3D model into a collection of subsequent 2D slices and converts it to a file format readable by the machine. Within this study only single coating layers will be processed which renders this step as relatively simple. Figure 7-2 includes the designed layout of experimental iterations onto the substrate.

The plate's surface was dulled with shot peening to reduce scattering of the laser, and the build chamber of the EOSINT M280 was fitted with a reduction unit wherein the plate can be fixed. The machine setup process was carried out again as elaborated in section 5.5.1.

When processing materials with the EOSINT M280, the initial powder layer must be applied by hand sieve and then levelled by the powder scraper conventionally used for layer application. This subjects the experimental results to a greater degree of variability due to possible operator error and uneven spread; when calculating the VED it is assumed that each layer is within the range of 50µm. The layers were produced with an alternating scan strategy in an inert nitrogen environment, which is the default setting for the machine. Figure 7-3 showcases the sample post production.

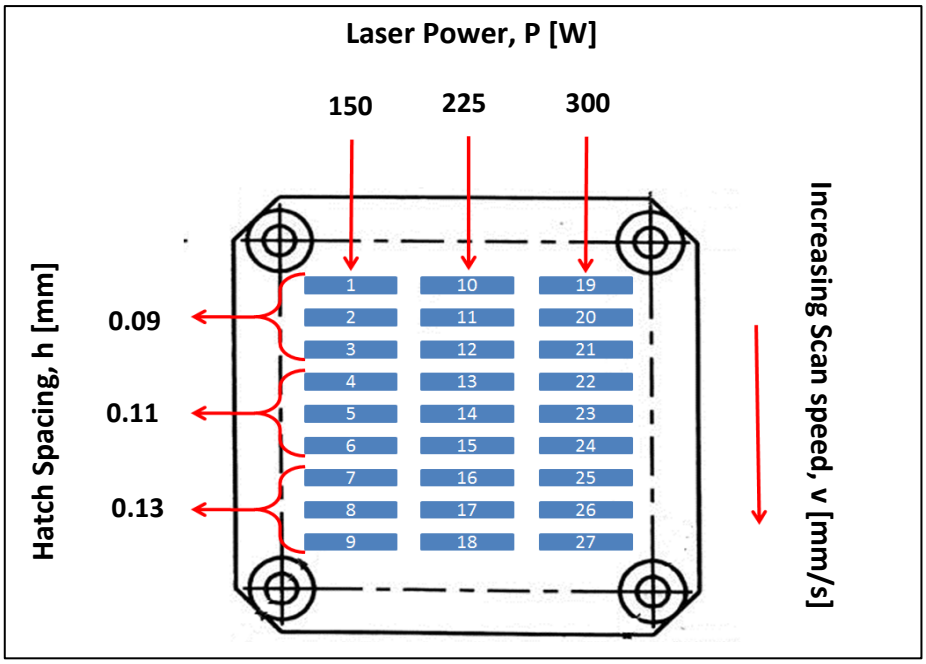

FIGURE 7-2: THE LAYOUT OF THE FINAL EXPERIMENT ON THE TI-6AL-4V PLATE

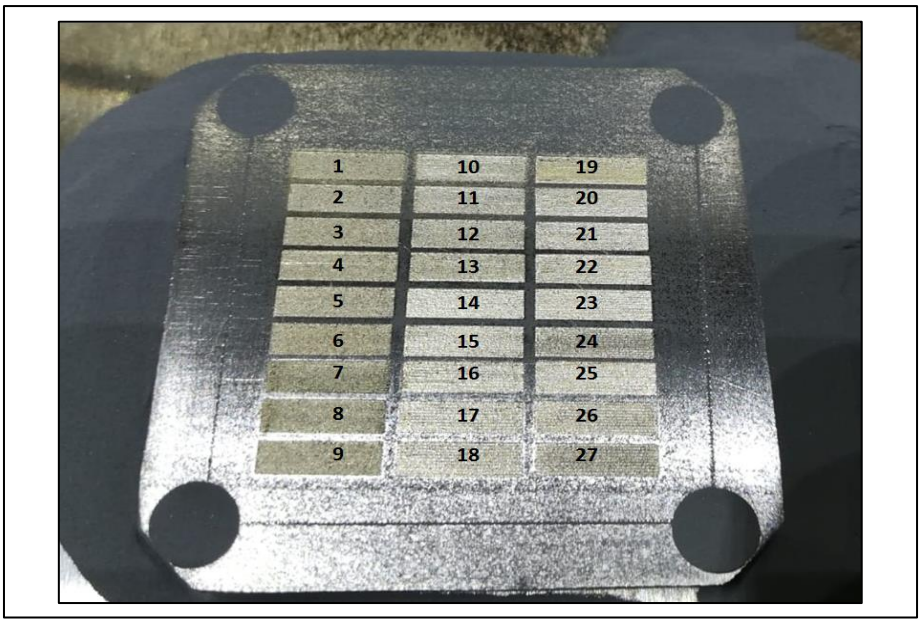

FIGURE 7-3: SAMPLE LAYERS POSTPRODUCTION

After production, the plate was cleaned in an ultrasonic cleaning apparatus for 15-minute intervals, first submerged in acetone, then ethanol, and lastly plain tap water to dissolve any residual salts. Three high resolution SEM image montages were then taken of the scanned surfaces to inspect their quality and morphologies. Each montage corresponded to a separate laser power block of 9 layers. The correlation between varying hatch spacings and the smoothness of layers or the presence of cracking was investigated. Layers containing a multitude of cracks were analysed by measuring the average length of cracks across the surface with the ImageJ analysis software.

Following the crack inspection, compositional line scans of each layer's surface were taken. A single line scan is comprised of 40 discreet measurements across the surface progressing perpendicular to the scan direction. Each discrete measurement provides a reading of the elements present at that point by weight percentage [wt.%], and the 40 measurements combined provide a representation of how the elemental composition changes across the layer surface.

Two lines were measured for each layer, at its centre and at a 100 µm offset from the left most edge. Figure 7-4 provides an example of how compositional line scans were positioned and a full spectrum analysis of each layer is included in Appendix H. The elements highlighted in the compositional analysis are tungsten (W), carbide (C), nickel (Ni), titanium (Ti), vanadium (V), and Aluminium, (Al). Traces of Nitrogen (Ni) contamination were also present but were ignored as its effects do not fall in the scope of this study.

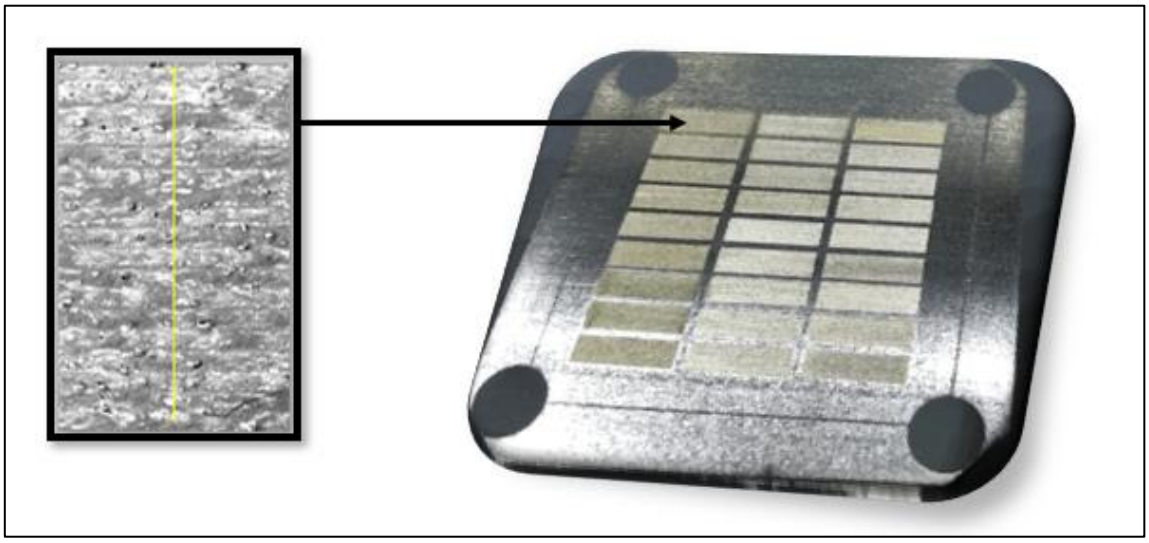

FIGURE 7-4: EXAMPLE OF HOW COMPOSITIONAL LINE SCANS WERE POSITIONED ON EACH LAYER.

After the compositional analysis of the layer surfaces, the plate was sectioned with a wire cutting device according to Figure 7-5. Each piece was then mounted before being grinded, polished and etched with the same hydrofluoric acid solution discussed in chapter 6. This preparation was conducted before analysing the cross sections of each layer on a light microscope so that the penetration into the substrate would be visible. Appendix J includes the cross-section images of each layer taken during the analysis.

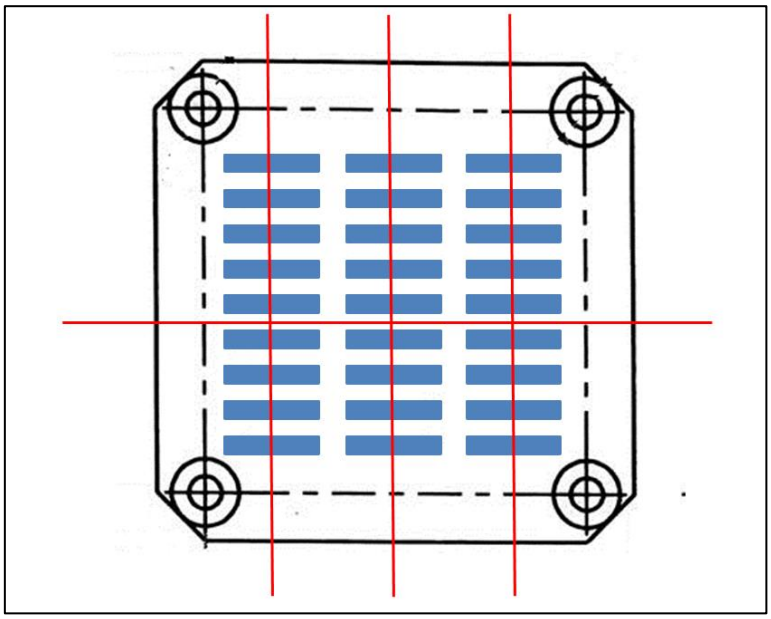

FIGURE 7-5: ILLUSTRATION OF THE SECTIONED PLATE.

When inspecting the cross sections, three types of measurements were taken, namely, the total depth (D), the depth of the interfusion zone (IZ), and the height of the clad zone (CZ) above the substrate. In this research the total thickness of the coating is defined as the sum of the clad zone and interfusion zone. A visual representation of these metrics is included in Figure 7-6. Six measurements of each zone were taken at all 27 cross sections, and the data was analysed in order to find a correlation between machine parameters and the penetration into the substrate as well as the quality of the coatings.

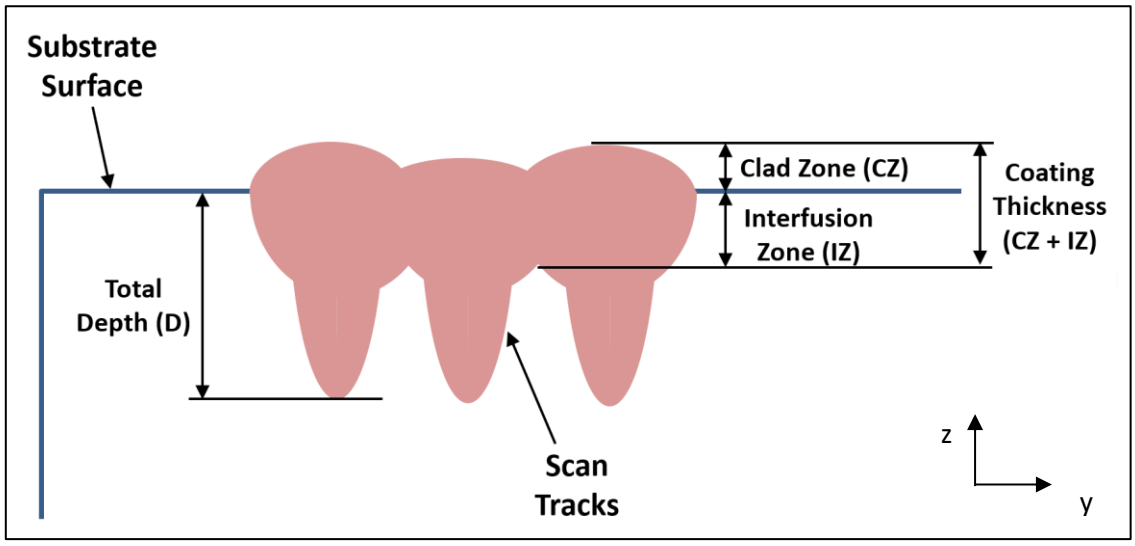

FIGURE 7-6: ILLUSTRATION OF TOTAL DEPTH (D), INTERFUSION ZONE (IZ) AND CLAD ZONE ON CLAD SAMPLES.

After the measurements were conducted, the samples were once again polished and cleaned in the ultrasonic cleaner before constructing EDS Maps of each cross section with the SEM apparatus. The maps indicated which elements are present throughout the depth of the coatings, the mixture of elements and to what extent they penetrated the substrate. The maps also indicate the degree of melting that particles underwent during laser processing. The elements that are of primary concern are tungsten (W), carbide (C), nickel (Ni), titanium (Ti).

The EDS maps of each cross section for individual elements and layered maps of W, C, and Ni combinations are included in Appendix K. Finally, for validation on the effects of VED levels on the diffusion of WC-Ni into the substrate, compositional line scans were conducted on the cross sections of 6 layers. The layers were chosen specifically to represent the highest, lowest and intermediate VED levels. Scans followed the same procedure of analysis where 40 discrete points were inspected to generate a compositional plot along the penetration depth.

7.2 SURFACE MORPHOLOGY AND COMPOSITION

The following section uses quantitative measurements to compile a qualitative summary of the effects of the various machine parameter combinations on each layer. Specifically, the presence of WC located at the surface of each layer, macrocracking and morphology of samples.

7.2.1 SURFACE COMPOSITION

Good coatings require both proper adhesion to the substrate, and a dense layer of the coating material at the substrate surface. This analysis aims to identify which parameter combinations result in a good WC-Ni presence at the coating surface. This will then be compared to the penetration and diffusion of depositions into the substrate in subsequent sections. It is necessary to find the optimal position in the trade-off between diffusion and surface presence. It was concluded that successive layers will have to be scanned over the initial deposition to achieve a denser coating, however, it is still necessary to minimize the number of additional scans.

Throughout the line scans, to approximate the WC presence, the tungsten and carbide contents at each discrete measurement were summed together. Additionally, descriptive statistics are included for each line scan; the minimum and maximum presence for each element was determined, and the standard deviation calculated. In order to better present the data, both the compositional scans on each layer (middle and edge) were averaged to create an approximate composition for each layer and is represented in Figures 7-10, 7-11 and 7-12 below arranged according to the experimental blocks highlighted in table 7-1. In

Appendix H the descriptive statistics for each line scan are included, along with the averaged contents across the corresponding layer

Smoother layers correlated with deeper penetration into the substrate. This may be attributed to increased melting of titanium at the surface, inducing a deeper molten pool. The molten Ti-6Al-4V acted as a binder material alternative to nickel and powder particles consolidated therein. At narrow hatch spacings, deeper penetration is present as a high VED induces greater surface temperatures and greater probability of keyhole formation. This results in the submergence of tungsten into the molten substrate, reducing its surface protrusion and in turn smoothing the layer.

Consistent with the parameter combinations and experimental blocks indicated in Table 7-1, the trend produced by speed variation is visible in every 3 successive points, and the effects of hatch spacing occurs in blocks of 3. For example, the respective speed values for layers 1, 2 and 3 is identical to those at 4, 5 and 6, but layers 4 - 6 incorporate a wider hatch spacing parameter. Figures 7-7, 7-8, and 7-9 represent the progression of layer quality with an increase in hatch spacing and scan speed at each laser power block.

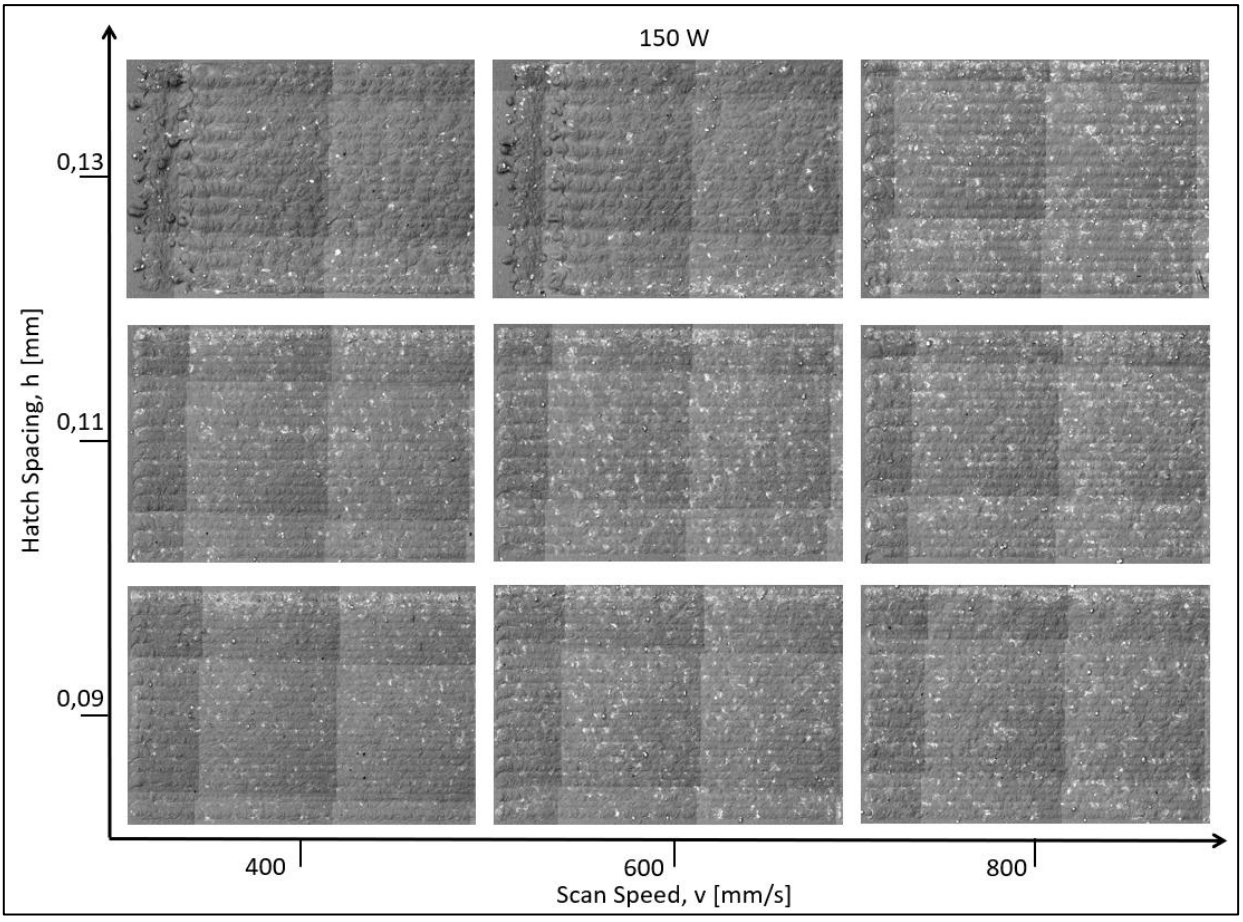

FIGURE 7-7: PROGRESSION OF SURFACE QUALITY WITH CHANGE IN SCAN SPEED AND HATCH SPACING AT 150W LASER POWER

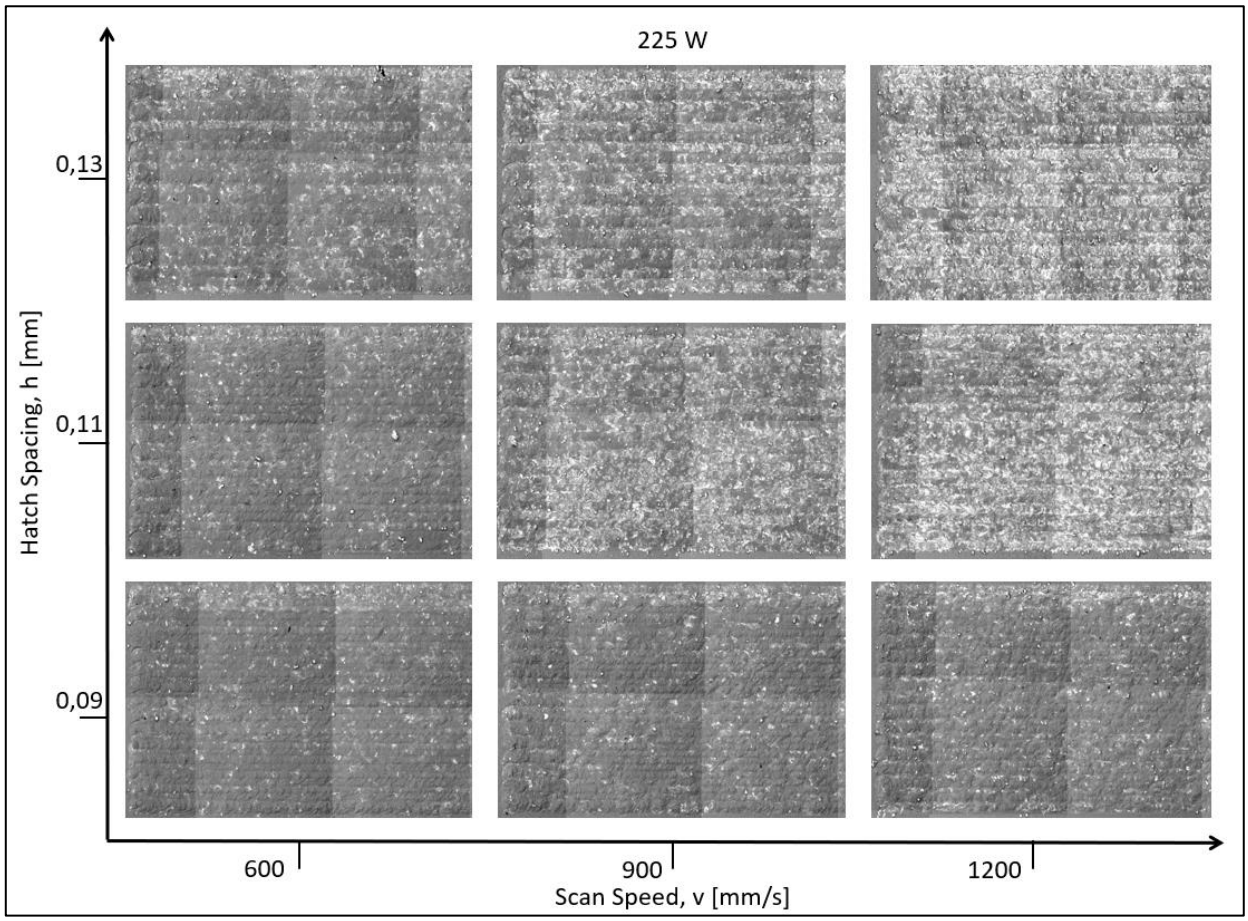

FIGURE 7-8: PROGRESSION OF SURFACE QUALITY WITH CHANGE IN SCAN SPEED AND HATCH SPACING AT 225W LASER POWER

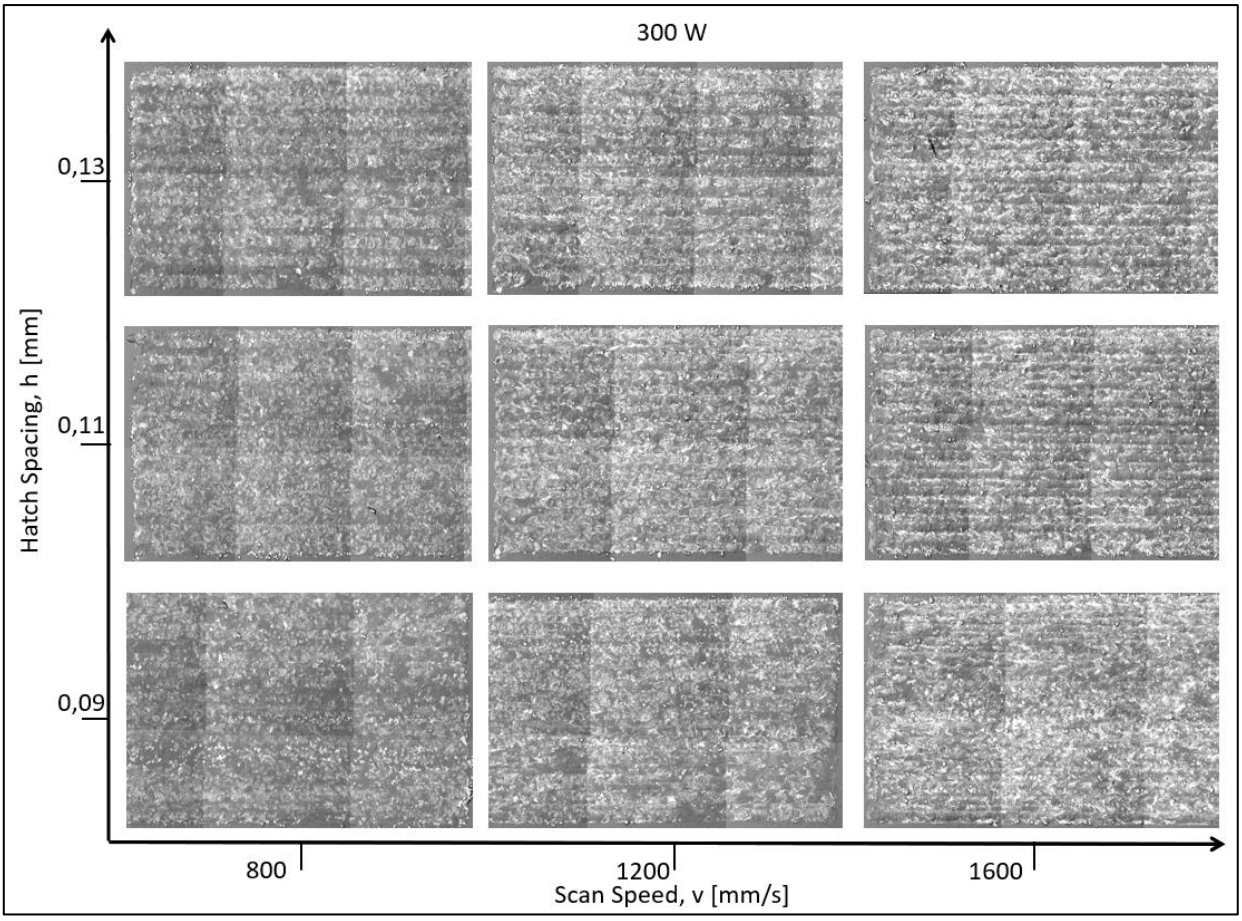

FIGURE 7-9: PROGRESSION OF SURFACE QUALITY WITH CHANGE IN SCAN SPEED AND HATCH SPACING AT 300W LASER POWER

150-WATT LASER POWER

In Block 1 due to the deeper melt pool penetration, large amounts of titanium are present at the surfaces. The presence of WC varied between 0% and 70% though the areas with high tungsten content are far less common. Average WC-content at the surfaces vary between 12wt.% and 0wt. %, peaking at layer 5. When inspecting individual line scans, random peaks in WC-Ni content occur throughout individual layers. Which suggests that these anomalies may be due to experimental setup and uneven powder application rather than a result of the process.

Throughout the entire 150W trial, nickel is represented in the lowest quantities of all constituents, never exceeding an average content of 2 Wt.%. Nickel contents are lower at narrower hatch spacings, which supports the hypothesis that evaporation of nickel occurred and ejected material from the melt pool. Hatch spacing, and scanning speed does not present a clear effect on the trend of surface elements in this block, which suggests that the effect of laser power was far greater than that which speed and hatch spacing could account for.

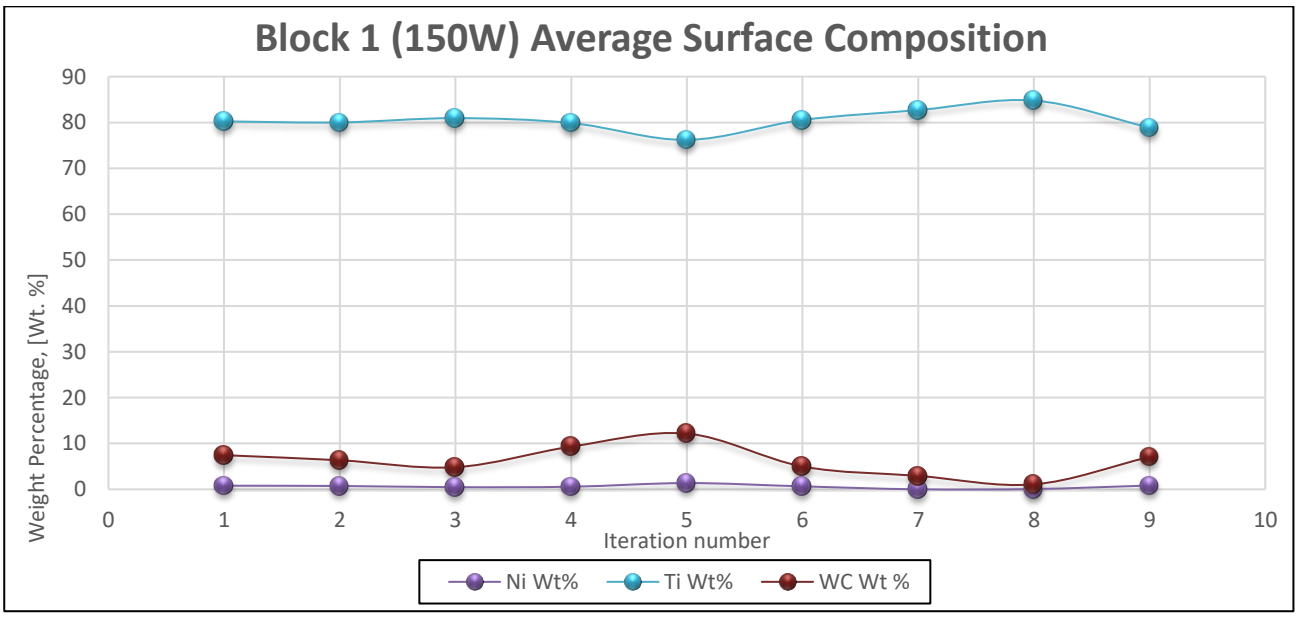

FIGURE 7-10: AVERAGE COMPOSITION CONTENT OF LAYERS 1-9 PRODUCED AT 150-WATT.

225-WATT LASER POWER

The iterations conducted in Block 2 show a considerable increase in the WC contents found at the layer surfaces. It includes the highest recorded average surface contents in the entire experiment at layers 15 and 18. The coating material occurs in average quantities between 10 wt.% and 40 wt.%. A clear increasing trend in WC-presence coincides with both slower scan speeds and wider hatch spacings. Cyclical peaks and troughs are due to speed variation and the overall increasing trend may be attributed to the widening of hatch spacings. Thus, supporting literature stating iterations with lower surface temperatures and likely shallower penetration into the substrate result in more thorough surface coatings.

Moreover, the lesser constituents such as nickel, aluminium and vanadium all have consistent values between 0 wt.% and 5wt.%. Nickel being the least abundant of all constituents. This lack of binder material may be a major contribution to the presence of cracking at the surfaces of the layers in these iterations.

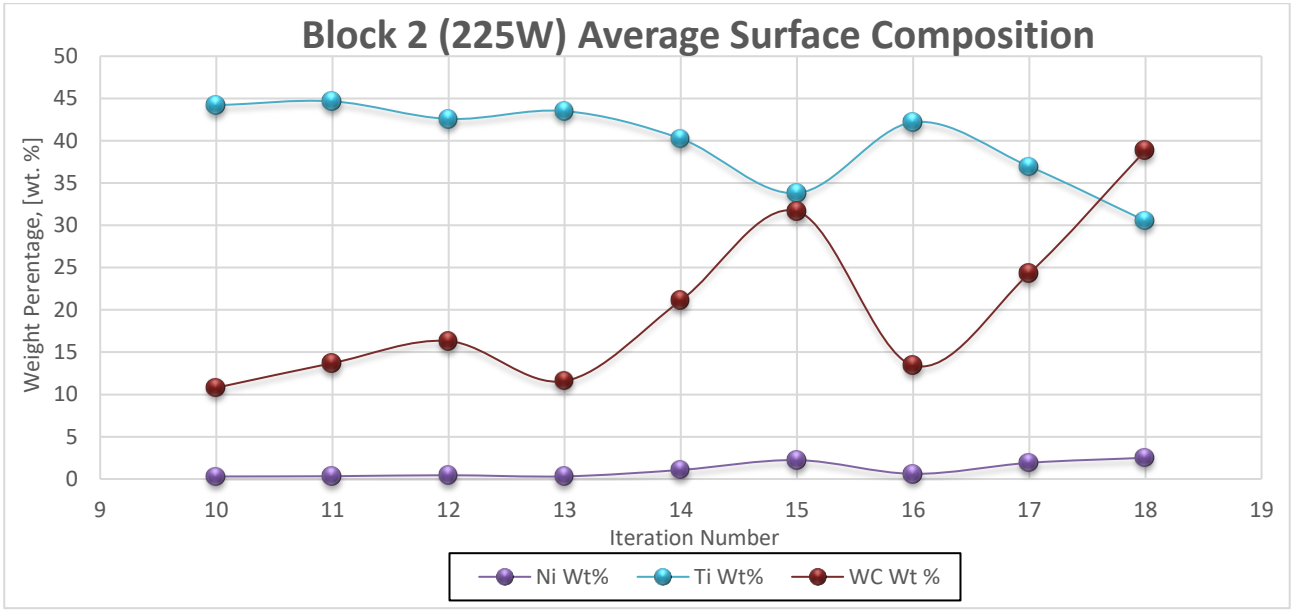

FIGURE 7-11: AVERAGE COMPOSITION CONTENT OF LAYERS 10-18 PRODUCED AT 225-WATT LASER POWER

300-WATT LASER POWER

The highest consistent WC-contents were found at the surface of layers deposited in the Block 3. Averaging between 15 wt.% and 30 wt.%. An increasing trend in the presence of WC is notable for wider hatch spacings, albeit a more modest incline. The slowest scan at each hatch spacing yields less coating material at the surface than its successive speeds. However, a sharp peak in the coating contents at layer 23 offsets the increasing trend found throughout for speed. Once again lesser constituents, nickel, vanadium and aluminium have consistently low values, and nickel contents never exceed 5wt.%.

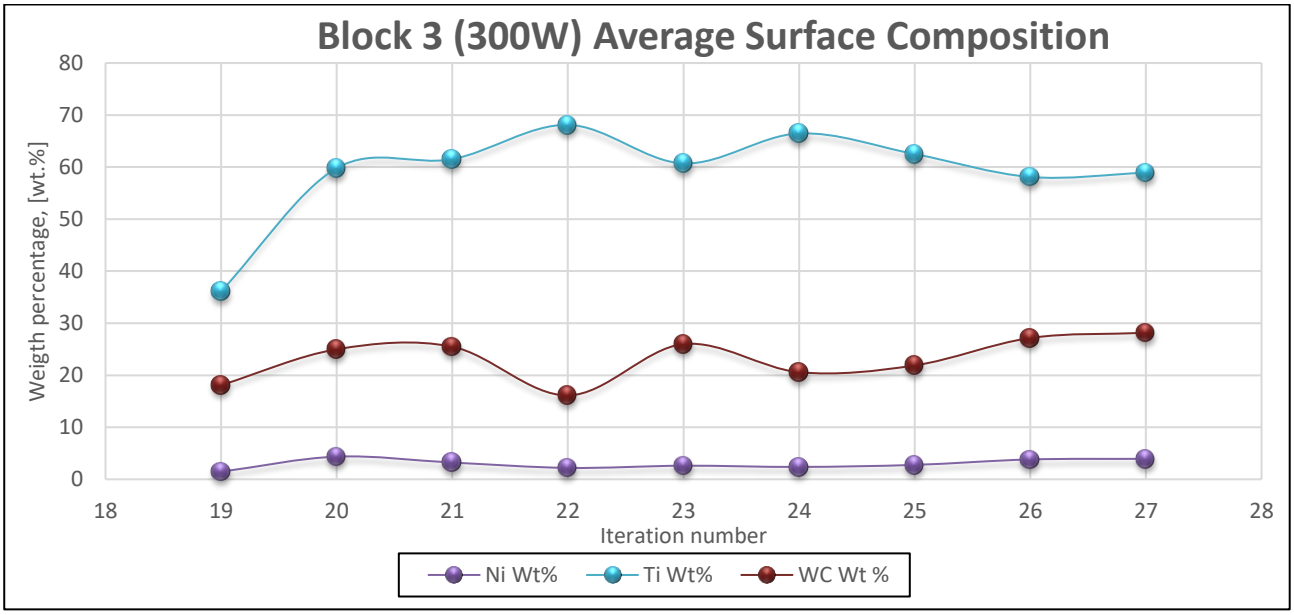

FIGURE 7-12: AVERAGE COMPOSITION CONTENT OF LAYERS 19-27 PRODUCED AT 150-WATT

STATISTICAL ANALYSIS OF SURFACE CONTENTS FOR WC.

A general regression model was implemented to estimate the significance of input factors on the responses for WC-content present at the surface of coatings. The regression analysis included both a linear and quadratic model as the linear model indicated no significant interactions for the sample space investigated. Thus, in order to determine if there are perhaps compounding effects present with significant contributions to the response the quadratic model was also inspected.

Table 7-2 and 7-3 includes the results of the linear and quadratic regression analyses. Despite clear trends in WC-content at the surface of coatings in Block 2 due to hatch spacing and speed variation, the models did not acknowledge its significance. This is likely due to the high variability in the rest of the iterations, and the lack of any trends in Block 1.

TABLE 7-2: LINEAR UNIVARIATE PARAMETER ESTIMATES FOR WC SURFACE PRESENCE.

Effect	Univariate Tests of Significance for WC wt % Sigma-restricted parameterization Effective hypothesis decomposition; Std. Error of Estimate: 5.7886				
	SS	Degr. of Freedom	MS	F	p
Intercept	10.2689	1	10.26894	0.306465	0.585994
power(W)	31.739	1	31.73902	0.947215	0.342054
speed(mm/s)	1.2118	1	1.21181	0.036165	0.851092
Hatch Spacing (mm)	4.8968	1	4.89679	0.146139	0.706285
power(W)*speed(mm/s)	86.7832	1	86.78325	2.589947	0.123215
power(W)*Hatch Spacing (mm)	1.1736	1	1.17357	0.035024	0.853431
speed(mm/s)*Hatch Spacing (mm)	40.8174	1	40.81738	1.218148	0.282827
Error	670.1545	20	33.50772		

In the linear model, the parameters with the greatest statistical significance are scan speed (B) and laser power (A), though the p-values for these factors indicated that the data does not include enough apparent trends for any terms to be significant. On the contrary, the model's statistics concluded a significant p-value and R^2 values above 0.7, which points to good reliability of its predictions. The equation to describe the WC surface contents was estimated as seen in equation 7.1 below. Laser power is denoted by (A), scanning speed as (B), and hatch spacing (C).

$$WC\ wt.\% = -17.32 + 0.1744(\mathrm{A}) + 0.0065(\mathrm{B}) - 99.31(\mathrm{C}) - 0.0001.63(\mathrm{AB}) - 0.2897(\mathrm{AC}) + 0.2966(\mathrm{BC}) \quad (7.1)$$

The quadratic regression model showed similar results to that of the linear model, with most factors indicating insignificant effects. Two factors were only borderline insignificant: laser power (A), and the laser power squared terms (A^2).

TABLE 7-3:UNIVARIATE TESTS OF SIGNIFICANCE FOR WC WT. % INCLUDING QUADRATIC TERMS.

Effect	Univariate Tests of Significance for WC wt % - Sigma-restricted parameterization Effective hypothesis decomposition; Std. Error of Estimate: 5.6692				
	SS	Degr. Of Freedom	MS	F	p
Intercept	24.5545	1	24.5545	0.763999	0.39426
power(W)	122.799	1	122.799	3.820817	0.067268
power(W)^2	119.1944	1	119.1944	3.708662	0.071024
speed(mm/s)	5.7837	1	5.7837	0.179958	0.676729
speed(mm/s)^2	23.5258	1	23.5258	0.73199	0.404137
Hatch Spacing (mm)	2.0886	1	2.0886	0.064985	0.801842
Hatch Spacing (mm)^2	3.6712	1	3.6712	0.114228	0.739519
power(W)*speed(mm/s)	14.6216	1	14.6216	0.454942	0.509067
power(W)*Hatch Spacing (mm)	1.1736	1	1.1736	0.036515	0.85072
speed(mm/s)*Hatch Spacing (mm)	40.8174	1	40.8174	1.270008	0.275422
Error	546.3709	17	32.1395		

It is apparent that an increase in WC-content coincides with lower laser powers and VEDs. The laser power squared term indicates an exponential trend in the response as this parameter is changed, i.e. a unit increment in laser power produces an exponentially larger effect on the response, thus a small power difference can result in a great difference in WC content at the coating surface.

The model parameters for this regression also revealed a significant p-value and strong R^2 terms. Equation 7.2 was estimated to predict the WC surface contents. Counterintuitively, the estimates for A^2, B^2, and AB were all low enough to have an unnoticeable contribution to the prediction.

$$WC\ wt.\% = -66.91 + 0.51(\mathrm{A}) - 0.02(\mathrm{B}) + 330.92(\mathrm{C}) - 0.29(\mathrm{AC}) + 0.3(\mathrm{BC}) - 1955.56\ (\mathrm{C}^2) \quad (7.2)$$

The surface plots generated by this equation are showcased in Figure 7-13 and coincide with the trends found throughout the prior section. Higher scan speeds and hatch spacings both increase the surface content of WC, but speed has a more significant effect. Laser power and scan speed are heavily dependent on each other and produce the best outcomes when both are increased or decreased together proportionally.

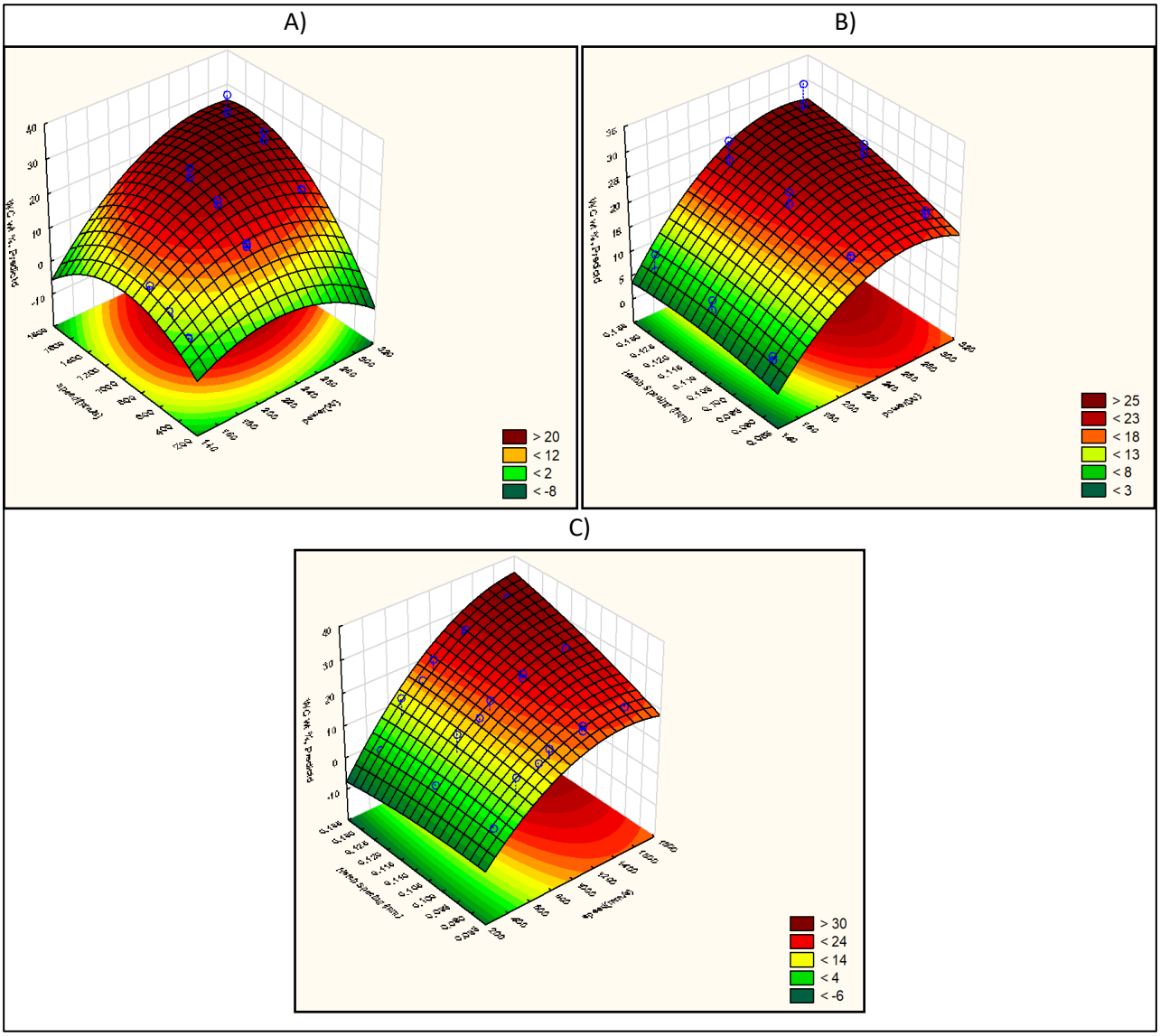

FIGURE 7-13: SURFACE PLOT PREDICTING WC WT.% AT THE LAYER SURFACES FOR INTERACTION PARAMETERS FOR, (A) POWER (W) VS. SPEED (MM/S), (B) POWER VS. HATCH SPACING (MM), (C) SPEED VS. HATCH SPACING.

7.2.2 Layer Quality and Cracking

Significant levels of cracking were observed in more than half the samples, especially in layers with increased amounts of tungsten at the surface. Cracks were observed to more likely initiate from the top of a layer closer to first scan track and propagate perpendicular to the scan direction across the layer (in the y-direction as indicated in Figure 7-14). In line with literature, SLM/SLS parts' residual stresses are less prominent in the scan direction than its perpendicular[78].

The presence of cracking reduces further down from the top of the layers. This is likely due to a smaller temperature difference between the substrate and the laser contact area in these sections [130]. As the layer develops, the area adjacent to each scan track is preheated via thermal conduction and the temperature difference decreases, which reduces residual stresses that lead to cracking.

As the hatch spacing is increased, noticeably less cracking occurs at the layer surfaces. This phenomenon was described by Oosthuizen et al. [77] in a similar study on single layer production of tungsten carbides onto tool steel. The research characterised the effects of high hatch spacings on shrinking and residual stresses in cemented tungsten carbide layers. The melt pool temperature should conventionally be limited to just above the binder material's melting point; reducing the presence of evaporation and limiting thermal expansion. Narrow hatch spacings coincided with increased melt pool temperatures and greater levels of expansion and brought about a steeper cooling gradient and excessive shrinkage. This leads to surface defects upon cooling of the layers such as delamination and cracking.

The layer quality is visibly smoother in Block 1 and the 0.09 mm hatch spacing iterations Block 2; minimal cracking was present for all layers in these groups, although some had defects at their edges such as splattering and deep cavities due to evaporation. The first 12 layers were nearly void of macrocracks at the surfaces, the cracks that were found were measured, though not enough instances could be recorded to produce a reliable average that is transferrable to successive experiments.

For layers 13 – 27 cracks were measured over the entire surface. 15 measurements were conducted for each layer, which corresponds to the minimum number of noticeable cracks in layer 13. Figure 7-14 includes a segment from the surface of iteration 22 to showcase the cracking present in samples.

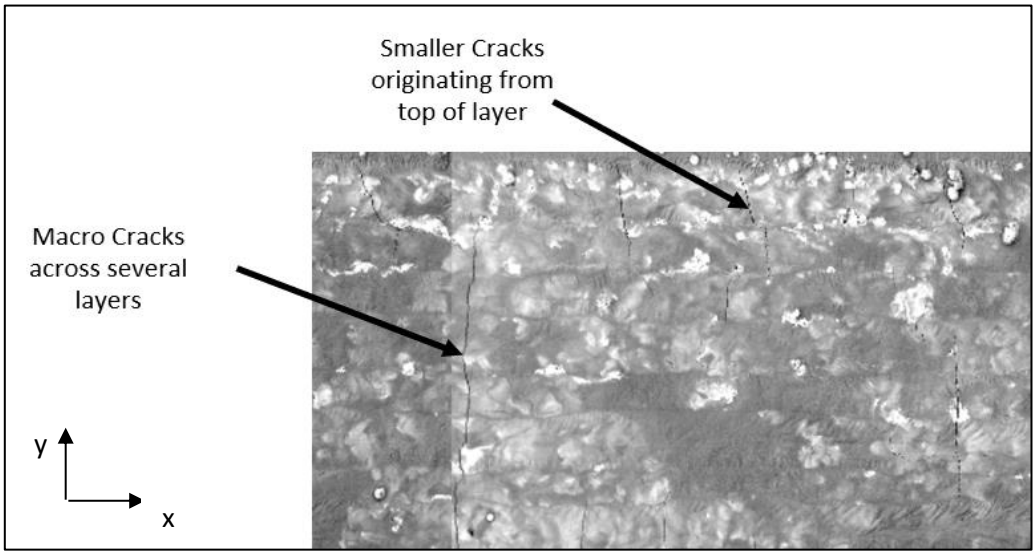

Figure 7-14: Example of cracking at layer surfaces, from iteration 22.

The graph in Figure 7-15 illustrates the average crack length for runs 13 – 27 and the corresponding VED at each experimental run. It can be noted that for iterations 13 - 18, the increasing hatch spacing of successive iterations does not lessen crack length. On the contrary, these groups tend to have an increasing trend in crack size with each successive scan. These contradicting trends are likely related to the shallower coating penetration recorded across Block 3. At deep penetrations, material is submerged into the substrate and the titanium acts as an abundant binder alternative, reducing cracking as seen in layers 1-9.

At iterations 13 – 18, coatings diffused deeper into the substrate on average and crack size increased with shallower penetration and more WC content at the surface. At iterations 19 – 27, the coating diffusion was shallower and more consistent overall, which resulted in a consistent WC-content at the surface. The reduced variation caused by deeper diffusion allowed the effects of scanning speed and hatch spacing to make a more significant contribution to the formation of cracks. Hence the clearer trends in these zones.

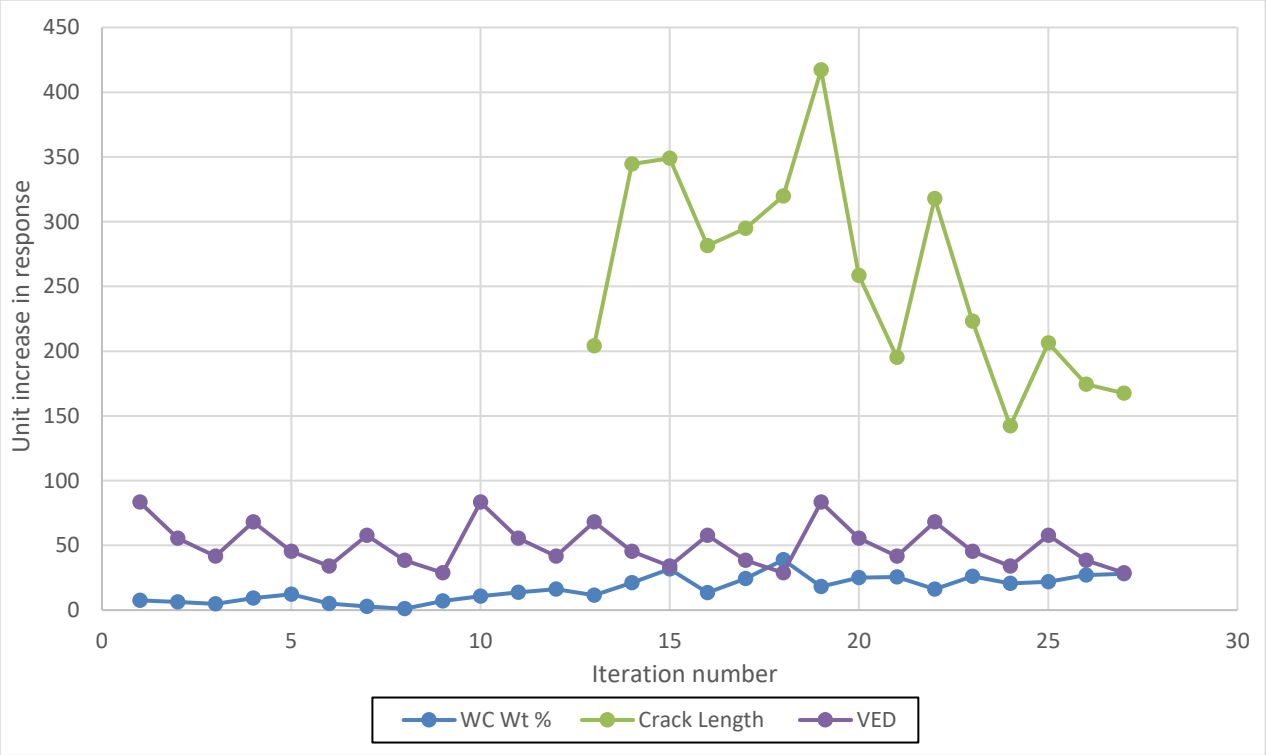

FIGURE 7-15: COMPARISON OF AVERAGE CRACK LENGTH, WC WT. % PRESENT AT THE SURFACE, AND VED

Table 7-4 provides a qualitative measure for the surface presence of WC, cracking, and the occurrence of additional defects at the layer. Some layers had other defects such as splattered zones, cavities or ragged edges which were also incorporated into the analysis. The quality of iterations is graded according to the presence of cracking and additional defects which are described. A (-) indicates virtually no cracking, (+) cells indicate moderate cracking, and (++) refers to layers with large quantities of macrocracks. Each factor was considered before giving the layer surface a qualitative rating of good (green), average (orange) or bad (red).

The presence of cracking at the initial layer may be mitigated in future work by increasing the binder content in the powder, experimenting with alternative scanning strategies, or applying a more thorough pre-heating process of the substrate. Alternatively, layer re-scanning can be conducted to re-melt the layer and reduce the residual stresses built up in the material [95]. Furthermore, the porosity of powder particles should be avoided, and solid spherical particles would be ideal.

TABLE 7-4: QUALITATIVE ANALYSIS OF SCAN TRACK SURFACE MORPHOLOGIES. GREEN CELLS INDICATE GOOD RESULTS, ORANGE - MODERATE DEFECTS, AND RED HIGH DEFECT RATES

Run #	WC Content at surface	Cracking	Surface Defects	Average crack length	Surface Quality
1	Low	+	Minor Cracks, 50µm – 120µm in length		Bad
2	Low	_	None	-	Bad
3	Low	_	None	-	Bad
4	Low	_	None	-	Bad
5	Medium	_	None	-	Average
6	Low	_	None	-	Bad
7	Low	_	Splattering & material loss at sides between 400µm (Left) to 800µm (Right).	-	Bad
8	Low	_	Splattering & material loss at sides between 400µm (Left) to 950µm (Right).	-	Bad
9	Low	_	None	-	Bad
10	Medium	+	Minor Cracks, 70µm – 370µm in length	-	Average
11	Medium	+	Minor Cracks, 40µm – 80µm in length	-	Average
12	Medium	+	Minor Splattering at edges. Minor Cracks, 40µm – 250µm in length.	-	Average
13	Medium	+	None	204.00	Average
14	High	++	None	344.43	average
15	Very High	++	Minor Splattering at edges	348.87	Good
16	Medium	+	Minor Splattering at edges	281.49	Good
17	High	++	None	294.89	Good
18	Very High	++	None	319.69	Good
19	Medium	++	None	417.10	Average
20	High	++	None	258.52	Average
21	High	+	Minor Splattering at edges	195.25	Good
22	Medium	++	None	317.89	Average
23	High	++	Splattering & material loss for400µm at both sides.	223.10	average
24	High	+	None	142.22	Good
25	High	+	None	206.24	Good
26	High	+	Splattering & material loss for 200µm at both sides.	174.31	Average
27	High	+	Splattering & material loss for 200µm at both sides.	167.46	Average

7.3 PENETRATION DEPTH & EDS MAPPING.

The following section characterises the effects of machine parameters on coating penetration into the substrate and the elements presence at the interface cross section. Each of the 27 layers' cross sections were inspected under an Olympus light microscope and SEM. Findings are correlated with those achieved for the surface presence of WC to obtain the optimal combination of parameters that will provide good coating penetration while maintaining desirable levels of WC at the substrate surface.

7.3.1 DIFFUSION AND PENETRATION INTO SUBSTRATE

The penetration of the deposited layer into the substrate was analysed by recording three average measurements at each layer. The total depth (TD), interfusion zone (IZ) and the cladding zone (CZ), as described in Figure 7-16. In this work, the total coating thickness is utilized as a metric to represent the size of initial coating layers onto the substrate and may be used to extrapolate the level of additional processing required on top of initial layers. It is defined as the sum of the interfusion zone and the clad zone (IZ + CZ). The interfusion zone is primarily responsible for adhesion of the coating to the substrate, and the clad zone describes the height of coated material present at the surface. A univariate statistical analysis was conducted to determine the interactions between machine parameters on the data collected for each measurement and are available in Appendix J.

Clear trends can be seen in the size of the penetration depth and the interfusion zone as the input factors are varied. Higher VED values coincide with deeper penetration. Thus, as scan speeds increase, and hatch spacings become wider there is less penetration by the energy source into the substrate. Large interfusion zones were recorded at both intermediate and high energy densities, though the highest penetration depths only occurred at the highest VED's.

Relative to penetration depth and interfusion zone size, the average clad zone height remains inconsistent throughout, with the only prominent trends being that some peaks in the CZ coincide with high VED levels, and the overall average CZ decreases with a decrease in interfusion zone size. Figures 7-16 and 7-17 below include graphs for each measurement (CZ, IZ, TD, and Coating Thickness) recorded at experimental runs.

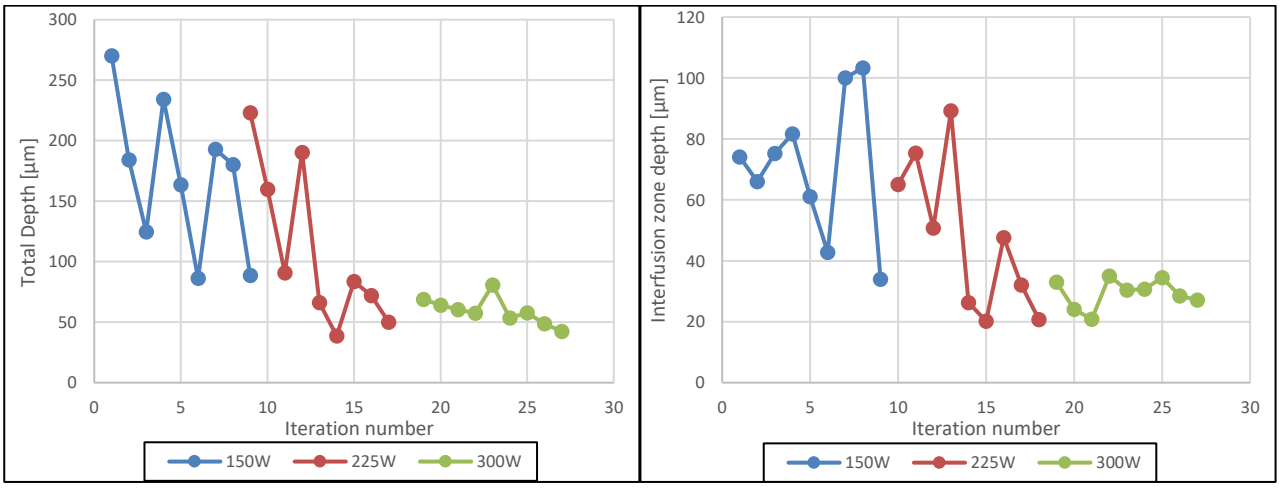

FIGURE 7-16: AVERAGE RESPONSE MEASUREMENTS AT EACH RESPECTIVE ITERATION FOR TOTAL DEPTH (LEFT), AND INTERFUSION ZONE (RIGHT)

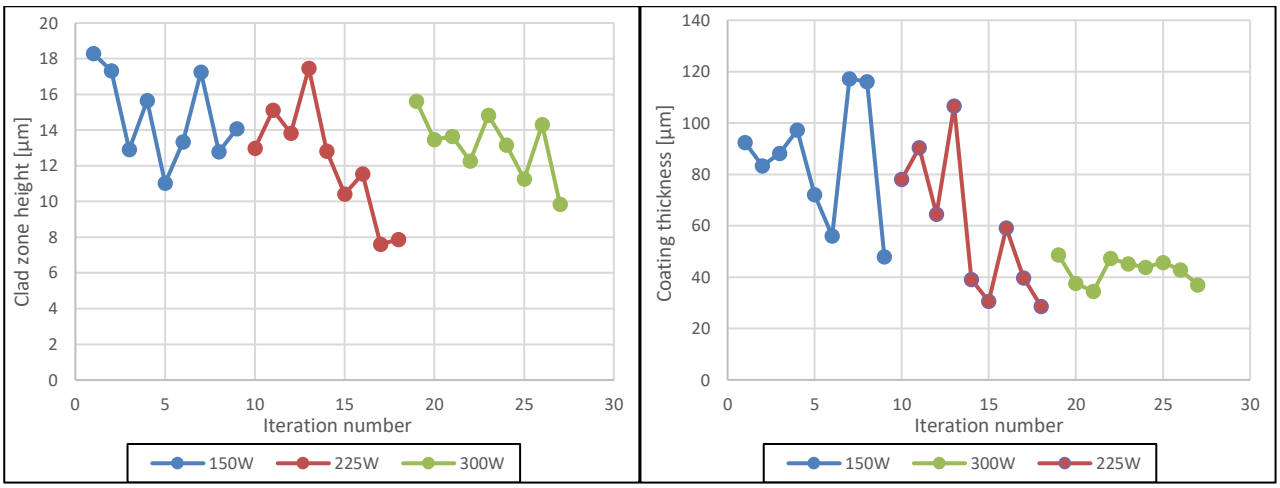

FIGURE 7-17: AVERAGE RESPONSE MEASUREMENTS AT EACH RESPECTIVE ITERATION FOR CLAD ZONE HEIGTH (LEFT), AND COATING THICKNESS (RIGHT).

Univariate tests of statistical significance were conducted to estimate the interactive effects of the three input factors on the response. The full spreadsheet data and response surfaces are included in Appendix L. The clad zone and interfusion zones were analysed separately in order to estimate effects of parameters on individual measurements.

The interfusion zone is the most important metric for coating adhesion, it acts as the foundation for attachment onto the substrate. Good interfusion zone depth translates to lower probability of adhesive failure. Though the required diffusion depth for a coating is dependent on the size of the area being coated and the thickness of the part. Table 7-5 includes the statistical tests for significance on interfusion zone depth for factors and their interactions.

TABLE 7-5: UNIVARIATE TESTS OF SIGNIFICANCE FOR COATING INTERFUSION ZONE

Effect	Univariate Tests of Significance for Depth Sigma-restricted parameterization Effective hypothesis decomposition; Std. Error of Estimate: 5.7886				
	SS	Degr. Of Freedom	MS	F	p
Intercept	1216.91	1.00	1216.91	4.35	0.05
power(W)	459.08	1.00	459.08	1.64	0.21
speed(mm/s)	118.40	1.00	118.40	0.42	0.52
Hatch Spacing (mm)	0.60	1.00	0.60	0.00	0.96
power(W)*speed(mm/s)	1237.04	1.00	1237.04	4.42	0.05
power(W)*Hatch Spacing (mm)	60.71	1.00	60.71	0.22	0.65
speed(mm/s)*Hatch Spacing (mm)	200.49	1.00	200.49	0.72	0.41
Error	5593.99	20.00	279.70		

The only factor with a significant contribution to the interfusion zone depth is the interaction between the laser power and scan speed. This is confirmed in literature as lower scan speeds commonly correlate with less penetration and larger amounts of material at the surface [98]. Hatch spacing values do have a significant effect in practice, however their range is statistically very small compared to the other factors and significant contribution diminishes after it exceeds the size of the spot diameter.

The equation to describe the total depth of penetration was estimated; it's p- value, characterising the validity of the model, is 0.0004, which indicates a reliable estimation. Additionally, the multiple and adjusted R^2 – values are both above 0.55 indicating a less reliable prediction.

$$Interfusion\ Zone = 188.63 - 663.4(\mathrm{A}) - 64.13(\mathrm{B}) - 34.89(\mathrm{C}) + 390.52 + 2083.76(\mathrm{AC}) - 657.33(\mathrm{BC}) \quad (7.3)$$

TABLE 7-6: UNIVARIATE TESTS OF SIGNIFICANCE FOR DEPTH

Effect	Univariate Tests of Significance for Depth Sigma-restricted parameterization Effective hypothesis decomposition; Std. Error of Estimate: 5.7886				
	SS	Degr. Of Freedom	MS	F	p
Intercept	20783.03	1	20783.03	22.86399	0.000114
power(W)	1515.83	1	1515.83	1.66761	0.211305
speed(mm/s)	11919.47	1	11919.47	13.11294	0.001702
Hatch Spacing (mm)	2187.22	1	2187.22	2.40622	0.136535
power(W)*speed(mm/s)	16959.38	1	16959.38	18.65748	0.000333
power(W)*Hatch Spacing (mm)	57.26	1	57.26	0.06299	0.804385
speed(mm/s)*Hatch Spacing (mm)	1059.84	1	1059.84	1.16596	0.293083
Error	18179.71	20	908.99		

From Table 7-6 the most significant contributions to the depth of layer penetration is the scan speed. However, speed is dependent on the intensity of the laser power, lower scan speeds would be required for lower laser power settings and vice versa. For this reason, it is sensible for the most significant interaction effect to be between these factors.

The equation to describe the total depth of penetration (7.4) is included below. The model p-value was significant and its R^2 values were all above 0.8, which indicates that parameters estimated in equation 6.1 below will produce a reliable approximation.

$$Total\ Depth = 779.54 - 1205.48(\mathrm{A}) - 643.43(\mathrm{B}) - 2098.76(\mathrm{C}) + 1445.95(\mathrm{AB}) - 2023.68(\mathrm{AC}) + 1511.34(\mathrm{BC}) \quad (7.4)$$

The univariate tests of significance for the clad zone height is included in Table 7-7 below. The only significant effect on the clad zone height is the combination of laser power and scanning speed. Despite this single predictive effect, the measured data did not appear to show any trends and was subject to high variability. At several occurrences throughout each layer, there would be no clad zone at the surface of the substrate, and rather a shallow cavity. It was hypothesised that successive layers would be required to achieve a dense coating at the surface, which this data has confirmed.

TABLE 7-7: UNIVARIATE TESTS OF SIGNIFICANCE FOR CLAD ZONE.

Effect	Univariate Tests of Significance for Depth Sigma-restricted parameterization Effective hypothesis decomposition; Std. Error of Estimate: 5.7886				
	SS	Degr. Of Freedom	MS	F	p
Intercept	34.67	1.00	34.67	8.41	0.01
power(W)	1.79	1.00	1.79	0.43	0.52
speed(mm/s)	7.84	1.00	7.84	1.90	0.18
Hatch Spacing (mm)	0.71	1.00	0.71	0.17	0.68
power(W)*speed(mm/s)	32.85	1.00	32.85	7.97	0.01
power(W)*Hatch Spacing (mm)	0.02	1.00	0.02	0.01	0.94
speed(mm/s)*Hatch Spacing (mm)	0.42	1.00	0.42	0.10	0.75
Error	82.44	20.00	4.12		

Equation 7.5 was determined to describe the clad zone height. The model p-value was far below 0.05 and indicated significance, though its R^2 values were all below 0.6, which indicates that the output is not as wholly reliable as the approximation for depth.

$$Clad\ Zone\ Height = 31.84 - 41.37(\mathrm{A}) - 16.5(\mathrm{B}) - 37.92(\mathrm{C}) + 63.63(\mathrm{AB}) - 40.42(\mathrm{AC}) + 30.172(\mathrm{BC}) \quad (7.5)$$

Figure 7-18 illustrates the relationship between the coating thickness (CZ + IZ) and the presence of WC at the surface of the layers. This further verifies the findings from univariate significance tests for both the interfusion and clad zones; that higher scanning speeds and shallower penetration depths produce more dense surface coatings. The increasing trends for coating penetration, and decreasing trend for WC-content presence as VED values increase correlate with the hypothesised response in section 4.6.

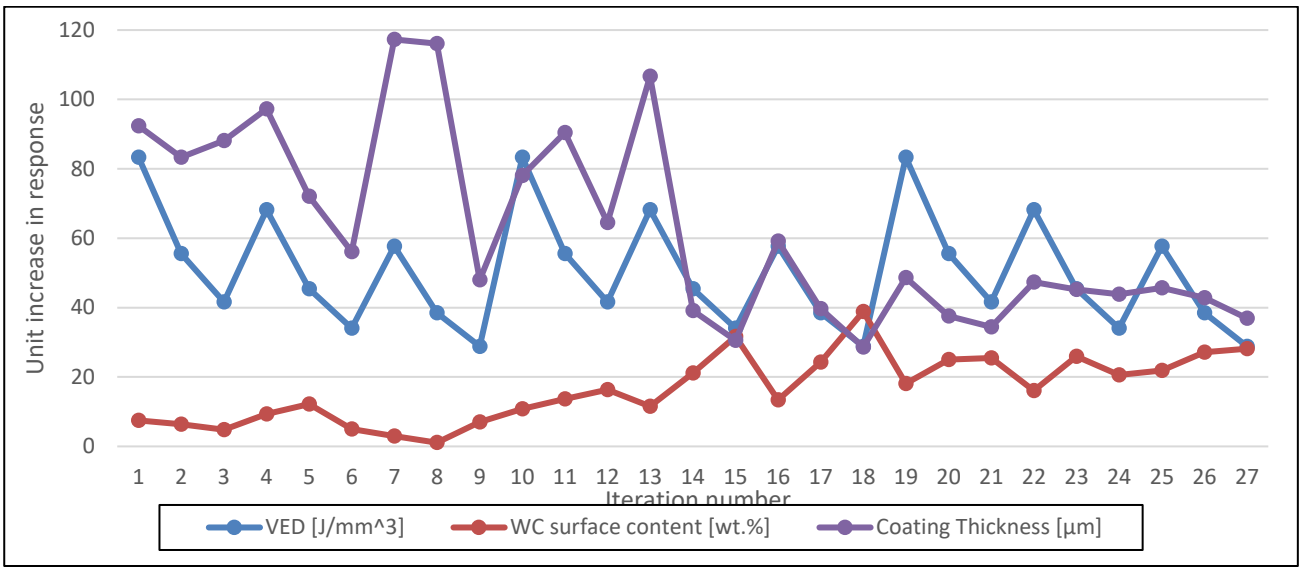

FIGURE 7-18: RELATIONSHIP BETWEEN COATING THICKNESS, WC SURFACE PRESENCE AND SURFACE CRACKING.

7.3.2 EDS MAPPING

During the SEM analysis of each layer's cross section, elemental maps were generated. The maps indicate the spread of elements throughout the layer and provide insight to how far the coating diffused into the substrate material. Layered maps illustrating the presence of W, C, Ni, and Ti are attached in Appendix K. Figure 7-19 includes examples of a microscope image and maps of the cross section at layer 16. Due to the carbon in the sample mounts, the EDS maps for carbon content were distorted, however the contents of tungsten, nickel and the combined presence of WC-Ni are presented.

Table 7-8 includes a qualitative summary of the EDS maps for each layer. It characterises the presence of WC-Ni throughout the layer in terms of three indicators: 1) The melting of powder particles, 2) diffusion of WC-Ni into the substrate, 3) and the consistency of the spread along the surface. Each category is ranked into either low (-), medium (+) or high (++).

For powder melting, the lower bound refers to particles that are still relatively spherical and un-melted, compared to fully molten particles. Diffusion is determined by how deep WC-Ni penetrated the substrate. Either localised at the surface, spread throughout the interfusion zone, or all the way into the total depth. Lastly, spread consistency describes whether particles are conglomerated into groups at the surface or dispersed evenly. The positive effects are green, negative is red, and orange describes the mid-range.

Figure 7-19 includes various images of layer 16's cross section from the Olympus light microscope and EDS mapping. This layer provides an example of a desirable coating, adequate particle dispersion, good penetration and intermediate melting of powder particles. High levels of WC partial melting coincided with the highest VED ranges and deepest penetration.

In processing ranges where keyhole formation is present, it would indicate that evaporation of the Ti-6Al-4V material occurred. The boiling point of the alloy is 3287 °C which exceeds the melting temperature of tungsten carbide at 2870 °C. Though particle melting improves dispersion at the surface, at iterations where the melt pool temperature is too high, and molten particles diffuse too deep into the substrate, very little WC is left at the coating zone.

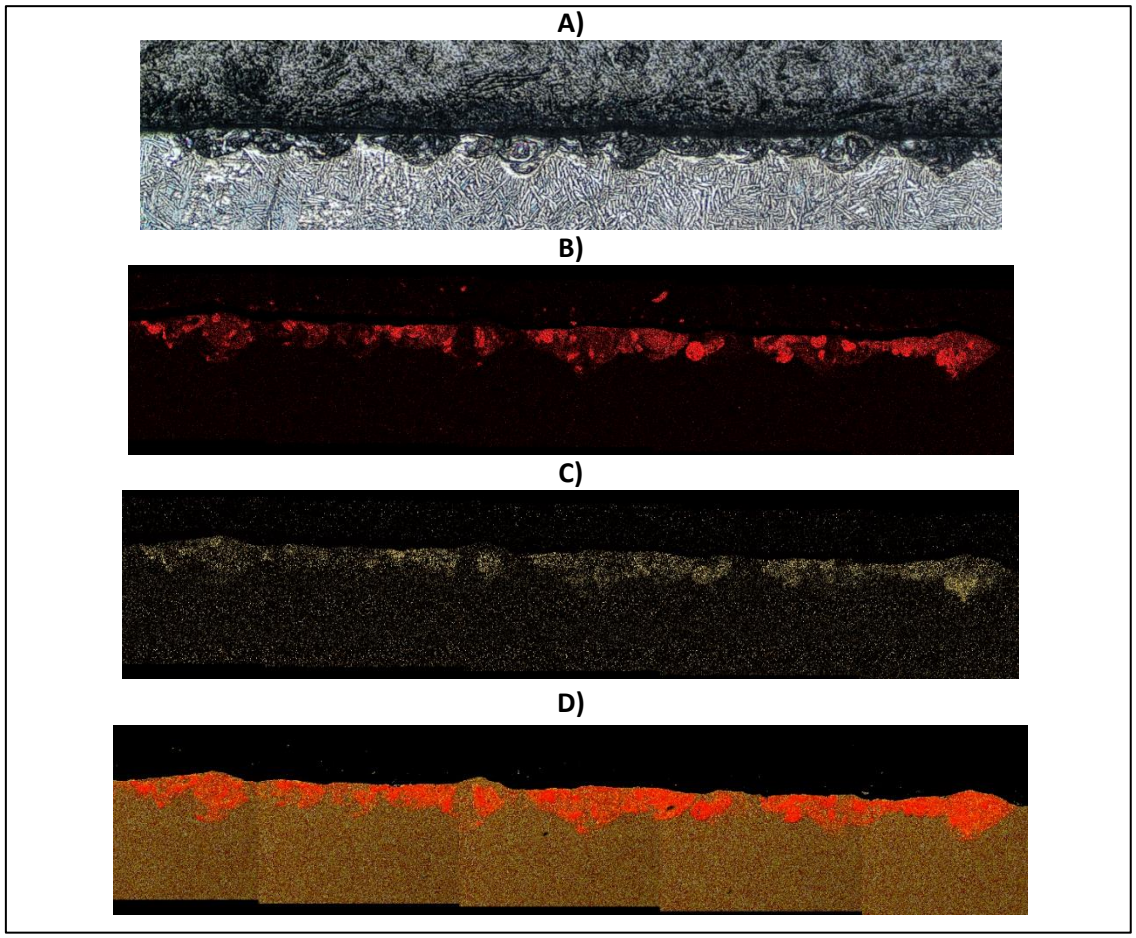

FIGURE 7-19: A) CROSS SECTION OF LAYER 16 CAPTURED WITH OLYMPUS LIGHT MICROSCOPE, B) EDS MAP OF TUNGSTEN PRESENCE AT LAYER SURFACE, C) EDS MAP OF NI PRESENCE AT LAYER SURFACE, D) LAYERED MAP OF W, C, AND NI PRESENCE AT LAYER SURFACE.

As stated by Parikh et. al [57], for carbides to be effective, the hard phases must be sintered together to yield a strong carbide/binder interface devoid of anomalous carbide growth. To achieve a dense composition, melting must occur at the lowest possible temperature while easily wetting carbide surfaces in order to develop an uninterrupted binder distribution. Carbide on carbide interfaces should be minimized for optimal properties. Figure 7-20 displays a layered EDS image of the first iteration in Block 1. This recorded the deepest penetration and displays how the powder particles underwent excessive melting and diffused too deep into the substrate for a significant WC presence at the substrate surface. Thus, high particle melting at intermediate penetration depths would be the most desirable outcome.

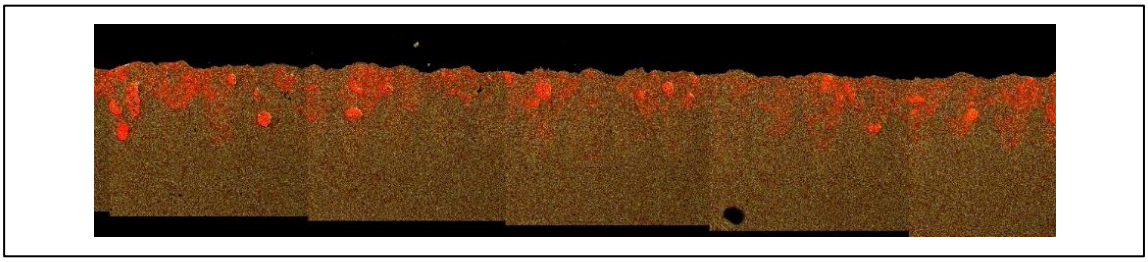

FIGURE 7-20: CROSS SECTION EDS MAP OF LAYER 1, INDICATING MELTING OF WC-NI PARTICLES AND THEIR DIFFUSION INTO THE SUBSTRATE

TABLE 7-8: QUALITATIVE GRADING OF LAYER QUALITY BASED ON POWDER MELTING, PENETRATION DEPTH INTO THE SUBSTRATE AND ITS SPREAD CONSISTENCE AT THE SURFACE.

Run #	Melting	Penetration	Spread Consistency	Layer Quality
1	++	++	-	Bad
2	++	++	-	Bad
3	+	++	-	Bad
4	+	++	-	Bad
5	++	++	-	Bad
6	+	++	+	Bad
7	+	++	-	Bad
8	+	++	+	Bad
9	+	++	+	Bad
10	+	++	+	Average
11	+	++	+	Bad
12	++	+	-	Bad
13	+	++	++	Average
14	+	++	-	Bad
15	+	-	+	Average
16*	++	+	++	Exceptional
17	+	+	++	Good
18	+	+	++	Good
19*	++	+	++	Exceptional
20	+	+	+	Average
21	-	-	+	Bad
22	+	+	+	Average
23	+	-	-	Bad
24*	+	+	++	Exceptional
25	+	+	+	Good
26	-	+	-	Bad
27	+	-	-	Bad

7.3.3 Scan Depth Composition

The cross sections of eight layers were analysed under SEM to produce EDS compositional line scans of their cross sections. Each layer consisted of 40 discrete points where the composition was measured. Layers were chosen at high, intermediate and low energy densities to estimate the effect of VED on the diffusion of elements into the substrate. The scans originate from the layer surface and proceed along the penetration depth (Figure 7-21).

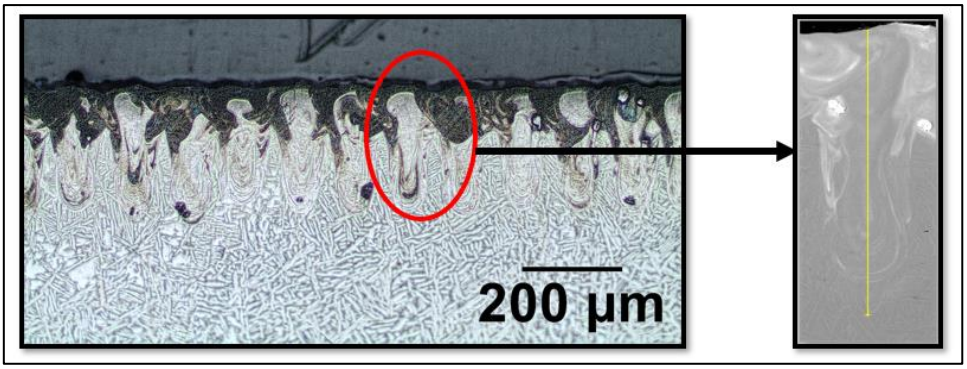

Figure 7-21: Compositional line scan procedure for layer penetration

High Volumetric Energy Density

Scan tracks were taken at layer 1 and 22, corresponding to volumetric energy densities of 83.3 J/mm^3 and 68.18 J/mm^3. The two line-scans illustrate the compositional changes surrounding whole powder particles embedded into the substrate. Figure 7-22 includes images of the cross sections evaluated and a graph illustrating the compositional variations along the penetration depth. Despite the peaks at powder particles, and the varying contents between successive spirals in the melt pool, the spread of WC throughout the penetration depth is relatively consistent. The nickel content is consistently low throughout and peaks in Ni-content only occur in tandem with that of WC.

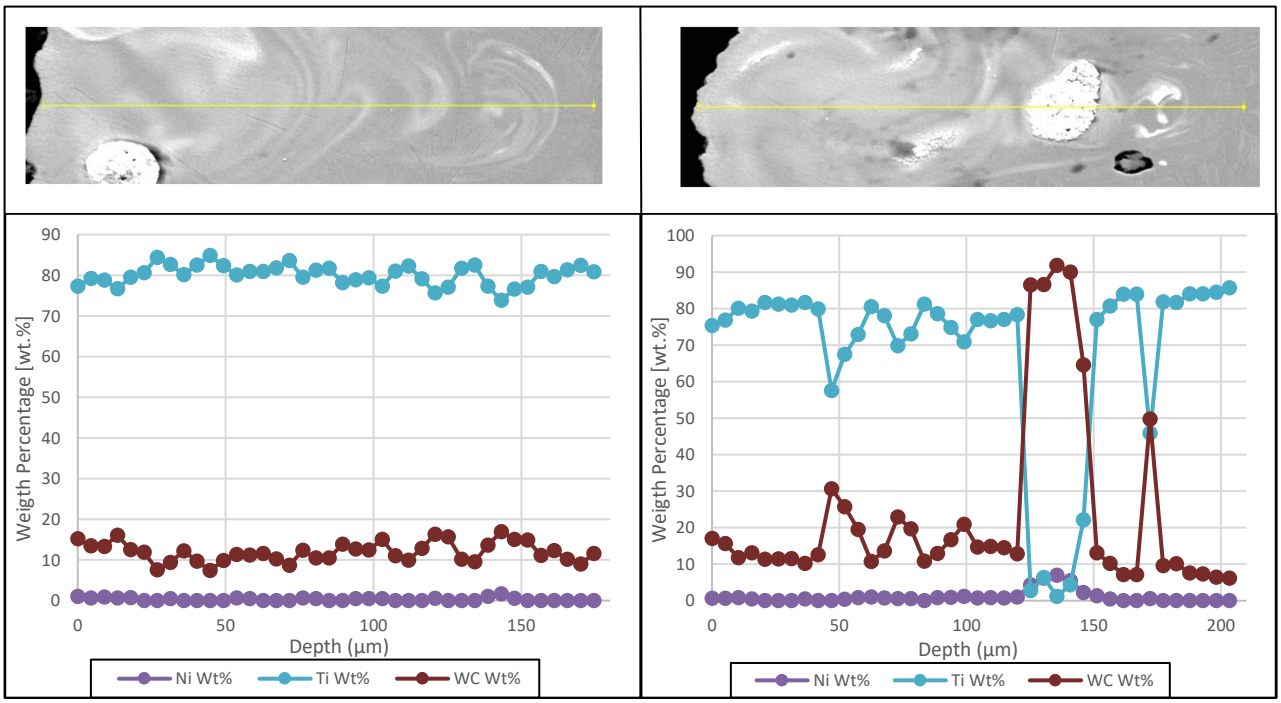

Figure 7-22: Compositional changes along penetration depth of layer 1 (Left) with smoothed diffusion, and layer 22 (Rigth) with particles embedded in the melt pool.

From this analysis it is evident that the WC content peaks in the ranges of the WC particles. The partially molten particles let off streaks of WC, seen in the white swirls on the sections above which have higher concentrations of the coating material. This “swirl” is caused due to the Marangoni effect, wherein the laser force drives powder particles into the melt pool. As particles reach the depth of the pool a vortex-like phenomenon occurs, and the powder is sent into an upward spiral. As the particles perpetuate through this movement, they gradually melt and leave traces of WC-Ni in their wake across the depth of the melt pool [131].

INTERMEDIATE VOLUMETRIC ENERGY DENSITY

The two layers selected in the VED mid-range were at iterations 11 and 14. With corresponding VED values of 55.56 J/mm^3 and 45.45 J/mm^3. The same phenomenon was noticed where tungsten carbide contents increased significantly in the areas of particles imbedded in the molten material. In this range the traces of the Marangoni effect are clearly visible, however due to lower temperatures in the molten pool, the particles underwent less melting and their contents were not spread throughout the penetration depth as gradually as with the higher VED ranges. Nickel content has a minimal presence as with prior layers and is only present at high concentrations of WC.

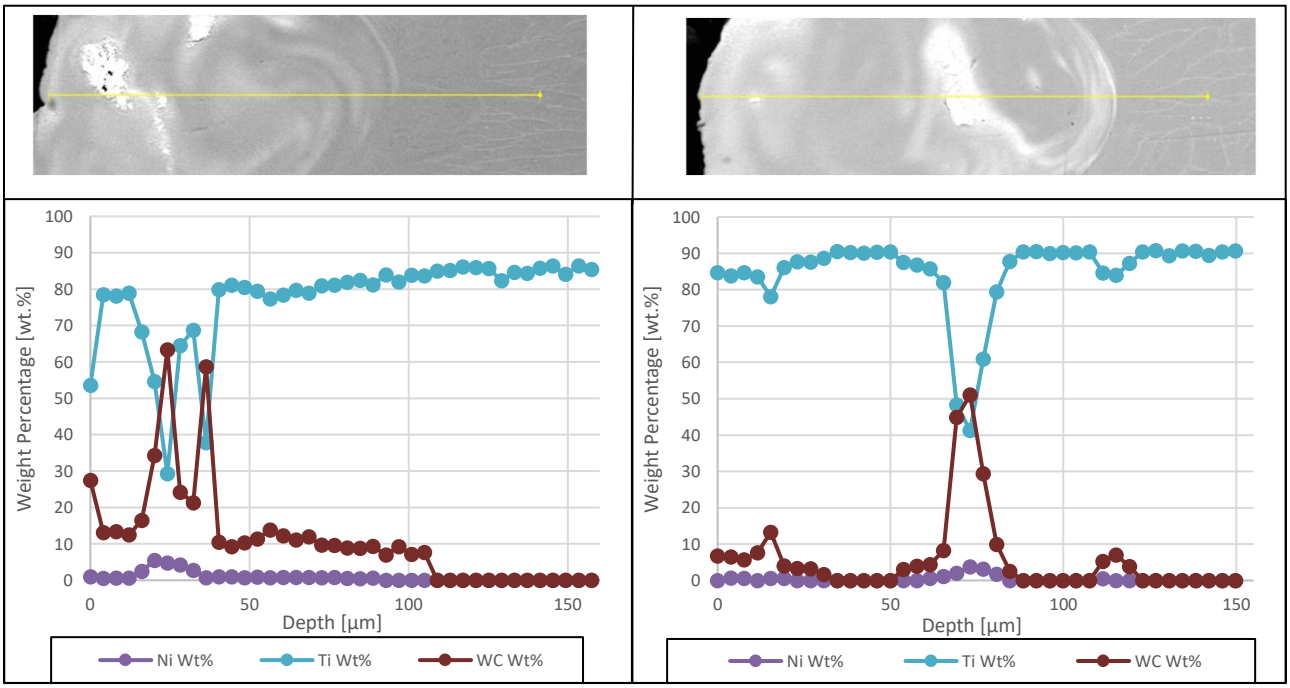

FIGURE 7-23: COMPOSITIONAL CHANGES ALONG PENETRATION DEPTH OF LAYER 11, (LEFT), AND LAYER 14 (RIGHT).

LOW-RANGE VOLUMETRIC ENERGY DENSITY

The layers selected for analysis were from iterations 18 and 24, with respective VED levels of 34.09 J/mm^3 and 28.85 J/mm^3. In these ranges the Marangoni effect was less prominent and much of the WC- presence was located at the bottom of the melt pool. This is likely because at higher speeds and less laser contact time in the melt pool, the particles do not melt as thoroughly as at higher VED’s. Therefore, less time is available for the Marangoni effects to take place and the particles to dissolve in the melt pool. The nickel content follows a similar trend to prior layers and peaks with the content increase in WC.

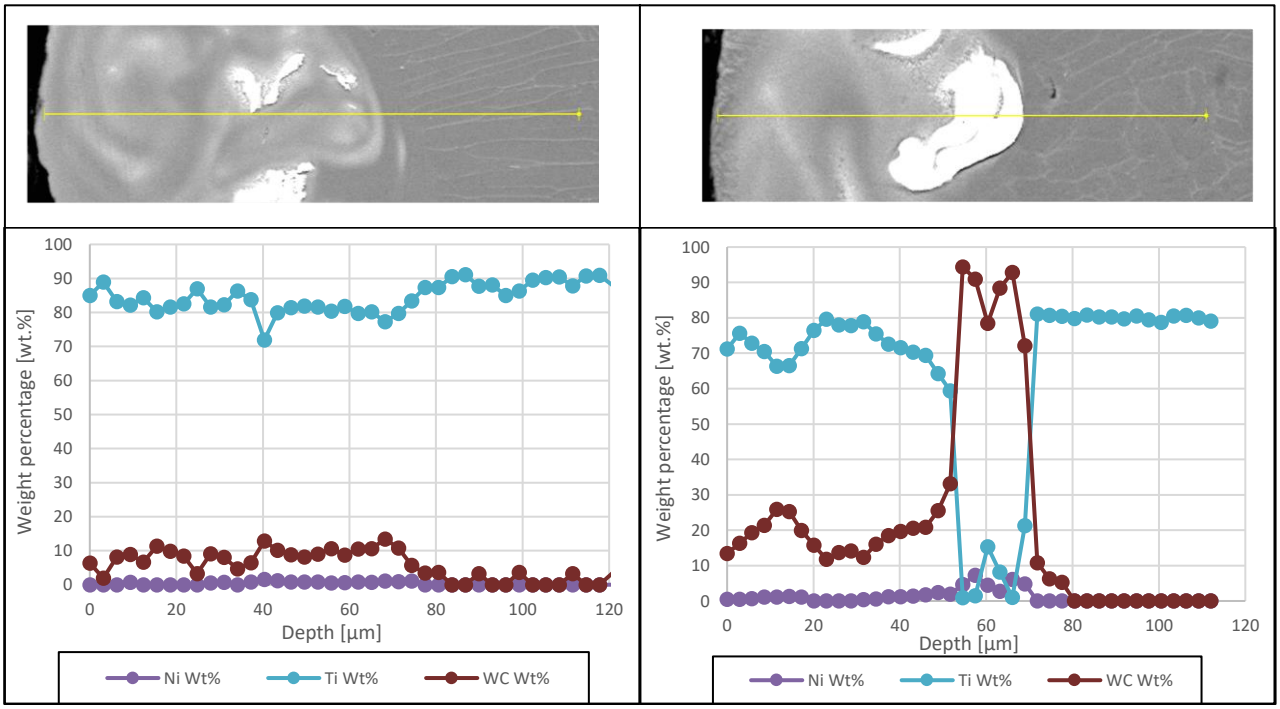

FIGURE 7-24:COMPOSITIONAL CHANGES ALONG PENETRATION DEPTH OF LAYER 18, (LEFT), AND LAYER 24 (RIGHT).

7.4 SUMMARY MAPS

To condense the findings throughout this section a qualitative map of the design space was generated. It indicates which parameter combinations provide the best process window for deposition of the initial layer of WC-Ni onto a Ti-6Al-4V substrate. The goal of the illustration in Figure 7-25 is to suggest a parameter range that is transferrable to different laser additive manufacturing technologies for this coating purpose. Table 7-9 includes a legend describing the colour coding utilised in the summary and gives insight to how the classification is achieved.

Tables 7-4 and 7-8 were used to determine if a desirable (+) or undesirable (-) response was recorded for the three investigated coating characteristics at each layer. Namely, the WC surface presence, surface quality of layers and the diffusion of deposited materials into the substrate. These qualitative gradings resulted in eight possible combinations that layers may be subject to.

TABLE 7-9: LEGEND EXPLAINING THE COLOUR CODING USED IN FIGURE 68

Legend								
WC Surface Presence	+	+	-	+	-	+	-	-
Surface Quality	+	-	+	+	-	-	+	-
Substrate diffusion	+	+	+	-	+	-	-	-

Higher energy densities resulted in deeper penetration and good diffusion of the coating into the substrate but lacked sufficient presence of the coating material at the substrate surface. It was concluded that higher laser powers and high hatch spacings combined with intermediate scan speeds produced the most desirable coatings. This corresponded to depositions in the energy density range of 28,25 J/mm^3 and 57,69 J/mm^3.

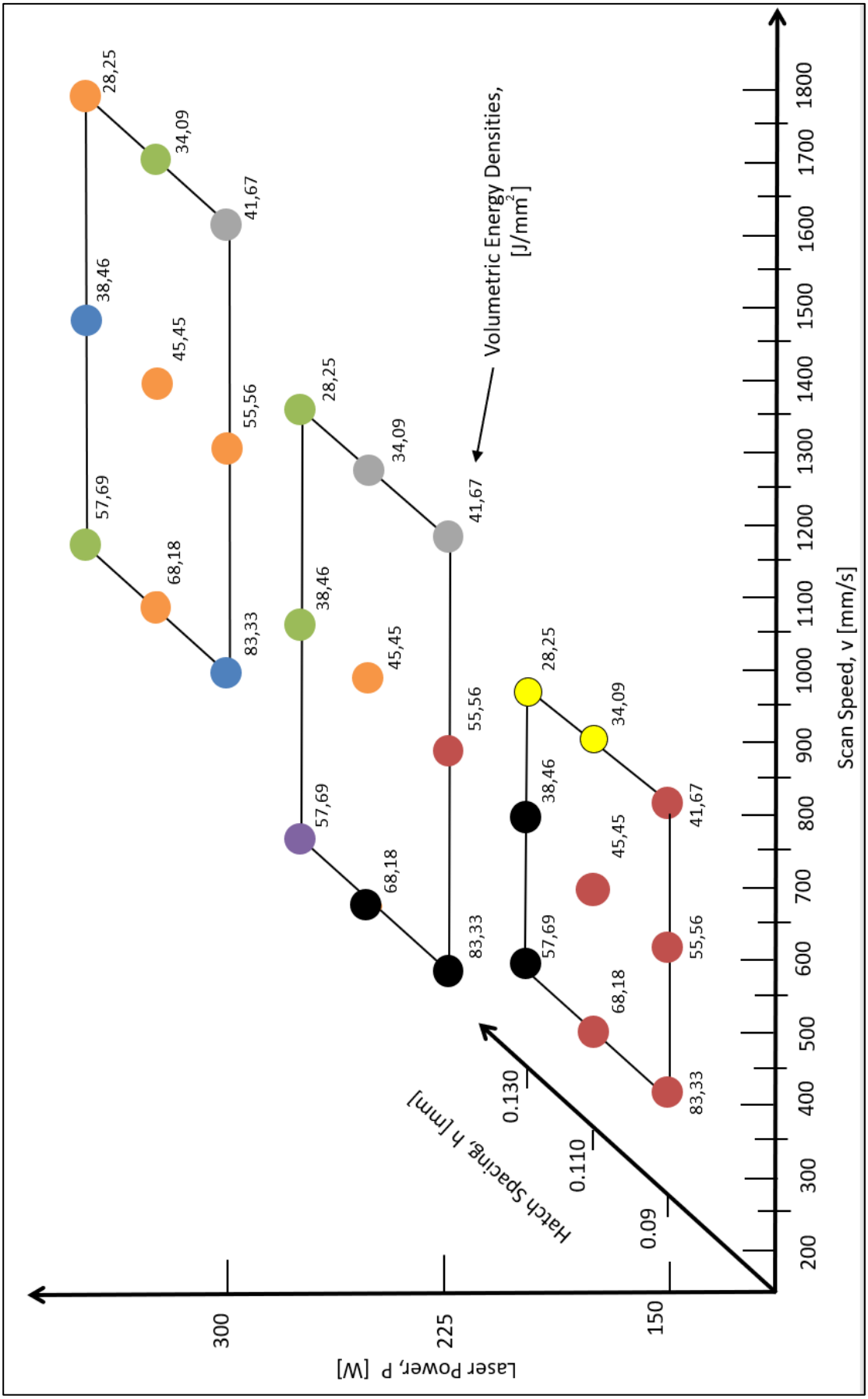

FIGURE 7-25: SUMMARY PLOT ILLUSTRATING A QUALITATIVE GUIDELINE FOR COATING QUALITY AT EACH PARAMETER COMBINATION THROUGHOUT THE EXPERIMENT

CHAPTER 8

8. CONCLUSION AND RECOMMENDATIONS

In this section, conclusions drawn throughout experimental chapters 5 – 7 will be discussed and translated into recommendations for future research.

8.1 CONCLUSION

8.1.1 MATERIAL ANALYSIS

The material analysis confirmed that the WC-Ni powder particles tend towards a spherical geometry, which improves the flowability of the material and eases the application of successive layers. In the estimation of the PSD, the particle sizes varied between 7µm and 58µm, which is a wider range than that specified by the OEM of 16µm - 53µm. The mean particle size was approximated at 28.32µm, indicating that most particles are below 50µm in diameter and that the powder will be suitable for processing at 50µm layer thicknesses. A prominent concern is that some particles appear to be hollow or include small cavities and may increase the porosity of depositions.

WC-Ni (10%) was selected for this study due to the availability of literature for its comparison with WC-Co powder. A concurrent note is that there was determined to be insufficient binder in the chosen material. The high temperatures required to achieve enough surface penetration and diffusion into the substrate were on the verge of nickel's evaporation temperature and resulted in material loss. In addition, the low binder content also brought about cracking at sample surfaces.

8.1.2 SINGLE TRACK SCREENING

In the screening experiment, 3 laser power levels (50W, 150W and 300W) were each evaluated at 8 different speeds to investigate an overall specific energy density range of 1.5 J/mm^2 – 16.67 J/mm^2. The surface quality of tracks was illustrated in a qualitative analysis in Figure 6-5. It was noted that the process window sensitivity is greater at lower laser powers. At 50W laser power, minimal increments in scan speed induced large variations in the measured responses. The effects of this process window sensitivity are illustrated in the steep trend in 50W iterations compared to the higher laser power iterations in Figures 6-7 and 6-11.

At 50W no tracks were of a desirable quality for further analysis and consisted of either pre-balling and broken geometries with irregular shape or were discontinuous and partially melted. Iterations throughout the screening experiment with straight continuous tracks and good surface qualities, were tracks 9, 10 and 11 at 150W, and 17,18,19 and 20 at 300W laser power.

Upon inspecting track width, the thickest tracks coincided with the highest specific energy densities at iterations 1, 2 and 3 conducted at 50W laser power. Though, none of the tracks in the 50W block were of good quality. The highest variability in track width occurred throughout iterations 9 - 16 in the 150W laser power block. The lowest track width variation occurred in the 300W block. Consistent with findings throughout literature, the statistical analysis concluded that speed has a more significant effect on the track width than that of laser power. The best quality tracks selected for further analysis ranged between 130µm and 180µm in width.

The microscope images of the single-track cross sections showed that the lowest average depth occurred in the 50W laser power grouping (48 µm), despite having far greater specific energy densities than iterations at higher laser powers. The average penetration depth of tracks at 150W and 300W were 75µm and 78µm,

respectively, this similarity reinforces the observation that process window sensitivity decreases at higher laser powers. Tracks 9 – 16 conducted at 150W had the most consistent depth throughout tracks lengths. Both laser power and scan speed were statistically significant contributors to the depth response, though as hypothesised in literature, laser power was far more significant.

A fully formed keyhole mode in penetration was found at iteration 9. This corresponded to a specific energy density of 7.5 J/mm^2. At the 300W-block, penetration modes were mainly conductive, with a tendency towards keyhole mode formation at iteration 17. This iteration was subject to the highest specific energy density in this block at 6 J/mm^2. In contrast, at 50W half of the tracks were conducted at energy densities greater than 7.5 J/mm^2 and consisted exclusively of conductive modes.

In the layered experiment, the single-track specific energy density of 7.5 J/mm^2 was investigated at 300W, and inspection of the cross section indicated that keyhole formation occurred. Therefore, iterations which initiate the vaporization of Ti-6Al-4V and allows for the transition to keyhole modes occurs between 6 J/mm^2 and 7.5 J/mm^2. This corresponds to surface temperatures of up 3287 °C which exceeds the melting point of tungsten carbide at 2870 °C.

The single-track screening proved that the ideal scan tracks with regards to track quality, width and penetration depth were achieved at experimental iterations 9, 10, 11, 17, 18, 19 & 20. These iterations were within the specific energy density range of 3.5 J/mm^2 to 7.5 J/mm^2 which was further investigated in layered depositions.

8.1.3 Layered Deposition Experiment

Throughout Chapter 7 the effects of process parameters on the quality of single layer depositions were inspected. Each of the three experimental blocks (150W, 225W and 300W) evaluated the exact same energy density repetitions, but varied parameter values to identify their effects on the response.

High levels of nickel evaporation occurred at all layers, which worsened the effects of the already insufficient binder content and the porosity of the power particles. Smoother layers correlated with deeper penetration into the substrate. This is attributable to increased melting of titanium at the surface, which induces a deeper molten pool. The molten Ti-6Al-4V acts as a binder material alternative to nickel and powder particles consolidated therein. At narrow hatch spacings and slower scan speeds, deeper penetration is present as a higher VED increases the probability of keyhole formation. Though it may be advised that keyhole formation should be avoided as it results in minimal presence of WC content at layer surfaces.

The parameter combinations of layers 1 – 9 in Block 1 did not produce desirable surface qualities and is the subset with the lowest overall WC-content present at the surfaces (0 wt.% - 12wt.%). No cracking was present in this block, but several layers were subject to excessive splatter of molten titanium and the formation of surface cavities due to material evaporation. The iterations in this block had the deepest penetration, which left most of the WC-Ni material submerged in the melt pool.

At iterations 10 – 18 in Block 2, there was a clear increase in the WC content at layer surfaces. This grouping portrayed a visible relationship between the effects of hatch spacing and scanning speeds on the WC surface presence. Wider hatch spacings accounted for a modest increasing trend in WC contents, and speed accounted for a sharp increase between iterations. The WC-contents in this group varied between 10wt.% and 40wt.%, with the highest contents recorded at lowest scan speed and highest hatch spacings.

At 300W laser power, layers had the most consistent WC surface presence and the highest overall average. The contents varied between 15wt.% and 30wt.%, though higher WC content also coincided with more surface cracking as a result of insufficient binder material and the porosity of powder particles. The statistical model concluded that laser power has the most significant effect on the WC surface content at layer surfaces.

High levels of cracking were observed in more than half the samples, especially prevalent in layers with large amounts of tungsten at the surface, therefore at layers with deeper diffusion into the substrate

cracking diminished. Cracks are more likely to initiate from the top of a layer around the first scan tracks and propagate perpendicular to the scan direction down the layer. The presence of cracking reduces further down from the top of the layers as the substrate is preheated by conduction of the laser energy.

At 300W (Block 3), the size of cracks increased with higher VED input, which correlates with literature as higher temperature gradients influence cracking. At iterations 13 – 18 in Block 2, identical VEDs were investigated, though crack size increases with decreasing energy densities. This is likely because higher WC surface content is present at these lower energy densities, and the lack of binder induces larger cracks.

By analysing the penetration of depositions into the substrate and measuring the total depth and interfusion zone depth, the data concluded that increasing VED values resulted in deeper penetration overall. Though parameter combinations that result in identical energy densities yielded different penetration depths when evaluated at each laser power. Those that incorporate higher laser powers tend to have less penetration. It is apparent that the speed increase required to keep the VED consistent is disproportionate to the actual effects in practice.

The clad zone height measurements were subject to the most inconsistency. Clad layers at the substrate surface contained alternating peaks and cavities between scans. The statistical model did not recognize enough trends to produce accurate predictions. This irregularity of the clad zone proves that successive layer depositions will be required when producing full coatings. The coating thickness, measured as the sum of the clad zone and interfusion zones, was more consistent at higher laser powers and scan speeds with better particle spread throughout the interface.

The EDS maps of layer cross sections provided insight to how deep WC-Ni particles penetrated the substrate, their degree of melting, and dispersion at the surface layer. The iterations with the best overall rating in these three metrics were layers 16, 17, 18, 19, 24 and 25, with exceptional properties at layers 16, 19 and 24.

Compositional line scans conducted on the cross sections of 6 tracks indicated increased rates of particle melting occurred at higher VED values, which also coincided with deeper penetration of particles. Marangoni effects were noticeable throughout all cross sections, especially prominent in those that with fully formed keyhole modes. Trails left by molten particles where more prominent Marangoni effects occurred brought about an even distribution of tungsten content throughout the penetration depth. Better dispersion of the coating material occurred at intermediate scan speeds and lower hatch spacings. Some degree of melting is required to allow for a denser layer at the surface, but at the expense of deeper penetration into the melt pool.

Finally, conclusions were summarised into a qualitative illustration in Figure 7-25 which proposes that optimal layer quality occurs at higher laser powers, high hatch spacings and intermediate scanning speeds. in the energy density range of 28,25 J/mm^3 and 57,69 J/mm^3. It is also a noteworthy conclusion from all aspects of experimentation in this study, that the specific energy density and volumetric energy density are not wholly reliable metrics for predicting scan track characteristics.

When inspecting the single-track quality, iterations with far higher specific energy density values resulted in sub-par quality scans compared to the repetitions at higher laser powers and lower energy densities. Furthermore, the three blocks wherein layered depositions were grouped consisted of identical VED values, and in spite thereof, the interactive effects of scan speed, hatch spacing, and laser power resulted in layers with varying characteristics. It is apparent that the speed increase required to maintain a consistent VED level at increased laser powers is too high to facilitate conditions for similar melt pool phenomenon. These findings coincide research by Prashanth et al [106], which evaluated the validity of the VED equation in practice. It is noticeable that the machine parameter with the most prominent effect on layer quality was the laser power and its interactive effect with scan speed.

8.2 RECOMMENDATIONS AND FUTURE WORK

This section aims to provide suggestions to improve the results and guide future investigation.

1. The binder content utilised in the WC-Ni powder should be increased to mitigate cracking and improve the flowability of the melt. This will aid in achieving better dispersion of particles at lower energy densities.

2. In further investigations, it is recommended that the spherical powder particles be solid and void of any porosities or cavities, as this contributed to coating irregularities and initiation of cracking.

3. The use of alternative layer scanning or re-scanning strategies should be investigated to minimize residual stresses that lead to cracking and deformation. This should be done while maintaining an energy density range wherein coatings will diffuse into the substrate and maintain enough surface presence of the WC material.

4. This study's aim was to identify process windows and investigate the effects of parameters on the coating/substrate interaction. Further analysis will have to include the deposition of successive layers to form denser coatings with a desirable finish. Only then can mechanical and thermal properties of the coating be investigated.

5. In future research the deposition of coatings onto titanium materials should occur in an inert argon atmosphere to mitigate contamination of surface layers with nitrogen.

6. This study concluded that in future research the volumetric energy density range investigated should be lowered. Intermediate substrate penetration provided the most suitable results and keyhole formation should be avoided.

7. It is advised that greater layer thicknesses be investigated, and the initial layer be applied with autonomous deposition technology. More surface material would reduce the trade-off between surface presence of the WC material and penetration into the substrate, while more even application of the powder would allow for better particle dispersion.

8. The use of nickel binder for the application of WC coatings shows promise should lower energy densities, higher binder content and larger layer thicknesses be employed. However, alternative binders should be investigated. Nickle's high vapour pressure may become a significant obstacle for processing coatings in practice, as it increases surface irregularities and processing chamber contamination.

SOURCES

[1] P. C. Pandey, “Engineering Applications of Composites Materials,” in *Module 11: Engineering Applications of Composite Materials*, 2011, pp. 1–89.

[2] R. D. Matthews, F. L. Rawlings, *Composite materials : engineering and science*. Cambridge: Woodhead publishing ltd., 1994.

[3] R. D. Farahani, M. Dubé, and D. Therriault, “Three-Dimensional Printing of Multifunctional Nanocomposites: Manufacturing Techniques and Applications.”

[4] D. J. De Beer, “Establishment of rapid prototyping / additive manufacturing in South Africa,” *J. South. African Inst. Min. Metal.*, vol. 111, no. MARCH, pp. 211–215, 2011.

[5] V. A. Tracey, “Nickel in hardmetals,” *Int. J. Refract. Met. Hard Mater.*, vol. 11, no. 3, pp. 137–149, 1992.

[6] R. Boyer, G. Welsch, and E. W. Collings, *Materials properties handbook : titanium alloys*. ASM International, 1994.

[7] C. Guo *et al.*, “Effects of WC-Ni content on microstructure and wear resistance of laser cladding Ni-based alloys coating,” *Surf. Coatings Technol.*, vol. 206, no. 8–9, pp. 2064–2071, 2012.

[8] A. C. van Staden, “A Fundamental Analysis on Additive Manufacturing of a Cemented Tungsten Carbide,” no. December, 2015.

[9] L. Thijs, F. Verhaeghe, T. Craeghs, J. Van Humbeeck, and J. P. Kruth, “A study of the microstructural evolution during selective laser melting of Ti-6Al-4V,” *Acta Mater.*, vol. 58, no. 9, pp. 3303–3312, 2010.

[10] D. . Pham and R. . Gault, “A comparison of rapid prototyping technologies,” *Int. J. Mach. Tools Manuf.*, vol. 38, no. 10–11, pp. 1257–1287, Oct. 1998.

[11] J.-P. Kruth, M. C. Leu, and T. Nakagawa, “Progress in Additive Manufacturing and Rapid Prototyping,” *CIRP Ann. - Manuf. Technol.*, vol. 47, no. 2, pp. 525–540, 1998.

[12] A. C. Van Staden, “A Fundamental Analysis on Additive Manufacturing,” no. December, 2015.

[13] D. Hagedorn-Hansen, R. Cichon, M. B. Bezuidenhout, P. A. Hugo, and G. A. Oosthuizen, “Geometric Deviation of Hybrid Parts Produced by Selective Laser Melting,” *Rapid Prod. Dev. Assoc. South Africa*, pp. 1–9, 2015.

[14] R. I. Campbell, D. J. De Bee, and E. Pei, “Additive manufacturing in South Africa: building on the foundation,” vol. 17. pp. 156–162, 2011.

[15] Statista, “Value of the Additive Manufacturing (3D printing) Market worldwide from 2011 to 2021,” 2014. [Online]. Available: http://www.statista.com/statistics/261693/3d-printing-market-value-forecast/. [Accessed: 20-Jun-2016].

[16] E. Campbell, R.I. De Beer, D.J. Pei, “Additive manufacturing in South Africa: building on the foundations,” *Rapid Prototyp. J.*, vol. 17, no. 2, pp. 156–162, 2011.

[17] S. Van Der Berg, “Current poverty and income distribution in the context of South African history,” *Work. Pap. Dep. Econ. Bur. Econ. Res. Univ. Stellenbosch*, pp. 1–23, 2010.

[18] S. Wild, “SA joins 3D printing revolution,” *Mail & Guardian*. [Online]. Available:

http://mg.co.za/article/2014-09-26-sa-joins-3d-printing-revolution. [Accessed: 16-Mar-2016].

[19] F. Authors, “Rapid prototyping in South Africa : past , present and future.” 2012.

[20] R. I. Campbell and D. J. De Beer, “Rapid prototyping in South Africa: past, present and future,” *Rapid Prototyp. J.*, vol. 11, no. 4, pp. 260–265, 2005.

[21] B. Berman, “3-D printing: The new industrial revolution,” *Business Horizons*, vol. 55, no. 2, pp. 155–162, 2012.

[22] C. Aligner, I. Transcribed, S. Dna, S. Nucleotide, P. Snp, and S. N. P. Ssr, “improvements in the capability profile of 3-d printing: an update,” vol. 16, no. 2, pp. 295–300, 2014.

[23] D. Dimitrov, K. Schreve, N. de Beer, and P. Chritiane, “Three dimensional printing in the South African industrial environment,” *South African Journal …*, vol. 19, no. May 2008. pp. 195–213, 2008.

[24] C. Tuck, R. J. M. Hague, and N. D. Burns, “Rapid manufacturing impact on supply chain methodologies and practice,” *Int. J. Serv. Oper. Manag.*, vol. 3, no. 1, pp. 1–22, 2007.

[25] S. H. Huang, P. Liu, A. Mokasdar, and L. Hou, “Additive manufacturing and its societal impact: A literature review,” *International Journal of Advanced Manufacturing Technology*, vol. 67, no. 5–8. pp. 1191–1203, 2013.

[26] Y. Luo, Z. Ji, M. C. Leu, and R. Caudill, “Environmental Performance Analysis of Solid Freeform Fabrication Processes,” *Int. Symp. Electron. Environ.*, pp. 1–6, 1999.

[27] ATKINS, “Manufacturing a low carbon footprint,” 2007.

[28] A. Drizo and J. Pegna, “Environmental impacts of rapid prototyping: an overview of research to date,” *Rapid Prototyping Journal.*, vol. 12, no. 2, pp. 64–71, Mar. 2006.

[29] G. Janaki Ram, C. Robinson, Y. Yang, and B. Stucker, “Rapid Prototyping Journal Use of ultrasonic consolidation for fabrication of multi-material structures) "Use of ultrasonic consolidation for fabrication of multi-material"Integrating stereolithography and direct print technologies for 3D structu,” *Rapid Prototyp. J. Rapid Prototyp. J. Iss Rapid Prototyp. J.*, vol. 13, no. 03, 2010.

[30] S. L. Campanelli, N. Contuzzi, A. Angelastro, and A. D. Ludovico, “Capabilities and Performances of the Selective Laser Melting Process,” *ew Trends Technol. Devices, Comput. Commun. Ind. Syst.*, p. Chapter 13, 2010.

[31] D. . Pham and R. . Gault, “A comparison of rapid prototyping technologies,” *Int. J. Mach. Tools Manuf.*, vol. 38, no. 10–11, pp. 1257–1287, 1998.

[32] A. Bandyopadhyay, B. V. Krishna, W. Xue, and S. Bose, “Application of Laser Engineered Net Shaping (LENS) to manufacture porous and functionally graded structures for load bearing implants,” in *Journal of Materials Science: Materials in Medicine*, 2009, vol. 20, no. SUPPL. 1.

[33] F. Weng, C. Chen, and H. Yu, “Research status of laser cladding on titanium and its alloys: A review,” *Mater. Des.*, vol. 58, no. November, pp. 412–425, 2014.

[34] K. Maeda and T. H. C. Childs, “Laser sintering (SLS) of hard metal powders for abrasion resistant coatings,” *J. Mater. Process. Technol.*, vol. 149, no. 1–3, pp. 609–615, 2004.

[35] S. Bremen, W. Meiners, and A. Diatlov, “Selective Laser Melting. A manufacturing technology for the future?,” *Laser Tech. J.*, vol. 9, pp. 33–38, 2012.

[36] J. Kruth and P. Mercelis, “Binding mechanisms in selective laser sintering and selective laser melting,” *Rapid Prototyping Journal*, vol. 11, no. 1. pp. 44–59, 2005.

[37] D. D. Gu, W. Meiners, K. Wissenbach, and R. Poprawe, “Laser additive manufacturing of metallic components: materials, processes and mechanisms,” *Int. Mater. Rev.*, vol. 57, no. 3, pp. 133–164, 2012.

[38] C. Hauser, T. H. . Childs, C. Taylor, and M. Badrossamay, “Direct Selective Laser Sintering of Tool Steel Powders to High Density. Part A: Effects of Lasr Beam Width and Scan Strategy,” *14th Proc. Solid Free. Fabr. Symp.*, p. 12, 2003.

[39] E. Toyserkani, A. Khajepour, and S. Corbin, *Laser Cladding*, vol. 119. CRC Press, 2004.

[40] S. Nowotny, A. Richter, and K. Tangermann, “Surface Protection of Light Metals by One-Step Laser Cladding with Oxide Ceramics.”

[41] C. Leyens, F. Brückner, E. Lopez, and M. Riede, “Successes and Challenges of SLM and LMD for Industrial Production,” vol. 49, no. Il, 2017.

[42] I. Gurrappa, “Characterization of titanium alloy Ti-6Al-4V for chemical, marine and industrial applications,” *Mater. Charact.*, vol. 51, no. 2, pp. 131–139, 2003.

[43] M. J. Donachie, *Titanium : a technical guide*. ASM International, 2000.

[44] D. Hagedorn-Hansen, “The Effects of Developed Selective Laser Melting Strategies on Titanium Hybrid Parts by,” no. March, pp. 1–117, 2017.

[45] W. D. Callister and D. G. Rethwisch, *Materials Science and Engineering Materials Science and Engineering*, 9th Editio. Wiley, 2013.

[46] G. Lütjering, J. C. Williams, and A. Gysler, “MICROSTRUCTURE AND MECHANICAL PROPERTIES OF TITANIUM ALLOYS,” in *Microstructure and Properties of Materials*, WORLD SCIENTIFIC, 2000, pp. 1–77.

[47] Y. C. Lin, B. H. Yan, and Y. S. Chang, “Machining characteristics of titanium alloy (Ti–6Al–4V) using a combination process of EDM with USM,” *J. Mater. Process. Technol.*, vol. 104, no. 3, pp. 171–177, 2000.

[48] J. H. Zuo, Z. G. Wang, and E. H. Han, “Effect of microstructure on ultra-high cycle fatigue behavior of Ti–6Al–4V,” *Mater. Sci. Eng. A*, vol. 473, no. 1, pp. 147–152, 2008.

[49] A. Hasçalık and U. Çaydaş, “Electrical discharge machining of titanium alloy (Ti–6Al–4V),” *Appl. Surf. Sci.*, vol. 253, no. 22, pp. 9007–9016, 2007.

[50] H. Nortjé, “An Investigation of Fretting Wear in Aerospace Applications by,” no. December, 2011.

[51] E. Labban, H. F, E. R. I, and A. Wadai, “Laser cladding of Ti - 6Al - 4V alloy with vanadium carbide particles,” pp. 159–167, 2014.

[52] S. Yang, N. Chen, W. Liu, M. Zhong, Z. Wang, and H. Kokawa, “Fabrication of nickel composite coatings reinforced with TiC particles by laser cladding,” *Surf. Coatings Technol.*, vol. 183, no. 2, pp. 254–260, 2004.

[53] S. Kumar and J.-P. Kruth, “Composites by Rapid Prototyping Technology,” *Mater. Des.*, vol. 31, no. 2, pp. 850–856, 2010.

[54] C. M. Fernandes and A. M. R. Senos, “Cemented carbide phase diagrams: A review,” *Int. J. Refract. Met. Hard Mater.*, vol. 29, no. 4, pp. 405–418, 2011.

[55] Z. Yao, J. Stiglich, and T. S. Sudarshan, “WC-Co enjoys proud history and bright future,” *Met. Powder Rep.*, vol. 53, no. 2, pp. 32–36, 1998.

[56] N. Magnusson and Schmidt, “Understanding cemented carbides,” *Sandvik*, p. 20, 2008.

[57] N. M. PARIKH and M. HUMENIK, “Cermets: II, Wettability and Microstructure Studies in Liquid???Phase Sintering,” *J. Am. Ceram. Soc.*, vol. 40, no. 9, pp. 315–320, 1957.

[58] V. A. Tracey, “Nickel in hardmetals,” *Int. J. Refract. Met. Hard Mater.*, vol. 11, no. 3, pp. 137–149, Jan. 1992.

[59] “Engineering ToolBox,” 2001. [Online]. Available: https://www.engineeringtoolbox.com. [Accessed: 12-Jun-2018].

[60] A. Fernández Guillermet, “The Co-Fe-Ni-W-C Phase Diagram: A Thermodynamic Description and Calculated Sections for (Co-Fe-Ni) Bonded Cemented WC Tools,” *Zeitschrift für Met.*, vol. 80, no. 2, pp. 83–94, 1989.

[61] T. O. F. Contents, “International journal of refractory metals and hard materials,” *International Journal of Refractory Metals and Hard Materials*. pp. 1–11, 2011.

[62] D. Q. Zhang, Z. H. Liu, Q. Z. Cai, J. H. Liu, and C. K. Chua, “Influence of Ni content on microstructure of W-Ni alloy produced by selective laser melting,” *Int. J. Refract. Met. Hard Mater.*, vol. 45, pp. 15–22, Jul. 2014.

[63] D. Q. Zhang, Z. H. Liu, Q. Z. Cai, J. H. Liu, and C. K. Chua, “Influence of Ni content on microstructure of W-Ni alloy produced by selective laser melting,” *Int. J. Refract. Met. Hard Mater.*, vol. 45, pp. 15–22, 2014.

[64] J. Beddoes and M. J. Bibby, *Principles of Metal Manufacturing Processes*. Arnold, 1999.

[65] R. Asthana, A. Kumar, and N. Dahotre, *Materials Processing and Manufacturing Science*. 2006.

[66] B. Wittmann, W. D. Schubert, and B. Lux, “WC grain growth and grain growth inhibition in nickel and iron binder hardmetals,” *Int. J. Refract. Met. Hard Mater.*, vol. 20, no. 1, pp. 51–60, 2002.

[67] Federal Carbide Company, “Tungsten Carbide and Tungsten Carbide Components by Federal Carbide.” [Online]. Available: https://www.federalcarbide.com/tungsten_carbide.html. [Accessed: 27-Jul-2018].

[68] S. Sharafat, A. Kobayashi, S. Chen, and N. M. Ghoniem, “Production of high-density Ni-bonded tungsten carbide coatings using an axially fed DC-plasmatron,” *Surf. Coatings Technol.*, vol. 130, no. 2–3, pp. 164–172, 2000.

[69] J. Verwimp, M. Rombouts, E. Geerinckx, and F. Motmans, “Applications of laser cladded WC-based wear resistant coatings,” in *Physics Procedia*, 2011, vol. 12, no. PART 1, pp. 330–337.

[70] S. D. Guest, A. P. Gerlich, and P. F. Mendez, “Depositing Ni-WC wear resistant coatings with hot-wire assisted Oil Sands and Wear,” pp. 1–15, 2011.

[71] S. Y. Ahn, S. W. Kim, and S. Kang, “Microstructure of Ti(CN)-WC-NbC-Ni Cermets,” *J. Am. Ceram. Soc.*, vol. 84, no. 4, pp. 843–849, 2001.

[72] N. Eliaz, T. M. Sridhar, and E. Gileadi, “Synthesis and characterization of nickel tungsten alloys by electrodeposition,” *Electrochim. Acta*, vol. 50, no. 14, pp. 2893–2904, May 2005.

[73] R. Li, Y. Shi, J. Liu, Z. Xie, and Z. Wang, “Selective laser melting W-10 wt.% Cu composite powders,” *Int. J. Adv. Manuf. Technol.*, vol. 48, no. 5–8, pp. 597–605, 2010.

[74] I. Yadroitsev and I. Smurov, “Selective laser melting technology: From the single laser melted track stability to 3D parts of complex shape,” *Phys. Procedia*, vol. 5, no. PART 2, pp. 551–560, 2010.

[75] M. F. Zaeh and M. Ott, “Investigations on heat regulation of additive manufacturing processes for metal structures,” *CIRP Ann. - Manuf. Technol.*, vol. 60, no. 1, pp. 259–262, 2011.

[76] D. Zhang, Q. Cai, J. Liu, J. He, and R. Li, “Microstructural evolvement and formation of selective laser melting W-Ni-Cu composite powder,” *Int. J. Adv. Manuf. Technol.*, vol. 67, no. 9–12, pp. 2233–2242, 2013.

[77] A. C. Van Staden, D. Hagedorn-Hansen, G. A. Oosthuizen, and N. Sacks, “Characteristics of single layer Selective Laser Melted tool grade cemented tungsten carbide,” *Int. Conf. Compet. Manuf. COMA ’16*, pp. 141–146, 2016.

[78] H. Exner *et al.*, “Laser micro sintering: A new method to generate metal and ceramic parts of high resolution with sub-micrometer powder,” *Virtual Phys. Prototyp.*, vol. 3, no. 1, pp. 3–11, 2008.

[79] L. E. Murr *et al.*, “Metal Fabrication by Additive Manufacturing Using Laser and Electron Beam Melting Technologies,” *J. Mater. Sci. Technol.*, vol. 28, no. 281, pp. 1–14, 2012.

[80] D. Gu, Y. Shen, P. Dai, and M. Yang, “Microstructure and property of sub-micro WC-10 %Co particulate reinforced Cu matrix composites prepared by selective laser sintering,” *Trans. Nonferrous Met. Soc. China*, vol. 16, no. 2, pp. 357–362, 2006.

[81] D. Zhang, Q. Cai, and J. Liu, “Formation of nanocrystalline tungsten by selective laser melting of tungsten powder,” *Mater. Manuf. Process.*, vol. 27, no. 12, pp. 1267–1270, 2012.

[82] E. Yasa and J. Kruth, “Application of Laser Re-Melting on Selective Laser Melting Parts,” *Adv. Prod. Eng. Manag.*, vol. 6, no. 4, pp. 259–270, 2011.

[83] D. D. Gu, W. Meiners, K. Wissenbach, and R. Poprawe, “Laser additive manufacturing of metallic components: materials, processes and mechanisms,” *Int. Mater. Rev.*, vol. 57, no. 3, pp. 133–164, May 2012.

[84] R. Glardonl, N. Karapatisl, and V. Romanoz, “Influence of Nd : YAG Parameters on the Selective Laser Sintering of Metallic Powders,” *Manuf. Technol. J.*, vol. 50, no. 1, pp. 133–136, 2001.

[85] A. Simchi, “Direct laser sintering of metal powders: Mechanism, kinetics and microstructural features,” *Mater. Sci. Eng. A*, vol. 428, no. 1–2, pp. 148–158, 2006.

[86] D. Gu and Y. Shen, “Balling phenomena in direct laser sintering of stainless steel powder: Metallurgical mechanisms and control methods,” *Mater. Des.*, vol. 30, no. 8, pp. 2903–2910, 2009.

[87] J. Jhabvala, E. Boillat, T. Antignac, and R. Glardon, “On the effect of scanning strategies in the selective laser melting process,” *Virtual Phys. Prototyp.*, vol. 5, no. 2, pp. 99–109, 2010.

[88] V. Manvatkar, A. De, and T. DebRoy, “Spatial variation of melt pool geometry, peak temperature and solidification parameters during laser assisted additive manufacturing process,” *Mater. Sci. Technol.*, vol. 31, no. 8, pp. 924–930, 2015.

[89] H. Hassanin, F. Modica, M. A. El-Sayed, J. Liu, and K. Essa, “Manufacturing of Ti–6Al–4V Micro-Implantable Parts Using Hybrid Selective Laser Melting and Micro-Electrical Discharge Machining,” *Adv. Eng. Mater.*, vol. 18, no. 9, pp. 1544–1549, 2016.

[90] J. Butler, “Using selective laser sintering for manufacturing,” *Assem. Autom.*, vol. 31, no. 3, pp. 212–219, 2011.

[91] I. Yadroitsev, A. Gusarov, I. Yadroitsava, and I. Smurov, “Single track formation in selective laser melting of metal powders,” *J. Mater. Process. Technol.*, vol. 210, no. 12, pp. 1624–1631, Sep. 2010.

[92] E. C. Santos, M. Shiomi, K. Osakada, and T. Laoui, “Rapid manufacturing of metal components by

laser forming," *Int. J. Mach. Tools Manuf.*, vol. 46, no. 12–13, pp. 1459–1468, 2006.

[93] S. Kumar, "Manufacturing of WC-Co moulds using SLS machine," *J. Mater. Process. Technol.*, vol. 209, no. 8, pp. 3840–3848, 2009.

[94] C. P. Paul and A. Khajepour, "Automated laser fabrication of cemented carbide components," *Opt. Laser Technol.*, vol. 40, no. 5, pp. 735–741, 2008.

[95] B. Vrancken, "Study of Residual Stresses in Selective Laser Melting," *PhD Thesis; KU Leuven Arenb. Dr. Sch. Fac. Eng. Sci.*, no. June, pp. 1–253, 2016.

[96] M. F. Zaeh and G. Branner, "Investigations on residual stresses and deformations in selective laser melting," *Prod. Eng.*, vol. 4, no. 1, pp. 35–45, Feb. 2010.

[97] X. Wang, K. S. Hwang, M. Koopman, Z. Z. Fang, and L. Zhang, "Mechanical properties and wear resistance of functionally graded WC-Co," *Int. J. Refract. Met. Hard Mater.*, vol. 36, pp. 46–51, 2013.

[98] D. Wang, Y. Yang, X. Su, and Y. Chen, "Study on energy input and its influences on single-track,multi-track, and multi-layer in SLM," *Int. J. Adv. Manuf. Technol.*, vol. 58, no. 9–12, pp. 1189–1199, 2012.

[99] M. Rombouts, J. P. Kruth, L. Froyen, and P. Mercelis, "Fundamentals of selective laser melting of alloyed steel powders," *CIRP Ann. - Manuf. Technol.*, vol. 55, no. 1, pp. 187–192, 2006.

[100] W. T. Kwon, J. S. Park, S. W. Kim, and S. Kang, "Effect of WC and group IV carbides on the cutting performance of Ti(C,N) cermet tools," *Int. J. Mach. Tools Manuf.*, vol. 44, no. 4, pp. 341–346, 2004.

[101] H.-O. Andrén, "Microstructures of cemented carbides," *Mater. Des.*, vol. 22, no. 6, pp. 491–498, 2001.

[102] I. Yadroitsev, L. Thivillon, P. Bertrand, and I. Smurov, "Strategy of manufacturing components with designed internal structure by selective laser melting of metallic powder," *Appl. Surf. Sci.*, vol. 254, no. 4, pp. 980–983, 2007.

[103] N. K. Tolochko *et al.*, "Balling processes during selective laser treatment of powders," *Rapid Prototyp. J.*, vol. 10, no. 2, pp. 78–87, 2004.

[104] W. E. King *et al.*, "Observation of keyhole-mode laser melting in laser powder-bed fusion additive manufacturing," *J. Mater. Process. Tech.*, vol. 214, pp. 2915–2925, 2014.

[105] S. Ločs and I. Boiko, "Quality assessment of laser cladded HSS coatings with deep penetration into base material to obtain a smooth gradient of properties in coating-substrate interface," *Agron. Res.*, vol. 16, no. Special Issue 1, pp. 1095–1109, 2018.

[106] K. G. Prashanth, S. Scudino, T. Maity, J. Das, and J. Eckert, "Is the energy density a reliable parameter for materials synthesis by selective laser melting?," *Mater. Res. Lett.*, vol. 5, no. 6, pp. 386–390, 2017.

[107] O. Eso, Z. Fang, and A. Griffo, "Liquid phase sintering of functionally graded WC-Co composites," in *International Journal of Refractory Metals and Hard Materials*, 2005, vol. 23, no. 4–6 SPEC. ISS., pp. 233–241.

[108] C. H. Allibert, "Sintering features of cemented carbides WC ± Co processed from ® ne powders," *Int. J. Refract. Metals Hard Mater.*, vol. 19, pp. 53–61, 2001.

[109] L. N. Carter, C. Martin, P. J. Withers, and M. M. Attallah, "The influence of the laser scan strategy on grain structure and cracking behaviour in SLM powder-bed fabricated nickel superalloy," *J. Alloys Compd.*, vol. 615, pp. 338–347, Dec. 2014.

[110] J.-P. Kruth, J. Deckers, E. Yasa, and R. Wauthle, “Assessing and comparing influencing factors of residual stresses in selective laser melting using a novel analysis method,” *Proc. Inst. Mech. Eng. Part B J. Eng. Manuf.*, vol. 226, no. 6, pp. 980–991, 2012.

[111] M. Agarwala, D. Bourell, J. Beaman, H. Marcus, and J. Barlow, “Direct selective laser sintering of metals,” *Rapid Prototyp. J.*, vol. 1, no. 1, pp. 26–36, 1995.

[112] K. A. Mumtaz, P. Erasenthiran, and N. Hopkinson, “High density selective laser melting of Waspaloy?,” *J. Mater. Process. Technol.*, vol. 195, no. 1–3, 2008.

[113] M. Shiomi, K. Osakada, K. Nakamura, T. Yamashita, and F. Abe, “Residual Stress within Metallic Model Made by Selective Laser Melting Process,” *CIRP Ann. - Manuf. Technol.*, vol. 53, no. 1, pp. 195–198, 2004.

[114] M. C. Sinirlioglu, “Rapid Manufacturing of Dental and Medical Parts via LaserCUSING Technology using Titanium and CoCr Powder Materials,” *US-Turkey Work. Rapid Technol.*, pp. 89–92, 2009.

[115] D. Q. Zhang, Q. Z. Cai, J. H. Liu, L. Zhang, and R. D. Li, “Select laser melting of W-Ni-Fe powders: Simulation and experimental study,” *Int. J. Adv. Manuf. Technol.*, vol. 51, no. 5–8, pp. 649–658, 2010.

[116] D. S. Rickerby, “A review of the methods for the measurement of coating-substrate adhesion,” *Surf. Coatings Technol.*, vol. 36, no. 1–2, pp. 541–557, 1988.

[117] M. Eosint, “Technical Description EOSINT M 280 Technical description Technical Description EOSINT M 280,” *Eos (Washington. DC).*, no. December, pp. 1–33, 2010.

[118] “Laser sintering system EOSINT M 280 for the production of tooling inserts , prototype parts and end products directly in metal The Technology : Laser sintering - the Key to e-Manufacturing.”

[119] EOS, “Eosint M 280,” *Web page*, pp. 1–3, 2014.

[120] “PST_Powders_Solutions_Catalog_2014 (1).pdf.” .

[121] L. J. Prakash, “Application of fine grained tungsten carbide based cemented carbides,” *Int. J. Refract. Met. Hard Mater.*, vol. 13, no. 5, pp. 257–264, 1995.

[122] B. Liu, R. Wildman, C. Tuck, I. Ashcroft, and R. Hague, “Investigation the Effect of Particle Size Distribution on Processing Parameters Optimisation in Selective Laser Melting Process,” *Sff*, no. mm, pp. 227–238, 2011.

[123] N. SEMATECH, *NIST Engineering statistics handbook*. 2003.

[124] J. Antony, *Design of Experiments for Engineers and Scientists*, no. October. 2003.

[125] M. Cavazzuti, *Optimization methods: From theory to design scientific and technological aspects in mechanics*. 2013.

[126] R. H.Myers, D. C.Montgomery, and C. Anderson-Cook, M, *Response Surface Methodology: Process and Product Optimization Using Designed Experiments*. 2016.

[127] R. M. De Baun, S. Technometrics, and N. Feb, “American Society for Quality Response Surface Designs for Three Factors at Three Levels American Society for Quality Stable URL : http://www.jstor.org/stable/1266305 Linked references are available on JSTOR for this article : Response Surface Designs for ,” vol. 1, no. 1, pp. 1–8, 2018.

[128] “Pickling and Descaling - ASM International.” [Online]. Available: https://www.asminternational.org/news/-/journal_content/56/10192/ASMHBA0001229/BOOK-

ARTICLE. [Accessed: 19-Aug-2018].

[129] J. P. Kruth, B. Van der Schueren, J. E. Bonse, and B. Morren, “Basic Powder Metallurgical Aspects in Selective Metal Powder Sintering,” *CIRP Ann. - Manuf. Technol.*, vol. 45, no. 1, pp. 183–186, 1996.

[130] D. Tang, “Effect of substrate preheating temperature and coating thickness on residual stress in plasma sprayed hydroxyapatite coating,” *IOP Conf. Ser. Mater. Sci. Eng.*, vol. 87, no. 1, 2015.

[131] P. Yuan and D. Gu, “Molten pool behaviour and its physical mechanism during selective laser melting of TiC/AlSi10Mg nanocomposites: Simulation and experiments,” *J. Phys. D. Appl. Phys.*, vol. 48, no. 3, 2015.

[132] T. A. Campbell and O. S. Ivanova, “3D printing of multifunctional nanocomposites,” *Nano Today*, vol. 8, pp. 119–120, 2013.

[133] L. Lu, J. Fuh, and Y. S. Wong, *Laser-induced materials and processes for rapid prototyping*. Massachusetts 02061: Kluwer Academic Publishers, 2001.

[134] Karalekas D and Antoniou K., “Composite rapid prototyping: overcoming the drawback of poor mechanical properties,” *J Mat Pro Techno*, pp. 526–30, 2004.

[135] D. Klosterman, R. Chartoff, G. G., O. N., and P. B., “Interfacial characteristics of composites fabricated by laminated object manufacturing,” in *Composites Part A*, 1998, no. 29, pp. 1165–74.

[136] S. Onagoruwa, S. Bose, and A. Bandyopadhyay, “Fused deposition of ceramics (FDC) and composites,” in *Proceedings of Solid Freeform Fabrication Symposium*, 2001, pp. 224–231.

[137] R. W. Gray IV, D. G. Baird, and J. H. Bohn, “Effects of processing conditions on short TLCP fiber reinforced FDM parts,” *Rapid Proto J*, vol. 4, no. 1, pp. 14–25, 1998.

[138] P. Johansson, R. Jimbo, Y. Naito, P. Kjellin, F. Currie, and A. Wennerberg, “Polyether ether ketone implants achieve increased bone fusion when coated with nano-sized hydroxyapatite: a histomorphometric study in rabbit bone.,” *Int. J. Nanomedicine*, vol. 11, pp. 1435–42, 2016.

[139] I. Shishkovsky, I. Yadroitsev, P. Bertrand, and I. Smurov, “Alumina–zirconium ceramics synthesis by selective laser sintering/melting,” *Appl. Surf. Sci.*, vol. 254, no. 4, pp. 966–970, Dec. 2007.

[140] T. Alexandre, J. Giovanola, S. Vaucher, O. Beffort, and U. Vogt, “Layered manufacturing of porous ceramic parts from ceramic powders and preceramic polymers.,” pp. 497–504, 2004.

[141] D. Dimitrov, K. Schreve, and N. de Beer, “Advances in three dimensional printing – state of the art and future perspectives,” *Rapid Prototyp. J.*, vol. 12, no. 3, pp. 136–147, 2006.

[142] L. J. Wozniak, Graulet, Hazany, Kata D, “Highly loaded UV curable nanosilica dispersions for rapid prototyping applications.,” *J Euro Ceram. Soc*, vol. 29, no. 11, p. 2259–65., 2009.

[143] D. Hotza, C. M. Gomes, and J. G??nster, “Advances in additive manufacturing processes and materials,” *Adv. Mech. Eng.*, vol. 2014, 2014.

[144] S. K. Jing, G. H. Song, J. H. Liu, J. T. Zhou, and H. Zhang, “A Review of Product Design for Additive Manufacturing,” in *Applied Mechanics and Materials*, vol. 635–637, Trans Tech Publ, 2014, pp. 97–100.

[145] T. Grim, *Users Guide to Rapid Prototyping*. Society of Manufacturing Engineeers, 2004.

[146] I. Campbell, D. Bourell, and I. Gibson, “Additive manufacturing: rapid prototyping comes of age,” *Rapid Prototyp. J.*, vol. 18, no. 4, pp. 255–258, Jun. 2012.

[147] H. A. Hegab, “Design for additive manufacturing of composite materials and potential alloys: a

review," *Manuf. Rev.*, vol. 3, p. 11, 2016.

APPENDICES

APPENDIX A: PROJECT FINANCIALS

Table A-1 below includes a cost estimate of the project. The amounts are based on quotes and expenses realised in this study and was divided into costs related to experimentation, analysis, and logistics.

TABLE A-1: SUMMARY OF PROJECT FINANCIALS FOR EXPERIMENTATION ANALYSIS AND LOGISTICS

Phase	Item	Supplier	Cost (ZAR)
Experimentation	Acquisition of WC-Ni powder	Weartech	6296.98
	Ti6al4V acquisition	Tifab	1515
	Ti6al4V Base Plate Machining	STC	7550
	SLS deposition	CRPM	9062
Analysis	SEM analysis	Central Analytical Facilities	6550
	Statistical analysis	Stellenbosch University	900
Logistics	Shipping cost	DHL	290
		Total Amount	**32163.98**

APPENDIX B: POWDER MATERIAL AND EQUIPMENT

This Appendix includes specifications for the equipment and materials used to produce parts and analyse the specimens. An Olympus GX 51 was used to inspect single-track and layer cross sections and a MERLIN field emission scanning electron microscope (FE-SEM) to inspect surface qualities and assemble EDS maps. Images of the apparatuses are included in Figure B-1 and B-2.

FIGURE B-1: OLYMPUS GX51 LIGHT MICROSCOPE

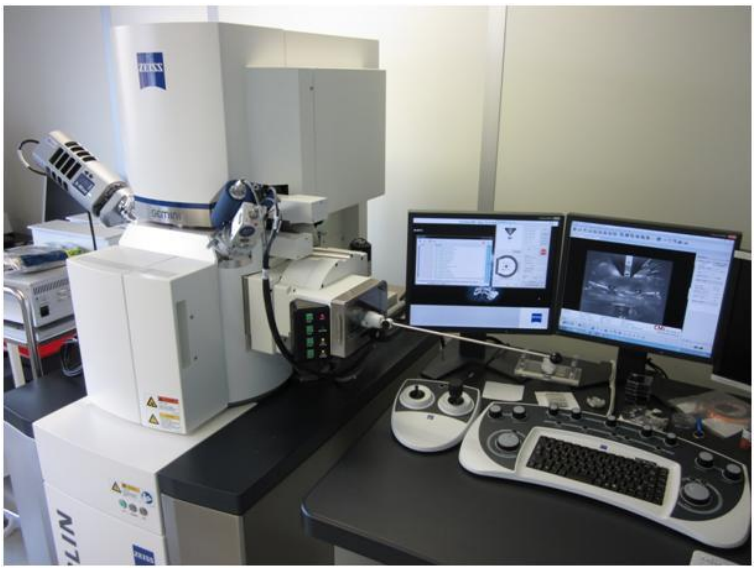

FIGURE B-2: MERLIN FE-SEM AT THE STELLENBOSCH CENTRAL ANALYTICAL FACILITIES

The product data sheets from original equipment manufacturers for the WC-Ni (WC-724/ 1310VF) powder material and the EOSINT M280 laser sintering system included below. The powder specifications consist of only an excerpt from the Praxair Surface Technology Powder Solutions catalogue, the entirety of the 43 page document is available in [120]. The brochure for the EOSINT M280 begins on page 129.

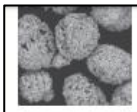

1343VM/WC-729-1

Carbide Powders

TUNGSTEN CARBIDE BASED POWDERS *(CONTINUED)*

Chemistry	Powder Name	Hall Flow / Density	Size	OEM Specs	Quick Facts
Co 16.8 C 5.2 W balance	WC-128-2	13 sec / 5.6 g/cc	-270 m / +20 µm (-53 / +20 µm)	CP 6004 DMR 33.019 MSRR 9507/1	• Sintered and crushed • Higher Co levels provide better toughness, impact strenth and ductility than WC-12Co • Densified structure promotes superior coating density and powder flow • Useful up to 900°F (482°C)
Co 16.8 C 5.2	WC-559	16 sec/ 4.0 g/cc W balance	-270 m / +20 µm (-53 / +20 µm)	B50TF167 CLA and CLC EMS 39660	• Plasma densified powder • Higher Co levels provide better toughness, impact strenth and ductility than WC-12Co • Densified structure promotes superior coating density and powder flow • Useful up to 900°F (482°C)
Co 17.0 C 5.0 W balance	WC-729 / 1343VF	neg. / 4.2 g/cc	-400 m / +11 µm (-38 / +11 µm)	PWA 36331-2 MSRR 9507/69	• Agglomerated and sintered • Higher Co levels provide better toughness, impact strenth and ductility than WC-12Co • Densified structure promotes superior coating density and powder flow • Excellent flowability • Useful up to 900°F (482°C)
	WC-729-1 / 1343VM	20 sec / 4.3 g/cc	-325 m / +16 µm (-45 / +16 µm)	ECS-L 2279 Annexe 1 BMS 10-67K Type I MSRR 9507/69 PWA 36331-1 AMS 7881 B50TF167 CLA	
	WC-729-5	--- / 4.7 g/cc	(-31 / +5.5 µm)	---	
Cr 20.0 Ni 6.3 C 5.9 W balance	WC-496	21 sec / 3.2 g/cc	-325 m / +16 µm (-45 / +16 µm)	MSV-067	• Sintered and crushed • Superior oxidation and corrosion properties than other WC-based materials • Better chemical resistance than other WC-based materials • Useful up to 1400°F (760°C)
Cr 20.0 Ni 6.5 C 5.8 W balance	WC-733 / 1356VM	20 sec / 4.4 g/cc	-325 m / +16 µm (-45 / +16 µm)	---	• Agglomerated and sintered • Similar properties as other WC-NiCr • Densified structure with fine carbide dispersion promotes finer microstructure, better DE, and denser, smoother coatings • Excellent flowability • Useful up to 1400°F (760°C)
Ni 10.0 C 5.5 W balance	WC-724 / 1310VF	19 sec / 4.5 g/cc	-325 m / +11 µm (-45 / +11 µm)	---	• Agglomerated and sintered • Better corrosion protection than WC-Co • Excellent low-temperature wear properties up to 900°F (482°C) • Superior deposition efficiency (DE)
	WC-724-1 / 1310VM	20 sec / 4.4 g/cc	-270 m / +16 µm (-53 / +16 µm)	---	
Ni 36.3 Cr 7.3 Fe 2.3 Si 2.3 B 1.6 WC-12Co balance	WC-735-1	22 sec / 4.3 g/cc	-270 m / +16 µm (-53 / +16 µm)	---	• Blended WC-12Co + NiCrSiFeB • Excellent combination of abrasion resistance and toughness • Economical solution to severe wear applications • Useful up to 900°F (482°C)

FIGURE B-3: AN EXCERPT FROM THE PRAXAIR SURFACE TECHNOLOGY POWDER SOLUTIONS CATALOGUE

Laser sintering system **EOSINT M 280**
for the production of tooling inserts, prototype parts
and end products directly in metal

Technical Data	
Building volume (including building platform)	250 mm x 250 mm x 325 mm (9.85 x 9.85 x 12.8 in)
Laser type	Yb-fibre laser, 200 W or 400 W (optional)
Precision optics	F-theta-lens, high-speed scanner
Scan speed	up to 7.0 m/s (23 ft./sec)
Variable focus diameter	100 - 500 µm (0.004 - 0.02 in)
Power supply	32 A
Power consumption	maximum 8.5 kW / typical 3.2 kW
Nitrogen generator	integrated
Compressed air supply	7,000 hPa; 20 m^3/h (102 psi; 706 ft^3/h)
Argon supply	4,000 hPa; 100 l/min (58 psi; 3.5 ft^3/min)
Dimensions (B x D x H)	
System	2,200 mm x 1,070 mm x 2,290 mm (86.6 x 42.1 x 90.1 in)
Recommended installation space	min. 4.8 m x 3.6 m x 2.9 m (189 x 142 x 114 in)
Weight	approx. 1,250 kg (2,756 lb)
Data preparation	
Software	EOS RP Tools; EOSTATE Magics RP (Materialise)
CAD interface	STL. Optional: converter for all standard formats
Network	Ethernet

APPENDIX C: SEM IMAGES OF WC-NI POWDER & PSD ANALYSIS

This Appendix includes the images generated by scanning electron microscopy of the WC-Ni powder, conducted to inspect the particle geometry and average diameter. These images were supplementary in the procedure mentioned in section 5.2 to estimate the particle size distribution. The 200X magnification image n Figure C-1 (c) was analysed in the ImageJ software suite. Here binary black and white images were generated and used to estimate the PSD. by use of equation 5.1. An example of the binary image is included in Figure C-2. Figure C – 3 provides the particle size distribution frequency plot obtained from a sample of 184 particles.

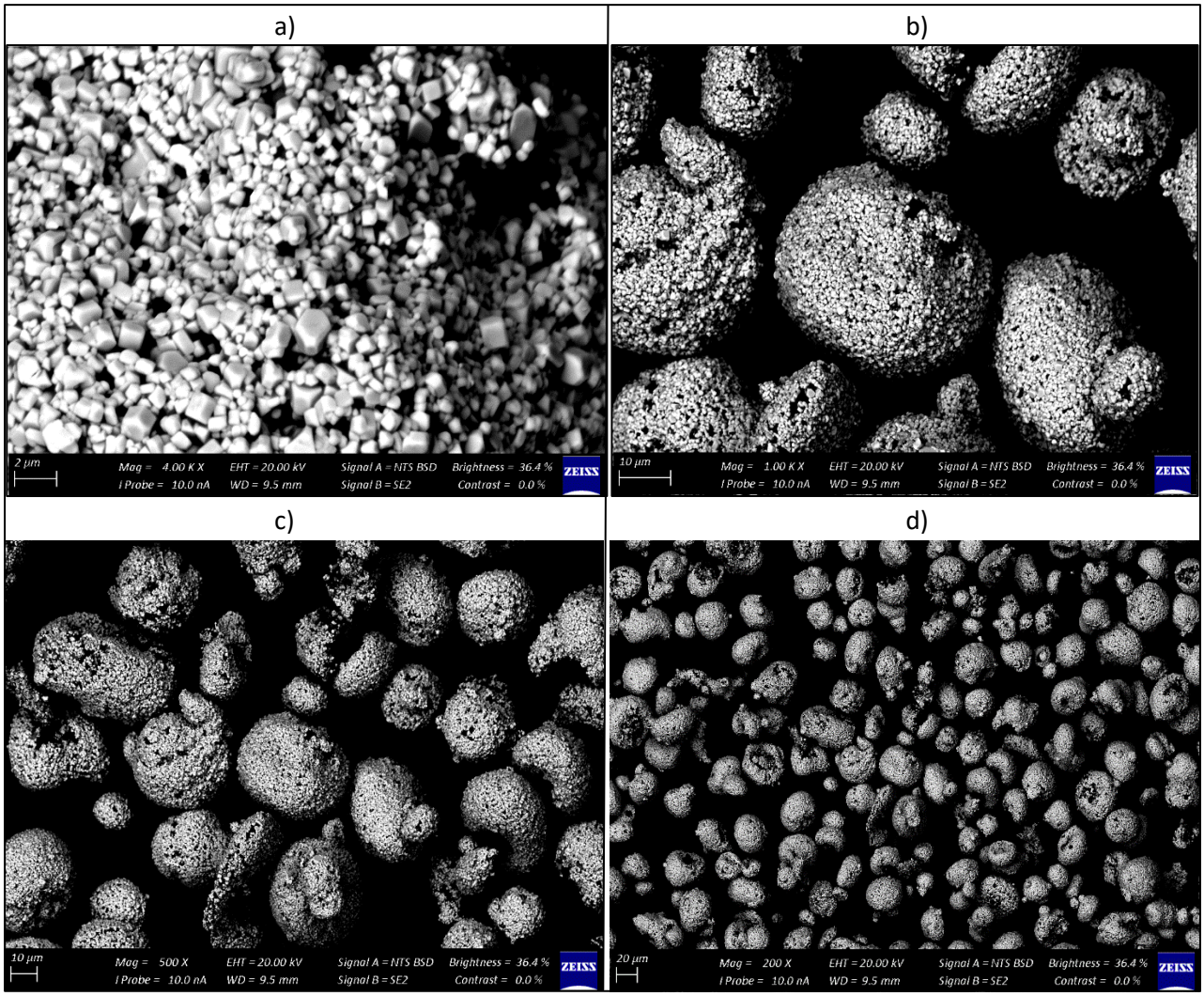

FIGURE C-1: SEM IMAGES OF THE WC-NI POWDER AT MAGNIFICATIONS: A) 4000X, B) 1000X, C) 500X, AND D) 200X.

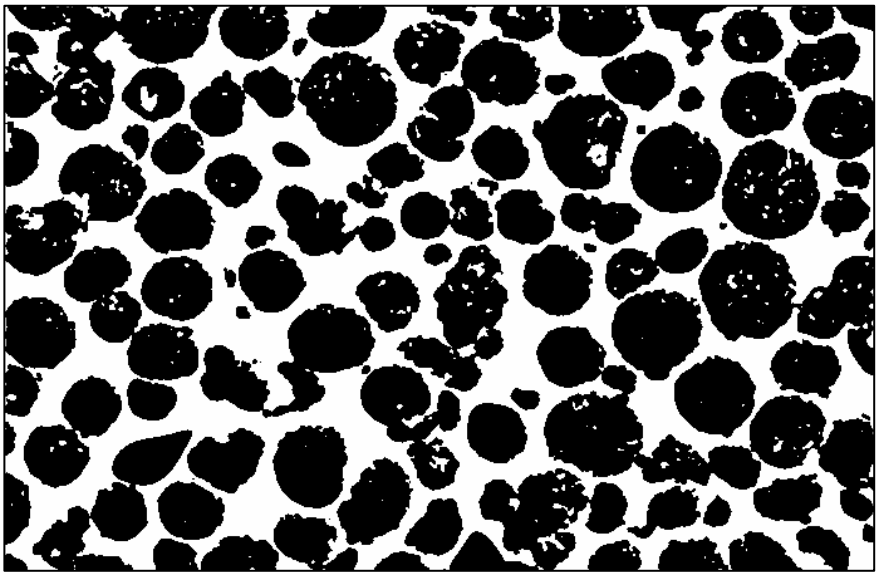

FIGURE C-2: EXAMPLE OF BINARY BLACK AND WHITE CONVERSION OF SEM IMAGES

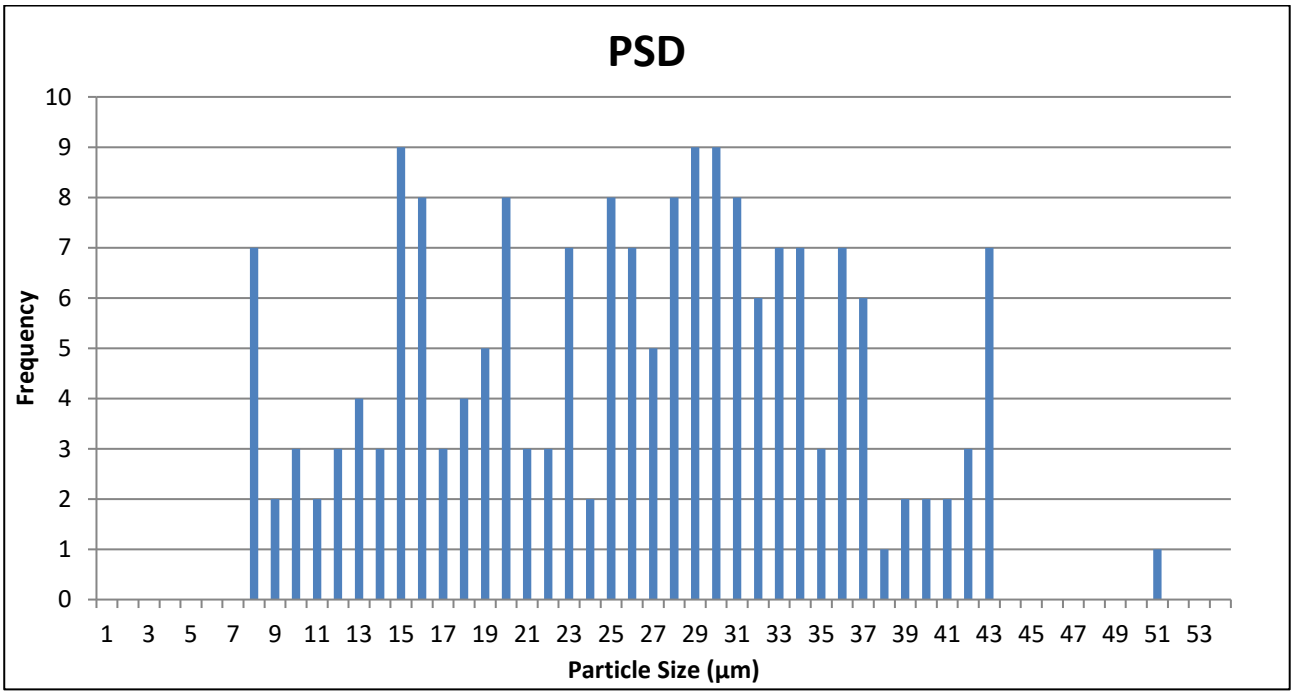

FIGURE C-3: PARTICLE SIZE DISTRIBUTION ESTIMATED FROM AVERAGE PARTICLE DIAMETERS.

APPENDIX D: TI-6AL-4V SUBSTRATE PRODUCTION

The substrate plates were produced from a solid round bar of Ti-6Al-4V (Ø = 75mm x 250mm). The bar was machined at the Stellenbosch Technology Centre (STC), where it was sliced into discs using a bandsaw. It was then machined according to the design specified by the CRPM to fit in the EOSINT M280's reduction unit. An image of the raw material is included in Figure D-1

APPENDIX FIGURE D-1: IMAGE OF THE TI-6AL-4V BILLET BEFORE MACHINING

Images of the machined plates and technical drawings utilised to machine the titanium discs and produce the base plates according to the volume reduction chamber are included if Figure D-2 and D-3.

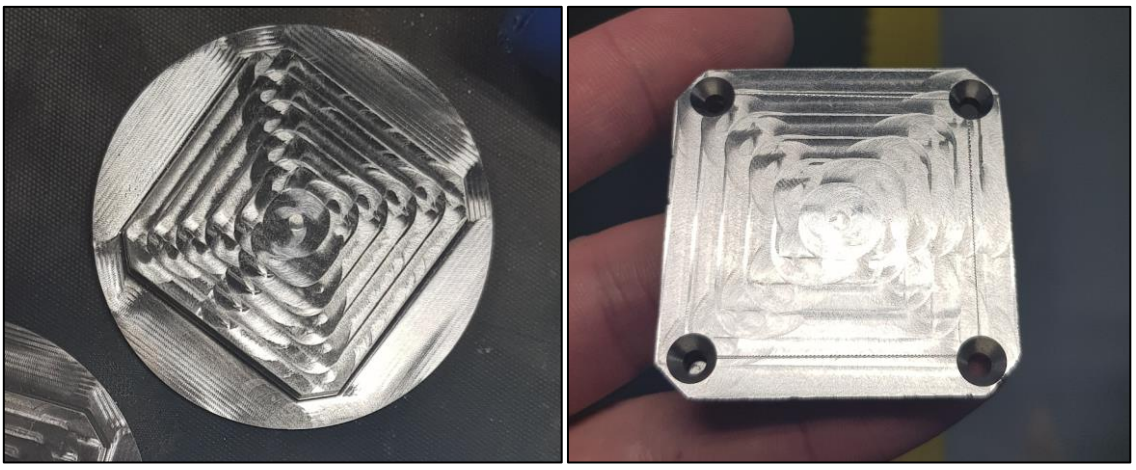

FIGURE D-2: DISC WITH TOP HALF MACHINED (LEFT), AND COMPLETED BASE PLATE (RIGHT)

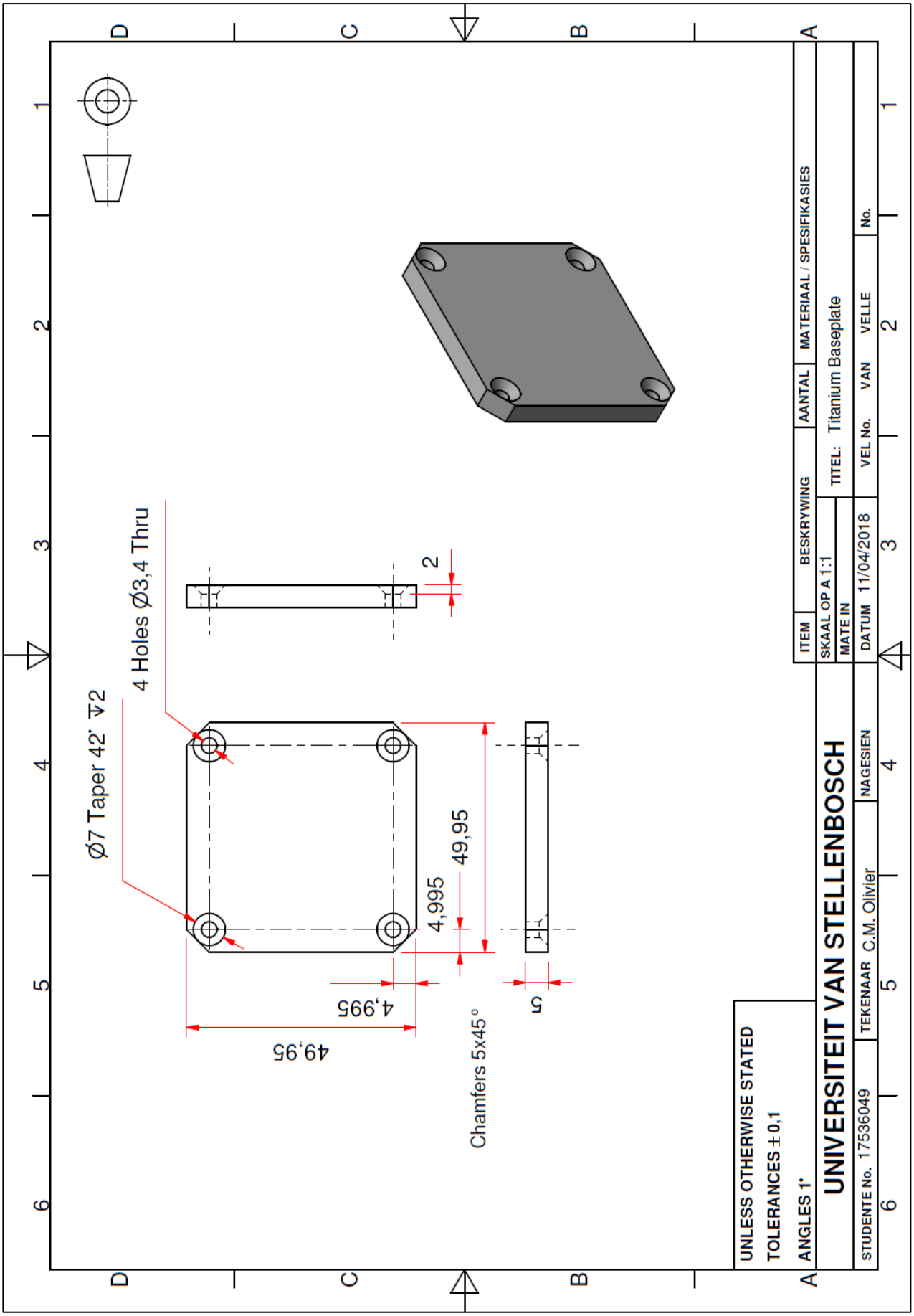

FIGURE D-3: TECHNICAL DRAWING FOR THE MACHINING OF BASE PLATES FOR USE IN THE EOSINT M280 REDUCTION UNIT

APPENDIX E: SEM ANALYSIS OF SINGLE-TRACK SCREENING

SEM images of the 48 single tracks created in the screening experiment are contained in Figures E-1 – E6. The tracks are numbered according to the experimental parameters specified in Table 6-1 and are arranged in order of increasing scanning speed from left to right.

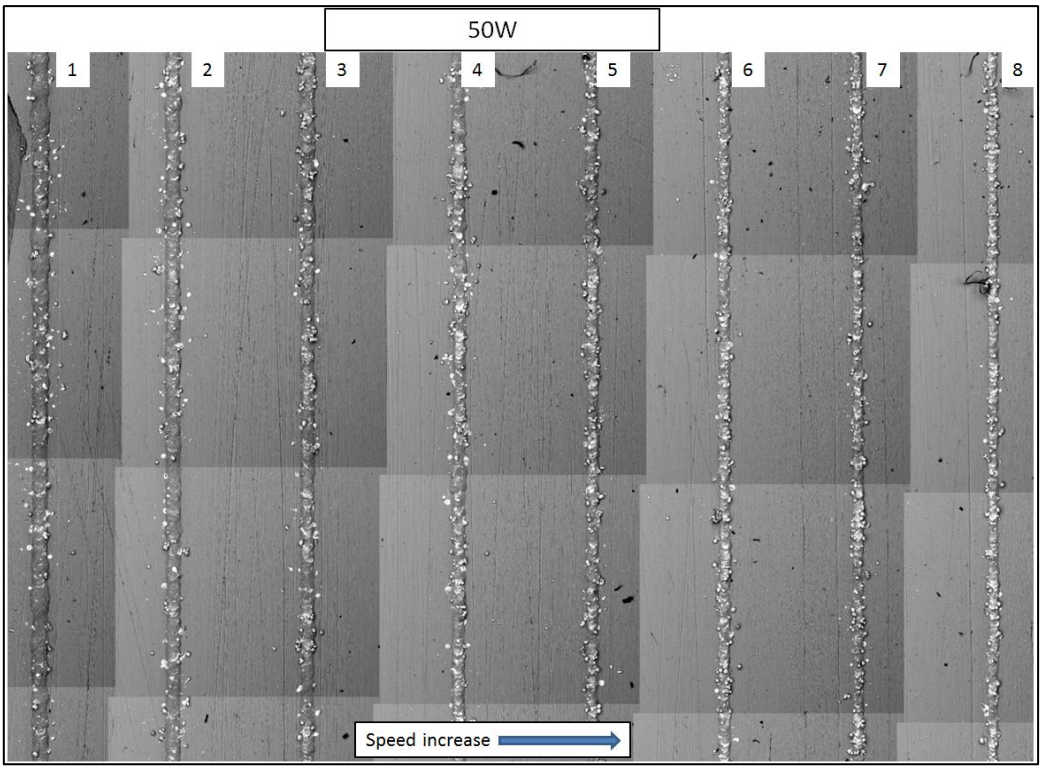

FIGURE E-1: SEM SURFACE IMAGES OF SINGLE TRACKS CONDUCTED AT VARIOUS SPEEDS FOR THE FIRST 50-WATT LASER POWER ITERATION

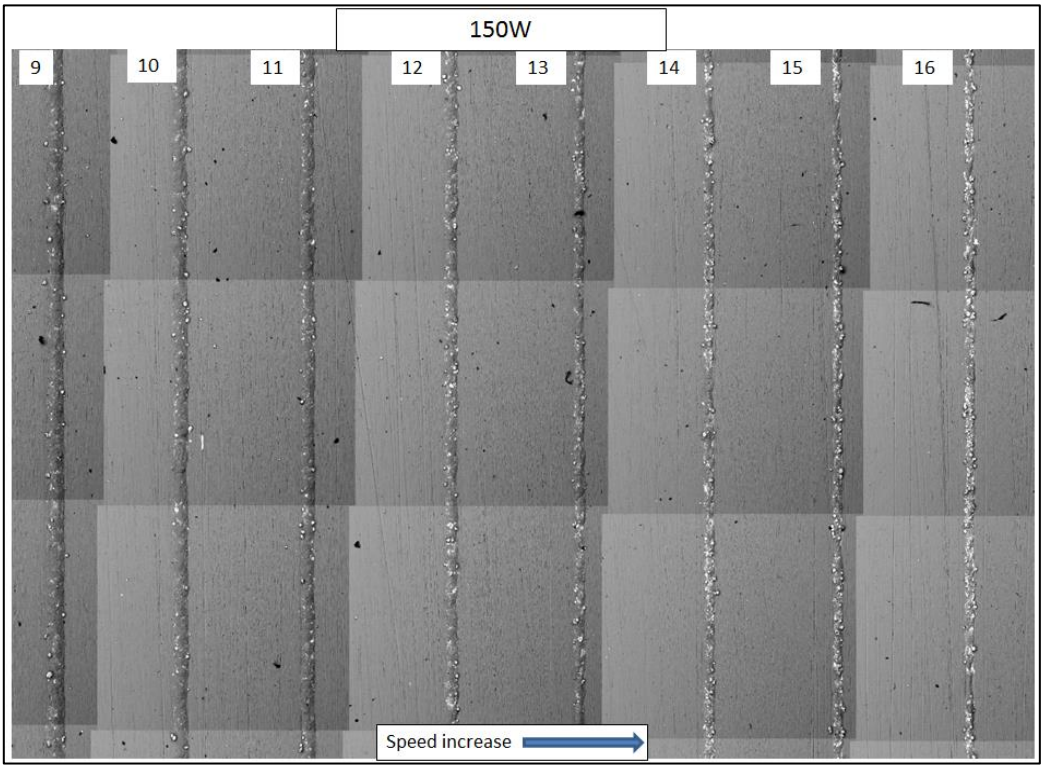

FIGURE E-2: SEM SURFACE IMAGES OF SINGLE TRACKS CONDUCTED AT VARIOUS SPEEDS FOR THE FIRST 150-WATT LASER POWER ITERATION

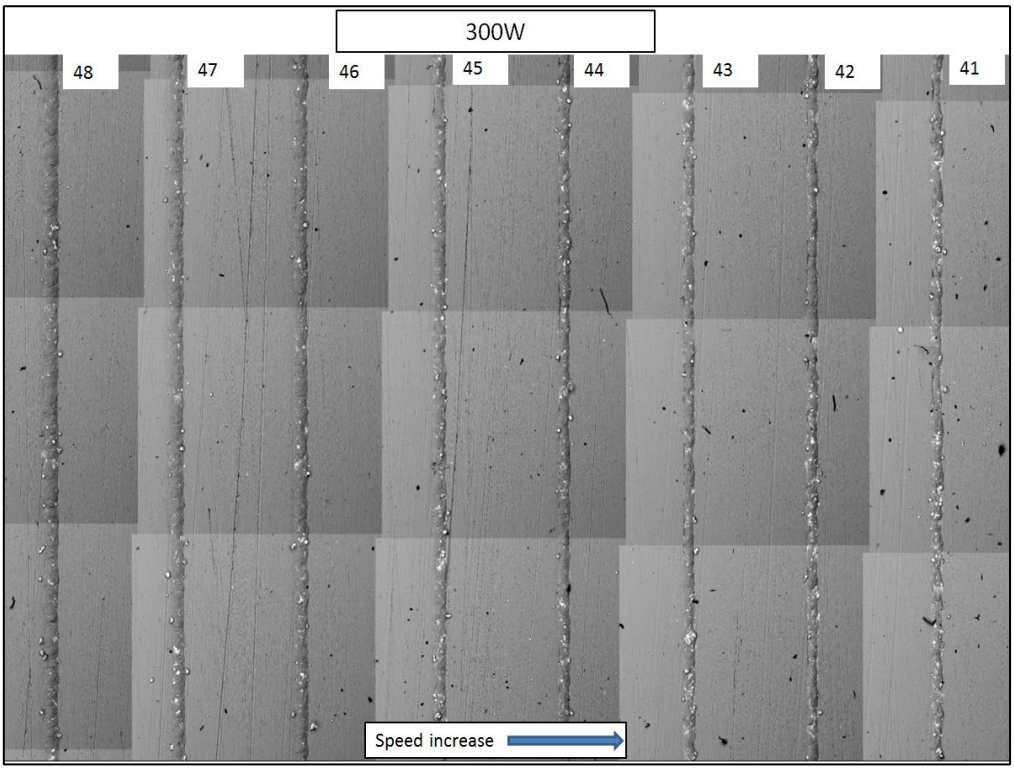

FIGURE E-3: SEM SURFACE IMAGES OF SINGLE TRACKS CONDUCTED AT VARIOUS SPEEDS FOR THE FIRST 300-WATT LASER POWER ITERATION

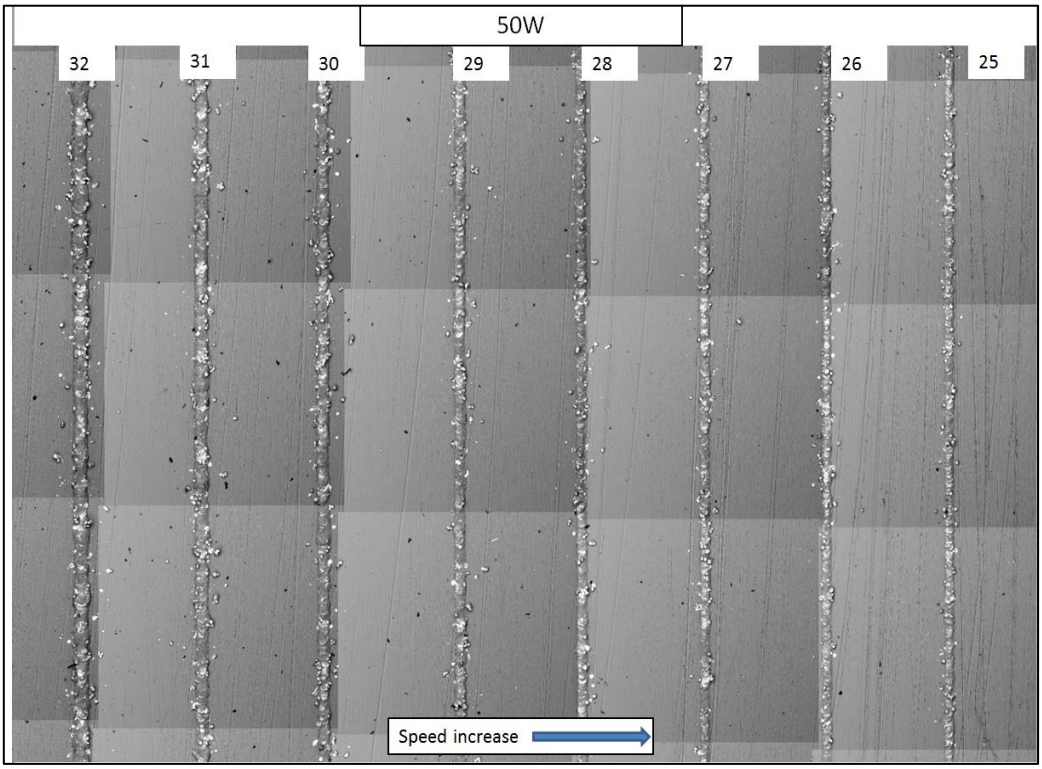

FIGURE E-4: SEM SURFACE IMAGES OF SINGLE TRACKS CONDUCTED AT VARIOUS SPEEDS FOR THE SECOND 50- WATT LASER POWER ITERATION

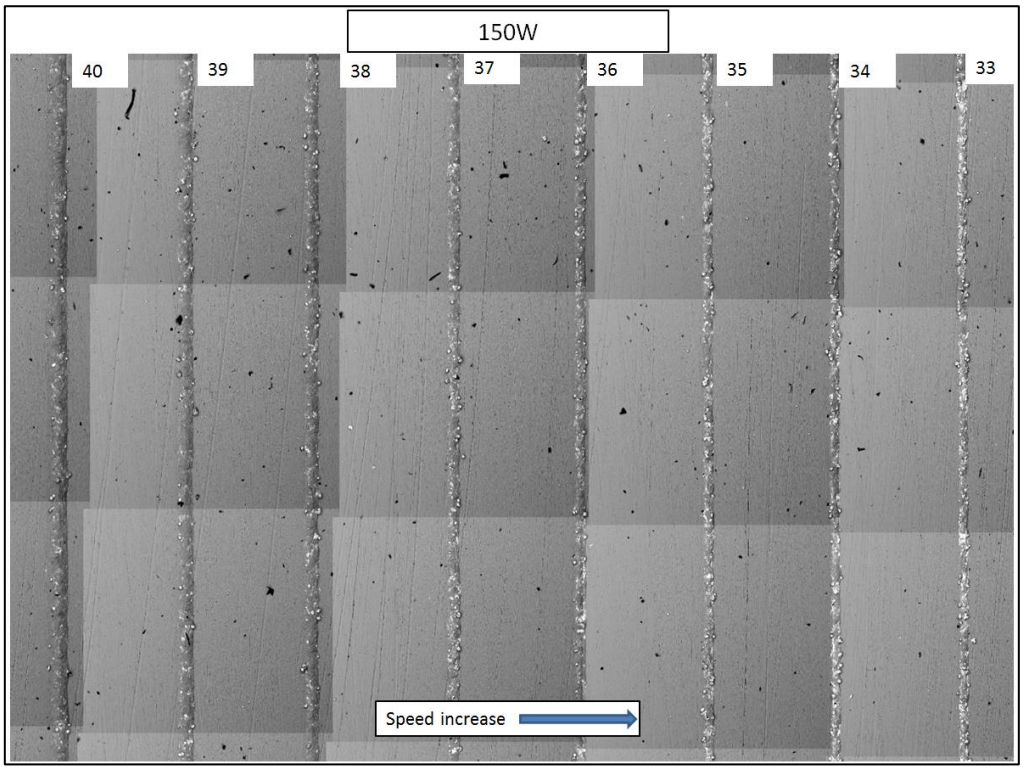

FIGURE E-5: SEM SURFACE IMAGES OF SINGLE TRACKS CONDUCTED AT VARIOUS SPEEDS FOR THE SECOND 150- WATT LASER POWER ITERATION

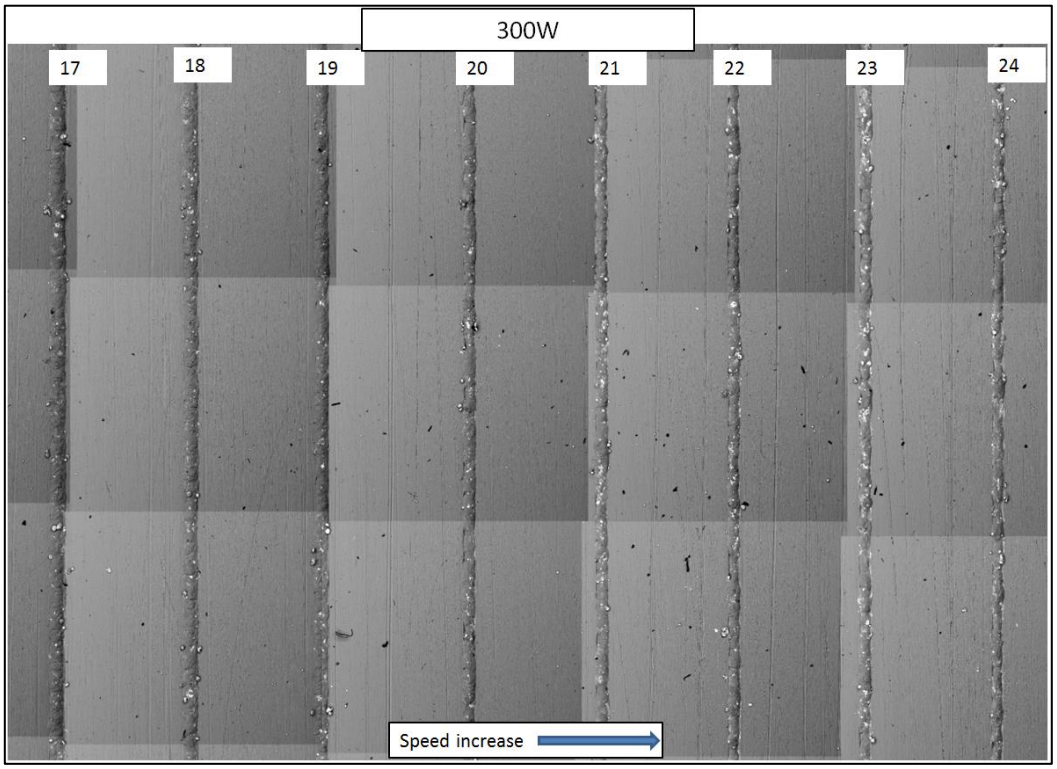

FIGURE E-6: SEM SURFACE IMAGES OF SINGLE TRACKS CONDUCTED AT VARIOUS SPEEDS FOR THE SECOND 300- WATT LASER POWER ITERATION

APPENDIX F: CROSS SECTIONS OF SINGLE-TRACK EXPERIMENTS

This Appendix includes cross section images from the single-track screening experiment, taken with the Olympus GX51 inverted Light microscope in Figure B-1. The scans are numbered in the same order as they appear in Table 6-1.

TABLE F-1: CROSS SECTIONAL IMAGES OF THE TOP, MID AND BOTTOM SECTIONS (LEFT TO RIGHT) OF EACH INDIVIDUAL SCAN TRACK, UTILISED TO MEASURE THE AVERAGE DEPTH OF PENETRATION THROUGHOUT EACH LASER POWER BLOCK

50-WATT		
1 - (60mm/s)		
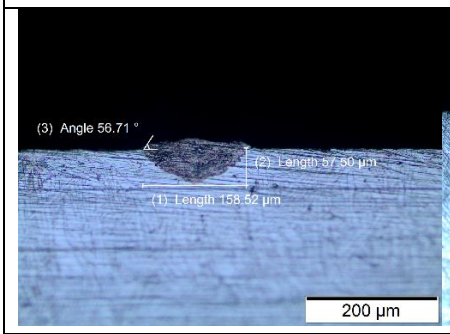	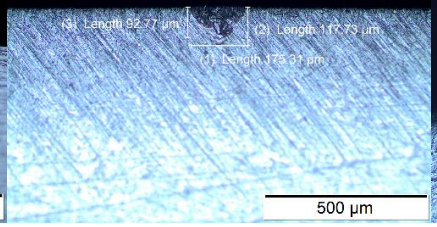	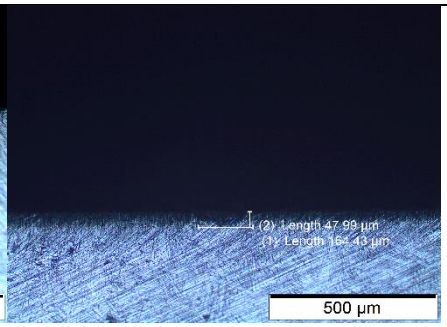
2 - (80mm/s)		
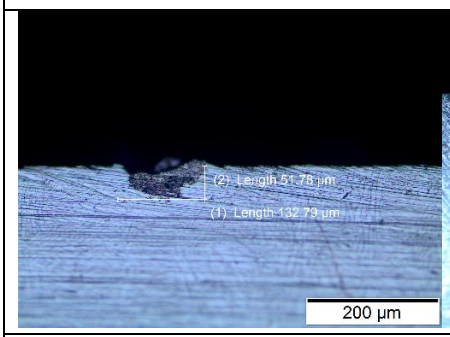	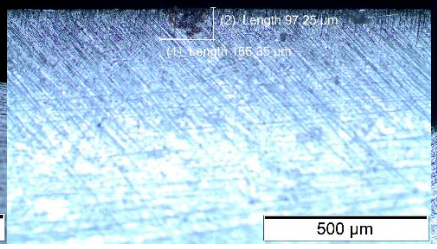	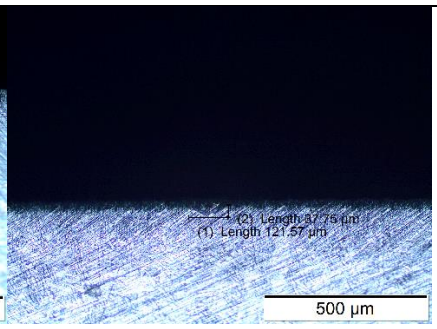
3 - (100mm/s)		
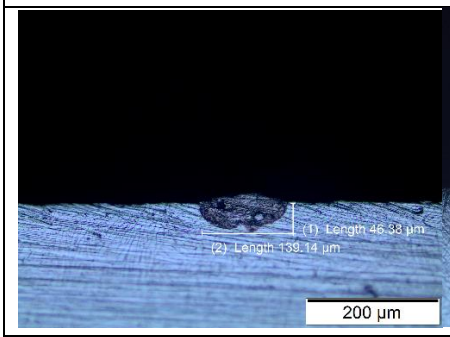	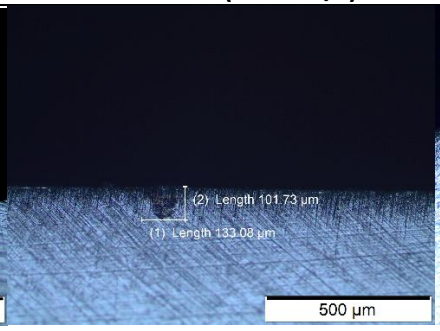	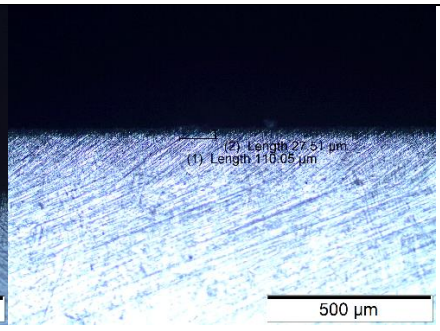
4 - (120 mm/s)		
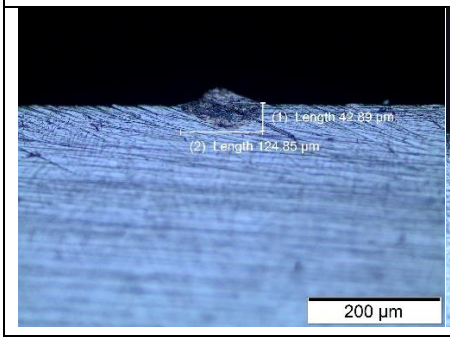	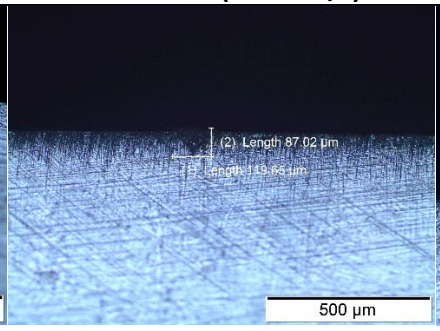	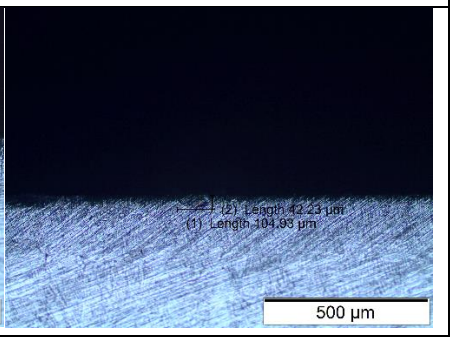

5 – (140 mm/s)

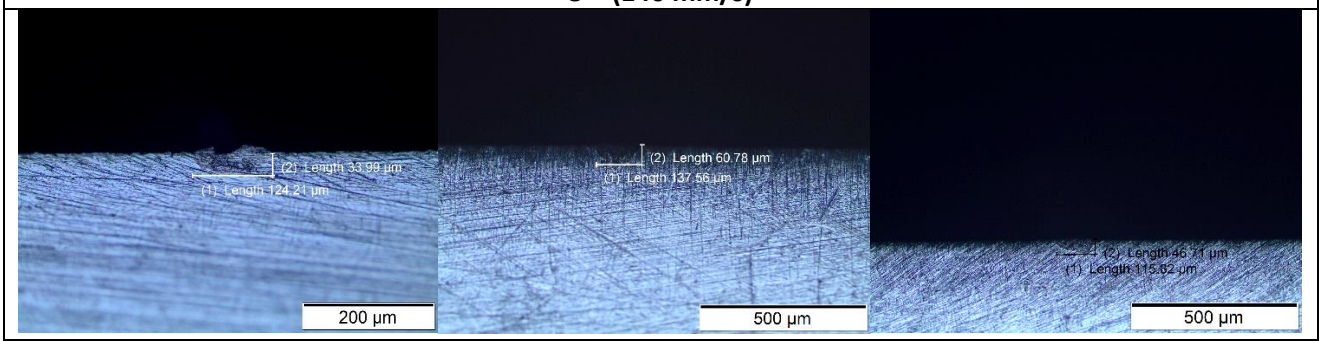

6 – (160 mm/s)

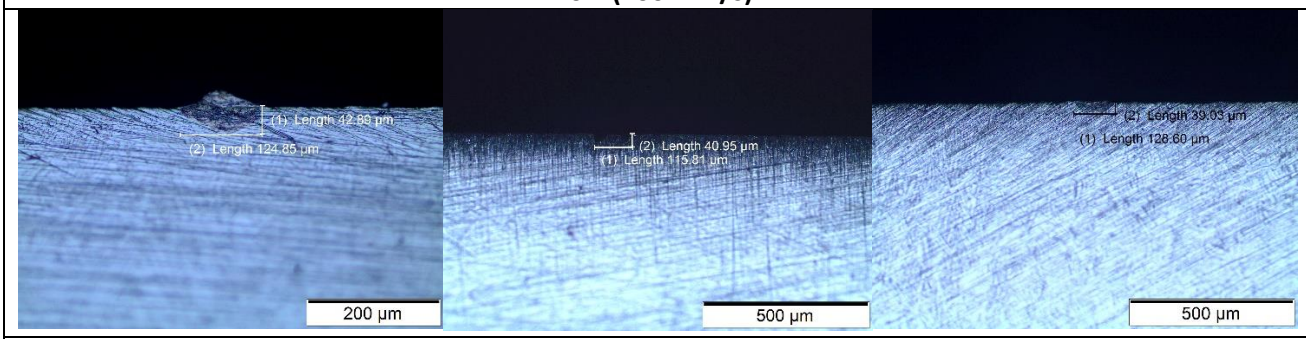

7 – (180 mm/s)

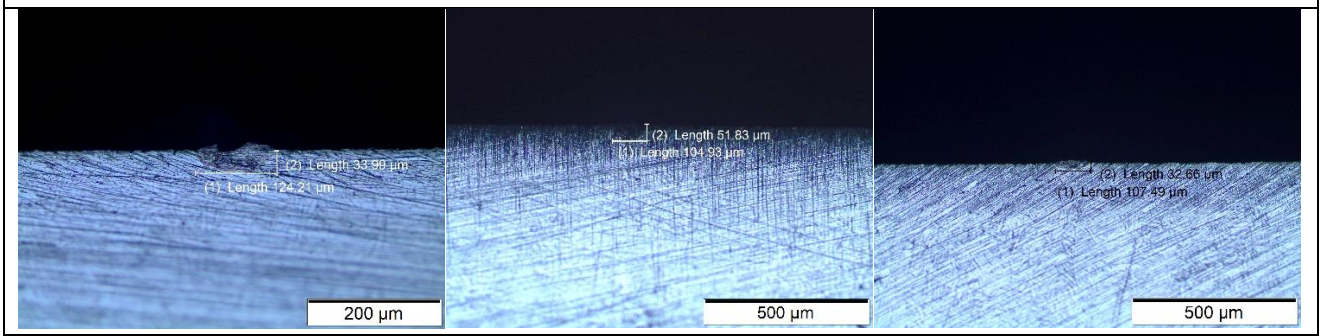

8 – (200 mm/s)

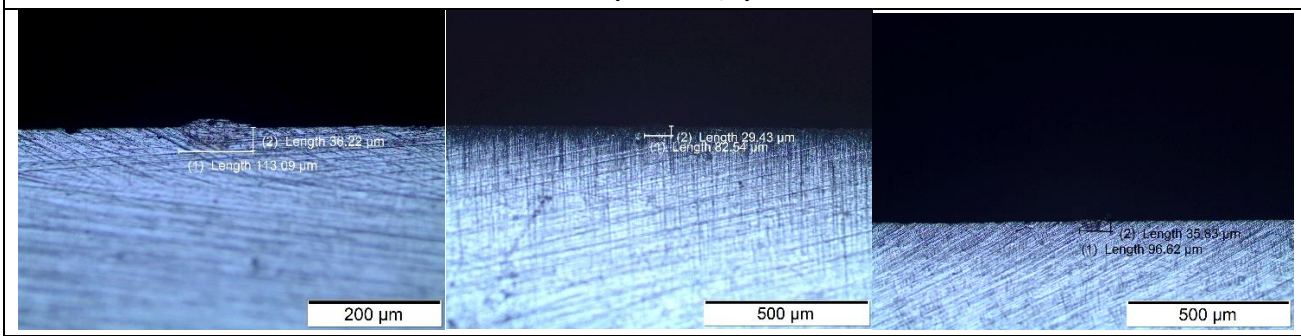

150-WATT

9 – (400 mm/s)

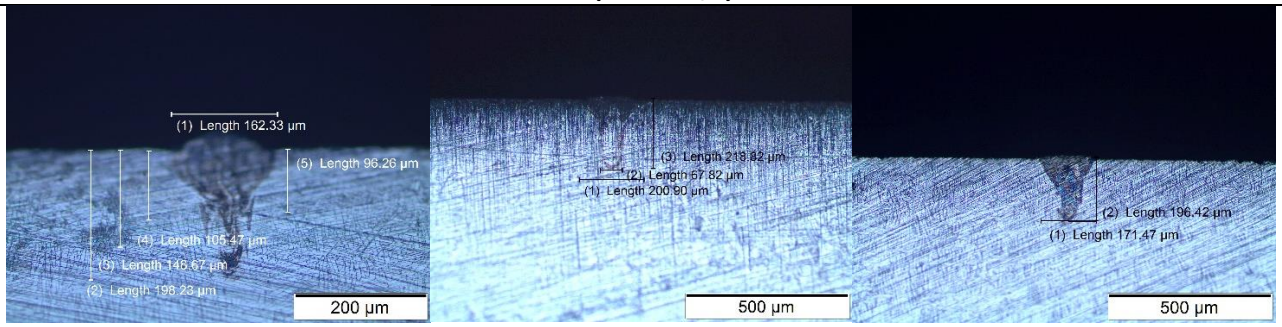

10 – (600 mm/s)

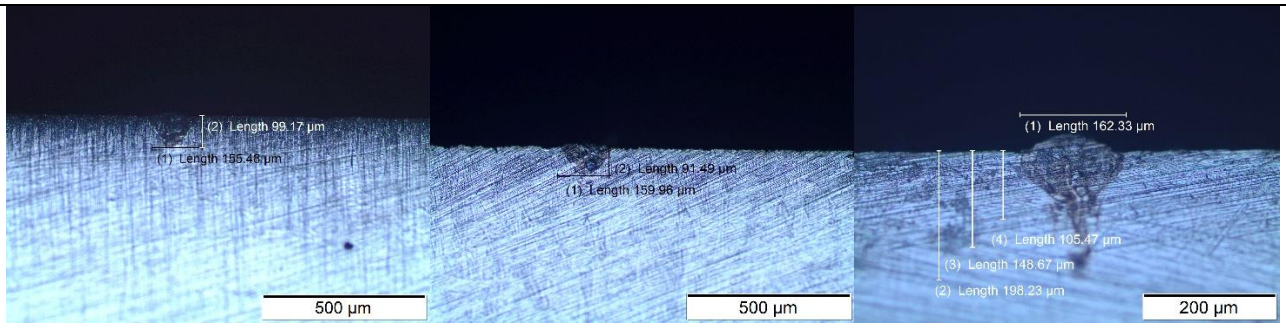

11 – (800 mm/s)

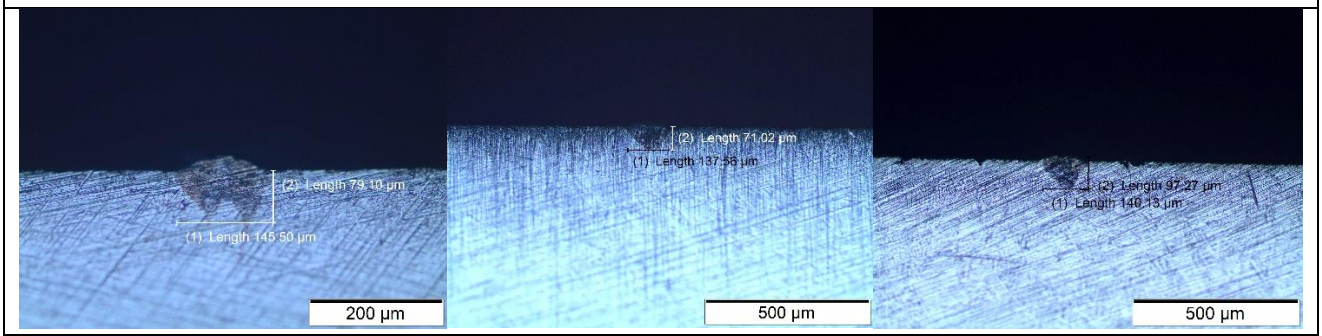

12 – (1000 mm/s)

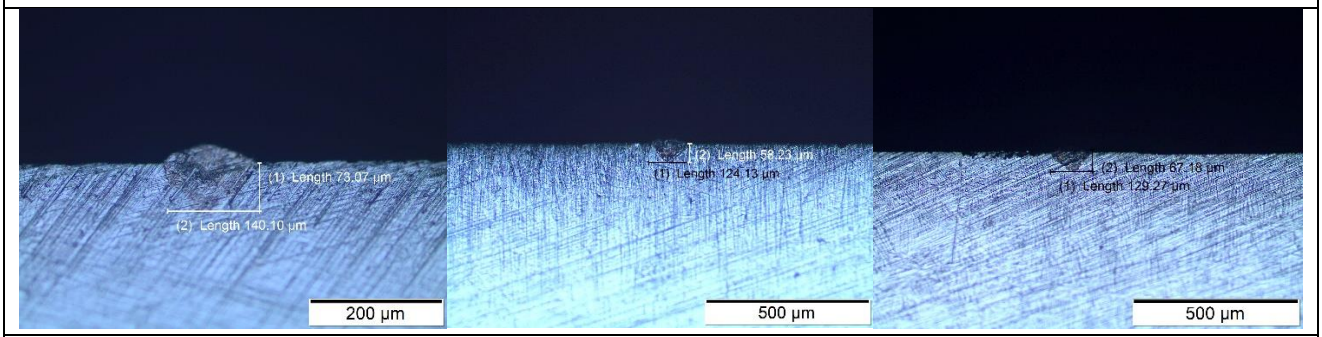

13 – (1200 mm/s)

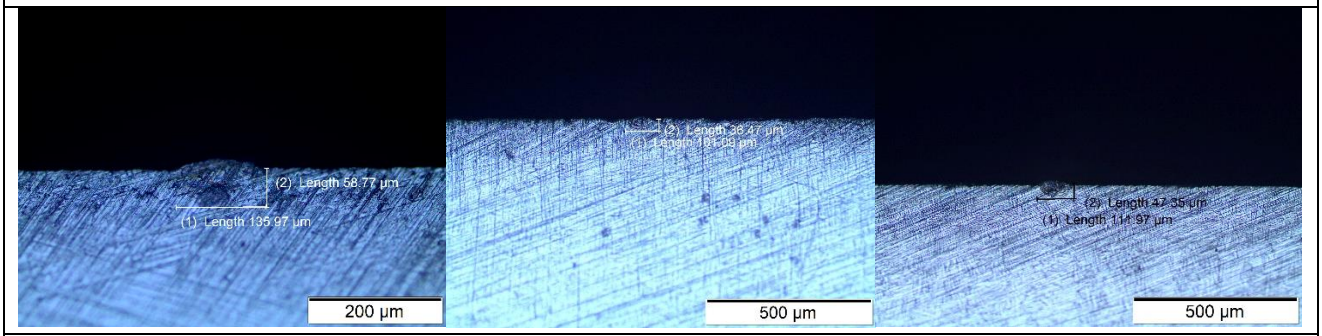

14 – (1400 mm/s)

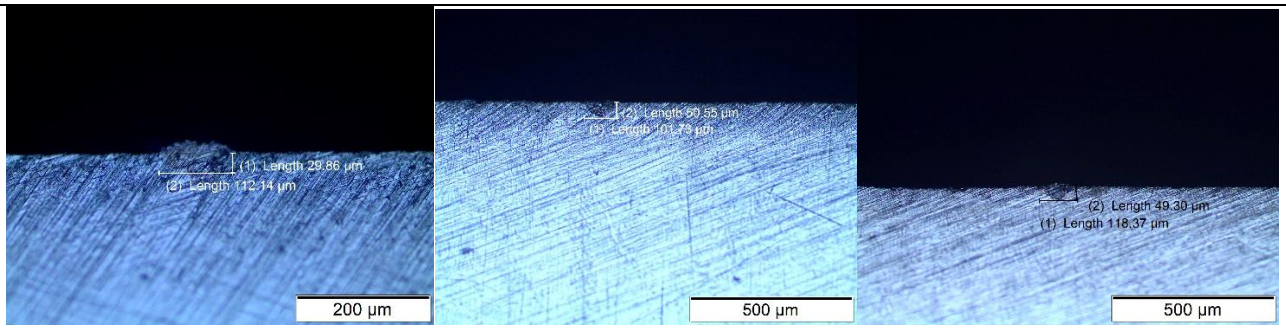

15 – (1600 mm/s)

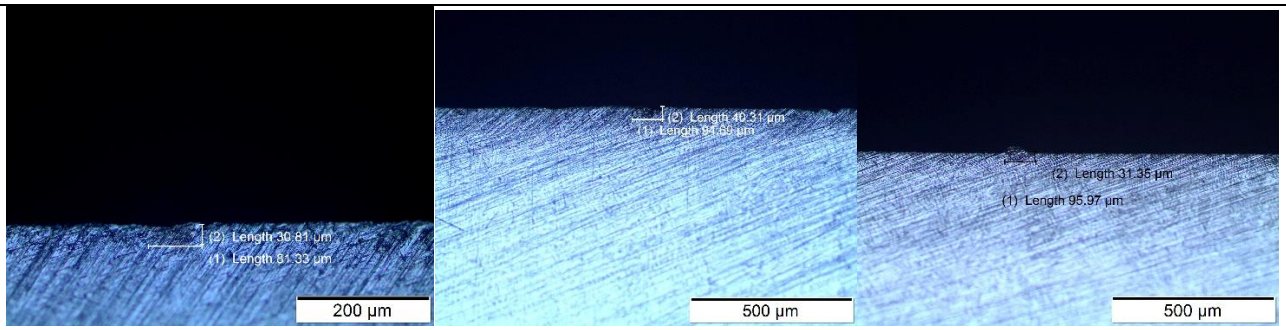

16 – (1800 mm/s)

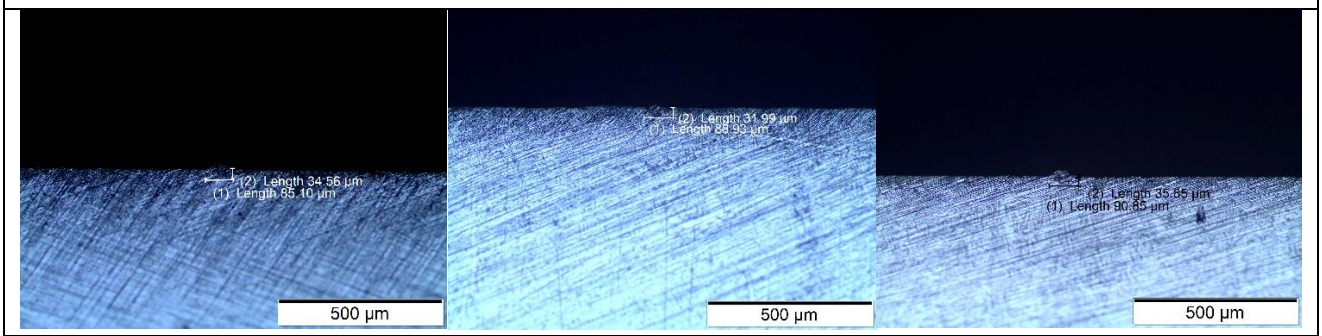

300-WATT

17 – (1000 mm/s)

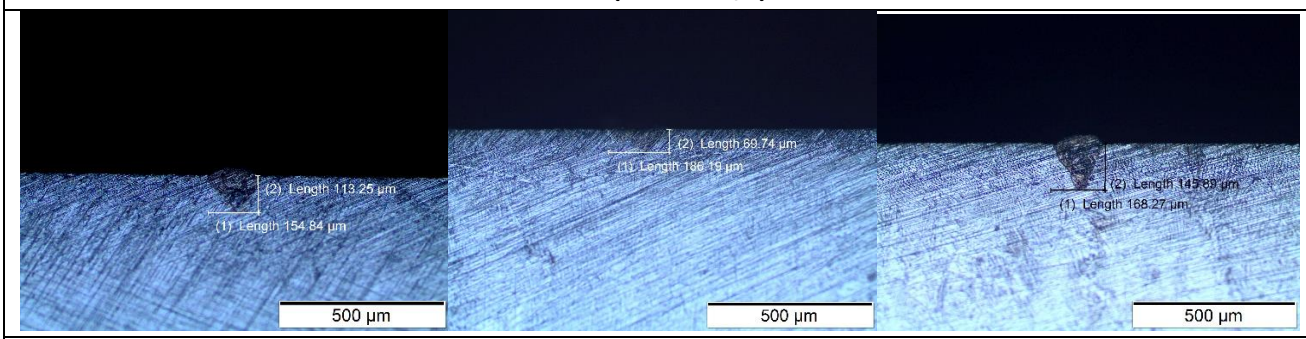

18 – (1200 mm/s)

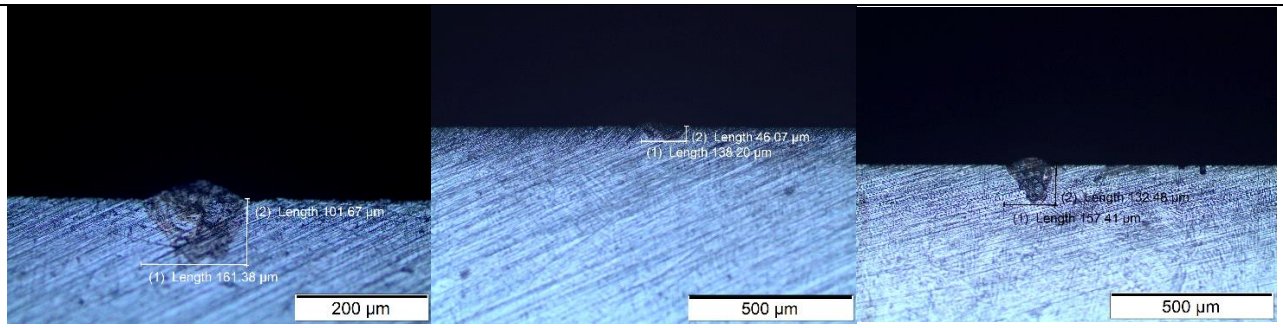

19 – (1400 mm/s)

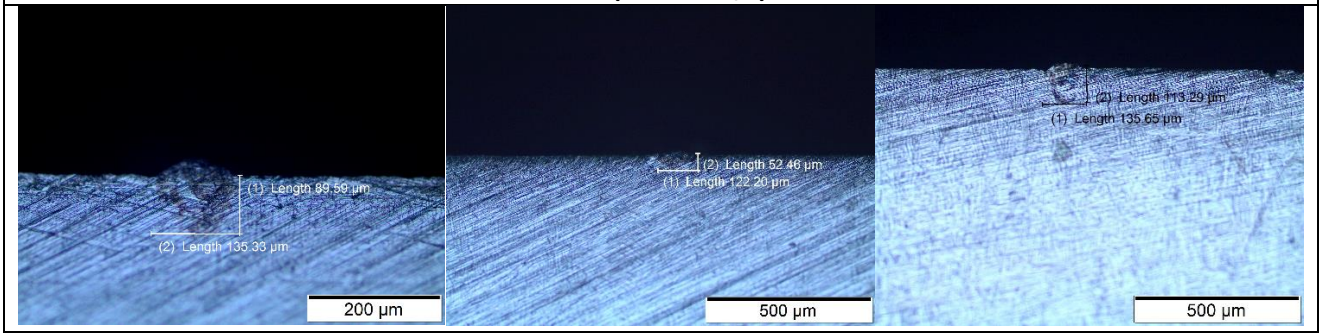

20 - (1600 mm/s)

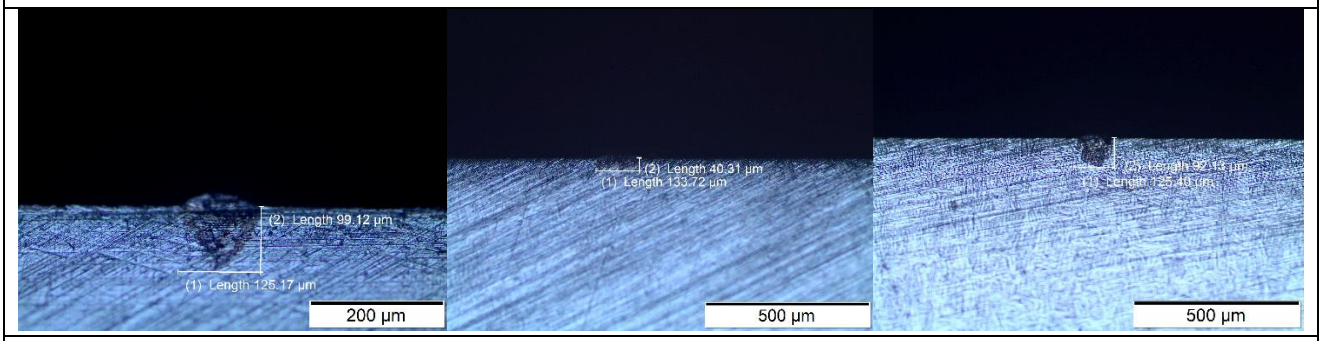

21 – (1800 mm/s)

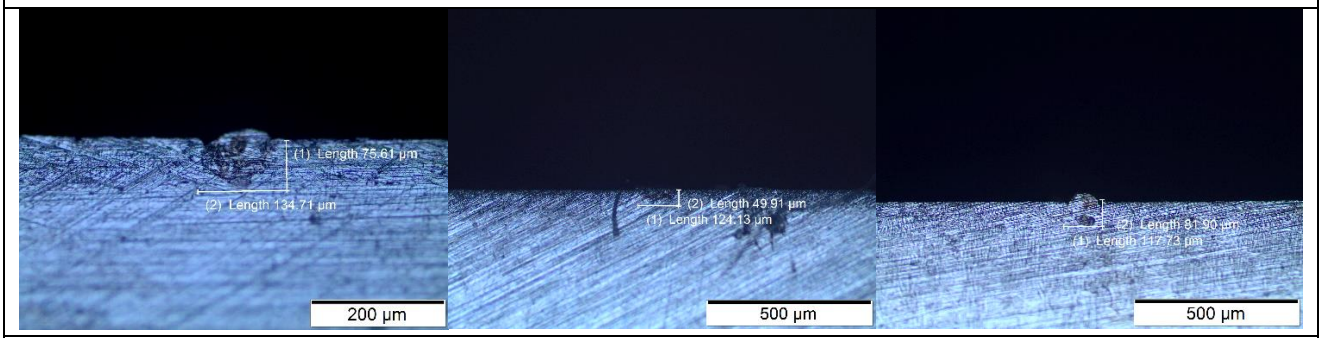

22 – (2000 mm/s)

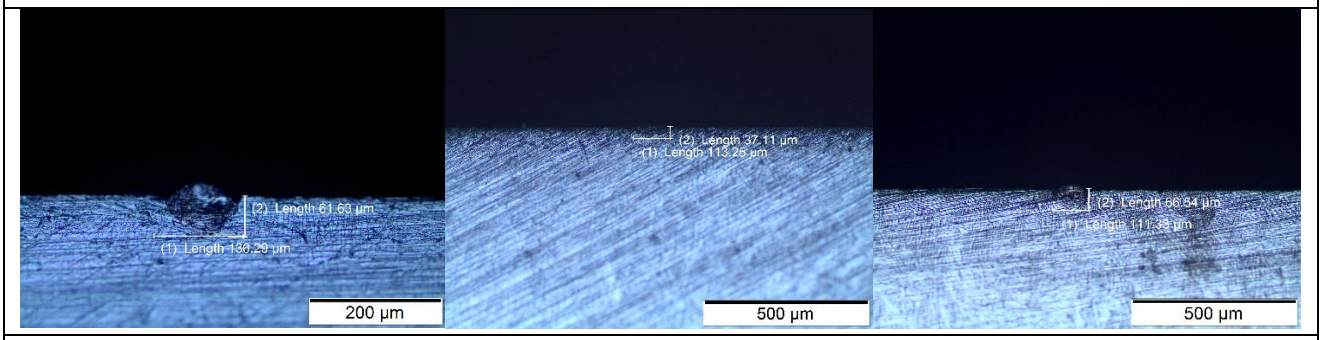

23 – (2200 mm/s)

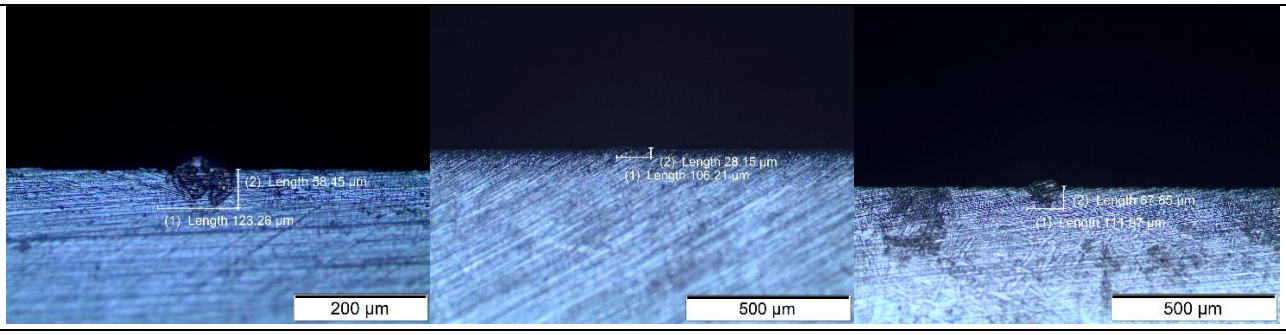

24 – (2400 mm/s)

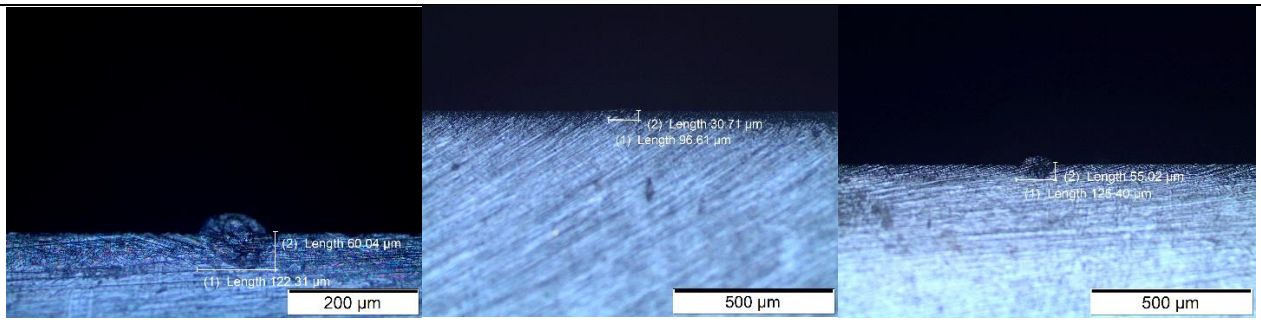

APPENDIX G: SINGLE-TRACK DATA & STATISTICAL ANALYSIS

The data included in this section was measured from the single-track top views and cross sections using the Olympus GX 51 inverted light microscope and ImageJ image processing software. Tables G-1, G-2, and G-3 include the measured data for scan track width and Tables G-4 – G-6 for penetration depth. The average response for each parameter combination and basic descriptive statistics are also indicated.

TABLE G-1: DATA POINTS AND DESCRIPTIVE STATISTICS DESCRIBING SINGLE TRACK WIDTH AT 50W- LASER POWER

50 W						
Speed	**Measure**	**Width top**	**Width bot**	**Measure avg.**	**Track AVG**	**Std. dev**
	Top	152	188	170		
	Mid	185	156	170.5		13.743
60	Bottom	164.02	162.667	163.3445	167.9482	
	Top	145.33	166	155.6665		
	Mid	142.67	156	149.3335		9.3366
80	Bottom	138.67	144	141.3335	148.7778	
	Top	133	140	136.5		
	Mid	158	132	145		8.9285
100	Bottom	136	145.333	140.6665	140.7222	
	Top	126.67	129.333	128		
	Mid	123	132	127.5		4.988
120	Bottom	138.67	133.333	136	130.5	
	Top	124	128	126		
	Mid	124	126.667	125.3335		6.6267
140	Bottom	134	112	123	124.7778	
	Top	121.33	114	117.6665		
	Mid	130.67	120	125.3335		6.0574
160	Bottom	124	112.667	118.3335	120.4445	
	Top	112	92	102		
	Mid	120	108	114		8.8243
180	Bottom	114.67	105	109.8335	108.6112	
	Top	106.67	98	102.3335		
	Mid	108	102	105		4.4821
200	Bottom	112	107	109.5	105.6112	
	Mean				131.07	
	SD				21.996	
	Min				92	
	Max				188	

TABLE G-2: DATA POINTS AND DESCRIPTIVE STATISTICS DESCRIBING SINGLE TRACK WIDTH AT 150W- LASER POWER

150W						
Speed	**Measure**	**Width top**	**Width bot**	**Measure avg.**	**Track AVG**	**Std. dev**
	Top	184	162	173		
	Mid	180	168	174		8.6959
400	Bottom	176	161.33	168.6665	171.8888	
	Top	145.33	138.67	142		
	Mid	160	156	158		9.1605
600	Bottom	162	141.33	151.6665	150.5555	
	Top	134.67	134.67	134.667		
	Mid	148	144	146		6.9281
800	Bottom	136	126.67	131.3335	137.3335	
	Top	121.33	116	118.6665		
	Mid	134.67	112	123.3335		8.0155
1000	Bottom	129.33	116	122.6665	121.5555	
	Top	107	94.667	100.8335		
	Mid	138	110.67	124.3335		13.56
1200	Bottom	118	104	111	112.0557	
	Top	118	89.333	103.6665		
	Mid	107	105.33	106.1665		8.7468
1400	Bottom	107	98.667	102.8335	104.2222	
	Top	101.33	97.333	99.333		
	Mid	92	98.667	95.3335		4.0479
1600	Bottom	105	101.33	103.1665	99.27767	
	Top	93.333	101.33	97.333		
	Mid	109.33	94	101.6665		6.6415
1800	Bottom	91	91	91	96.6665	
	Mean				124.19	
	SD				26.679	
	Min				90.167	
	Max				176	

TABLE G-3: DATA POINTS AND DESCRIPTIVE STATISTICS DESCRIBING SINGLE TRACK WIDTH AT 300W- LASER POWER

300W						
Speed	**Measure**	**Width top**	**Width bot**	**Measure avg.**	**Track AVG**	**Std. dev**
	Top	172	153.33	162.67		
	Mid	160	160	160		7.2078
1000	Bottom	154.67	149.33	152	158.2222	
	Top	144	137.33	140.67		
	Mid	146	142	144		4.9803
1200	Bottom	152	138	145	143.2222	
	Top	125.33	128	126.67		
	Mid	148	126.67	137.33		8.0247
1400	Bottom	128	125.33	126.67	130.2222	
	Top	117.33	124	120.67		
	Mid	124	121.33	122.67		2.9481
1600	Bottom	118.67	125.33	122	121.7777	
	Top	132	110.67	121.33		
	Mid	132	121.33	126.67		8.5929
1800	Bottom	116	112.67	114.33	120.7778	
	Top	120	113	116.5		
	Mid	103	109.33	106.17		7.0018
2000	Bottom	100	116	108	110.2222	
	Top	113.33	104	108.67		
	Mid	121.33	110.67	116		8.9992
2200	Bottom	92	109.33	100.67	108.4443	
	Top	104	113	108.5		
	Mid	116	112	114		5.9
2400	Bottom	98.667	106.7	102.68	108.3945	
	Mean				125.16	
	SD				18.325	
	Min				98	
	Max				166	

TABLE G-4: DATA POINTS AND DESCRIPTIVE STATISTICS DESCRIBING SINGLE TRACK DEPTH AT 50W- LASER POWER

50 W						
Speed	**Measure**	**Width top**	**Width bot**	**Measure avg.**	**Track AVG**	**Std. dev**
	top	57.5	56.94	57.22		
	mid	117.73	65.9	91.815		22.712
60	bot	50.99	58.22	54.605	67.88	
	top	51.78	47.99	49.885		
	mid	97.25	45.6	71.425		18.907
80	bot	40.25	53.74	46.995	56.10167	
	top	46.38	55.66	51.02		
	mid	101.73	42.87	72.3		22.276
100	bot	31.5	50.55	41.025	54.78167	
	top	42.89	45.43	44.16		
	mid	87.02	42.87	64.945		16.56
120	bot	42.33	40.31	41.32	50.14167	
	top	33.99	41.59	37.79		
	mid	60.78	47.35	54.065		8.0532
140	bot	46.71	43.71	45.21	45.68833	
	top	36.22	36.47	36.345		
	mid	40.95	26.87	33.91		4.4436
160	bot	39.03	37.11	38.07	36.10833	
	top	36.53	36.5	36.515		
	mid	51.83	30.71	41.27		7.2943
180	bot	32.66	44.79	38.725	38.83667	
	top	31.45	39.03	35.24		
	mid	29.43	40.31	34.87		3.8489
200	bot	35.83	34.56	35.195	35.10167	
	Mean				48.08	
	SD				18.388	
	Min				26.87	
	Max				117.73	

TABLE G-5: DATA POINTS AND DESCRIPTIVE STATISTICS DESCRIBING SINGLE TRACK DEPTH AT 150W- LASER POWER

150W						
Speed	**Measure**	**Width top**	**Width bot**	**Measure avg.**	**Track AVG**	**Std. dev**
	top	200.1	189.39	194.75		
	mid	218	215.4	216.7		10.524
400	bot	196.42	211.8	204.11	205.185	
	top	80	92.13	86.065		
	mid	99.17	110.06	104.62		9.4827
600	bot	91.49	102.37	96.93	95.87	
	top	73.07	72.94	73.005		
	mid	71.02	85.1	78.06		8.524
800	bot	95	82.54	88.77	79.945	
	top	58.77	51.2	54.985		
	mid	58.23	78.06	68.145		8.4067
1000	bot	67.18	63.35	65.265	62.79833	
	top	39.86	56.1	47.98		
	mid	36.47	52.46	44.465		7.6826
1200	bot	47.35	56.31	51.83	48.09167	
	top	30.81	51.19	41		
	mid	50.55	42.23	46.39		8.6348
1400	bot	49.3	31.36	40.33	42.57333	
	top	34.56	41.59	38.075		
	mid	40.31	37.11	38.71		6.4213
1600	bot	31.35	22.39	26.87	34.55167	
	top	50.55	43.51	47.03		
	mid	31.99	34.55	33.27		7.666
1800	bot	32.85	28.15	30.5	36.93333	
	Mean				75.744	
	SD				53.608	
	Min				22.39	
	Max				218	

TABLE G-6: DATA POINTS AND DESCRIPTIVE STATISTICS DESCRIBING SINGLE TRACK DEPTH AT 300W- LASER POWER

300W						
Speed	**Measure**	**Width top**	**Width bot**	**Measure avg.**	**Track AVG**	**Std. dev**
	top	113.25	115.81	114.53		
	mid	69.74	124.13	96.935		23.274
1000	bot	145.89	127.96	136.93	116.13	
	top	101.67	97.25	99.46		
	mid	46.06	111.97	79.015		26.371
1200	bot	132.48	107.49	119.99	99.48667	
	top	89.59	92.79	91.19		
	mid	52.46	92.77	72.615		18.182
1400	bot	113.29	81.9	97.595	87.133	
	top	99.12	96.61	97.865		
	mid	40.31	81.26	60.785		20.056
1600	bot	92.13	73	82.565	80.405	
	top	75.61	80.63	78.12		
	mid	49.91	81.9	65.905		11.462
1800	bot	81.9	80.62	81.26	75.095	
	top	61.63	84.48	73.055		
	mid	37.11	48.63	42.87		15.756
2000	bot	66.54	74.86	70.7	62.20833	
	top	58.45	71.02	64.735		
	mid	28.15	41.59	34.87		15.953
2200	bot	67.85	69.1	68.475	56.02667	
	top	60.04	63.34	61.69		
	mid	30.71	28.8	29.755		14.644
2400	bot	55.02	62.7	58.86	50.10167	
	Mean				78.323	
	SD				28.155	
	Min				28.15	
	Max				145.89	

TESTS FOR STATISTICAL SIGNIFICANCE OF PARAMETERS.

The Statistica statistical analysis software was used to analyse the data throughout the project. Regression models for single-track width and depth listed in the tables above. The information was acquired with the assistance of the Department of Statistics and Actuarial Sciences at Stellenbosch University.

TRACK WIDTH

TABLE G-7: UNIVARIATE TEST OF SIGNIFICANCE FOR TRACK WIDTH

Effect	Univariate Tests of Significance for Track Width - Std. Error of Estimate: 9.6984				
	SS	Degr. Of Freedom	MS	F	p
Intercept	9840.87	1	9840.9	104.62	0
Laser Power	2774.25	1	2774.3	29.495	4E-05
Laser Power^2	581.989	1	581.99	6.1875	0.0229
Speed	3477.5	1	3477.5	36.971	1E-05
Speed^2	958.486	1	958.49	10.19	0.005
Laser Power*Speed	139.767	1	139.77	1.4859	0.2386
Error	1693.06	18	94.059		

TABLE G-8: PARAMETER ESTIMATES FOR EQUATION 6-1

Effect	Parameter Estimates Sigma-restricted parameterization									
	Track Width Param.	Track Width Std.Err	Track Width t	Track Width p	-95% Cnf.Lmt	95.00% Cnf.Lmt	Track Width Beta (ß)	Track Width St.Err.ß	-95% Cnf.Lmt	95% Cnf.Lmt
Intercept	93.82	9.17	10.23	0.00	74.55	113.10				
Laser Power	1.16	0.21	5.43	0.00	0.71	1.60	5.67	1.04	3.48	7.86
Laser Power^2	0.00	0.00	-2.49	0.02	0.00	0.00	-2.95	1.18	-5.44	-0.46
Speed	-0.13	0.02	-6.08	0.00	-0.17	-0.08	-4.52	0.74	-6.09	-2.96
Speed^2	0.00	0.00	3.19	0.01	0.00	0.00	3.29	1.03	1.12	5.45
Laser Power*Speed	0.00	0.00	-1.22	0.24	0.00	0.00	-1.71	1.40	-4.66	1.24

TABLE G-9: TEST OF SS FOR WHOLE MODEL VS SS RESIDUAL

Dependent Variable	Test of SS Whole Model vs. SS Residual										
	Multiple R	Multipe R^2	Adjusted R^2	SS Model	df Model	MS Model	SS Residual	df Residual	MS Residual	F	p
Track Width	0.9162	0.8395	0.7949	8856	5	1771.2	1693.1	18	94.059	18.831	1E-06

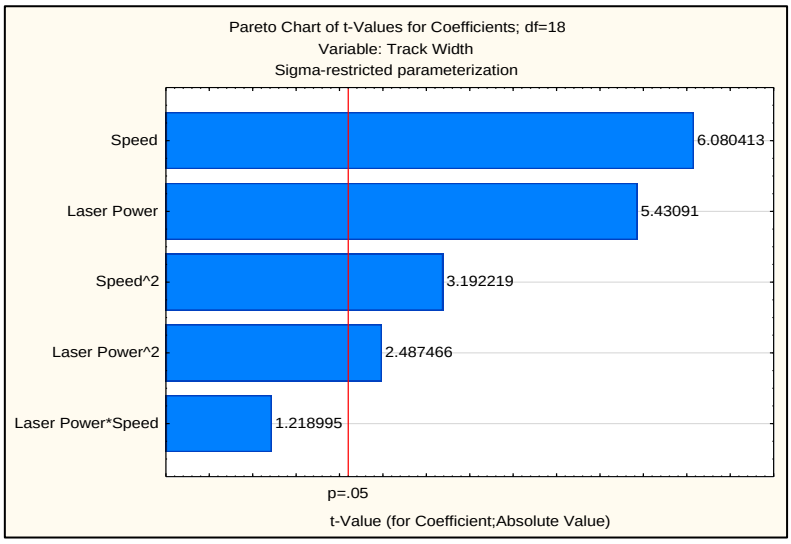

FIGURE G-1: PARETO CHART OF T-VALUES; DF = 18

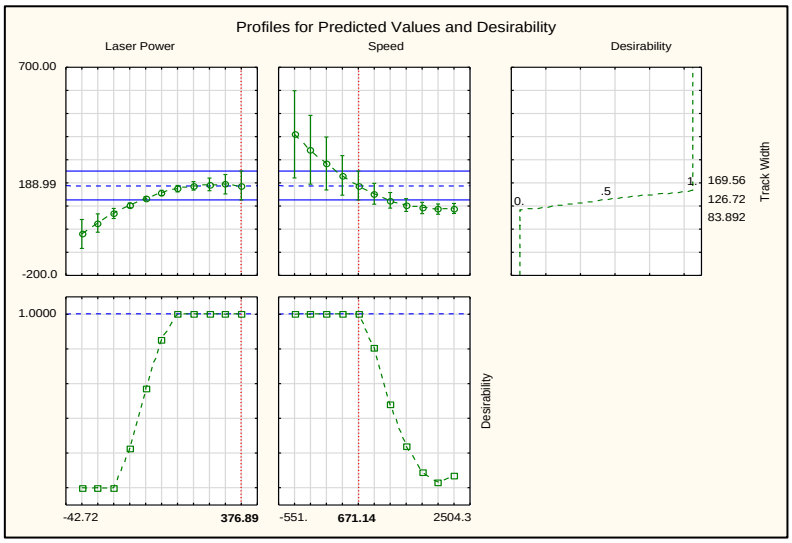

FIGURE G-2: PROFILES FOR PREDICTED VALUES AND DESIRABILITY

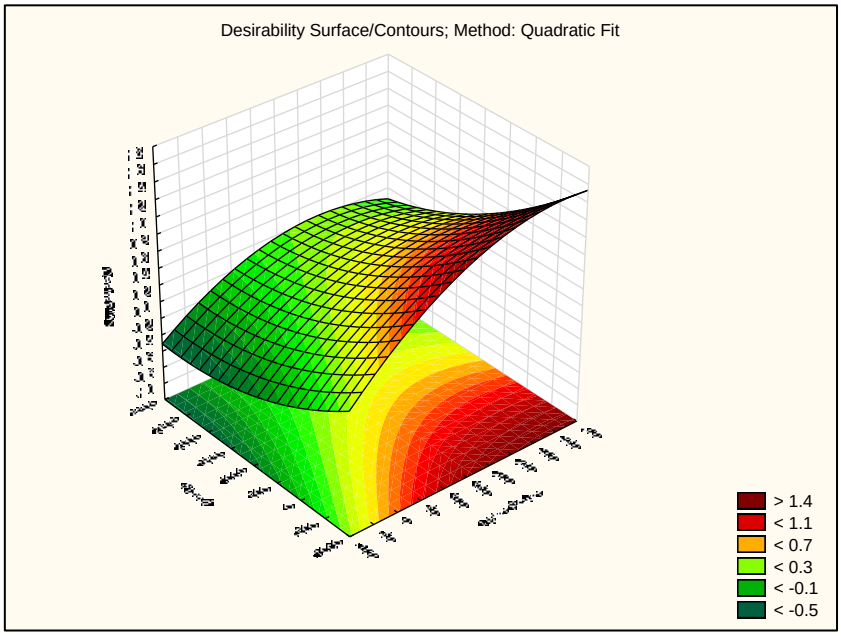

FIGURE G-3: DESIRABILITY SURFACE/ CONTOURS; METHOD: QUADRATIC FIT.

PENETRATION DEPTH

TABLE G-10: UNIVARIATE TEST OF SIGNIFICANCE FOR TRACK DEPTH

Effect	Univariate Tests of Significance for Track Depth- Std. Error of Estimate: 9.6984				
	SS	Degr. Of Freedom	MS	F	p
Intercept	2424.43	1	2424.43	10.52472	0.004503
Laser Power	15248.06	1	15248.06	66.1936	0
Laser Power^2	4505.78	1	4505.78	19.56012	0.000329
Speed	11003.43	1	11003.43	47.76718	0.000002
Speed^2	3038.48	1	3038.48	13.19041	0.001907
Laser Power*Speed	316.79	1	316.79	1.3752	0.256206
Error	4146.4	18	230.36		

TABLE G-11: PARAMETER ESTIMATES FOR EQUATION 6-2

Effect	Parameter Estimates Sigma-restricted parameterization									
	Track Width Param.	Track Width Std.Err	Track Width t	Track Width p	-95% Cnf.Lmt	95.00% Cnf.Lmt	Track Width Beta (ß)	Track Width St.Err.ß	-95% Cnf.Lmt	95% Cnf.Lmt
Intercept	-46.57	14.355	-3.244	0.0045	-76.73	-16.41				
Laser Power	2.713	0.3334	8.136	0	2.012	3.413	7.708	0.9474	5.718	9.699
Laser Power^2	-0.005	0.001	-4.423	0.0003	-0.007	-0.002	-4.757	1.0757	-7.017	-2.497
Speed	-0.226	0.0327	-6.911	2E-06	-0.294	-0.157	-4.669	0.6755	-6.088	-3.25
Speed^2	1E-04	2E-05	3.632	0.0019	0	1E-04	3.396	0.935	1.431	5.36
Laser Power*Speed	-2E-04	0.0002	-1.173	0.2562	-7E-04	2E-04	-1.493	1.2731	-4.168	1.182

TABLE G-12: TEST OF SS FOR WHOLE MODEL VS SS RESIDUAL

Dependent Variable	Test of SS Whole Model vs. SS Residual										
	Multiple R	Multipe R^2	Adjusted R^2	SS Model	df Model	MS Model	SS Residual	df Residual	MS Residual	F	p
Track Width	0.9315	0.8677	0.831	27197	5	5439.3	4146.4	18	230.36	23.613	0

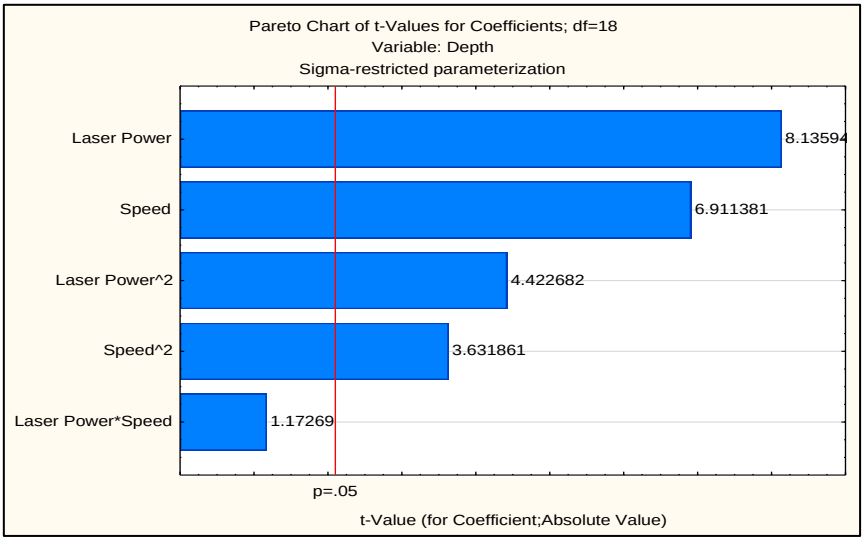

FIGURE G-4: PARETO CHART OF T-VALUES; DF = 18

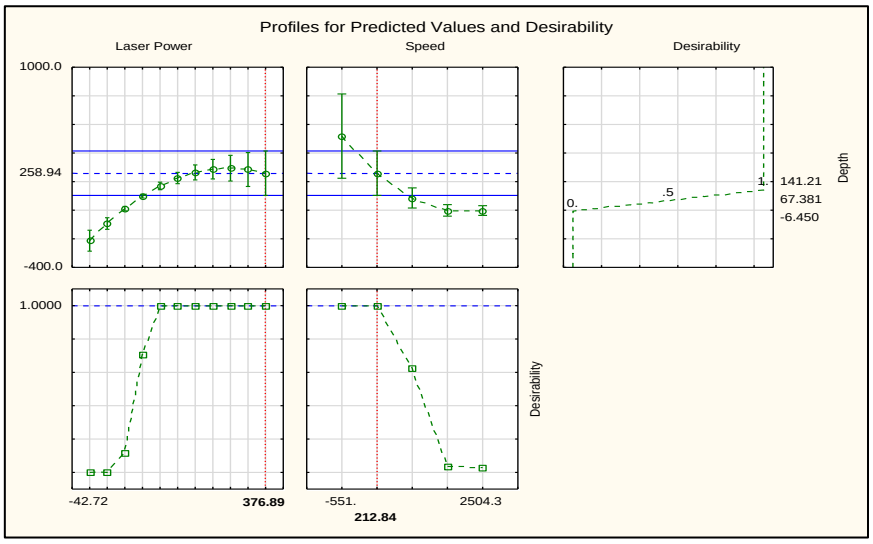

FIGURE G-5: PROFILES FOR PREDICTED VALUES AND DESIRABILITY

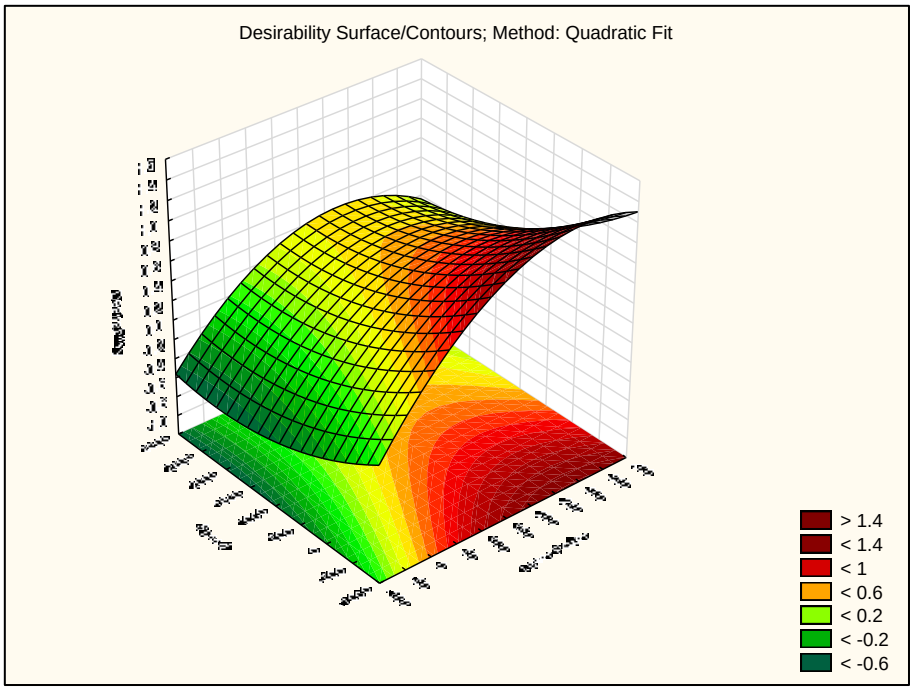

FIGURE G-6: DESIRABILITY SURFACE/ CONTOURS; METHOD: QUADRATIC FIT

APPENDIX H: COMPOSITIONAL LINE SCANS OF LAYERED MAPS

This Appendix provides the information from SEM compositional line scans conducted on each layer. To condense the findings, only graphs indicating the average weight percentage contents of Ni, Ti and WC at the surfaces are included in tables I-2, I-4, and I-6. The Vertical axes indicate the average weight percentage [wt.%] of the element, and the horizontal axes describe the distance from the top of the layer. Additionally, descriptive statistics are displayed for each line scan; these include standard deviations and minimum and maximum values for each element recorded in the analysis at the middle and edge of each layer.

150-WATT

TABLE H-1: DESCRIPTIVE STATISTICAL VALUES FOR SURFACE CONTENTS OF LAYERS

Layer #	Description	Al Wt%	C Wt%	N Wt%	Ni Wt%	Ti Wt%	V Wt%	W Wt%	WC Wt %
1	Mid std. dev	1.25486	1.730654	3.613695	1.534372	11.43865	0.457647	8.526382	9.964806
	Edge std dev	1.68413	0	5.02317	1.503038	9.233287	0.693239	7.714406	7.714406
	mid max	4.94	6.02	14.84	7.35	95.62	3.76	34.64	40.66
	mid min	0.37	0	0	0	48.02	1.42	0	0
	edge max	7.05	0	12.82	9.33	96.03	5.12	44.55	44.55
	edge min	0.18	0	0	0	50.3	1.94	0	0
2	Mid std. dev	1.693559	2.707257	3.106909	0.916322	9.272299	0.49989	5.095538	6.817241
	Edge std dev	1.424726	1.407593	3.357802	1.474324	8.13793	0.448614	5.989474	7.074401
	mid max	6.99	15.97	12.57	4.46	96.37	3.98	20.55	28.72
	mid min	0.47	0	0	0	56.71	1.69	0	0
	edge max	5.95	5.07	13.47	9.01	91.32	3.36	29.26	32.42
	edge min	0.71	0	0	0	53.63	1.67	0	0
3	Mid std. dev	1.529327	1.497399	2.93551	0.623903	8.042433	0.346579	5.532058	6.701663
	Edge std dev	1.90717	1.19266	3.289135	0.682858	7.004289	0.338261	3.381552	4.171272
	mid max	7.44	4.93	12.71	2.32	93.89	3.28	23.18	27.25
	mid min	0.83	0	0	0	58.48	1.57	0	0
	edge max	7.45	3.83	14.03	2.47	96.84	3.56	15.56	18.91
	edge min	0.26	0	0	0	62.27	1.98	0	0
4	Mid std. dev	1.36257	1.536251	2.88292	0.547829	7.054094	0.373596	3.891834	4.982071
	Edge std dev	1.443476	1.735793	3.392082	1.336046	8.323412	0.329786	3.985494	5.731382
	mid max	5.95	5.56	13.14	2.12	96.62	3.17	15.65	18.95
	mid min	0.23	0	0	0	64.77	1.68	0	0
	edge max	6.82	7.34	16.14	6.71	97.05	2.97	19.6	25.77
	edge min	0	0	0	0	60.89	1.61	0	0.41
5	Mid std. dev	1.600531	3.263398	3.233483	2.202705	15.38883	0.547843	10.44979	13.1227
	Edge std dev	1.235558	2.097532	3.218386	4.828176	9.807625	0.371319	5.731538	6.234963
	mid max	6.87	18.77	14.92	14.07	95.57	3.43	43.42	61.51
	mid min	0	0	0	0	9.5	0	0	0
	edge max	5.27	6.92	16.98	30.31	92.44	2.94	27.49	37.31
	edge min	0.52	0	0	0	41.76	1.45	0.62	4.23
6	Mid std. dev	1.560965	1.633558	2.714209	1.20798	8.723433	0.515125	6.948853	8.248365
	Edge std dev	1.63295	1.678379	3.55025	1.033886	8.386021	0.457586	4.024477	5.422197
	mid max	7.45	5.97	12.82	7.09	94.76	3.16	34.95	40.92
	mid min	0.44	0	0	0	49.48	0	0	0
	edge max	7.65	5.56	14.85	4.76	96.38	3.39	16.5	22.06
	edge min	0.38	0	0	0	58.09	1.71	0	0
7	Mid std. dev	1.464956	1.882791	3.203273	11.19084	0.465827	10.66815	12.41221	
	Edge std dev	1.220253	1.268831	4.519057	6.602108	2.132047	2.285495	3.23825	
	mid max	6.33	11.05	14.48	95.23	2.93	68.21	79.26	0
	mid min	0	0	0	20.74	0	0	0	0
	edge max	5.05	5.16	16.03	96.81	10.55	11.8	16.96	0
	edge min	0.45	0	0	65.16	1.74	0	0	0
8	Mid std. dev	1.352403	NA	2.55684	#DIV/0!	5.113415	0.253922	3.726633	0
	Edge std dev	1.469151	0.718196	4.725753	0.218814	6.179124	0.388095	0.981333	1.420719
	mid max	5.75	0	11.01	0	96.75	2.88	15.67	0
	mid min	0.19	0	0	0	72.04	1.58	0	0
	edge max	5.23	2.41	19.37	1.02	97.23	3.34	3.51	4.63
	edge min	0.2	0	0	0	75.73	1.61	0	0
9	Mid std. dev	1.273611	1.669616	2.102217	1.793536	8.834785	0.28361	6.032212	7.440435
	Edge std dev	1.727666	2.075997	2.51515	1.076691	12.23816	0.498304	10.71487	12.33277
	mid max	7.07	4.71	13.38	10.16	89.81	3.07	23.25	27.79
	mid min	1.41	0	3.37	0	57.99	1.9	0	0
	edge max	7.62	8.72	10.21	4.54	94.04	3.45	56.14	61.93
	edge min	0.65	0	0	0	24.83	0.87	0	0

TABLE H-2: AVERAGE WEIGHT PERCENTAGE CONTENTS OF NI, TI AND WC AT THE SURFACE OF LAYERS 1-9. THE VERTICAL AXES INDICATE THE AVERAGE WT.%, AND THE HORIZONTAL AXES DESCRIBE THE DISTANCE FROM THE TOP OF THE LAYER.

Layer 1 – [P = 150W, h = 0.09 mm, v = 400mm/s)

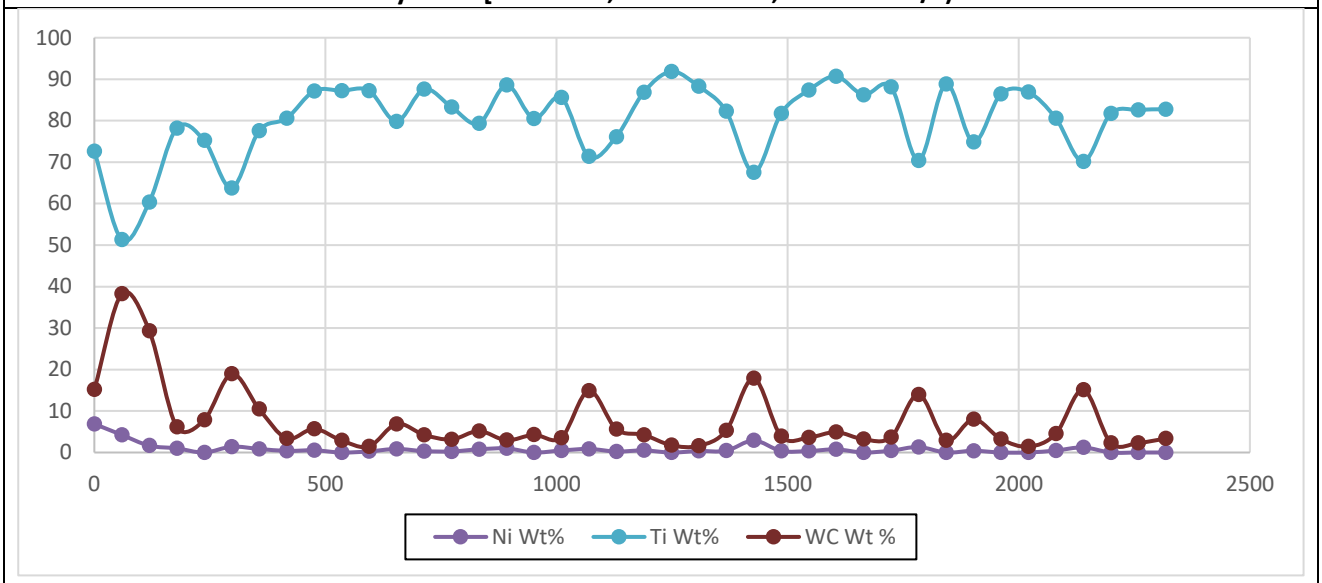

Layer 2 - (P = 150W, h = 0.09 mm, v = 600mm/s)

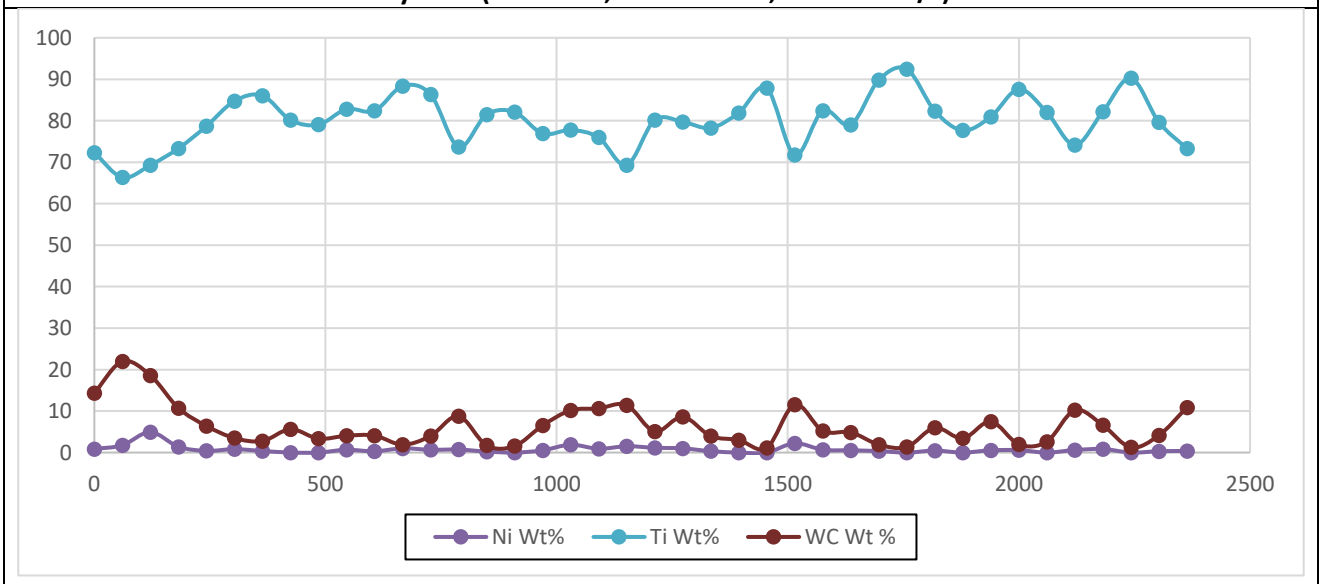

Layer 3 - (P = 150W, h = 0.09 mm, v = 800mm/s)

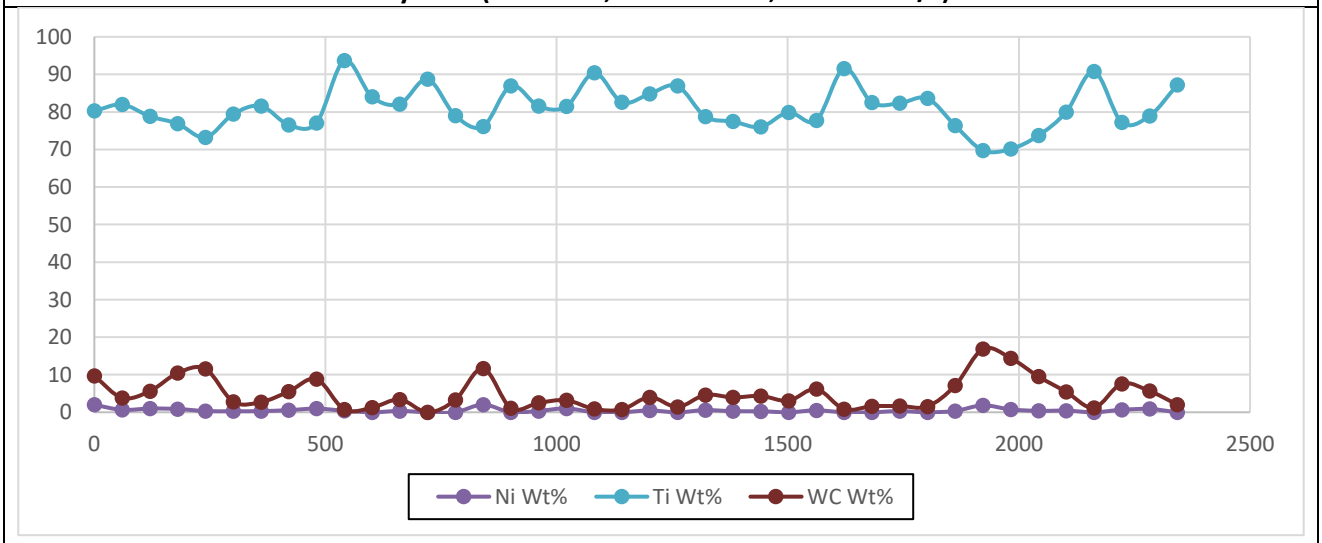

Layer 4 - (P = 150W, h = 0.11 mm, v = 400mm/s)

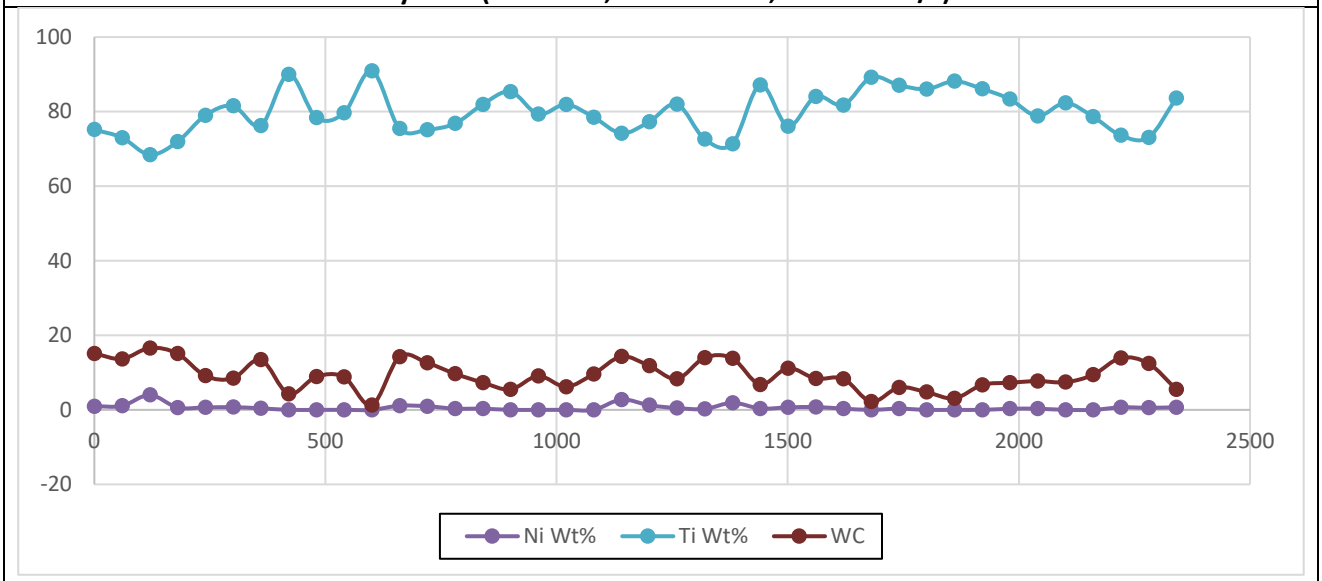

Layer 5 - (P = 150W, h = 0.11 mm, v = 600mm/s)

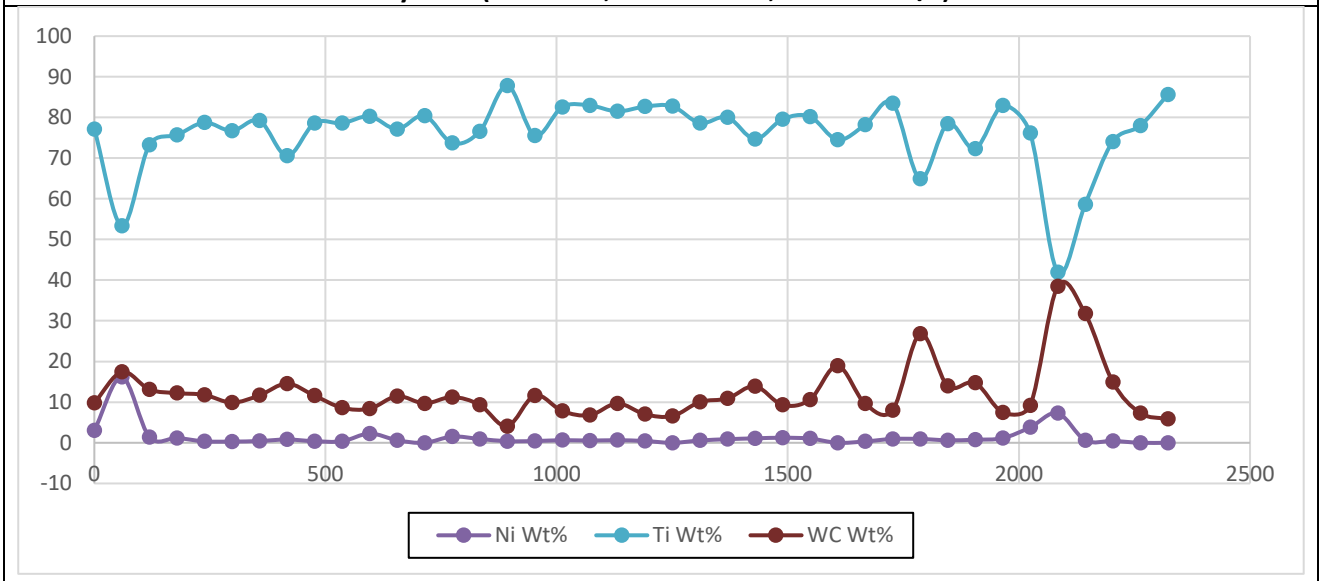

Layer 6 - (P = 150W, h = 0.11 mm, v = 800mm/s)

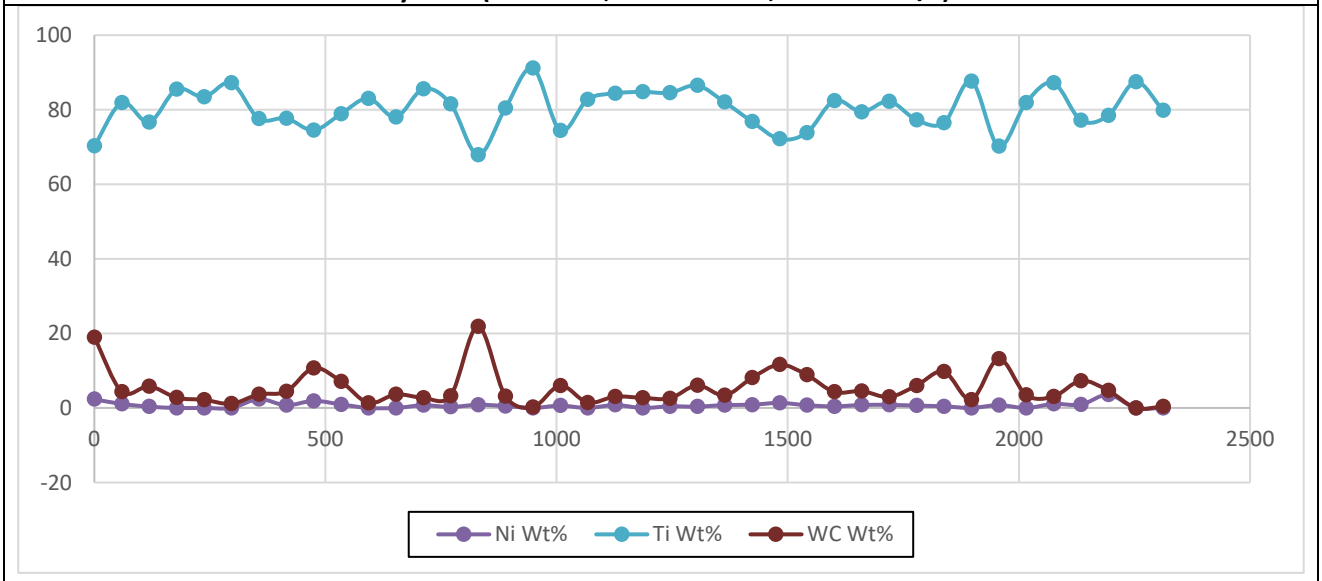

Layer 7 - (P = 150W, h = 0.13 mm, v = 400mm/s)

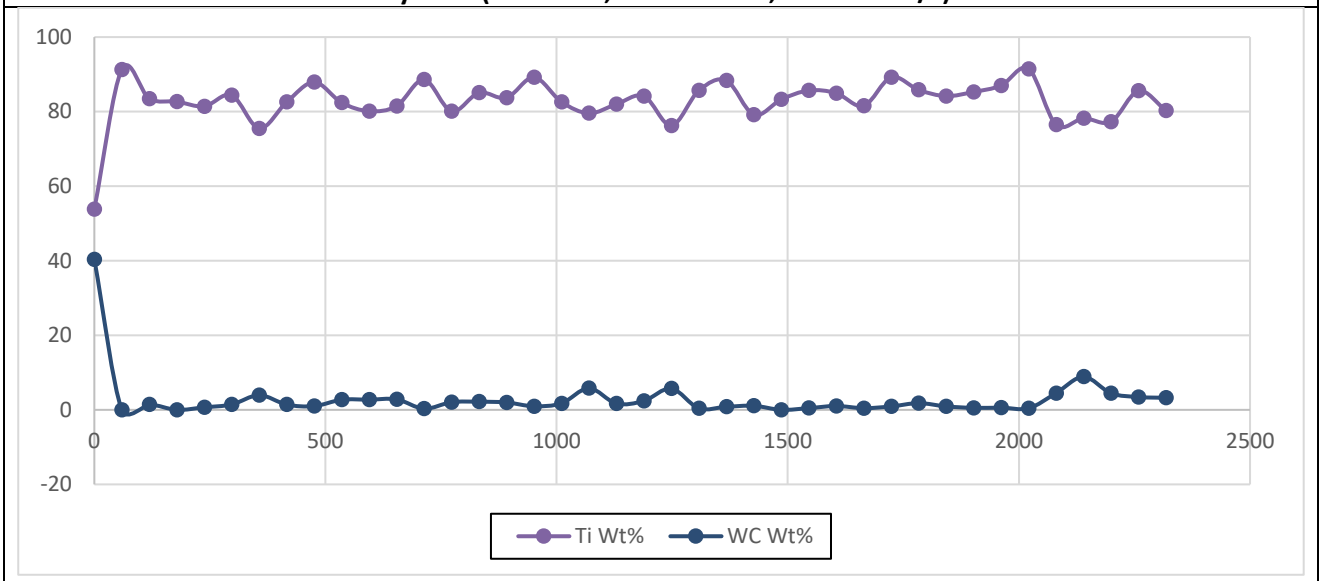

Layer 8 - (P = 150W, h = 0.13 mm, v = 600mm/s)

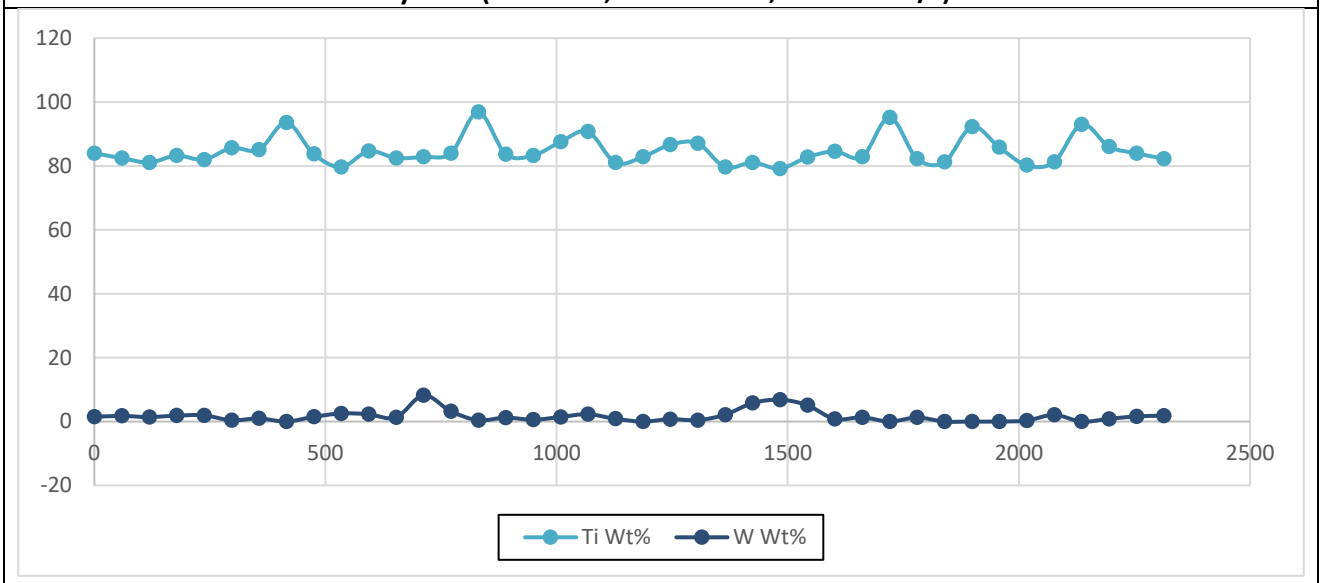

Layer 9 - (h = 0.13 mm, v = 800mm/s)

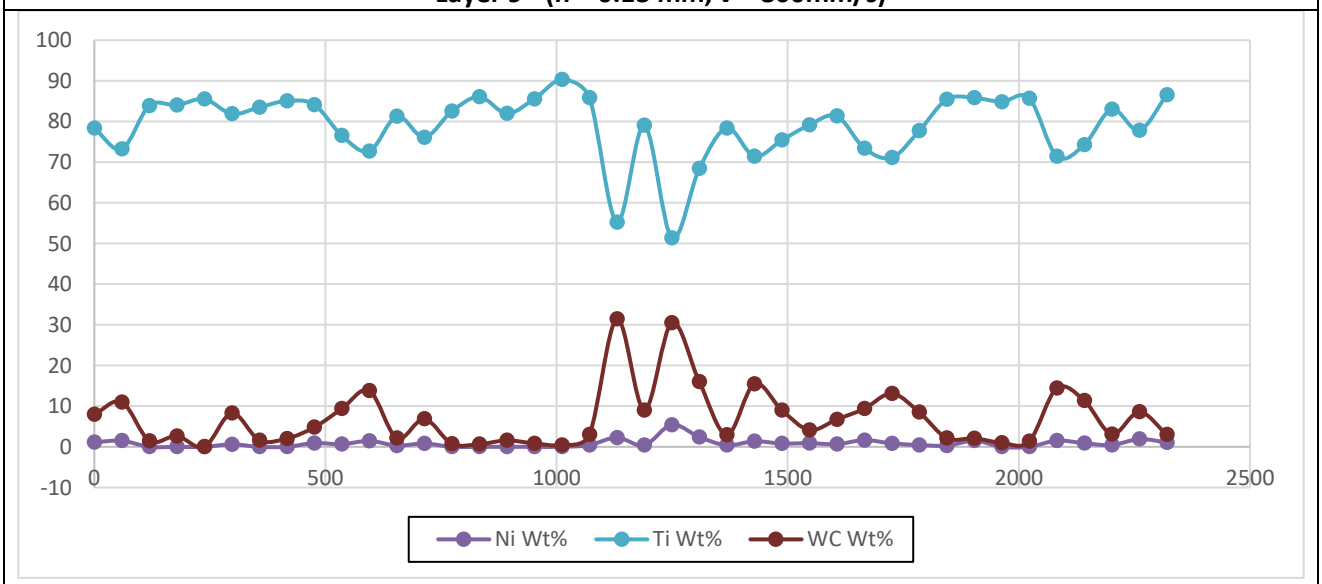

225-WATT

TABLE H-3: DESCRIPTIVE STATISTICAL VALUES FOR SURFACE CONTENTS OF LAYERS 10-18

Run #	Description	Al Wt%	C Wt%	N Wt%	Ni Wt%	Ti Wt%	V Wt%	W Wt%	WC Wt%
10	Mid std dev	0.70	7.98	10.93	0.30	15.73	0.54	3.10	9.96
	Edge std dev	0.57	8.15	8.46	0.51	14.10	0.43	4.83	11.44
	mid max	3.24	22.38	60.20	0.88	96.24	3.50	13.81	31.44
	mid min	0.27	0.00	0.00	0.00	24.51	0.67	0.00	0.00
	edge max	2.87	29.43	60.13	2.84	73.55	2.46	19.54	48.97
	edge min	0.50	0.00	20.45	0.00	12.93	0.54	1.19	1.26
11	Mid std dev	0.80	9.92	13.10	0.51	17.46	0.58	4.50	12.55
	Edge std dev	0.91	14.60	17.25	0.56	21.80	0.59	6.51	19.01
	mid max	3.65	35.26	53.02	1.96	96.32	3.37	22.36	47.14
	mid min	0.30	0.00	0.00	0.00	16.82	0.52	0.00	0.00
	edge max	4.56	79.33	60.22	3.14	97.06	2.79	39.27	95.91
	edge min	0.00	0.00	0.00	0.00	0.95	0.00	0.00	0.00
12	Mid std dev	0.97	19.41	13.61	0.82	18.22	0.60	6.50	23.98
	Edge std dev	0.71	8.73	12.32	0.52	15.19	0.51	5.58	13.02
	mid max	4.75	83.28	50.77	4.24	96.56	3.07	30.72	97.04
	mid min	0.00	0.00	0.00	0.00	0.70	0.00	0.00	0.00
	edge max	4.28	33.53	55.13	2.48	94.44	3.25	31.90	65.43
	edge min	1.08	0.00	0.00	0.00	25.59	0.61	0.35	0.51
13	Mid std dev	0.62	6.84	8.61	0.28	13.37	0.42	2.85	8.68
	Edge std dev	0.61	10.67	13.79	0.46	16.17	0.49	4.20	13.83
	mid max	3.48	19.53	56.69	0.91	82.61	2.57	13.97	31.68
	mid min	0.67	0.00	13.06	0.00	22.61	0.45	0.00	0.00
	edge max	2.74	55.43	57.60	1.73	97.13	2.87	25.20	80.63
	edge min	0.00	0.00	0.00	0.00	17.17	0.57	0.00	0.00
14	Mid std dev	0.89	19.96	16.30	0.82	16.42	0.52	12.11	29.44
	Edge std dev	0.67	8.68	6.86	1.16	12.50	0.37	5.68	13.33
	mid max	3.41	87.02	50.14	3.76	70.11	2.61	46.45	97.63
	mid min	0.00	0.00	0.00	0.00	1.19	0.00	0.00	0.00
	edge max	3.24	32.06	53.57	6.14	62.68	1.83	27.20	59.26
	edge min	0.79	0.00	24.64	0.00	5.78	0.26	0.62	0.62
15	Mid std dev	0.84	18.03	15.35	3.05	16.45	0.53	10.88	26.05
	Edge std dev	0.65	21.04	15.12	2.31	17.29	0.67	7.21	23.96
	mid max	3.21	80.66	50.41	14.51	71.42	2.39	45.79	97.86
	mid min	0.00	0.00	0.00	0.31	0.55	0.00	1.05	1.05
	edge max	2.79	86.48	50.79	13.16	92.79	4.19	37.36	97.53
	edge min	0.00	0.00	0.00	0.00	0.36	0.00	1.06	1.06
16	Mid std dev	0.81	9.84	6.95	0.87	12.15	0.44	6.25	13.92
	Edge std dev	0.59	9.61	9.98	0.62	14.70	0.46	4.16	12.39
	mid max	3.88	28.98	51.07	3.45	59.41	2.75	26.00	54.08
	mid min	0.29	0.00	23.22	0.00	9.70	0.00	0.00	0.00
	edge max	3.37	44.34	55.30	2.93	89.47	3.03	16.25	49.44
	edge min	0.34	0.00	0.00	0.00	14.91	0.47	0.00	0.00
17	Mid std dev	0.80	16.52	13.70	10.05	16.93	0.54	7.06	20.72
	Edge std dev	1.04	17.89	13.32	0.86	17.47	0.53	6.14	21.55
	mid max	3.30	84.90	51.21	64.43	75.82	2.53	29.91	98.42
	mid min	0.00	0.00	0.00	0.00	0.54	0.00	0.40	0.52
	edge max	5.57	82.66	53.55	4.09	94.43	2.38	24.97	96.62
	edge min	0.21	0.00	0.00	0.00	1.06	0.00	0.00	0.00
18	Mid std dev	1.03	15.03	14.56	2.11	14.71	0.48	12.00	25.21
	Edge std dev	1.10	20.16	19.94	3.78	19.67	0.66	15.33	31.74
	mid max	4.02	70.96	51.92	8.05	61.67	2.02	46.73	95.63
	mid min	0.12	0.00	0.00	0.00	1.07	0.00	0.00	0.00
	edge max	4.65	74.83	52.78	22.72	70.54	2.49	60.42	95.57
	edge min	0.00	0.00	0.00	0.00	0.41	0.00	0.00	0.00

TABLE H-4: AVERAGE WEIGHT PERCENTAGE CONTENTS OF NI, TI AND WC AT THE SURFACE OF LAYERS 10-18. THE VERTICAL AXES INDICATE THE AVERAGE WT.%, AND THE HORIZONTAL AXES DESCRIBE THE DISTANCE FROM THE TOP OF THE LAYER.

Layer 10 - (P = 225W, h = 0.09 mm, v = 600mm/s)

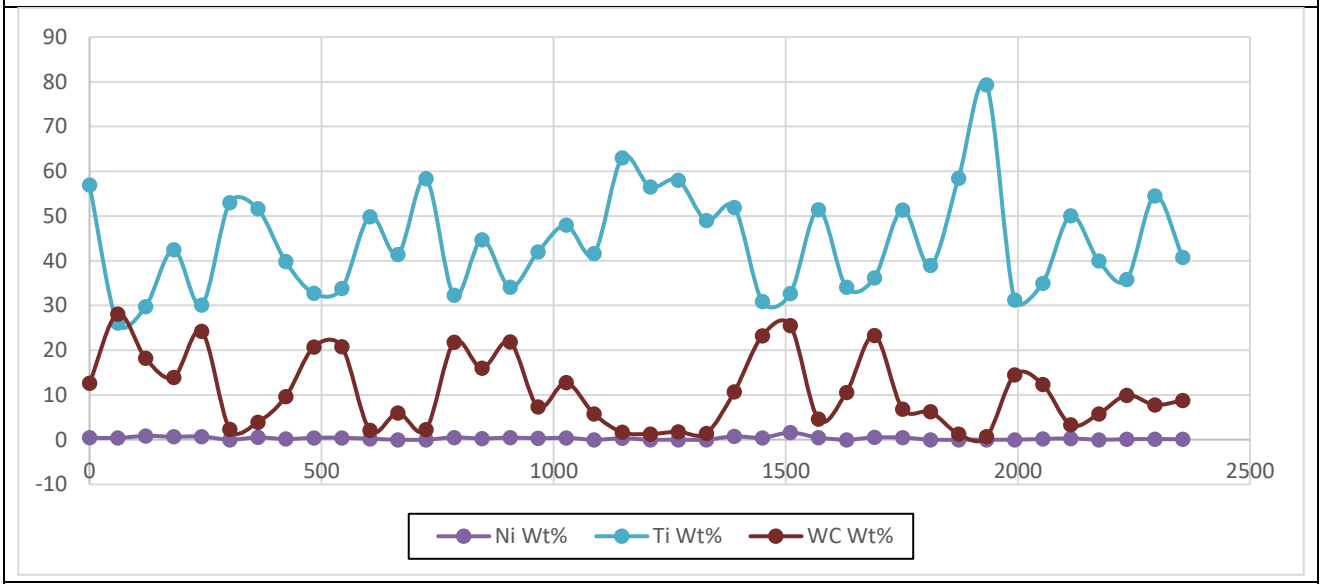

Layer 11 - (P = 225W, h = 0.09 mm, v = 900mm/s)

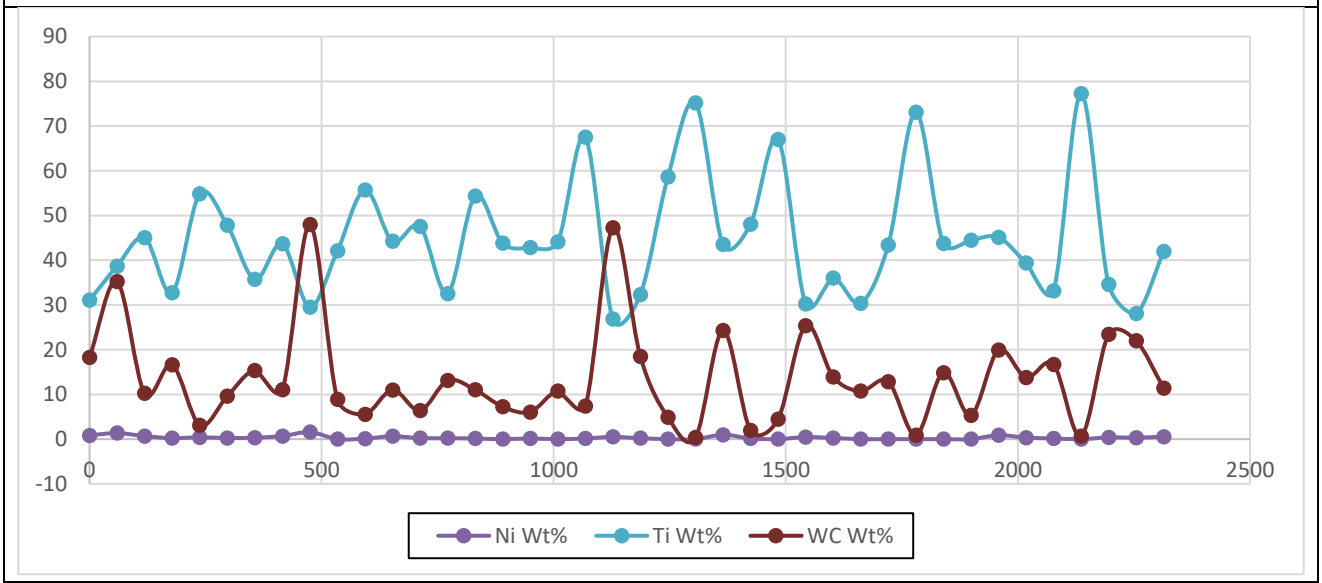

Layer 12 - (P = 225W, h = 0.09 mm, v = 1200mm/s)

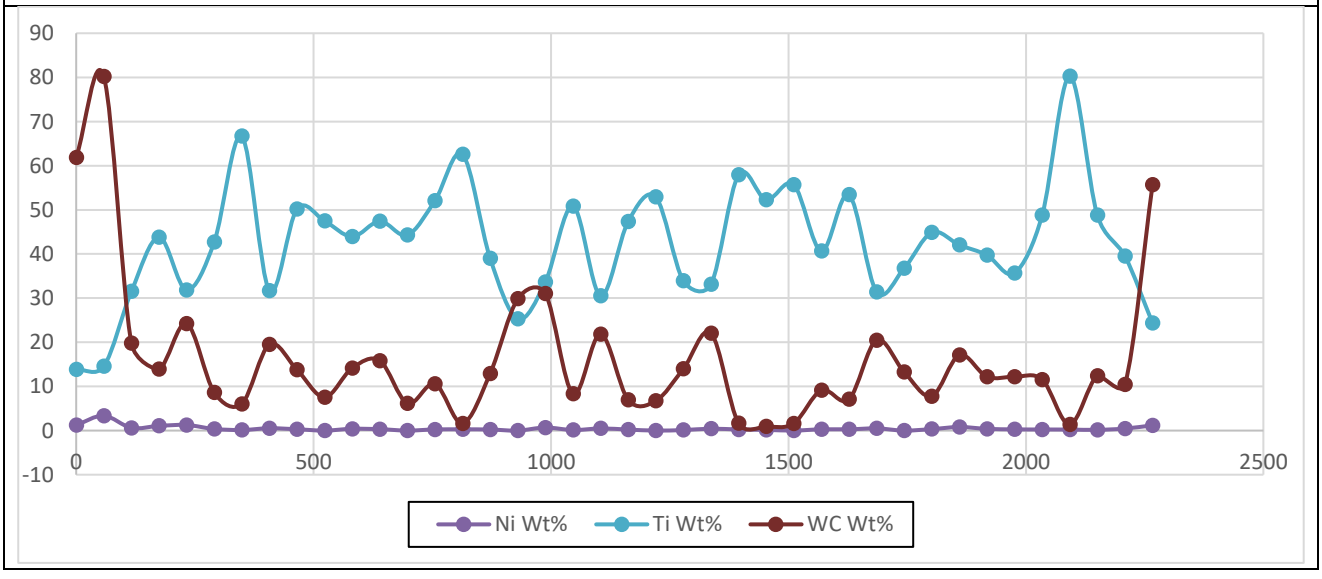

Layer 13 - (P = 225W, h = 0.11 mm, v = 600mm/s)

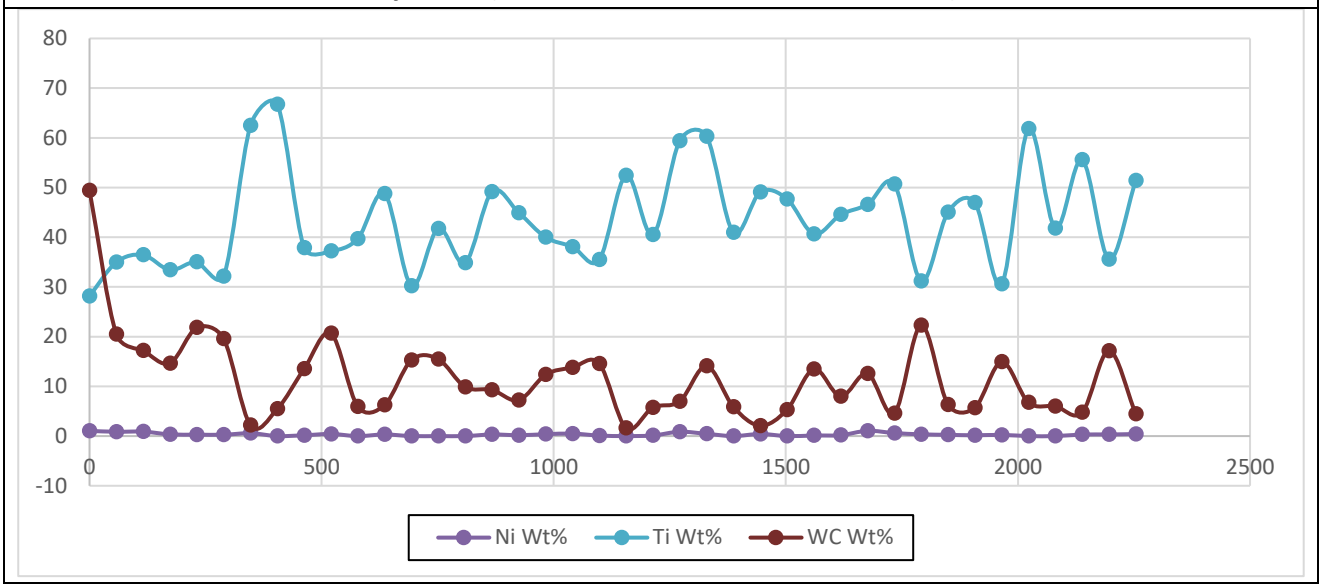

Layer 14 - (P = 225W, h = 0.11 mm, v = 900mm/s)

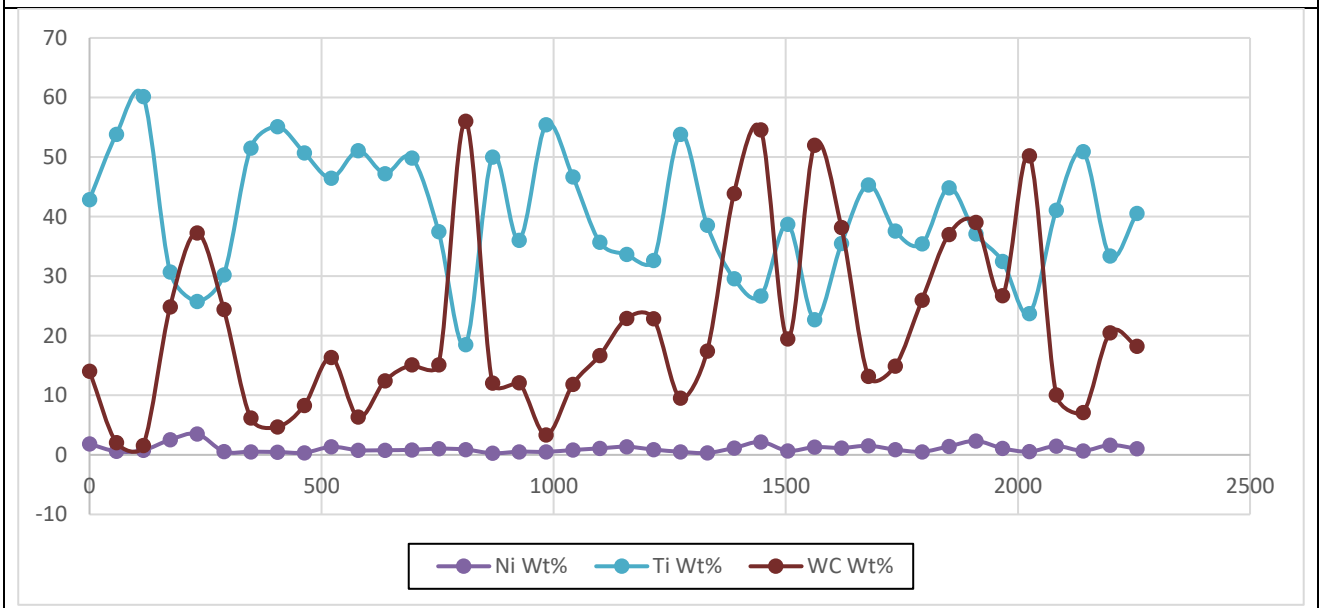

Layer 15 - (P = 225W, h = 0.11 mm, v = 1200mm/s)

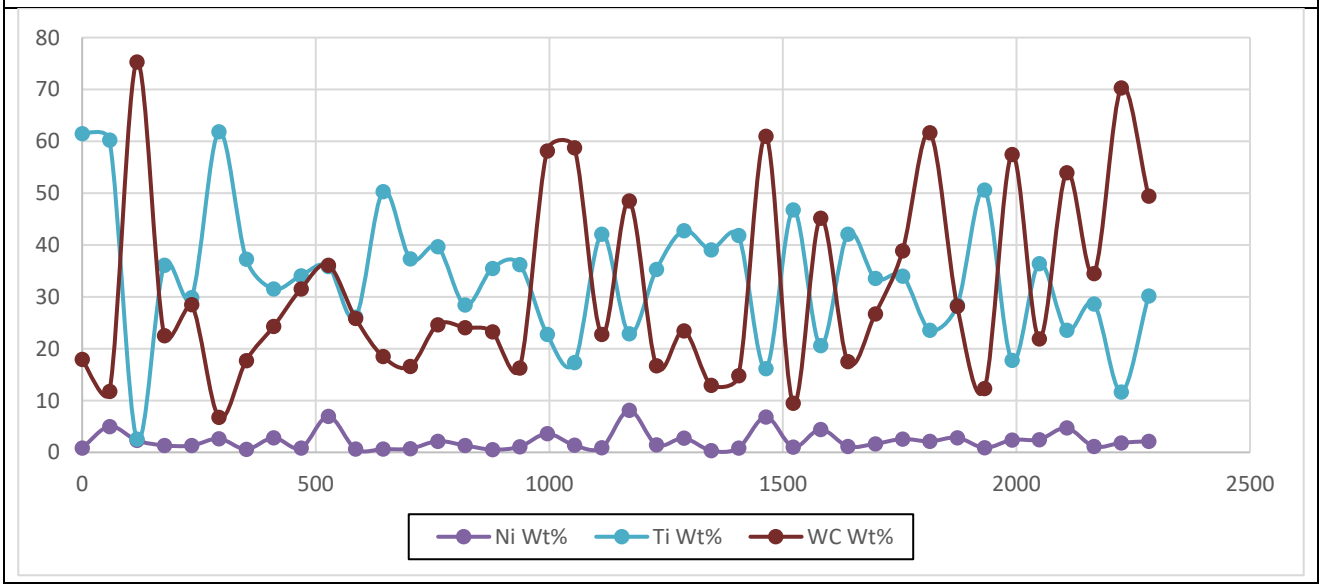

Layer 16 - (P = 225W, h = 0.13 mm, v = 600mm/s)

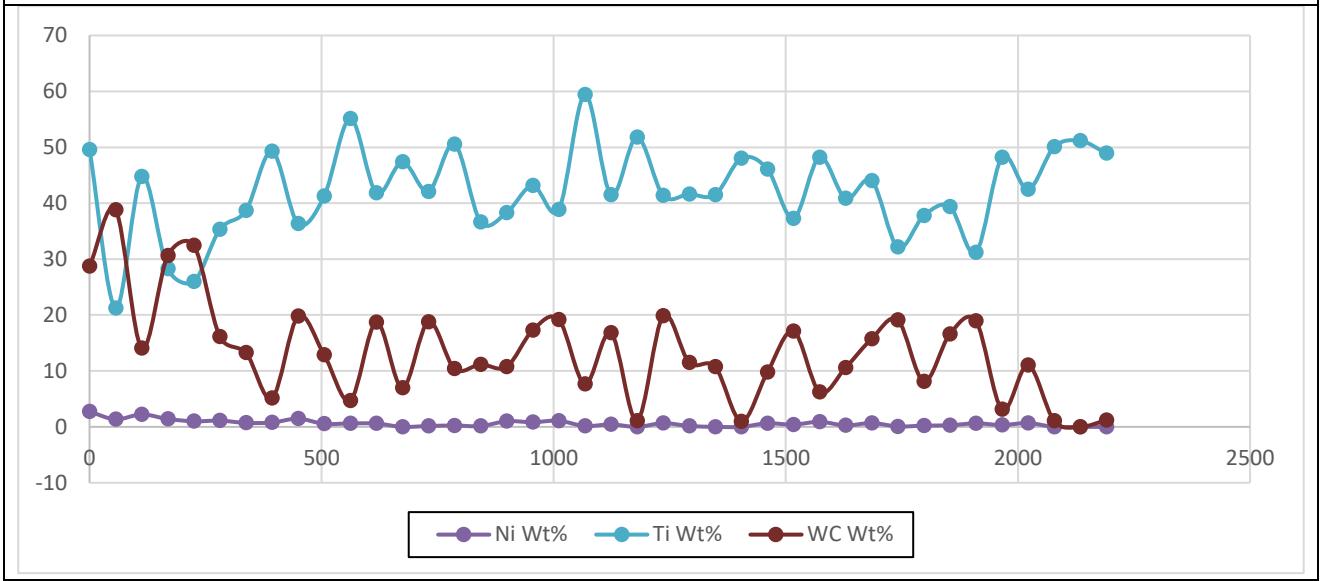

Layer 17 - (P = 225W, h = 0.13 mm, v = 900mm/s)

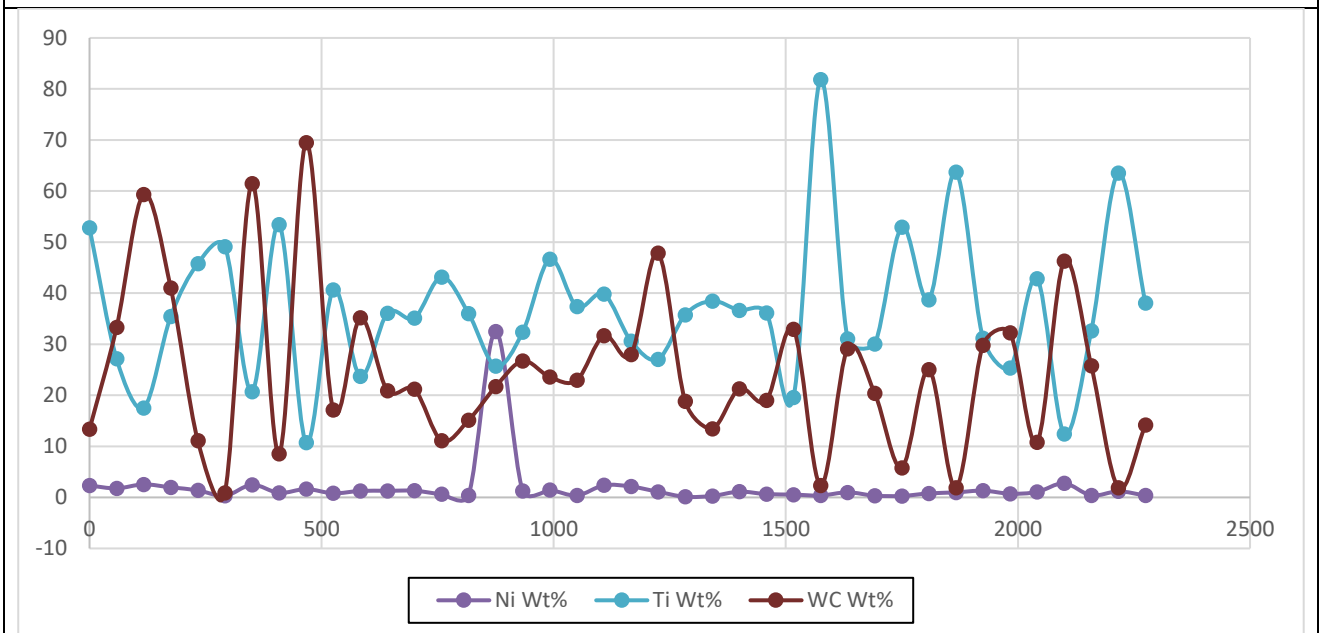

Layer 18 - (P = 225W, h = 0.13 mm, v = 1200mm/s)

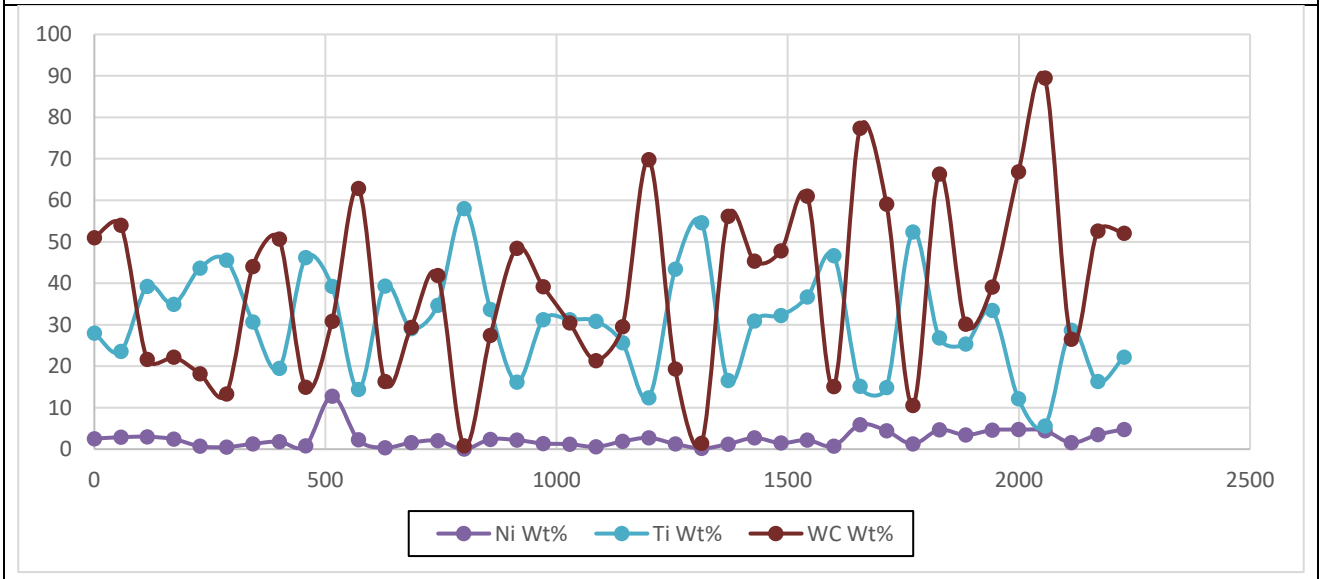

300-WATT

TABLE H-5: DESCRIPTIVE STATISTICAL VALUES FOR SURFACE CONTENTS OF LAYERS 10-18

Run #	Description	Al Wt%	C Wt%	N Wt%	Ni Wt%	Ti Wt%	V Wt%	W Wt%	WC Wt%
19	Mid std dev	0.53	11.34	12.79	1.17	9.31	0.31	5.12	15.29
	Edge std dev	0.78	13.60	9.06	1.23	13.18	0.36	5.22	17.64
	mid max	3.59	46.89	54.62	6.15	62.91	2.53	26.05	71.62
	mid min	0.87	0.00	0.00	0.00	17.36	0.42	0.72	0.90
	edge max	3.21	74.54	58.91	4.93	58.58	1.78	20.99	93.92
	edge min	0.00	0.00	0.00	0.00	1.15	0.00	0.73	1.09
20	Mid std dev	0.97	3.99	2.94	3.55	16.20	0.55	14.23	16.74
	Edge std dev	1.05	10.89	3.53	5.03	19.76	0.66	15.99	21.18
	mid max	4.74	19.11	10.93	17.20	85.64	2.98	57.36	66.82
	mid min	0.87	0.00	0.00	0.00	22.02	0.00	0.00	0.00
	edge max	4.78	70.39	13.05	25.31	85.53	2.91	67.87	92.50
	edge min	0.22	0.00	0.00	0.00	2.06	0.00	0.95	0.95
21	Mid std dev	1.25	7.68	2.59	2.42	19.41	0.69	15.06	21.23
	Edge std dev	1.43	7.56	3.85	3.61	24.36	0.81	20.60	26.43
	mid max	5.40	36.54	10.25	9.69	86.44	3.33	57.04	93.55
	mid min	0.00	0.00	0.00	0.00	0.62	0.00	0.00	0.78
	edge max	5.13	39.21	12.81	14.53	86.78	3.20	74.86	91.97
	edge min	0.00	0.00	0.00	0.00	0.80	0.00	0.00	0.00
22	Mid std dev	0.70	3.22	2.53	2.08	12.40	0.37	10.34	12.12
	Edge std dev	0.90	2.29	2.99	1.69	12.79	0.40	11.51	13.23
	mid max	4.20	17.27	11.33	10.00	87.86	2.83	44.47	50.27
	mid min	1.49	0.00	0.00	0.00	37.74	1.36	0.55	1.12
	edge max	4.79	8.81	23.37	6.90	84.39	2.71	52.09	58.90
	edge min	0.84	0.00	4.36	0.00	27.94	0.90	0.73	0.73
23	Mid std dev	1.31	10.06	2.99	2.24	22.70	0.79	18.15	24.67
	Edge std dev	0.95	2.85	3.42	2.56	17.21	0.57	16.99	19.21
	mid max	5.66	45.46	12.42	10.85	89.00	3.00	77.37	95.75
	mid min	0.00	0.00	0.00	0.00	1.89	0.00	0.00	0.00
	edge max	4.38	10.27	12.41	15.17	85.15	2.89	60.22	67.29
	edge min	0.78	0.00	0.00	0.00	21.98	0.00	0.00	0.00
24	Mid std dev	1.55	9.87	3.24	2.50	20.90	0.91	16.93	21.69
	Edge std dev	1.25	6.40	3.12	2.93	20.90	0.75	16.04	21.42
	mid max	6.36	61.79	11.42	11.79	90.39	5.49	80.39	88.64
	mid min	0.00	0.00	0.00	0.00	2.35	0.00	0.00	0.00
	edge max	4.93	29.76	11.90	16.44	100.00	3.06	69.42	89.53
	edge min	0.00	0.00	0.00	0.00	2.13	0.00	0.00	0.00
25	Mid std dev	0.84	5.63	4.47	4.04	16.37	0.55	13.92	15.34
	Edge std dev	0.87	4.50	2.90	2.00	17.71	0.50	16.25	19.96
	mid max	4.21	28.20	26.96	22.45	84.63	2.81	77.82	87.34
	mid min	0.50	0.00	0.00	0.00	8.15	0.00	0.85	1.82
	edge max	3.89	27.12	12.80	8.29	87.01	2.52	66.27	93.39
	edge min	0.00	0.00	0.00	0.00	2.50	0.00	0.86	0.86
26	Mid std dev	1.47	9.03	5.42	2.22	22.77	1.06	17.19	23.60
	Edge std dev	1.12	6.84	3.64	8.25	22.32	0.66	17.67	22.86
	mid max	5.84	35.42	32.31	8.51	100.00	6.63	68.22	95.16
	mid min	0.00	0.00	0.00	0.00	0.79	0.00	0.00	0.00
	edge max	5.20	31.48	13.96	50.64	83.72	2.49	68.21	93.60
	edge min	0.00	0.00	0.00	0.00	1.37	0.00	0.00	0.00
27	Mid std dev	1.54	7.19	3.45	4.93	27.00	1.00	22.05	27.07
	Edge std dev	1.36	6.52	3.41	4.44	24.04	0.83	19.40	25.04
	mid max	5.67	29.81	11.57	19.37	93.42	3.56	72.51	91.55
	mid min	0.00	0.00	0.00	0.00	1.63	0.00	0.00	1.29
	edge max	4.87	32.15	10.65	26.30	88.49	2.85	69.11	94.37
	edge min	0.00	0.00	0.00	0.00	0.51	0.00	2.45	3.83

TABLE H-6 : AVERAGE WEIGHT PERCENTAGE CONTENTS OF NI, TI AND WC AT THE SURFACE OF LAYERS 19-27. THE VERTICAL AXES INDICATE THE AVERAGE WT.%, AND THE HORIZONTAL AXES DESCRIBE THE DISTANCE FROM THE TOP OF THE LAYER.

Layer 19 - (P = 300W, h = 0.09 mm, v = 900mm/s)

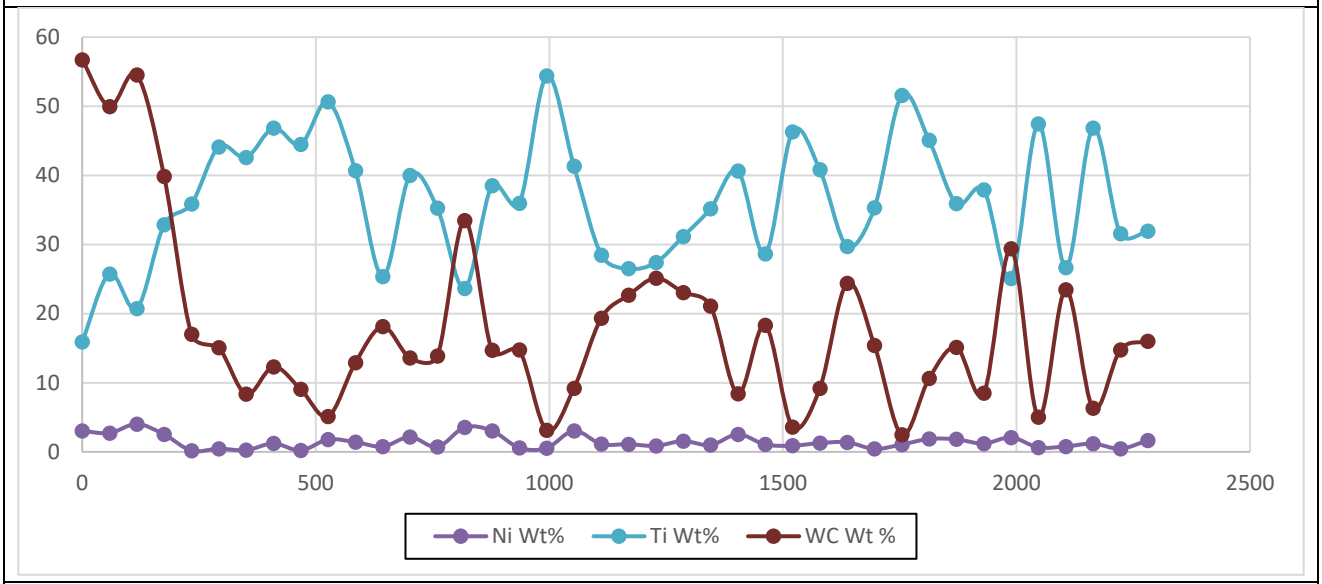

Layer 20 - (P = 300W, h = 0.09 mm, v = 1200mm/s)

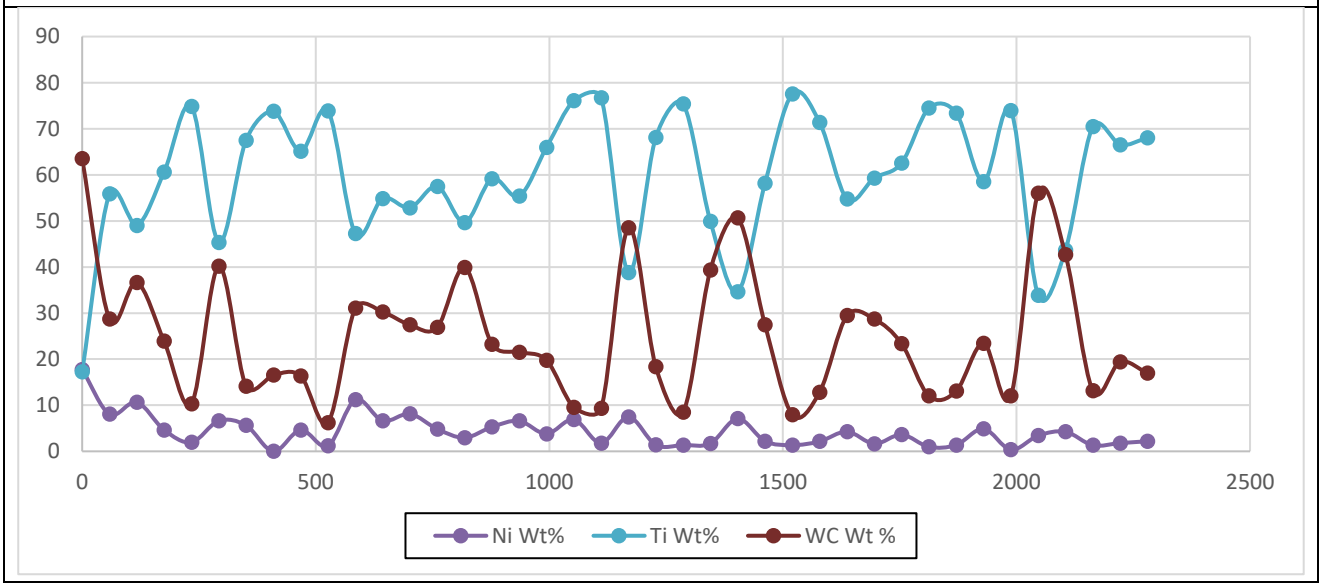

Layer 21 - (P = 300W, h = 0.09 mm, v = 1600mm/s)

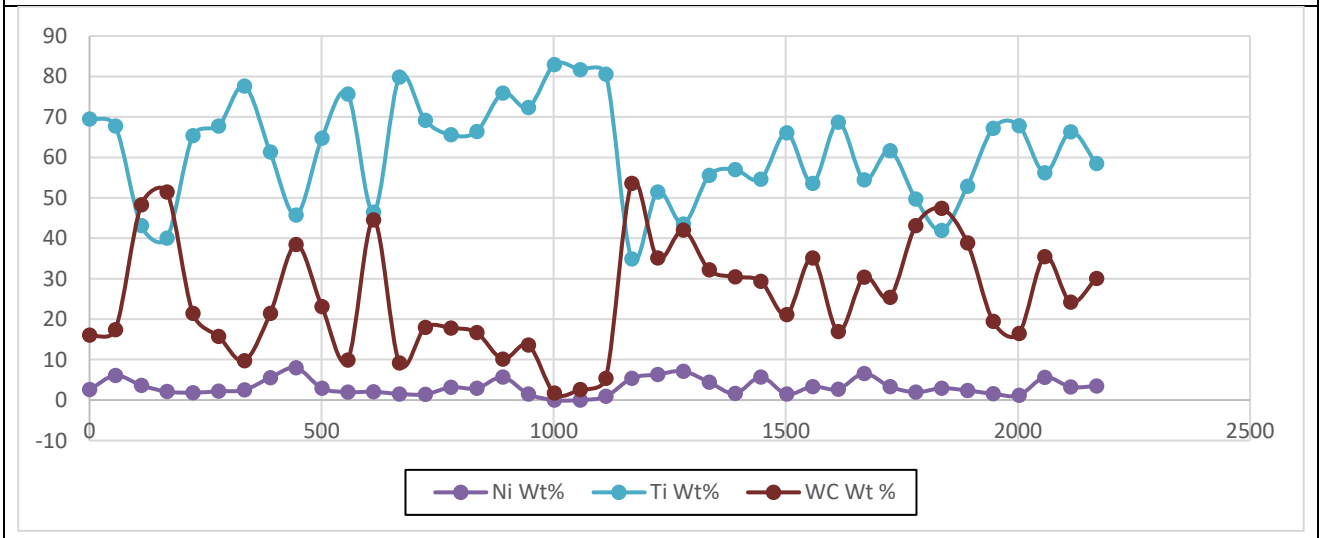

Layer 22 - (P = 300W, h = 0.11 mm, v = 800mm/s)

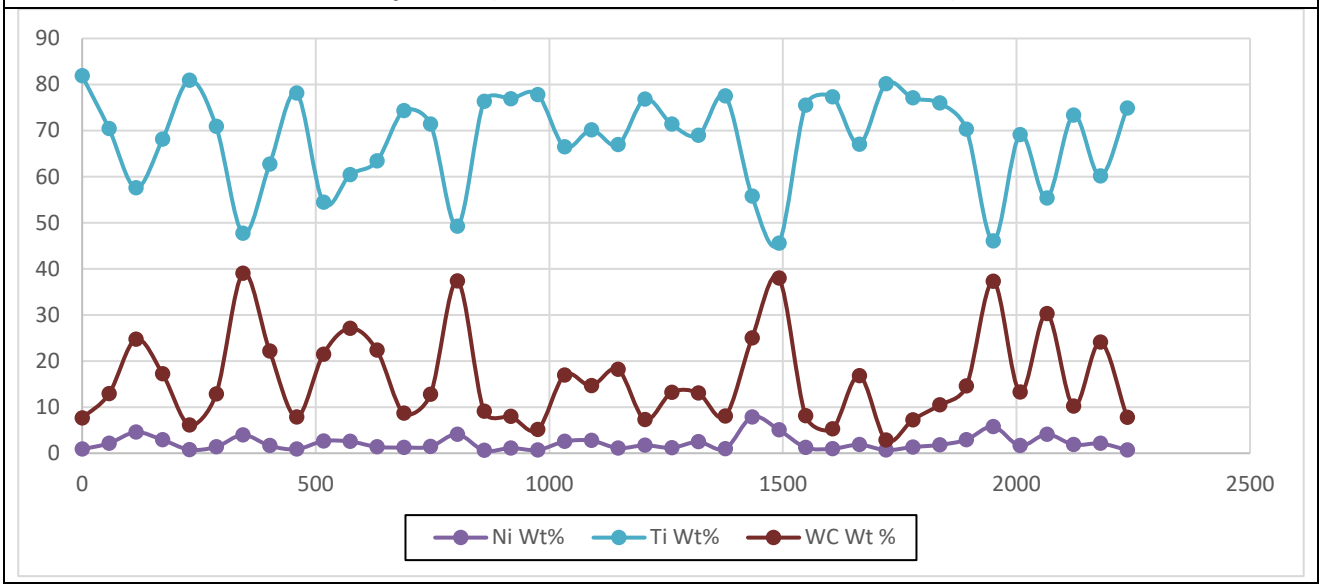

Layer 23 - (P = 300W, h = 0.11 mm, v = 1200mm/s)

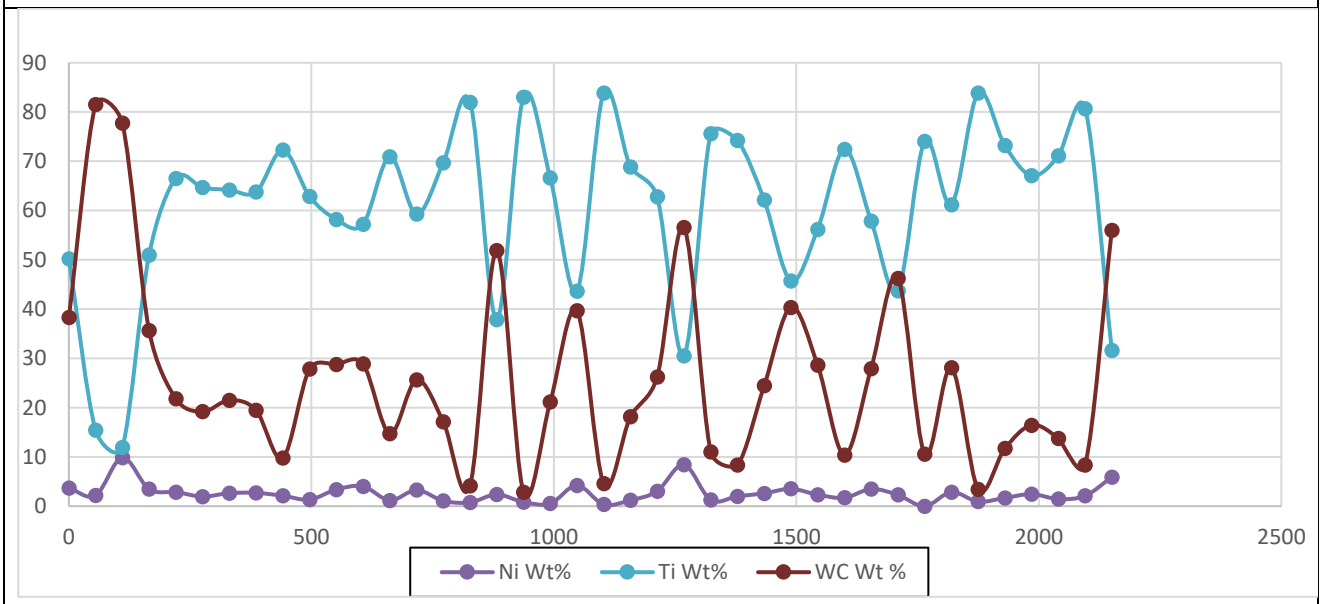

Layer 24 - (P = 300W, h = 0.11 mm, v = 1600mm/s)

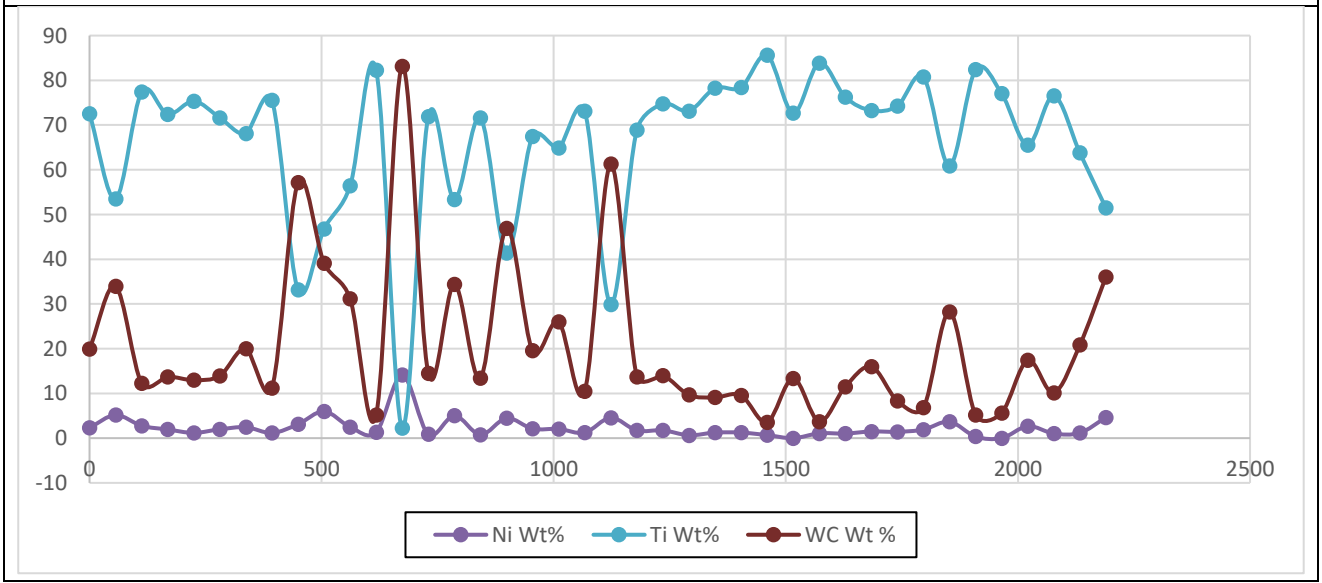

Layer 25 - (P = 300W, h = 0.13 mm, v = 800mm/s)

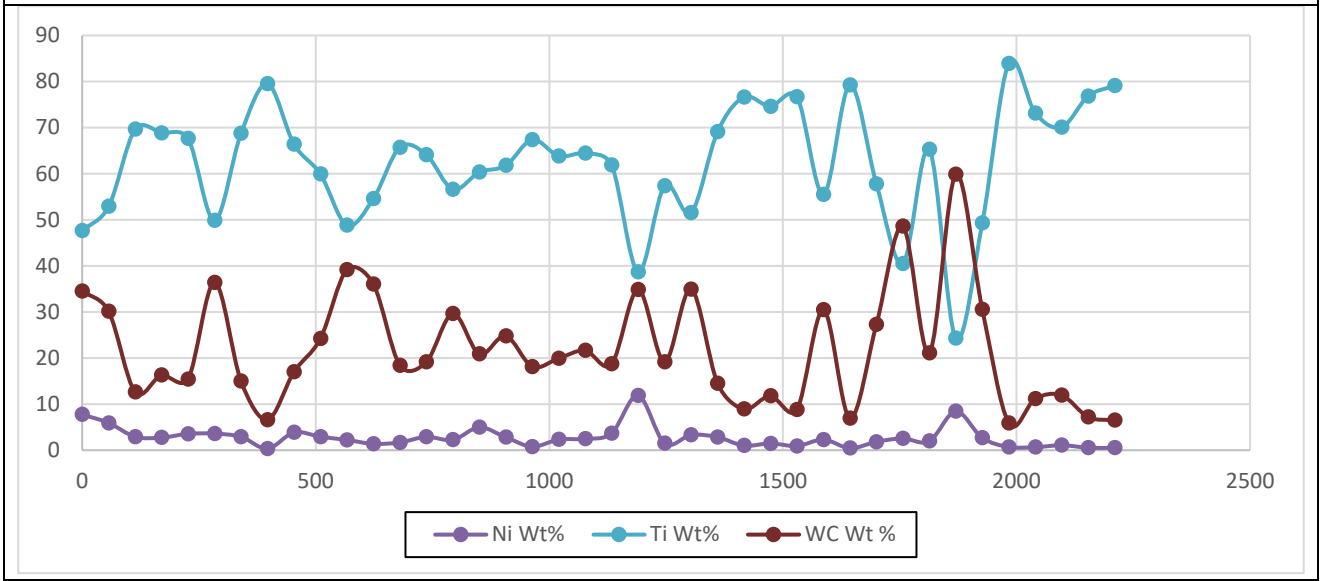

Layer 26 - (P = 300W, h = 0.13 mm, v = 1200mm/s)

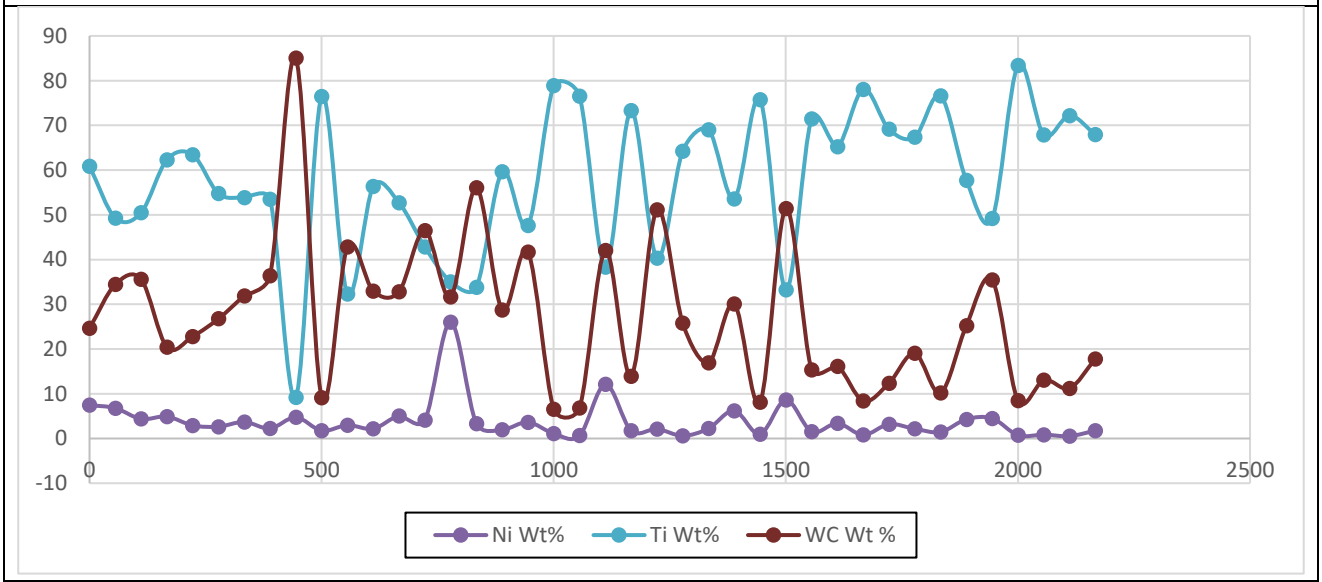

Layer 27 - (P = 300W, h = 0.13 mm, v = 1600mm/s)

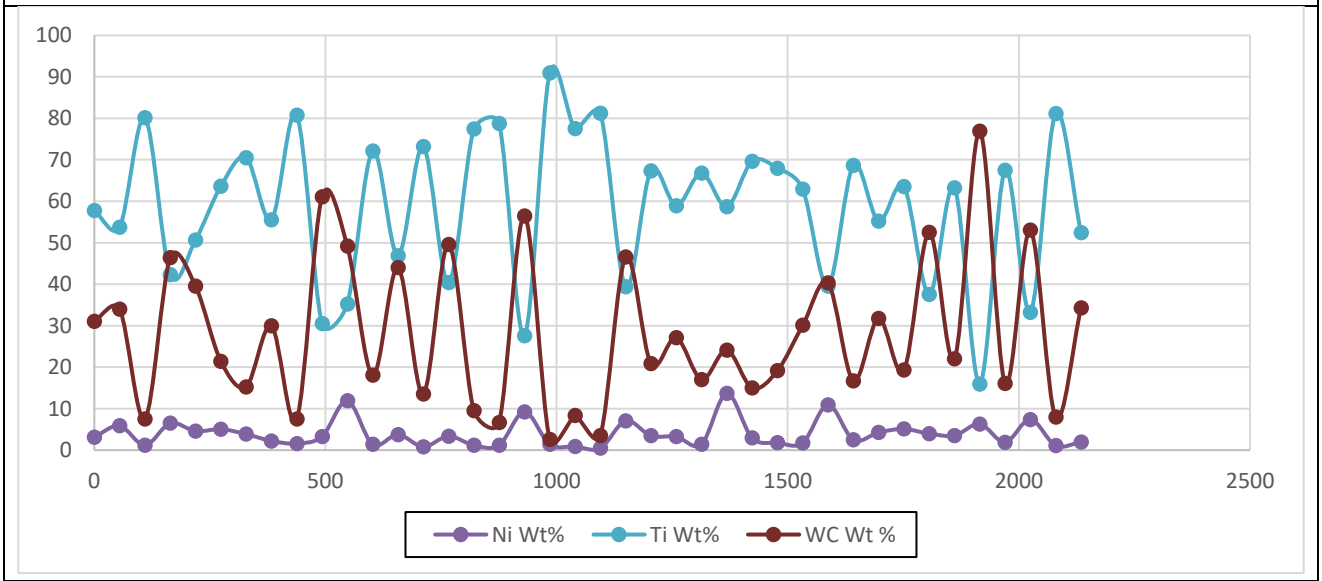

APPENDIX I: STATISTICAL ANALYSIS OF WC SURFACE PRESENCE ON LAYERED SCANS

The average surface contents estimated at each layer are included in Table J-1. The data on the WC-contents layer surfaces was used to conduct a univariate regression analysis in order to predict the effects of each response on the outcomes of the.

TABLE I-1: AVERAGE SURFACE CONTENTS FOR ELEMENTS AT EACH LAYER

Run #	Al Wt%	C Wt%	N Wt%	Ni Wt%	Ti Wt%	V Wt%	W Wt%	WC Wt %
1	2.91	0.66	6.17	0.79	80.24	2.45	6.79	7.44
2	3.40	1.06	7.02	0.73	80.01	2.51	5.27	6.34
3	3.88	0.97	7.39	0.47	80.95	2.50	3.85	4.82
4	3.23	1.27	8.46	0.57	79.89	2.32	4.27	9.31
5	3.38	1.98	8.06	1.36	76.20	2.30	6.71	12.15
6	3.99	1.27	7.38	0.64	80.54	2.47	3.70	4.97
7	3.21	0.72	8.41	0.00	82.70	2.76	2.22	2.93
8	2.79	0.32	9.00	0.06	84.78	2.28	0.76	1.08
9	4.01	1.48	6.77	0.83	78.89	2.44	5.59	7.07
10	1.57	7.13	41.90	0.30	44.19	1.24	3.67	10.80
11	1.78	10.45	38.27	0.33	44.66	1.25	3.26	13.71
12	2.09	11.88	37.27	0.45	42.59	1.30	4.43	16.31
13	1.67	8.26	41.70	0.31	43.51	1.22	3.34	11.59
14	1.90	12.04	34.45	1.07	40.24	1.21	9.08	21.12
15	1.51	20.26	29.75	2.23	33.81	1.05	11.39	31.65
16	1.71	8.32	40.89	0.61	42.19	1.16	5.11	13.43
17	1.60	16.78	34.12	1.91	36.95	1.09	7.55	24.32
18	1.58	23.60	25.63	2.51	30.53	0.90	15.25	38.85
19	1.76	11.41	41.53	1.46	36.12	1.04	6.68	18.10
20	2.75	5.19	6.22	4.35	59.80	1.90	19.80	24.99
21	2.75	5.35	5.03	3.22	61.53	2.00	20.12	25.48
22	2.89	3.16	8.71	2.19	68.11	1.98	12.96	16.12
23	2.54	5.41	6.26	2.61	60.71	1.90	20.57	25.98
24	2.84	5.43	5.63	2.37	66.46	2.11	15.15	20.58
25	2.47	5.42	8.58	2.77	62.50	1.79	16.46	21.88
26	2.59	6.87	6.56	3.81	58.10	1.78	20.29	27.16
27	2.48	6.05	4.65	3.93	58.92	1.87	22.10	28.15

LINEAR REGRESSION MODEL

TABLE I-2: LINEAR UNIVARIATE TEST OF SIGNIFICANCE FOR CARBIDE CONTENT % AT LAYER SURFACE

Effect	Univariate Tests of Significance for WC wt % Sigma-restricted parameterization Effective hypothesis decomposition; Std. Error of Estimate: 5.7886				
	SS	Degr. of Freedom	MS	F	p
Intercept	10.2689	1	10.26894	0.306465	0.585994
power(W)	31.739	1	31.73902	0.947215	0.342054
speed(mm/s)	1.2118	1	1.21181	0.036165	0.851092
Hatch Spacing (mm)	4.8968	1	4.89679	0.146139	0.706285
power(W)*speed(mm/s)	86.7832	1	86.78325	2.589947	0.123215
power(W)*Hatch Spacing (mm)	1.1736	1	1.17357	0.035024	0.853431
speed(mm/s)*Hatch Spacing (mm)	40.8174	1	40.81738	1.218148	0.282827
Error	670.1545	20	33.50772		

TABLE I-3: PARAMETER ESTIMATES FOR EQUATION 7-1

Effect	Parameter Estimates - Sigma-restricted parameterization									
	WC wt % Param.	WC wt % Std.Err	WC wt% t	WC wt% p	-95% Cnf Lmt	95% Cnf.Lmt	WC wt % Beta (ß)	WC wt % St.Err.ß	-95% Cnf Lmt	95% Cnf. Lmt
Intercept	-17.33	31.30	-0.55	0.59	-82.62	47.96				
power(W)	0.17	0.18	0.97	0.34	-0.20	0.55	1.12	1.15	-1.28	3.52
speed(mm/s)	0.01	0.03	0.19	0.85	-0.07	0.08	0.24	1.26	-2.39	2.87
Hatch Spacing (mm)	-99.31	259.77	-0.38	0.71	-641.18	442.57	-0.17	0.44	-1.10	0.76
power(W)*speed(mm/s)	0.00	0.00	-1.61	0.12	0.00	0.00	-1.40	0.87	-3.21	0.41
power(W)*Hatch Spacing (mm)	-0.29	1.55	-0.19	0.85	-3.52	2.94	-0.23	1.25	-2.85	2.38
speed(mm/s)*Hatch Spacing (mm)	0.30	0.27	1.10	0.28	-0.26	0.86	1.30	1.18	-1.16	3.76

TABLE I-4: TEST OF SS FOR WHOLE MODEL VS SS RESIDUAL

Dependent Variable	Test of SS Whole Model vs. SS Residual (Spreadsheet2 in Workbook6)										
	Multiple R	Multiple R^2	Adjusted R^2	SS Model	df Model	MS Model	SS Residual	df Residual	MS Residual	F	p
WC wt %	0.8531	0.7278	0.6461	1791.6	6	298.6	670.15	20	33.508	8.9113	8E-05

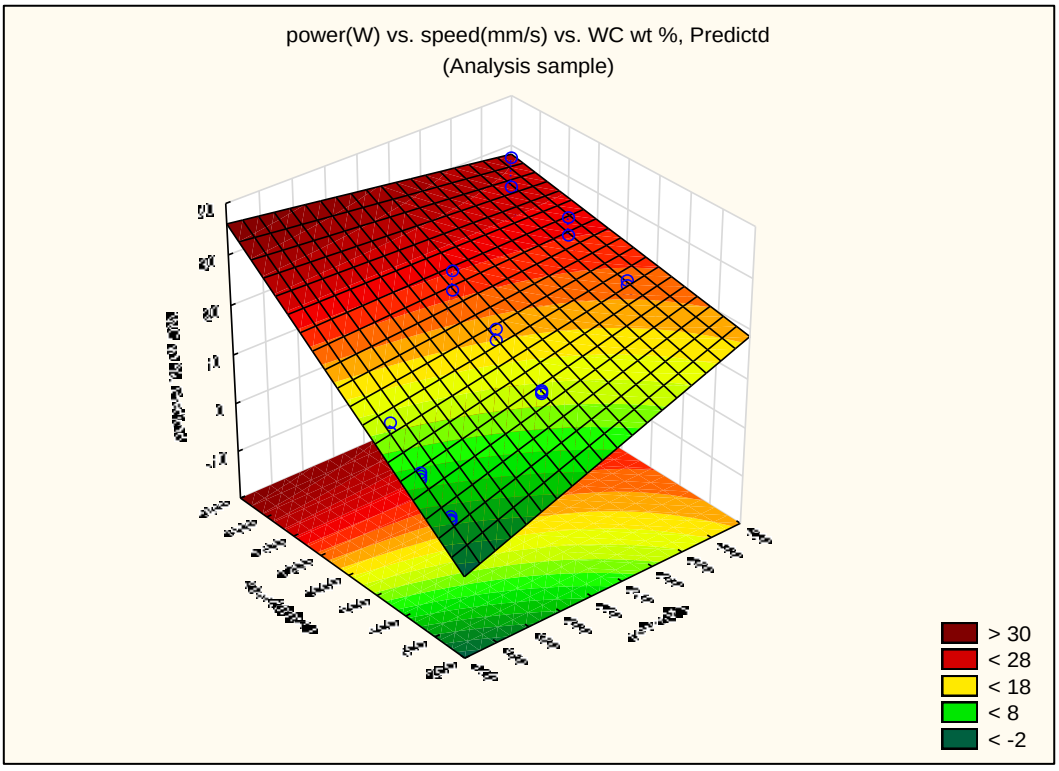

FIGURE I-1: POWER (W) VS. SPEED(MM/S) VS. WC WT. %, PREDICTED

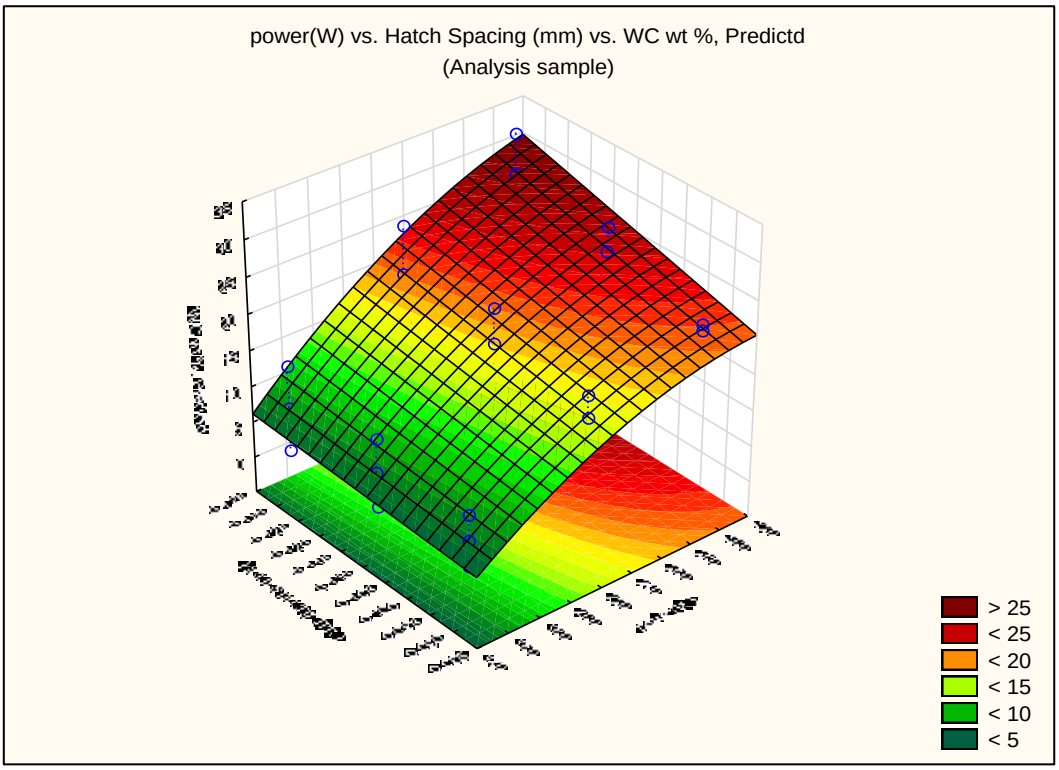

FIGURE I-2: POWER (W) VS. HATCH SPACING (MM) VS. WC WT. %, PREDICTED

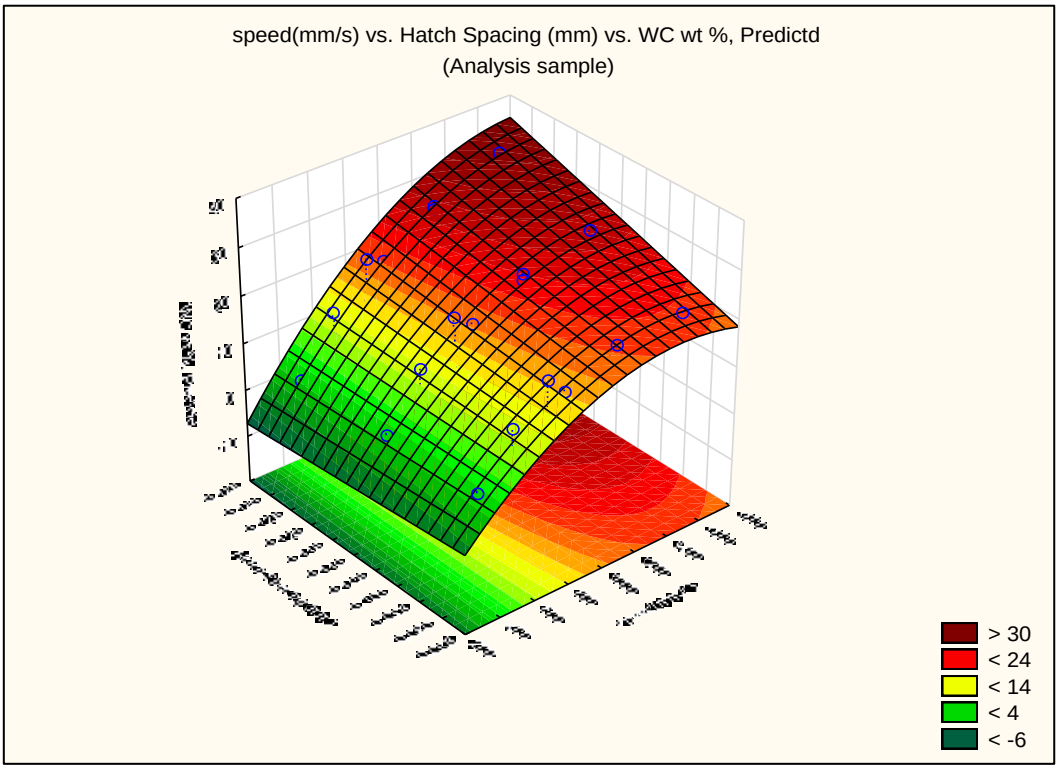

FIGURE I-3: SPEED (MM/S) VS. HATCH SPACING (MM) VS. WC WT%, PREDICTED.

QUADRATIC REGRESSION MODEL

TABLE I-5: LINEAR UNIVARIATE TEST OF SIGNIFICANCE FOR CARBIDE CONTENT % AT LAYER SURFACE

Effect	Univariate Tests of Significance for WC wt % - Sigma-restricted parameterization Effective hypothesis decomposition; Std. Error of Estimate: 5.6692				
	SS	Degr. of Freedom	MS	F	p
Intercept	24.5545	1	24.5545	0.763999	0.39426
power(W)	122.799	1	122.799	3.820817	0.067268
power(W)^2	119.1944	1	119.1944	3.708662	0.071024
speed(mm/s)	5.7837	1	5.7837	0.179958	0.676729
speed(mm/s)^2	23.5258	1	23.5258	0.73199	0.404137
Hatch Spacing (mm)	2.0886	1	2.0886	0.064985	0.801842
Hatch Spacing (mm)^2	3.6712	1	3.6712	0.114228	0.739519
power(W)*speed(mm/s)	14.6216	1	14.6216	0.454942	0.509067
power(W)*Hatch Spacing (mm)	1.1736	1	1.1736	0.036515	0.85072
speed(mm/s)*Hatch Spacing (mm)	40.8174	1	40.8174	1.270008	0.275422
Error	546.3709	17	32.1395		

TABLE I-6: PARAMETER ESTIMATES FOR EQUATION 7-2

Effect	Parameter Estimates - Sigma-restricted parameterization									
	WC wt% Param.	WC wt% Std.Err	WCwt% t	WC wt% p	-95% Cnf Lmt	95% Cnf.Lmt	WC wt % Beta (ß)	WC wt % St.Err.ß	-95% Cnf Lmt	95% Cnf. Lmt
Intercept	-66.91	76.553	-0.8741	0.3943	-228.4	94.6				
power(W)	0.51	0.263	1.9547	0.0673	0	1.07	3.3013	1.6889	-0.262	6.8646
power(W)^2	0	0.001	-1.9258	0.071	0	0	-3.3988	1.7649	-7.122	0.3248
speed(mm/s)	-0.02	0.036	-0.4242	0.6767	-0.1	0.06	-0.5589	1.3175	-3.339	2.2208
speed(mm/s)^2	0	0	-0.8556	0.4041	0	0	-1.3671	1.5979	-4.738	2.0041
Hatch Spacing (mm)	330.92	1298.1	0.2549	0.8018	-2408	3069.7	0.5659	2.22	-4.118	5.2498
Hatch Spacing (mm)^2	-1955.6	5786.1	-0.338	0.7395	-14163	10252	-0.7368	2.18	-5.336	3.8625
power(W)* speed(mm/s)	0	0	0.6745	0.5091	0	0	1.7179	2.5469	-3.656	7.0915
power(W)* Hatch Spacing (mm)	-0.29	1.516	-0.1911	0.8507	-3.5	2.91	-0.2348	1.2286	-2.827	2.3574
speed(mm/s)* Hatch Spacing (mm)	0.3	0.263	1.127	0.2754	-0.3	0.85	1.3012	1.1547	-1.135	3.7374

TABLE I-7: TEST OF SS FOR WHOLE MODEL VS SS RESIDUAL

Dependent Variable	Test of SS Whole Model vs. SS Residual (Spreadsheet2 in MC van Coller Content Experiment.stw)										
	Multiple R	Multiple R^2	Adjusted R^2	SS Model	df Model	MS Model	SS Residual	df Residual	MS Residual	F	p
WC wt %	0.8821	0.7781	0.6606	1915	9	212.8	546.37	17	32.139	6.621	0.0004

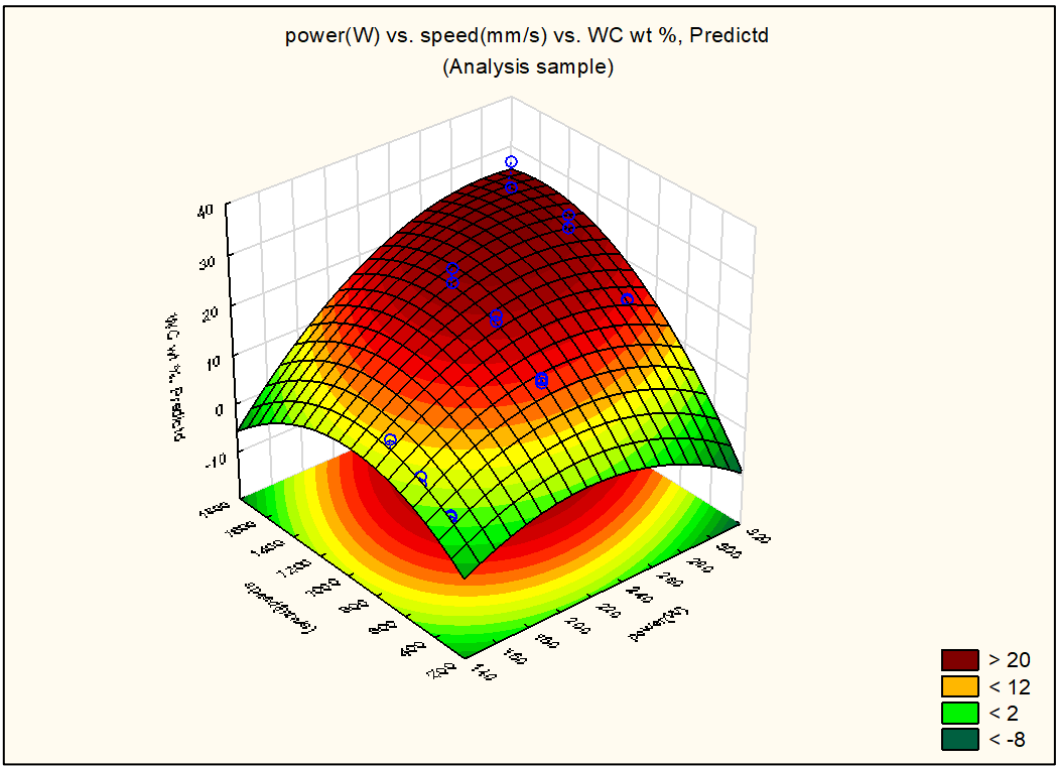

FIGURE I-4: POWER (W) VS. SPEED(MM/S) VS. WC WT. %, PREDICTED

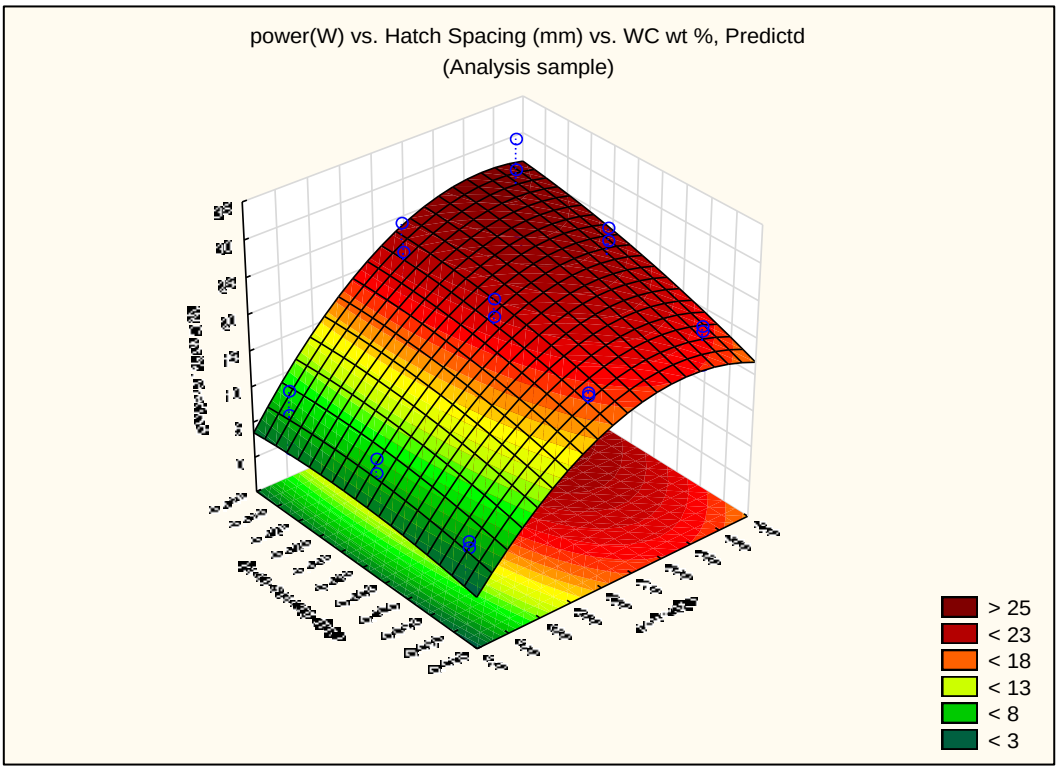

FIGURE I-5: POWER (W) VS. HATCH SPACING (MM) VS. WC WT. %, PREDICTED

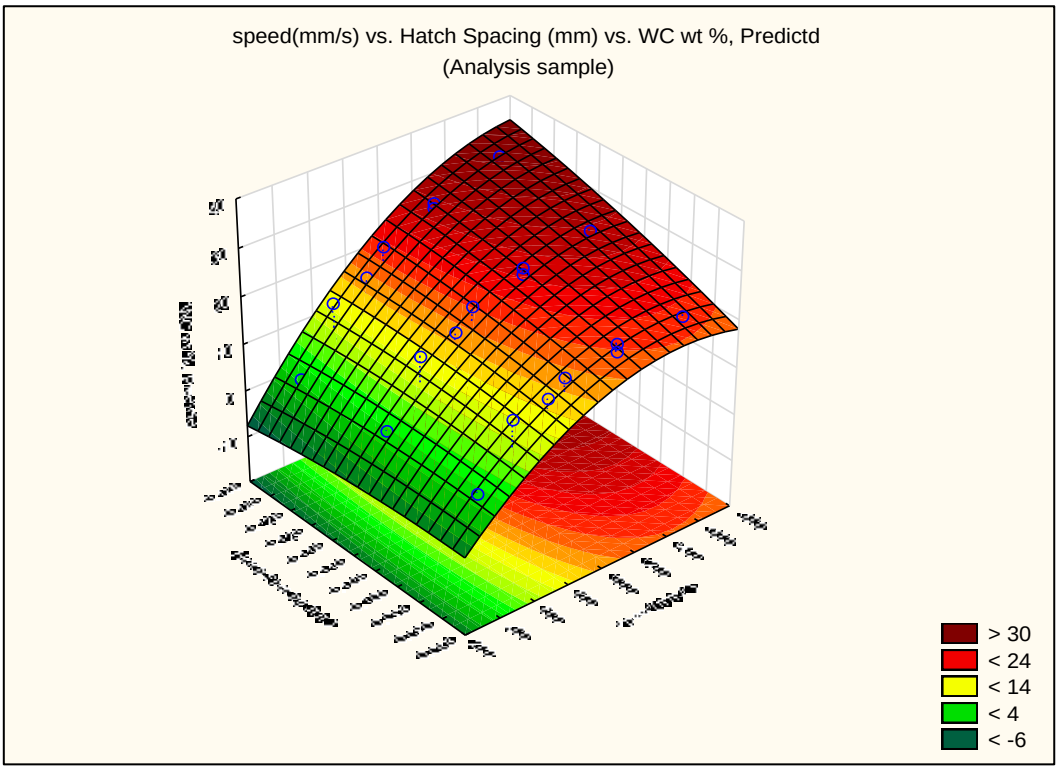

FIGURE I-6: SPEED (MM/S) VS. HATCH SPACING (MM) VS. WC WT%, PREDICTED

APPENDIX J: CROSS SECTION IMAGES OF LAYERS

The Olympus GX51 light microscope was used to inspect the cross sections of each layer. Images of each layer are included in Table K-1. Every image was taken at the same magnification (10X), except for layer number 5, which was taken at 20X magnification and has a smaller scale included. The numbering of the layers is consistent with the run numbers included in Table 7-1.

TABLE J-1: CROSS SECTION IMAGES OF LAYERS 1 - 27

150-WATT	
1	**2**
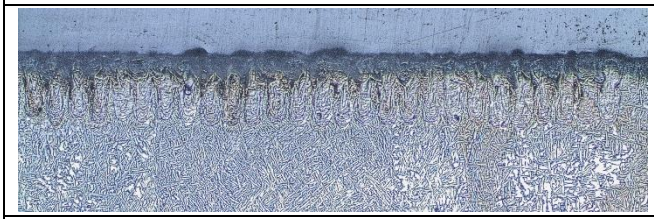	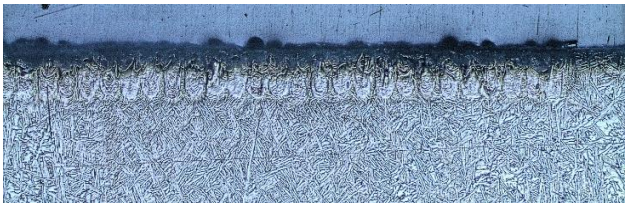
3	**4**
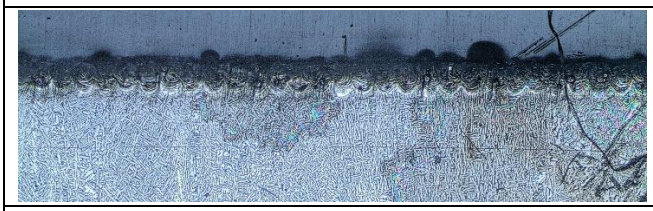	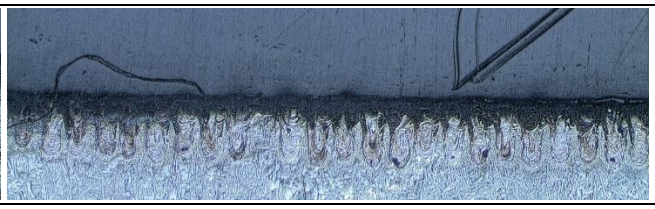
5	**6**
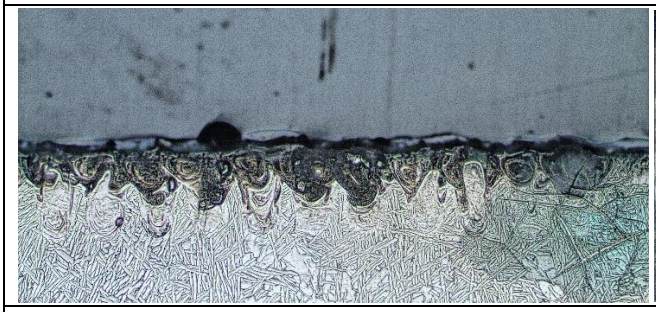	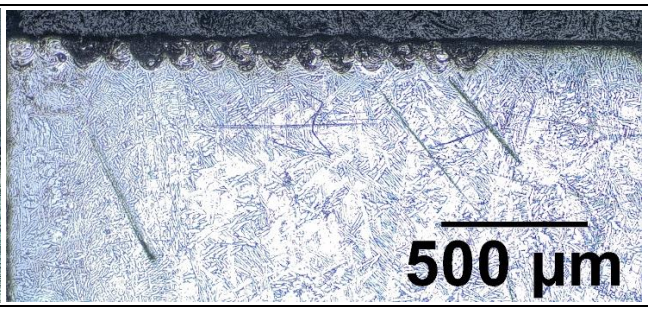
7	**8**
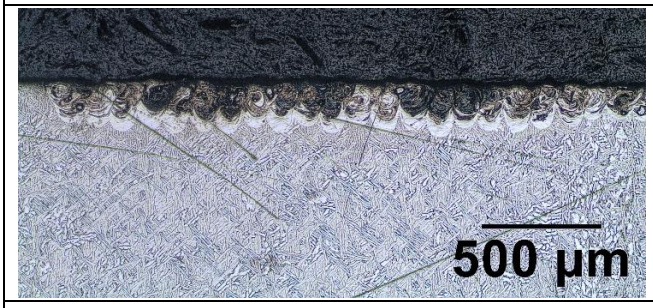	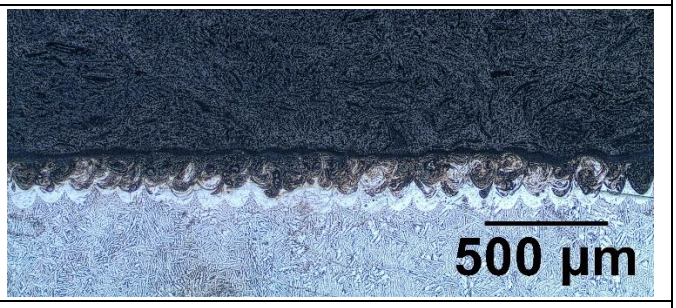
9	
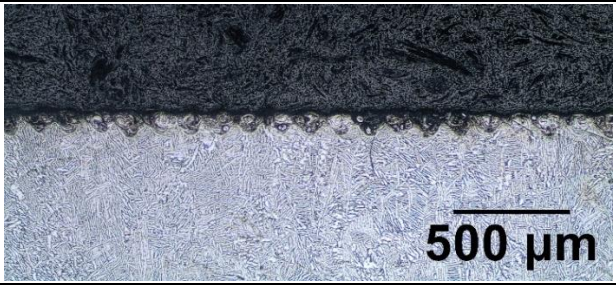	

225-WATT	
10	**11**
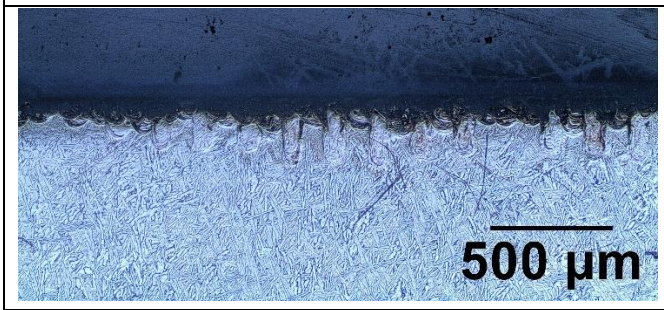	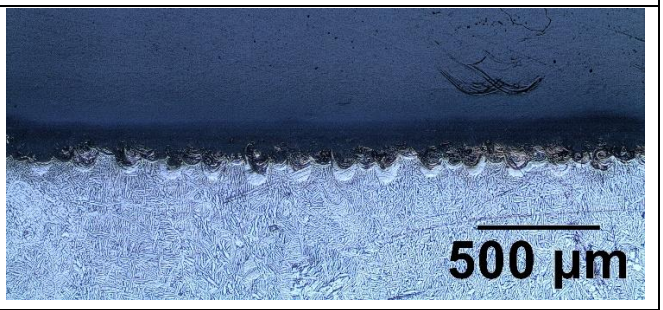
12	**13**
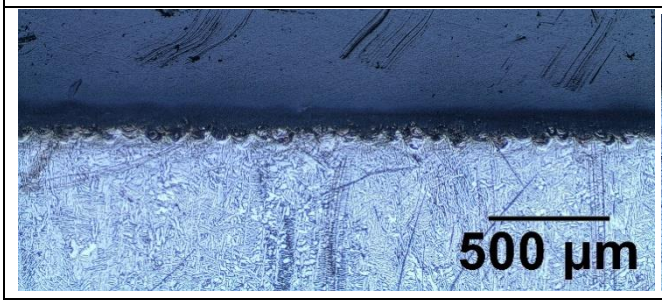	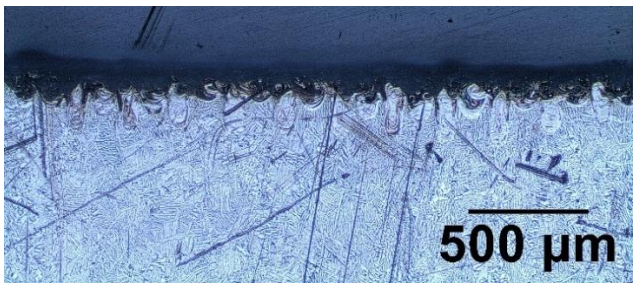
14	**15**
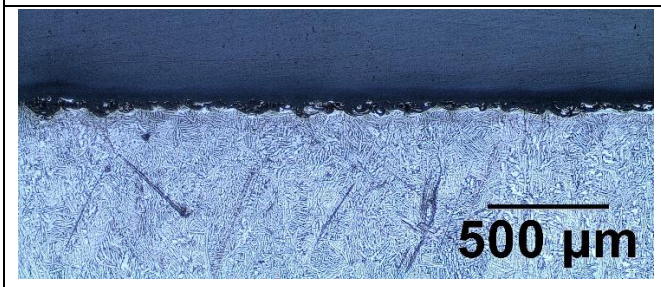	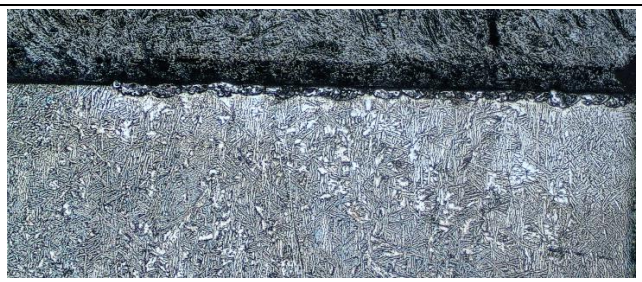
16	**17**
	
18	
	

300-WATT	
19	**20**
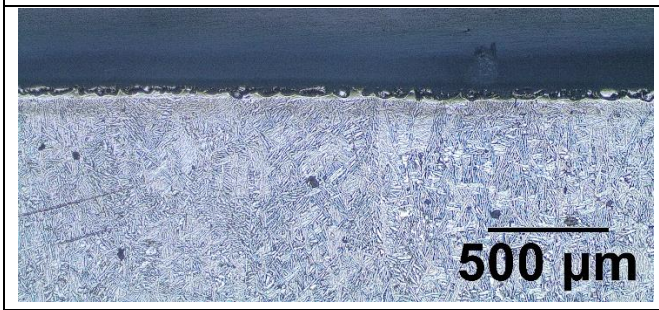	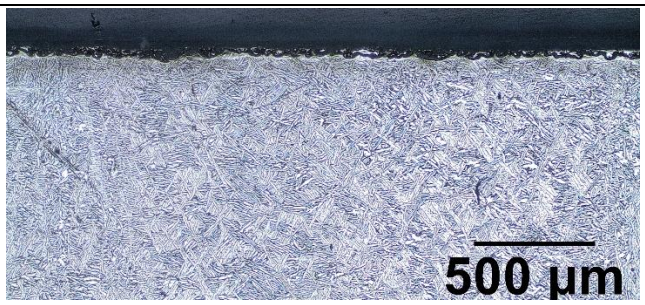
21	**22**
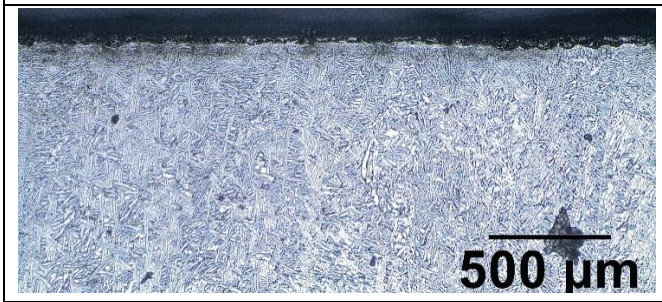	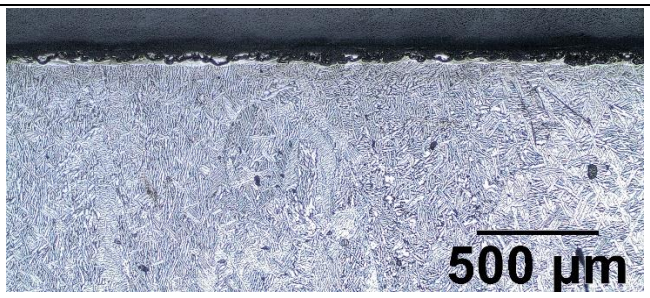
23	24
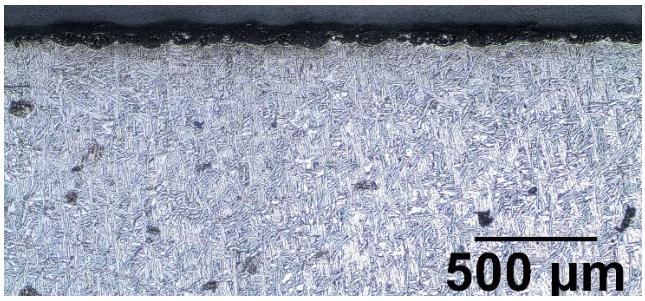	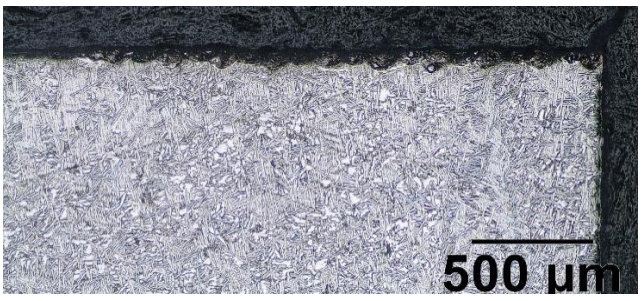
25	26
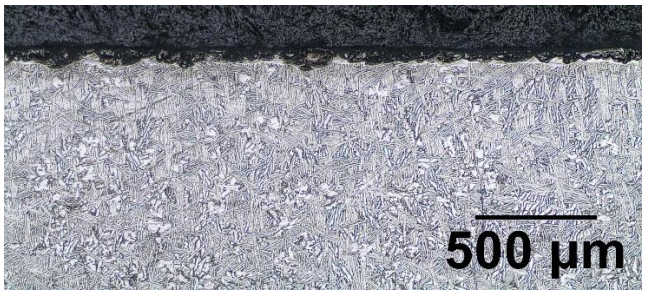	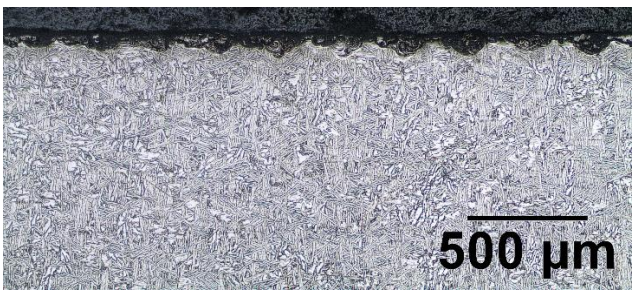
27	
	

APPENDIX K: EDS MAPS & OF LAYER CROSS SECTIONS

EDS maps of each layer cross section were taken to inspect the diffusion of elements into the substrate, dispersion of particles at the surface, and the degree of melting that occurred during processing. Table L-1 includes three EDS maps of each cross section for Tungsten, Nickel, and a layered map of Tungsten, Carbide and Nickel. The Images occur in the order of W, Ni, and the layered image throughout.

TABLE K-1: EDS MAPS OF EACH LAYER CROSS SECTION INDICATING THE CONTENTS OF W, NI, AND WC-NI LAYER

150-WATT
Layer 1 – (P = 150W, h = 0.09mm, v = 400mm/s)
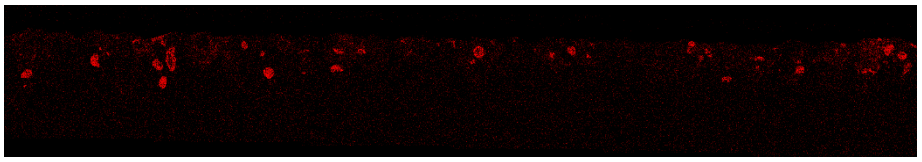
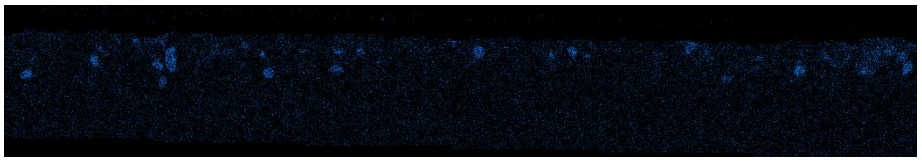
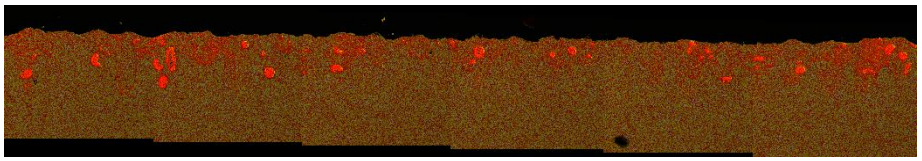
Layer 2 – (P = 150W, h = 0.09mm, v = 600mm/s)
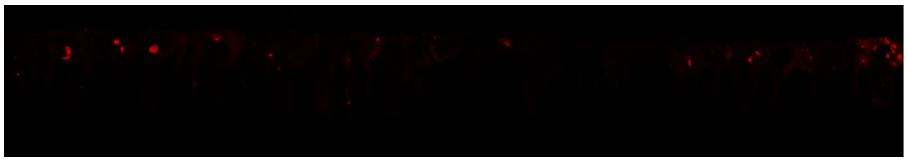
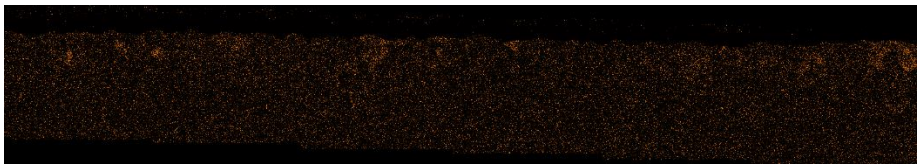
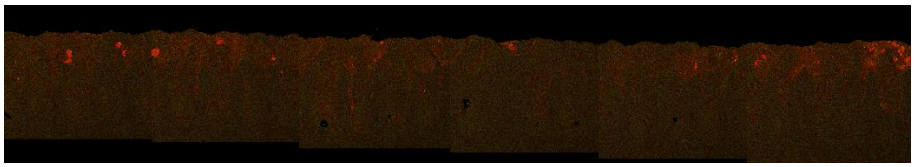
Layer 3 – (P = 150W, h = 0.09mm, v = 800mm/s)
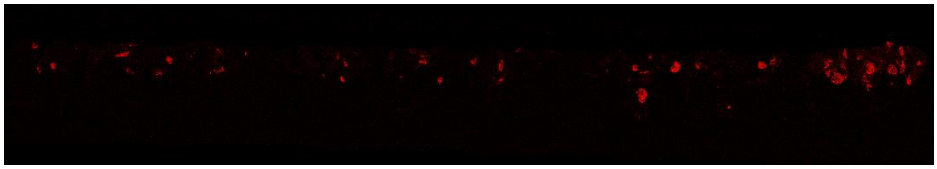
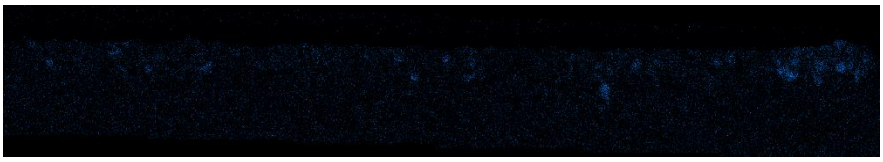

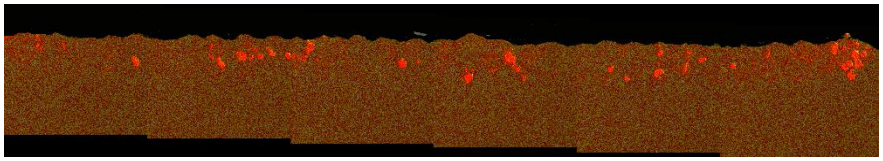

Layer 4 – (P = 150W, h = 0.11 mm, v = 400mm/s)

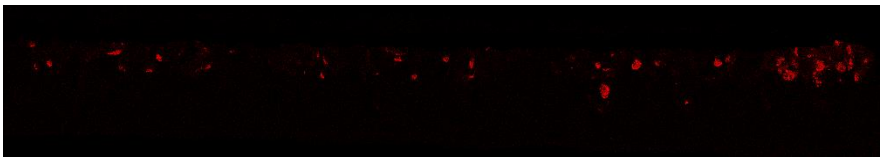

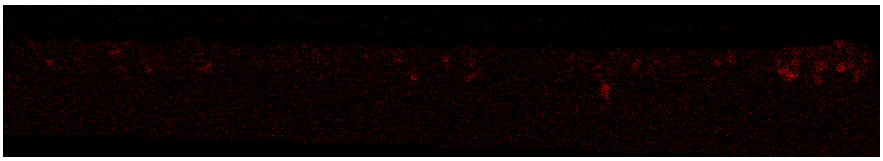

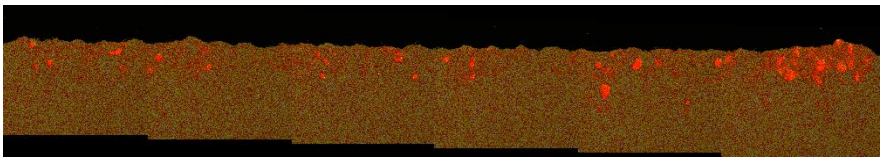

Layer 5 – (P = 150W, h = 0.11 mm, v = 600mm/s)

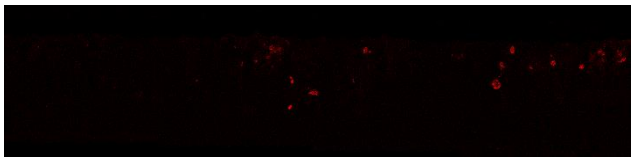

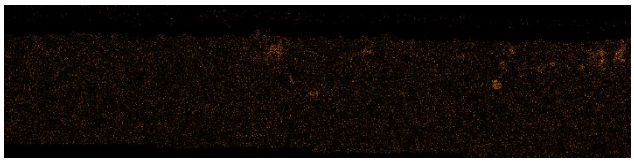

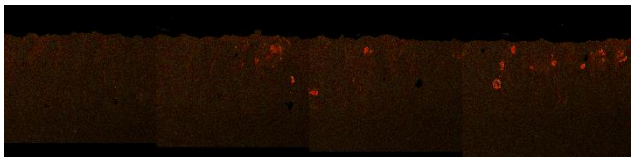

Layer 6 – (P = 150W, h = 0.11 mm, v = 800mm/s)

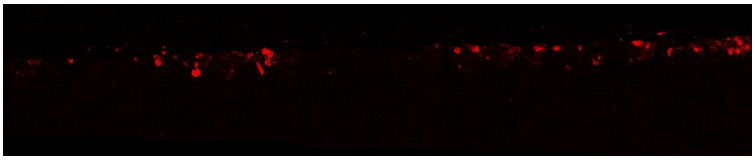

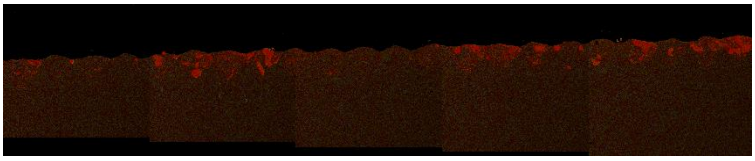

Layer 7 – (P = 150W, h = 0.13 mm, v = 400mm/s)
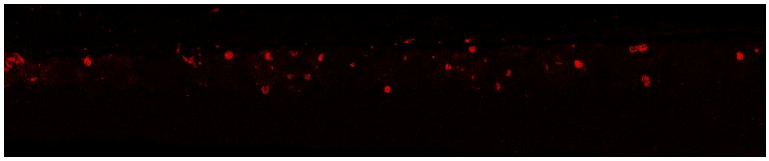
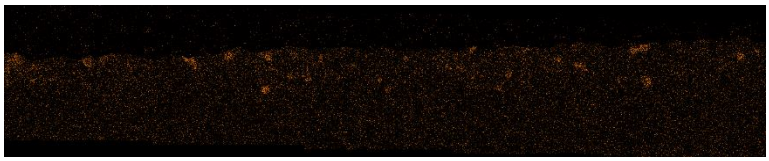
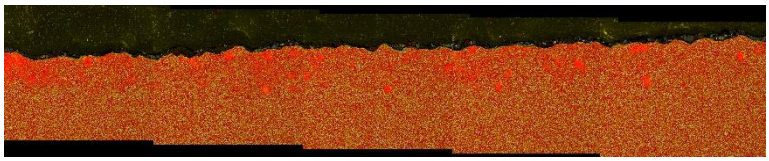
Layer 8 – (P = 150W, h = 0.13 mm, v = 600mm/s)
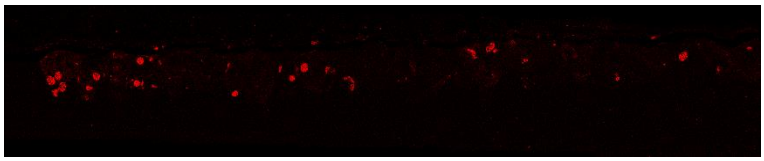
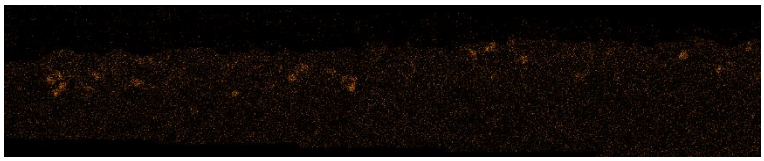
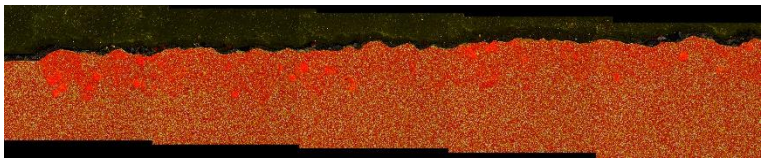
Layer 9 – (P = 150W, h = 0.13 mm, v = 800mm/s)
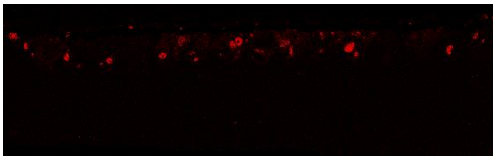
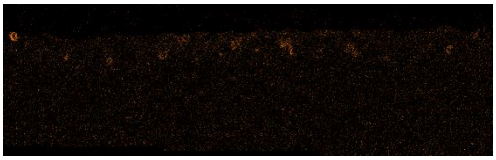
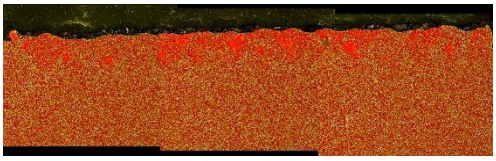

225-WATT
Layer 10 – (P = 225W, h = 0.09 mm, v = 600mm/s)
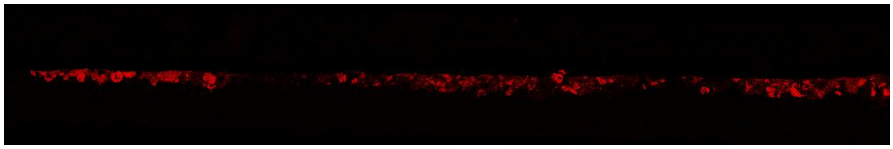
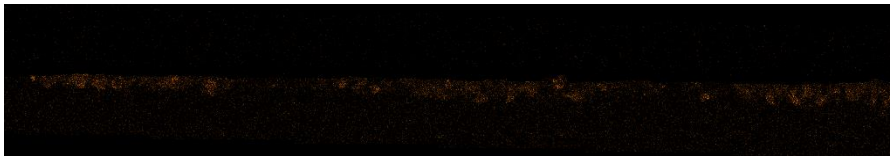
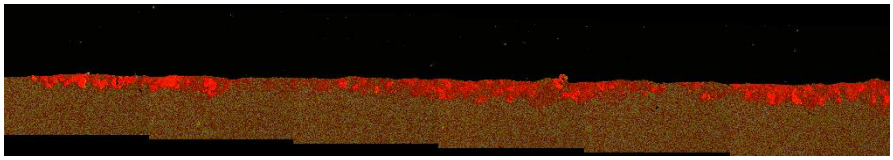
Layer 11 – (P = 225W, h = 0.09 mm, v = 900mm/s)
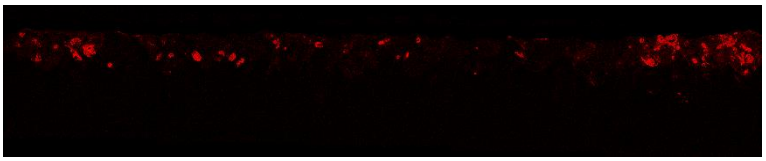

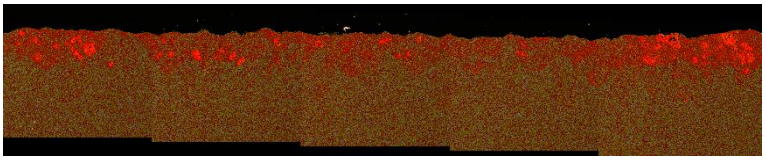
Layer 12 – (P = 225W, h = 0.09 mm, v = 1200mm/s)
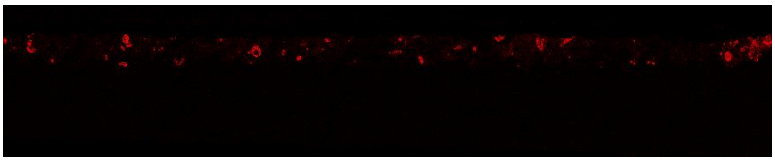
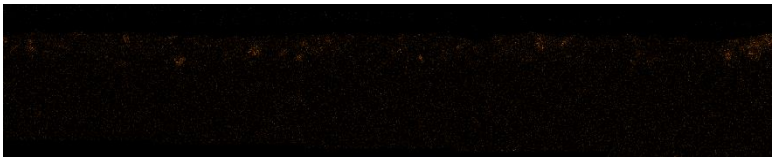
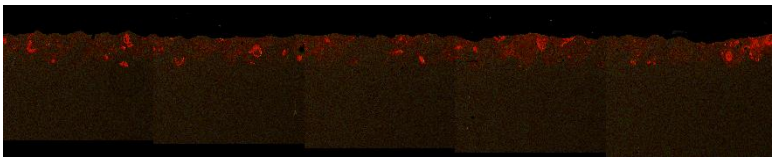
Layer 13 – (P = 225W, h = 0.11 mm, v = 600mm/s)
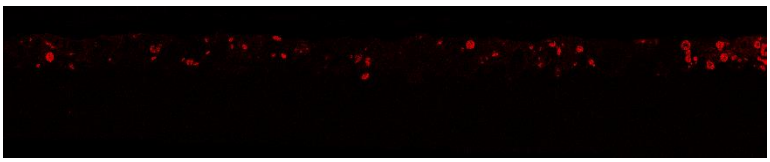

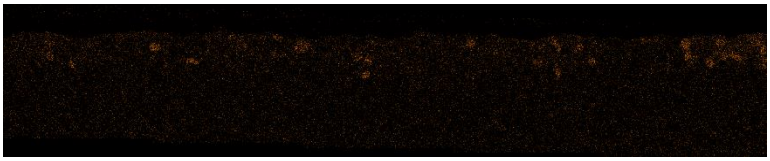

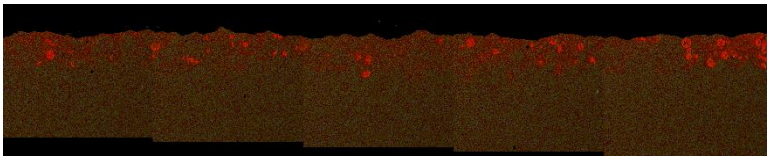

Layer 14 – (P = 225W, h = 0.11 mm, v = 900mm/s)

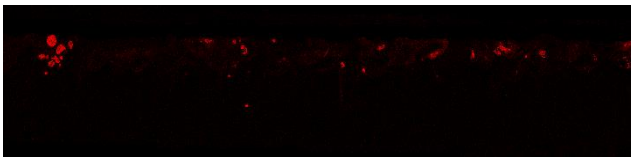

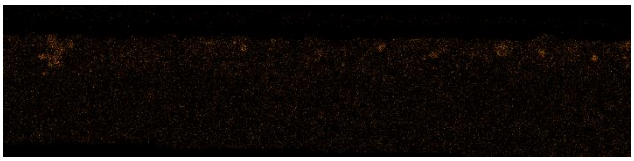

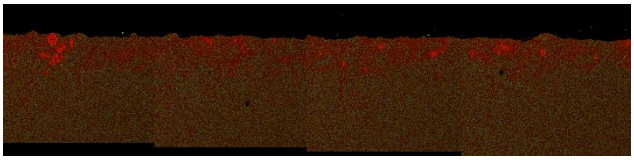

Layer 15 - (P = 225W, h = 0.11 mm, v = 1200mm/s)

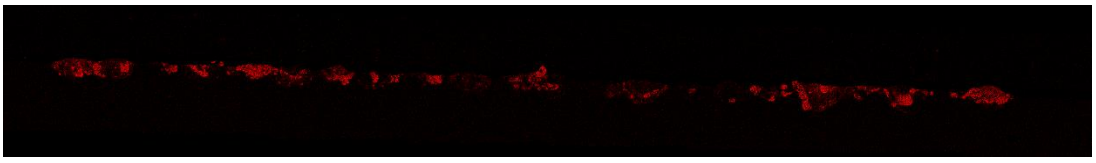

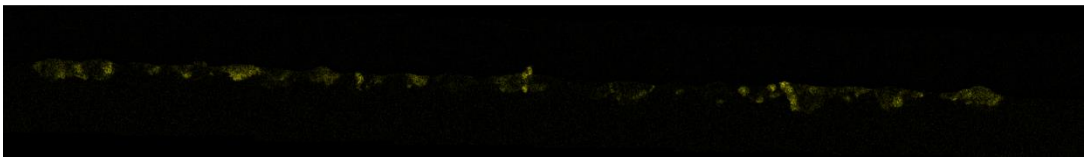

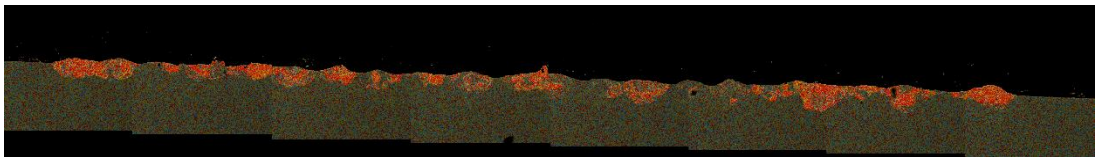

Layer 16 - (P = 225W, h = 0.13 mm, v = 1200mm/s)

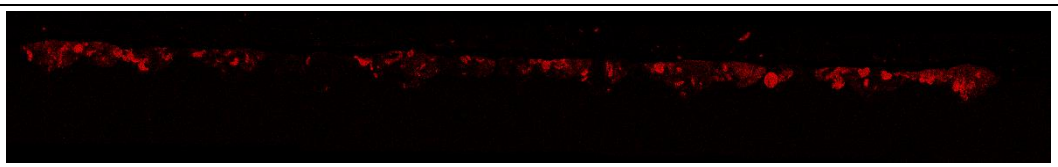

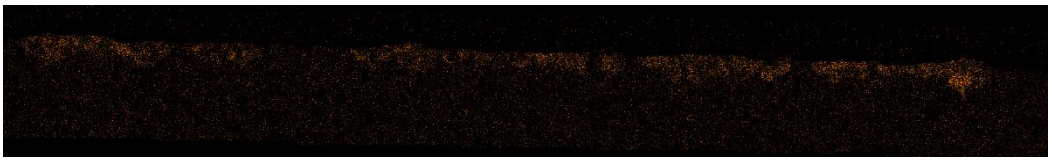

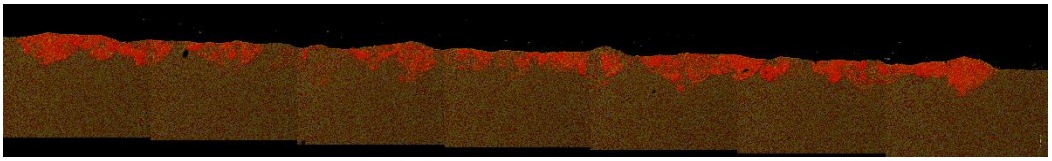

Layer 17 - (P = 225W, h = 0.13 mm, v = 1200mm/s)

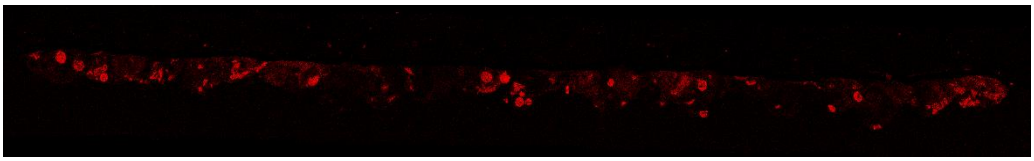

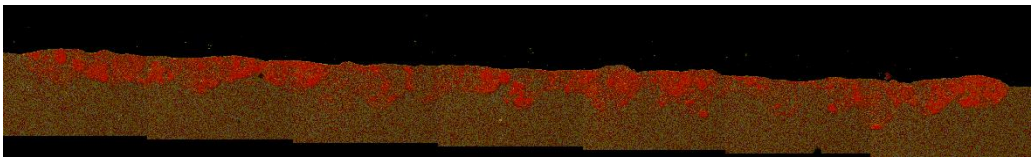

Layer 18 - (P = 225W, h = 0.13 mm, v = 1200mm/s)

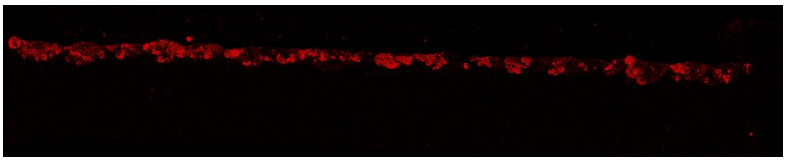

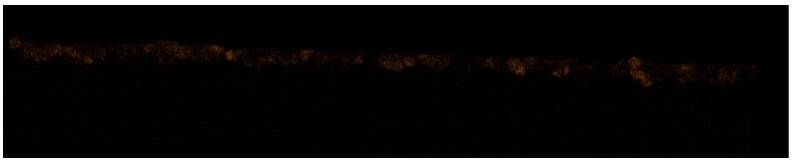

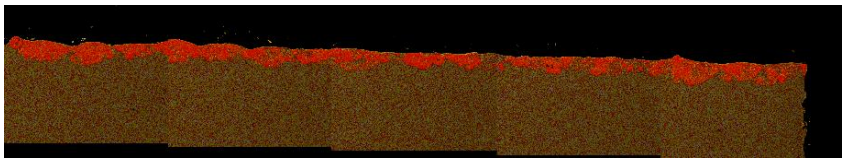

300-WATT

Layer 19 - (P = 300W, h = 0.09 mm, v = 1200mm/s)

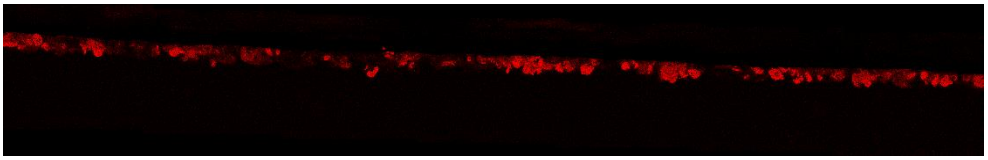

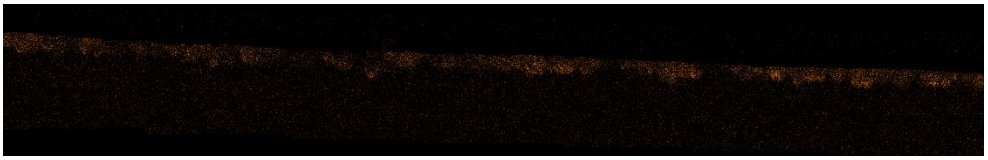

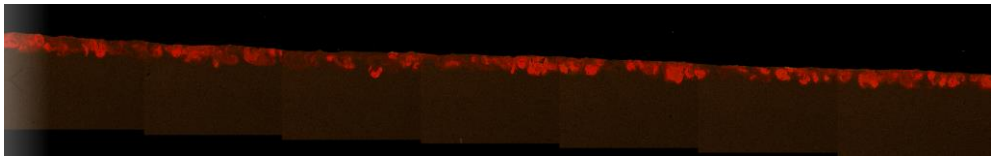

Layer 20 - (P = 300W, h = 0.09 mm, v = 1200mm/s)

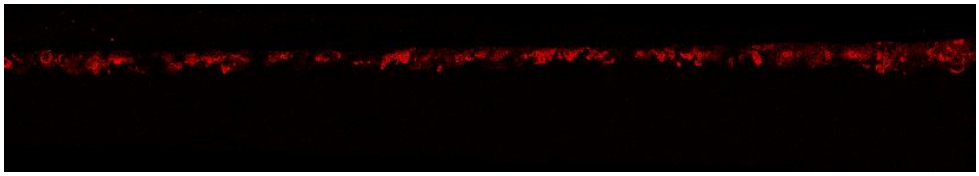

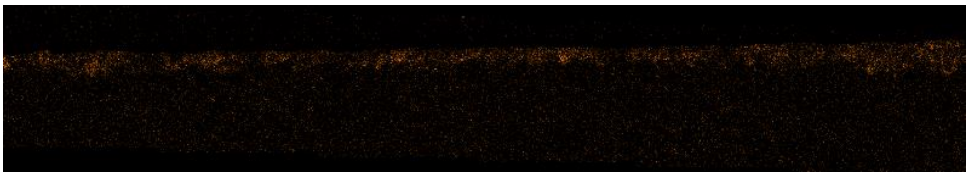

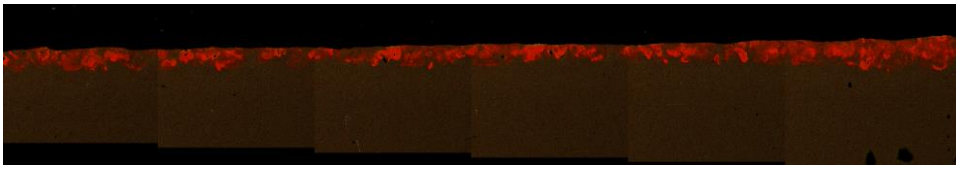

Layer 21 - (P = 300W, h = 0.09 mm, v = 1200mm/s)

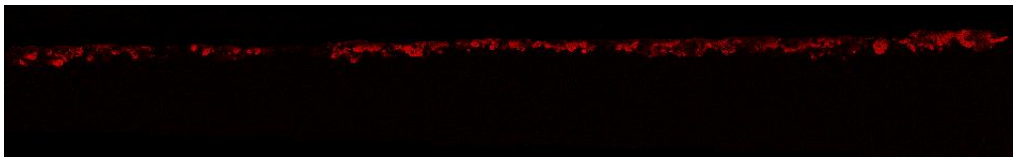

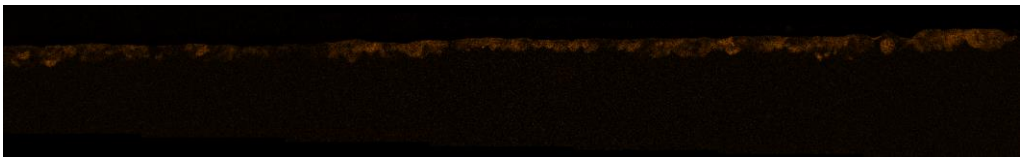

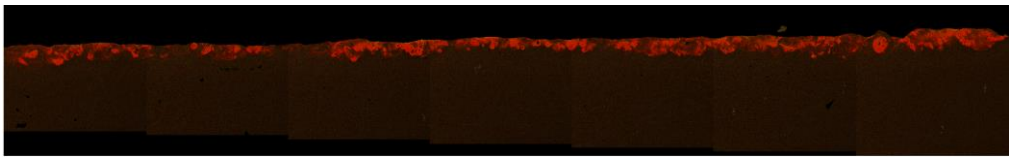

Layer 22 - (P = 300W, h = 0.11 mm, v = 1200mm/s)

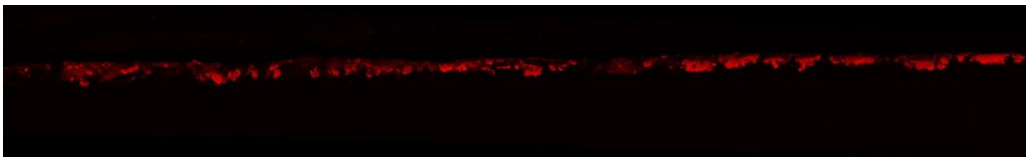

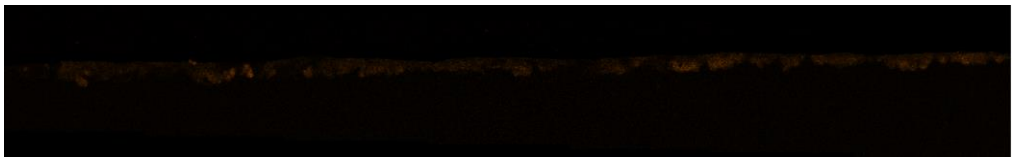

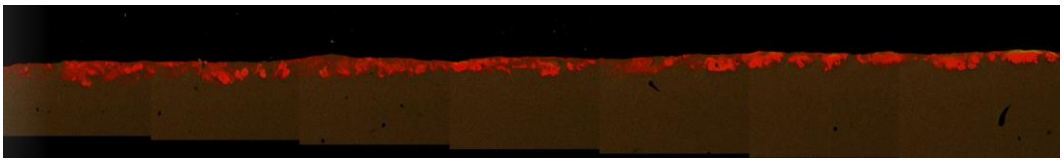

Layer 23 - (P = 300W, h = 0.11 mm, v = 1200mm/s)

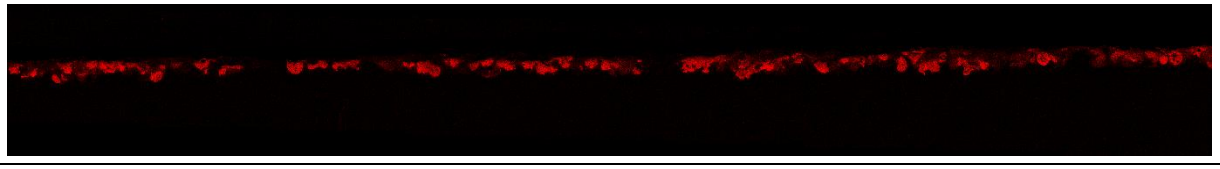

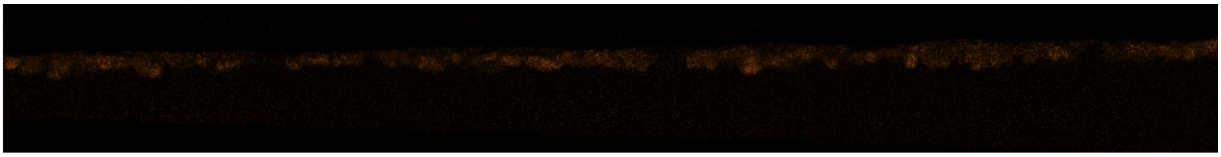

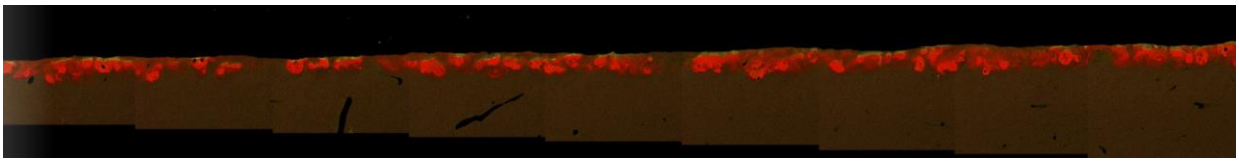

Layer 24 - (P = 300W, h = 0.11 mm, v = 1200mm/s)

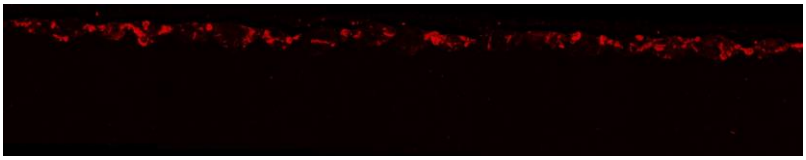

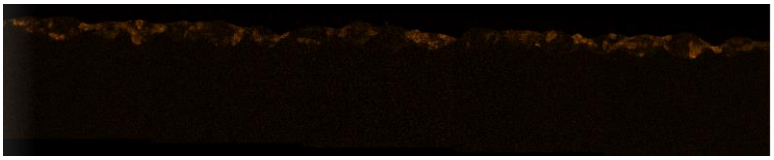

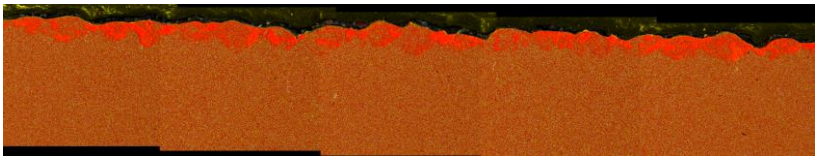

Layer 25 - (P = 300W, h = 0.13 mm, v = 1200mm/s)

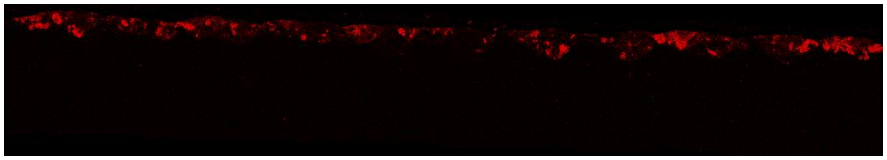

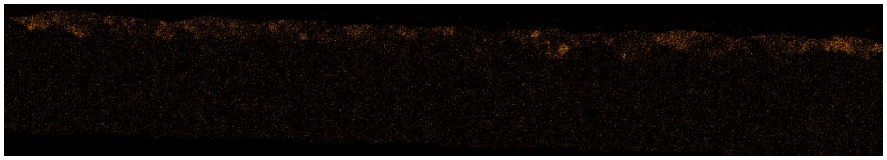

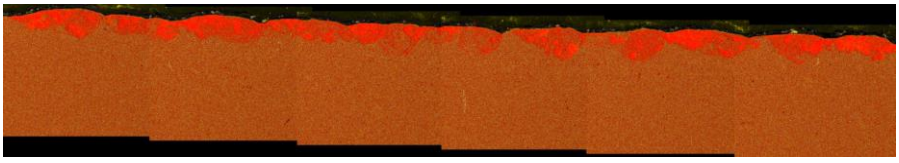

Layer 26 - (P = 300W, h = 0.13 mm, v = 1200mm/s)

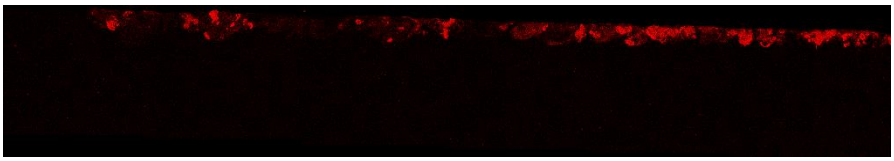

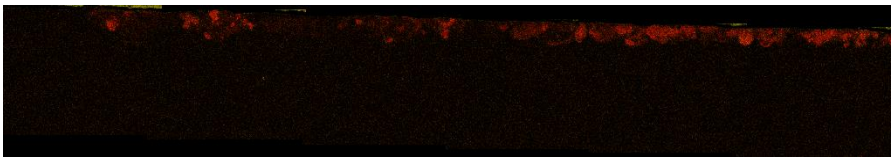

Layer 27 - (P = 300W, h = 0.13 mm, v = 1200mm/s)

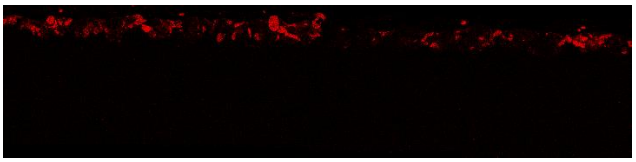

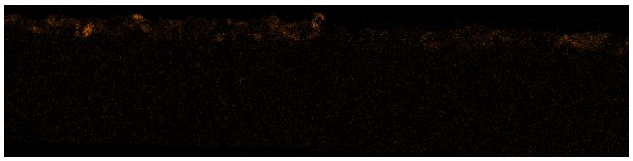

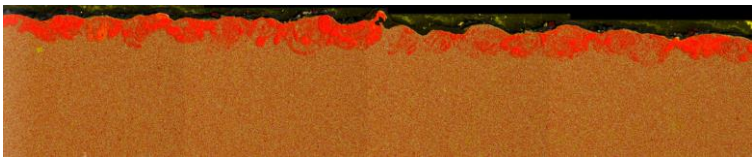

APPENDIX L: MEASUREMENTS AND STATISTICAL ANALYSIS OF LAYER CROSS SECTIONS.

Averages of the measured values for the total penetration depth, clad zone height, interfusion zone depth and coating thickness are listed in Table M-1. Linear regression models were implemented on the data to estimate the effects of input parameters on each measured response and are listed throughout this Appendix.

TABLE L-1: AVERAGE RESPONSE MEASUREMENTS FOR EACH LAYER

Run #	Power (W)	Speed (mm/s)	Hatch Spacing (mm)	Layer Thickness (mm)	VED	Depth	Clad Zone	Interfusion Zone	Coating thickness
1	150	400	0.09	0.05	83.33	270.21	18.29	74.14	92.42
2	150	600	0.09	0.05	55.56	184.14	17.33	66.02	83.34
3	150	800	0.09	0.05	41.67	124.74	12.92	75.23	88.15
4	150	400	0.11	0.05	68.18	234.31	15.66	81.63	97.29
5	150	600	0.11	0.05	45.45	163.68	11.03	61.09	72.11
6	150	800	0.11	0.05	34.09	86.19	13.35	42.76	56.11
7	150	400	0.13	0.05	57.69	193.05	17.24	100.05	117.30
8	150	600	0.13	0.05	38.46	180.16	12.79	103.31	116.10
9	150	800	0.13	0.05	28.85	88.78	14.07	33.92	47.99
10	225	600	0.09	0.05	83.33	223.21	12.99	65.09	78.08
11	225	900	0.09	0.05	55.56	159.84	15.13	75.33	90.46
12	225	1200	0.09	0.05	41.67	90.76	13.83	50.73	64.55
13	225	600	0.11	0.05	68.18	190.37	17.47	89.21	106.68
14	225	900	0.11	0.05	45.45	66.19	12.82	26.32	39.13
15	225	1200	0.11	0.05	34.09	38.57	10.42	20.18	30.59
16	225	600	0.13	0.05	57.69	83.66	11.55	47.62	59.17
17	225	900	0.13	0.05	38.46	72.14	7.61	32.06	39.67
18	225	1200	0.13	0.05	28.85	50.02	7.87	20.76	28.63
19	300	800	0.09	0.05	83.33	68.91	15.62	33.04	48.66
20	300	1200	0.09	0.05	55.56	64.18	13.47	24.11	37.58
21	300	1600	0.09	0.05	41.67	60.46	13.66	20.81	34.46
22	300	800	0.11	0.05	68.18	57.54	12.28	35.04	47.32
23	300	1200	0.11	0.05	45.45	80.75	14.83	30.44	45.26
24	300	1600	0.11	0.05	34.09	53.49	13.16	30.73	43.89
25	300	800	0.13	0.05	57.69	57.85	11.26	34.46	45.72
26	300	1200	0.13	0.05	38.46	48.64	14.31	28.48	42.79
27	300	1600	0.13	0.05	28.85	42.35	9.84	27.09	36.94

PENETRATION DEPTH

TABLE L-2 :LINEAR UNIVARIATE TEST OF SIGNIFICANCE FOR TOTAL PENETRATION DEPTH

Effect	Univariate Tests of Significance for Depth Sigma-restricted parameterization Effective hypothesis decomposition; Std. Error of Estimate: 5.7886				
	SS	Degr. Of Freedom	MS	F	p
Intercept	20783.03	1	20783.03	22.86399	0.000114
power(W)	1515.83	1	1515.83	1.66761	0.211305
speed(mm/s)	11919.47	1	11919.47	13.11294	0.001702
Hatch Spacing (mm)	2187.22	1	2187.22	2.40622	0.136535
power(W)*speed(mm/s)	16959.38	1	16959.38	18.65748	0.000333
power(W)*Hatch Spacing (mm)	57.26	1	57.26	0.06299	0.804385
speed(mm/s)*Hatch Spacing (mm)	1059.84	1	1059.84	1.16596	0.293083
Error	18179.71	20	908.99		

TABLE L-3: PARAMETER ESTIMATES FOR EQUATION 7-3

Effect	Parameter Estimates - Sigma-restricted parameterization									
	WC wt % Param.	WC wt % Std.Err	WC wt% t	WC wt% p	-95% Cnf Lmt	95% Cnf.Lmt	WC wt % Beta (ß)	WC wt% St.Err.ß	-95% Cnf Lmt	95% Cnf. Lmt
Intercept	779.54	163.03	4.78	0.00	439.50	1119.61				
power(W)	-1205.48	933.50	-1.29	0.21	-3152.70	741.76	-1.10	0.85	-2.88	0.68
speed(mm/s)	-643.43	177.69	-3.62	0.00	-1014.10	-272.79	-3.39	0.93	-5.34	-1.44
Hatch Spacing (mm)	-2098.76	1353.00	-1.55	0.14	-4921.10	723.53	-0.51	0.33	-1.20	0.18
power(W)*speed(mm/s)	1445.94	334.75	4.32	0.00	747.70	2144.22	2.78	0.64	1.44	4.13
power(W)*Hatch Spacing (mm)	-2023.68	8062.91	-0.25	0.80	-18842.60	14795.25	-0.23	0.93	-2.17	1.71
speed(mm/s)*Hatch Spacing (mm)	1511.34	1399.65	1.08	0.29	-1408.30	4430.95	0.94	0.87	-0.88	2.77

TABLE L-4: TEST OF SS FOR WHOLE MODEL VS SS RESIDUAL

Dependent Variable	Test of SS Whole Model vs. SS Residual (Spreadsheet2 in Workbook6)										
	Multiple R	Multiple R^2	Adjusted R^2	SS Model	df Model	MS Model	SS Residual	df Residual	MS Residual	F	p
WC wt %	0.92207	0.85022	0.80529	10320	6	17200.	18179.7	20	908.9853	18.92239	0

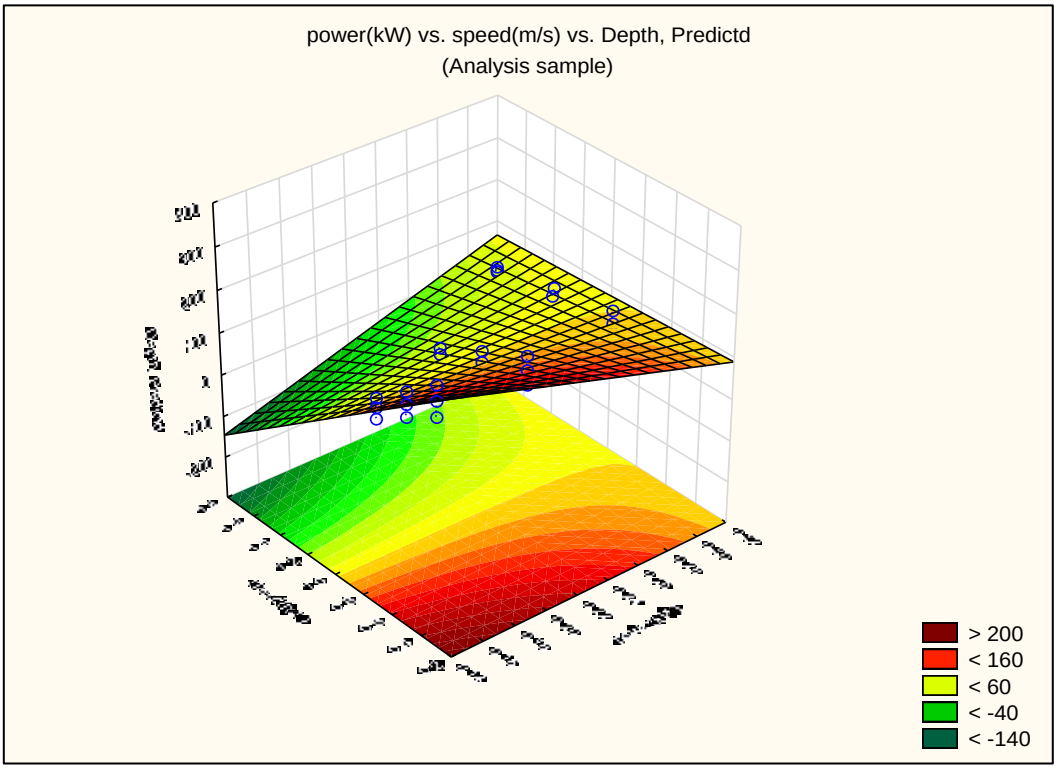

FIGURE L-1: POWER(KW) VS. SPEED(M/S) VS. DEPTH, PREDICTED

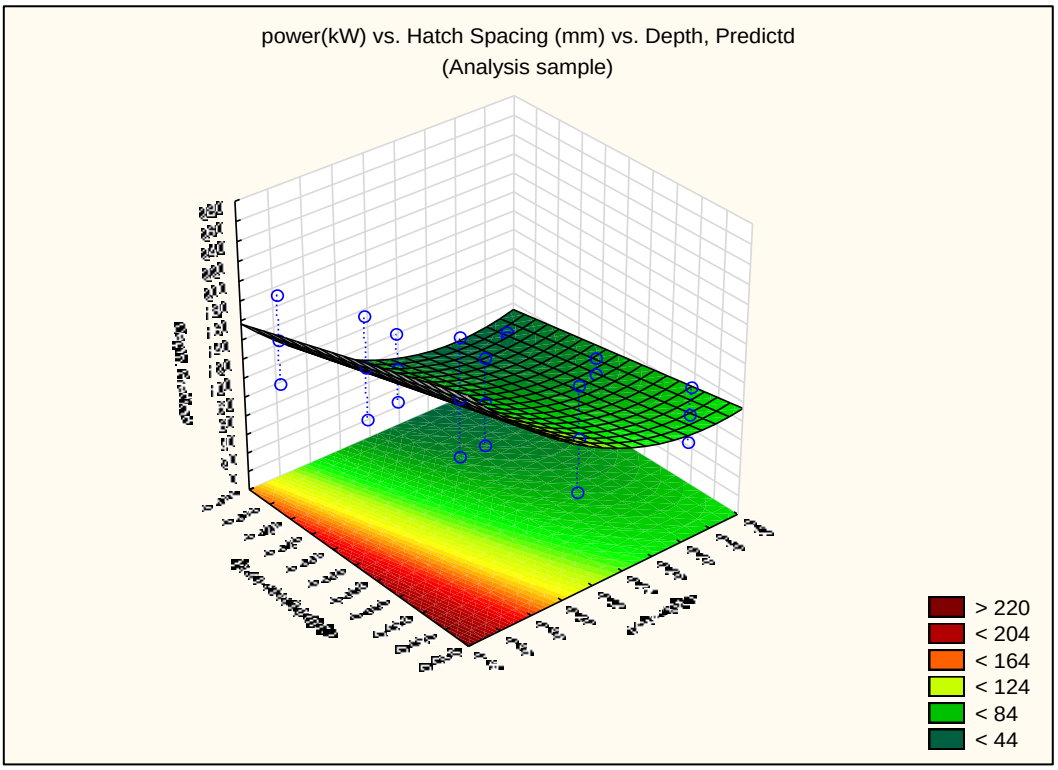

FIGURE L-2: POWER(KW) VS. HATCH SPACING (MM) VS. DEPTH, PREDICTED

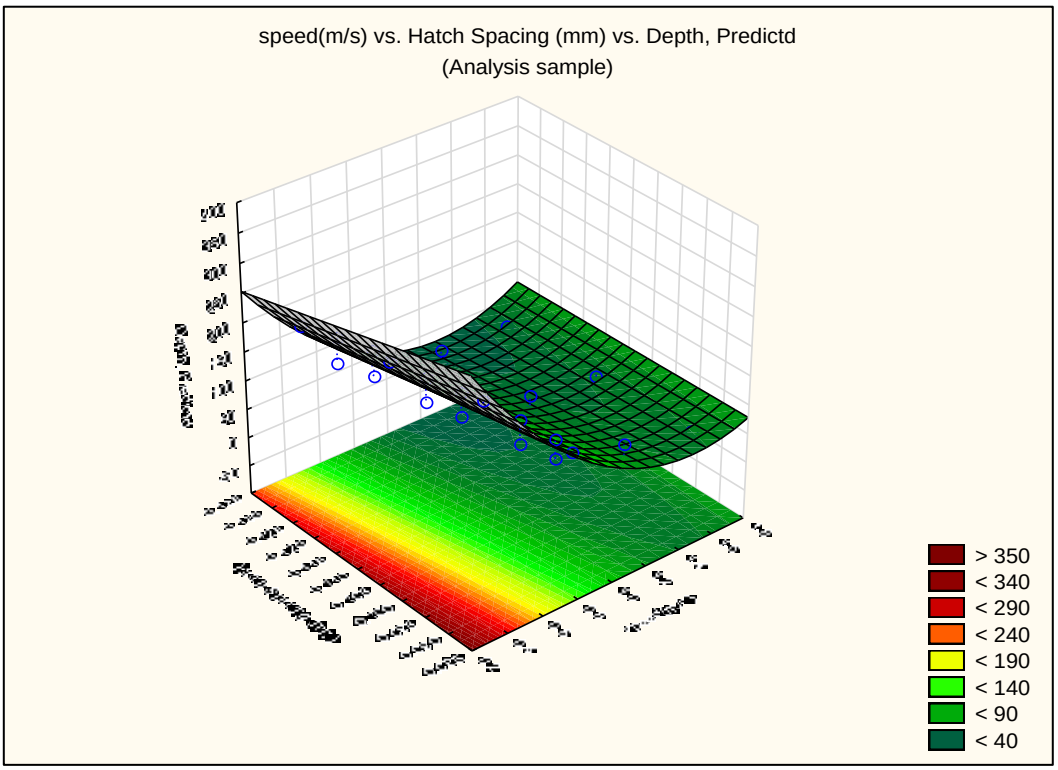

FIGURE L-3: SPEED(M/S) VS. HATCH SPACING (MM) VS. DEPTH, PREDICTED

CLAD ZONE

TABLE L-5 :LINEAR UNIVARIATE TEST OF SIGNIFICANCE FOR TOTAL CLAD ZONE HEIGHT

Effect	Univariate Tests of Significance for Depth Sigma-restricted parameterization Effective hypothesis decomposition; Std. Error of Estimate: 5.7886				
	SS	Degr. Of Freedom	MS	F	p
Intercept	34.67	1.00	34.67	8.41	0.01
power(W)	1.79	1.00	1.79	0.43	0.52
speed(mm/s)	7.84	1.00	7.84	1.90	0.18
Hatch Spacing (mm)	0.71	1.00	0.71	0.17	0.68
power(W)*speed(mm/s)	32.85	1.00	32.85	7.97	0.01
power(W)*Hatch Spacing (mm)	0.02	1.00	0.02	0.01	0.94
speed(mm/s)*Hatch Spacing (mm)	0.42	1.00	0.42	0.10	0.75
Error	82.44	20.00	4.12		

TABLE L-6: PARAMETER ESTIMATES FOR EQUATION 7-4

Effect	Parameter Estimates - Sigma-restricted parameterization									
	WC wt % Param.	WC wt % Std.Err	WC wt% t	WC wt% p	-95% Cnf Lmt	95% Cnf.Lmt	WC wt % Beta (ß)	WC wt% St.Err.ß	-95% Cnf Lmt	95% Cnf. Lmt
Intercept	31.84	10.98	2.90	0.01	8.94	54.74				
power(W)	-41.37	62.86	-0.66	0.52	-172.50	89.75	-0.96	1.46	-3.99	2.08
speed(mm/s)	-16.50	11.97	-1.38	0.18	-41.46	8.46	-2.20	1.60	-5.53	1.13
Hatch Spacing (mm)	-37.92	91.11	-0.42	0.68	-227.97	152.13	-0.23	0.56	-1.41	0.94
power(W)*speed(mm/s)	63.63	22.54	2.82	0.01	16.61	110.66	3.11	1.10	0.81	5.40
power(W)*Hatch Spacing (mm)	-40.42	542.95	-0.07	0.94	-1172.99	1092.14	-0.12	1.59	-3.43	3.19
speed(mm/s)*Hatch Spacing (mm)	-30.17	94.25	-0.32	0.75	-226.78	166.43	-0.48	1.49	-3.59	2.64

TABLE L-7: TEST OF SS FOR WHOLE MODEL VS SS RESIDUAL

Dependent Variable	Test of SS Whole Model vs. SS Residual (Spreadsheet2 in Workbook6)										
	Multiple R	Multiple R^2	Adjusted R^2	SS Model	df Model	MS Model	SS Residual	df Residual	MS Residual	F	p
WC wt %	0.75	0.56	0.43	106.50	6.00	17.75	82.44	20.00	4.12	4.31	0.01

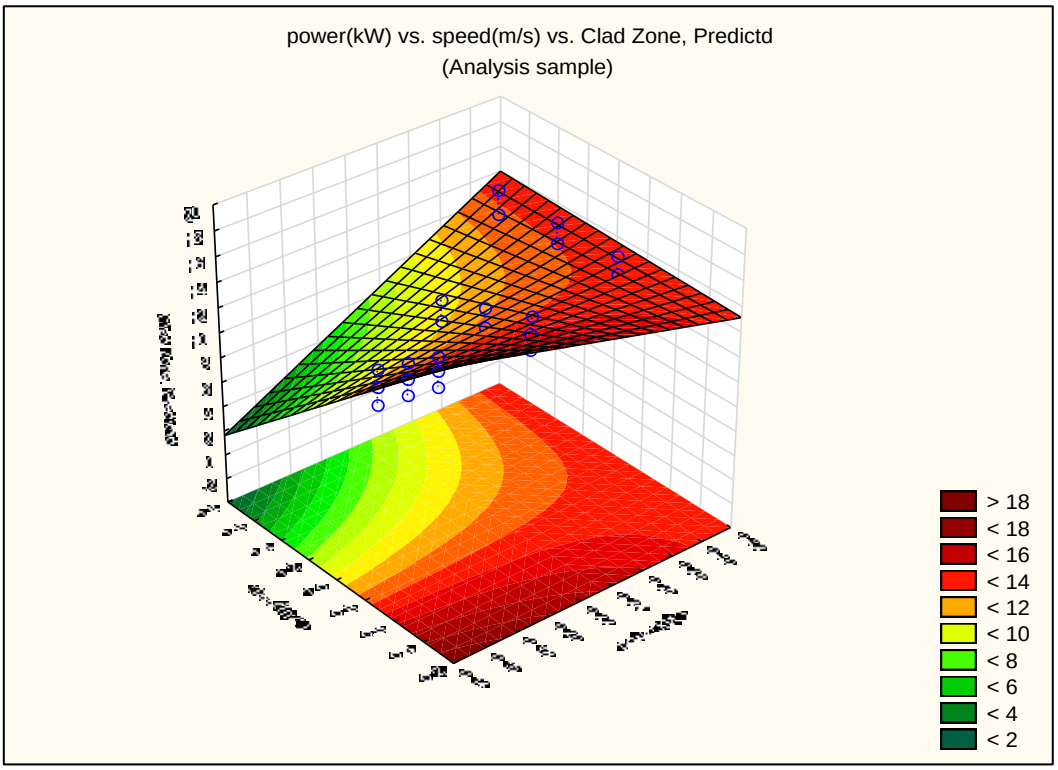

FIGURE L-4: POWER(KW) VS. SPEED(M/S) VS. CLAD ZONE, PREDICTED

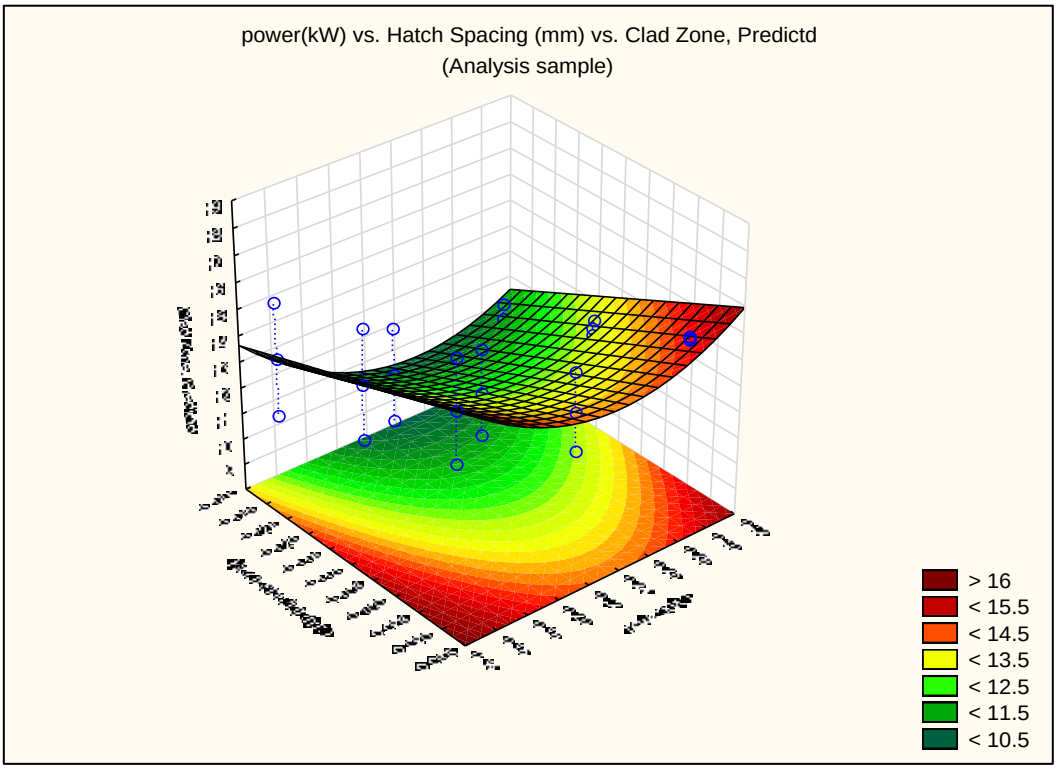

FIGURE L-5: POWER(KW) VS. HATCH SPACING (MM) VS. CLAD ZONE, PREDICTED

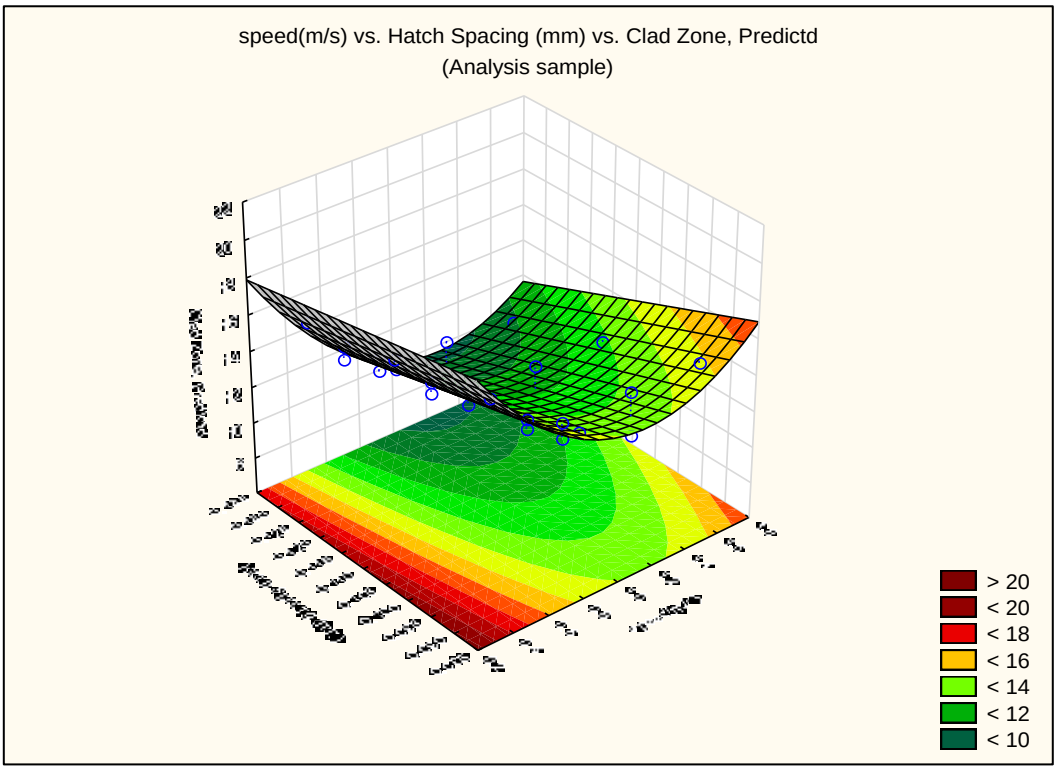

FIGURE L-6: SPEED(M/S) VS. HATCH SPACING (MM) VS. CLAD ZONE, PREDICTED

INTERFUSION ZONE

TABLE L-8 :LINEAR UNIVARIATE TEST OF SIGNIFICANCE FOR TOTAL CLAD ZONE HEIGHT

Effect	Univariate Tests of Significance for Depth Sigma-restricted parameterization Effective hypothesis decomposition; Std. Error of Estimate: 5.7886				
	SS	Degr. Of Freedom	MS	F	p
Intercept	1216.91	1.00	1216.91	4.35	0.05
power(W)	459.08	1.00	459.08	1.64	0.21
speed(mm/s)	118.40	1.00	118.40	0.42	0.52
Hatch Spacing (mm)	0.60	1.00	0.60	0.00	0.96
power(W)*speed(mm/s)	1237.04	1.00	1237.04	4.42	0.05
power(W)*Hatch Spacing (mm)	60.71	1.00	60.71	0.22	0.65
speed(mm/s)*Hatch Spacing (mm)	200.49	1.00	200.49	0.72	0.41
Error	5593.99	20.00	279.70		

TABLE L-9: PARAMETER ESTIMATES FOR EQUATION 7-4

Effect	Parameter Estimates - Sigma-restricted parameterization									
	WC wt % Param.	WC wt % Std.Err	WC wt% t	WC wt% p	-95% Cnf Lmt	95% Cnf.Lmt	WC wt % Beta (ß)	WC wt% St.Err.ß	-95% Cnf Lmt	95% Cnf. Lmt
Intercept	188.63	90.43	2.09	0.05	-0.01	377.27				
power(W)	-663.40	517.82	-1.28	0.21	-1743.56	416.76	-1.60	1.25	-4.22	1.01
speed(mm/s)	-64.13	98.57	-0.65	0.52	-269.73	141.47	-0.89	1.37	-3.76	1.97
Hatch Spacing (mm)	-34.89	750.52	-0.05	0.96	-1600.45	1530.67	-0.02	0.48	-1.03	0.99
power(W)*speed(mm/s)	390.52	185.69	2.10	0.05	3.17	777.86	1.99	0.95	0.02	3.97
power(W)*Hatch Spacing (mm)	2083.76	4472.59	0.47	0.65	-7245.90	11413.41	0.64	1.37	-2.22	3.49
speed(mm/s)*Hatch Spacing (mm)	-657.33	776.40	-0.85	0.41	-2276.87	962.22	-1.09	1.28	-3.77	1.59

TABLE L-10: TEST OF SS FOR WHOLE MODEL VS SS RESIDUAL

Dependent Variable	Test of SS Whole Model vs. SS Residual (Spreadsheet2 in Workbook6)										
	Multiple R	Multiple R^2	Adjusted R^2	SS Model	df Model	MS Model	SS Residual	df Residual	MS Residual	F	p
WC wt %	0.822574	0.676627	0.579616	11704.91	6	1950.819	5593.992	20	279.6996	6.974693	0.000412

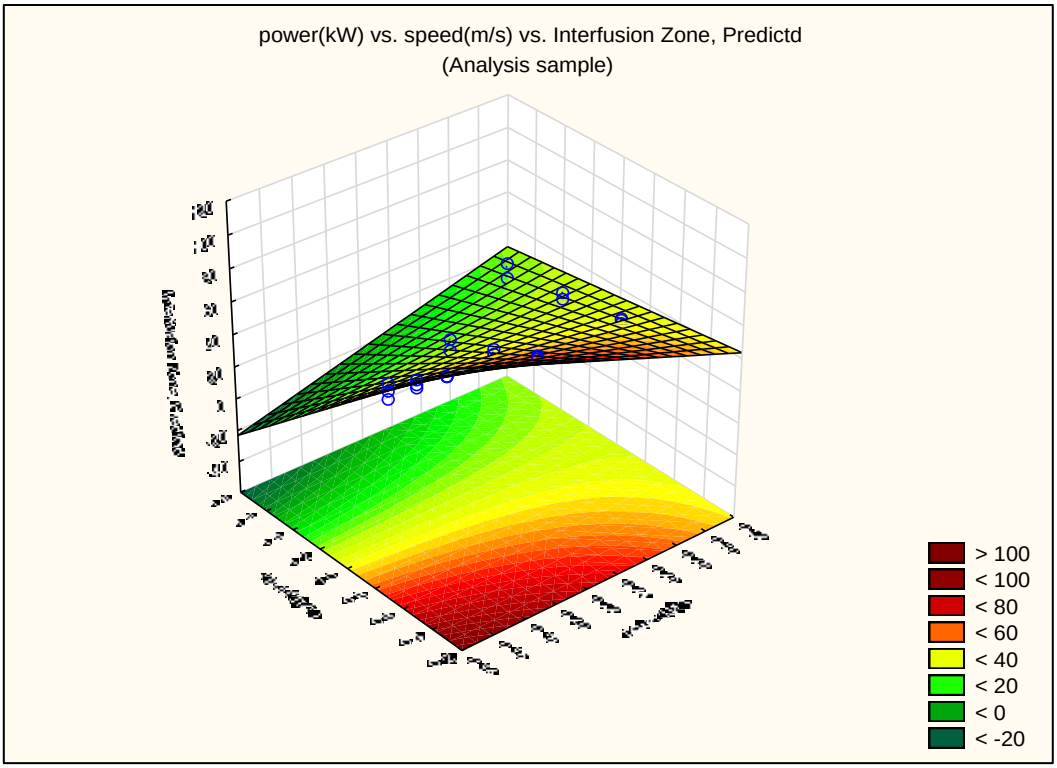

FIGURE L-7: POWER(KW) VS. SPEED(M/S) VS. INTERFUSION ZONE, PREDICTED

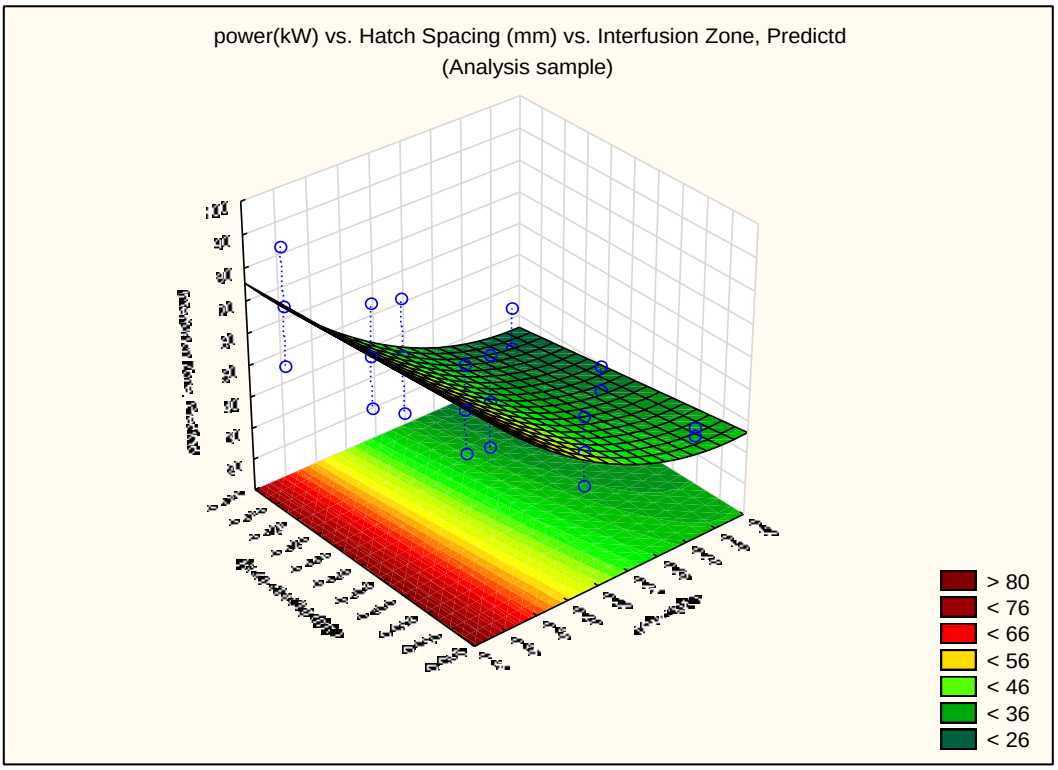

FIGURE L-8: POWER(KW) VS. HATCH SPACING (MM) VS. INTERFUSION ZONE, PREDICTED

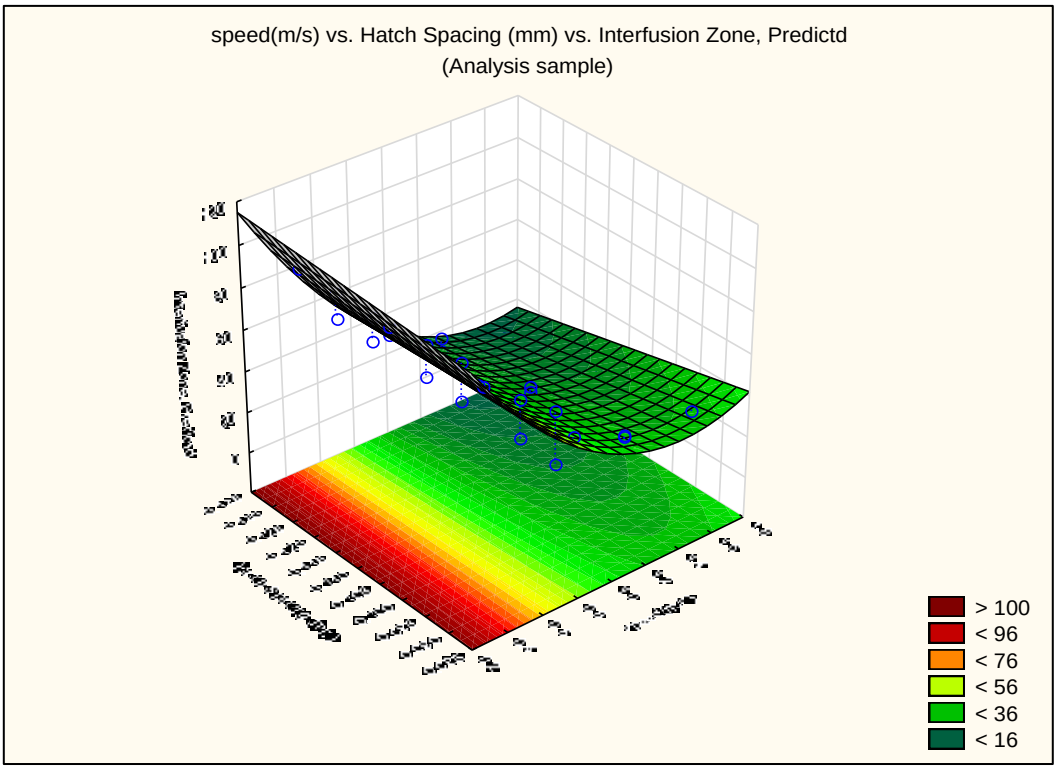

FIGURE L-9: SPEED(M/S) VS. HATCH SPACING (MM) VS. INTERFUSION ZONE, PREDICTED

APPENDIX M: ARTICLE SUBMITTED FOR THE ANNUAL RAPDASA CONFERENCE PROCEEDINGS.

The RAPDASA conference article, which has been submitted, accepted, and reviewed for this work, is presented here. This is the final revision format that was published in the conference proceedings for RAPDASA 2017

REVIEW OF COMPOSITE MATERIALS PRODUCED WITH ADDITIVE MANUFACTURING.

M.C. van Coller[1, 3*], C.M. Olivier[1, 3*], D. Du Toit[1, 3*], G.A. Oosthuizen[1*] & N. Sacks[2, 3*]

[1]Department of Industrial Engineering
University of Stellenbosch, South Africa
17693195@sun.ac.za

[2]School of Chemical & Metallurgical Engineering,
University of the Witwatersrand, South Africa

[3]DST-NRF Centre of Excellence in Strong Materials,
South Africa

ABSTRACT

Composites relate to the concept of combining distinct materials to engineer a new material with a unique combination of properties, also referred to as the principle of combined action. Composites are capable of catering to a diversity of applications in specialist industries, namely: dental, pharmaceutical, medical, tooling, aviation, automotive and electronics. These sectors operate with customized materials that continuously evolve in complexity as manufacturers innovate their products. Additive manufacturing (AM), when compared to standard manufacturing applications, has superior process flexibility and can produce highly complex parts with relative ease. Thus, manufacturing composites via AM may improve the current supply chain capabilities for part production and refurbishment within the above-mentioned industries. This study aims to review the current state of technology regarding composites produced with AM, along with trends for future developments in nanocomposite materials.

INTRODUCTION

The principle of combined action is a naturally occurring phenomenon, and is prevalent in many composites found in nature, such as bones and wood [45]. Humans have been combining materials to achieve improved mechanical properties for years, even before understanding the material structure thereof. Concrete, for example, consisting of sand, rock and cement, is much stronger than any of its constituent materials and has been a popular building material since the roman era.

Following the invention of carbon fibre, and boron fibre reinforcements in the 1960s, a rapid increase in the production of synthetic composite materials has occurred. The market was dominated largely by products consisting of fine fibrous particles enclosed within polymers. Predictions suggest that the demand for composite materials will increase consistently as designs become more daring and complex, particularly with emphasis placed on metal and ceramic based materials [2]. In modern industries, continuous product and process innovation is necessary to stay relevant in competitive environments. As product designs become more complex, so does the need for materials and manufacturing techniques to bring them to life. There is a continuous pursuit for improved performance, specified by criteria like a higher strength to weight ratio, cost effectiveness, and range of applications.

Composite materials are a promising solution to this cycle as the multitude of material combination add to their adaptability to varying environments [2]. In the same manner that requirements for specialized materials have shaped the composite industry, the need for innovation in production techniques lead to the rise of additive manufacturing. AM has garnered remarkable praise from both industry and academia for the mass of applications it can cater to in a variety of fields. It includes a collective of flexible, resource-efficient and cost-effective technologies that facilitate the fabrication of complex parts that range in size from sub-micrometer to several meters. AM technology is easy to use, reliable, and can accommodate a multitude of materials [3].

At the intersection of AM and composite material technologies, new research avenues are exposed resulting in 3D engineered materials that display multi functionality and superior mechanical properties. Traditionally AM technologies produced parts exclusively from homogenous polymers or alloys, but the addition of ceramic and metal particles resulted in versatile multi-phase composite materials. Through this integration several new applications have arisen with regards to the production of near net shape composite parts [3]. There are several AM techniques available in industry, but only a few of them have been used to produce composite parts, the technologies included in this paper are: Selective Laser Sintering/Melting (SLS/SLM), Ultrasonic Consolidation (UC), Laser Engineered Net Shaping (LENS), Laminated Object Manufacturing (LOM), Three-Dimensional Printing (3DP), Stereolithography (SL) and Fused Deposition Modelling (FDM) [53].

Additionally, the paper also deals with material addition processes involving nanocomposite materials and recent developments within this industry. This branch of composite materials is still only emerging and has only experienced an innovation boom in recent years. The materials can be designed to accommodate improved mechanical, magnetic, thermal, optical, electrical, transport, and biological properties [45]. Nanocomposite technologies addressed throughout this paper include: Inkjet printing, Powder-bed technology (Binding-based inkjet printing), Micro-stereolithography (MSL), Dynamic optical projection stereolithography (DOPsL), Direct-wire assembly (DW), Liquid Deposition Modelling (LDM), Conformal 3DP (C-3DP) and UV-Assisted 3DP (UV-3DP).

According to Callister et al. [45], composites may be defined as multiphase materials that can be artificially produced, resulting in a combination of desirable properties from its constituent base phases. Conventionally two phases are present within the material, 1) a dispersed phase of reinforcement particles, and 2) the matrix phase which completely surrounds the dispersed particles. Within this review, composites will be referred to according to 4 classifications, namely, particle-reinforced, fibre-reinforced, structural, and nanocomposite. These classifications are included in Figure1.

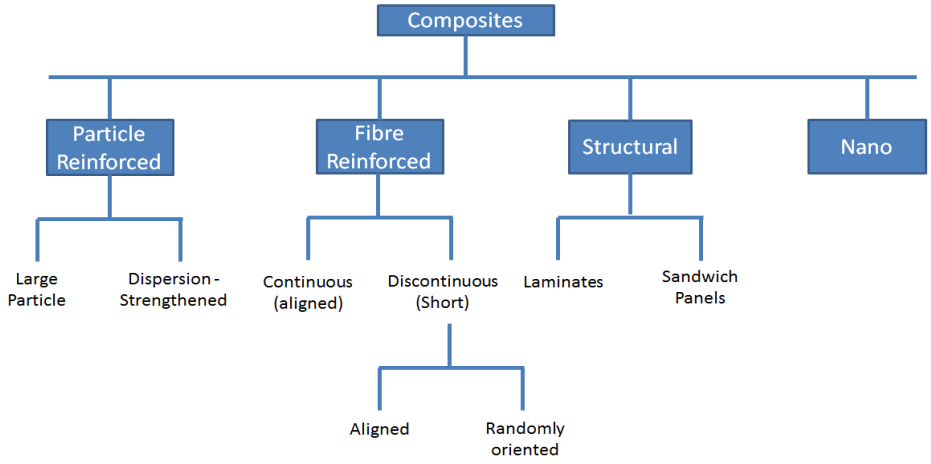

Figure 1: Classifications of composite materials

The production of fibre reinforced composites by AM is a popular endeavour, mainly pursued utilizing SL, FDM and LOM as the processing characteristics of these technologies support the addition of fibrous particles. Alternatively, in powder based AM techniques it is notoriously difficult to produce fibre-reinforced composite parts due to the inability to draw smooth layers of the powder-fibre mixture, resulting in hollow cavities throughout the material and increased risk of crack propagation. Structural composites have been produced with layer manufacturing technologies such as UC, LOM, and SL. These processes can produce sturdy laminar composites with either long or short fibre reinforcements. Though in cases using LOM and UC, fibre reinforced layers have to be fabricated prior to production with conventional production techniques [53], [132].

The review places emphasis on the production of composites with laser technology and is supplementary to current research being conducted at Stellenbosch University. The investigation entails the coating of Titanium (Ti-6Al-4V) with a tungsten carbide nickel coating via SLM. The specimens will be tested in terms of their tribological and thermal dissipation compared to conventional coatings used in industry. The research venture requires a comprehensive understanding of composites and AM technology which is has been adapted as an independent article.

The following section will aim to provide a review of composite structures and their methods of production via AM technologies. Significant focus will be placed on powder based AM technologies, specifically SLS and SLM as this is the primary concern of the study that the review is supplementary towards.

FIBRE REINFORCED COMPOSITES

Fibre reinforced composites are the most versatile of the several composite classifications and have the greatest potential for efficient reinforcement. These materials are often capable of high strength and stiffness compared to their weight. An applied load is transmitted through the more ductile matrix phase to the fibres. At the fibre extremities reinforcement discontinues, thus the efficiency of the reinforcement depends on the length of the fibres and the strength of the bonds between the matrix and fibre [45].

The matrix phase that surrounds the fibrous particles is categorized by the matrix type, which entails metal-, ceramic-, and polymer-matrix composites, though they are conventionally made of polymers or metals. This phase serves to perform three functions, namely, 1) bind together the fibres and diffuse externally applied loads onto them, 2) Shield fibres from surface damage, and 3) prevent crack propagation between fibres. A similar Matrix structure dynamic is present in particle reinforced composites, the only major difference being that instead of a fibrous phase the material is reinforced with a hardened particulate phase. Table 1 includes a briefing of the different matrix-structure combinations that are popular in composite materials.

Table 1: Descriptions and acronyms of popular fibre reinforced and particle reinforced composites within binder matrices sourced from [45]

Matrix material	Description
Polymer-Matrix Composite (PMC)	**These composites are the most popular and diverse due to easy fabrication and low cost for their desirable properties. A polymer resin represents the matrix phase which is reinforced with fibres intended for use at room temperatures.**
Metal-Matrix Composite (MMC)	**In these materials, the matrix phase consists of ductile metals and the reinforcement either continuous or discontinuous fibres or particulates. MMCs can withstand higher working temperatures than PMCs and have improved stiffness, abrasion resistance, creep resistance, specific strength, dimensional stability, and thermal conductivity.**
Ceramic- Matrix Composite (CMC)	**Ceramic materials are often praised due to their resistance to oxidation and weakening in high temperature environments, but these properties are countered by the material's affinity to brittle fracture. CMCs improve the brittle nature of ceramics by embedding ceramic particulates and fibres into a ceramic matrix material. The improved fracture toughness is due to dispersed phase particles that interact with advancing cracks through various toughening techniques.**
Hybrid Composite (HC)	**Hybrid composites may be obtained by combining two different fibre materials within a matrix, which comply with the principle of combined action in producing a part that has superior properties compared to the constituent materials. The most common variety contains carbon and glass fibre reinforcements. Where the carbon provides stiffness and strength, and the glass is utilized as a more cost-effective reinforcement.**

Stereolithography

SL is the most widespread additive manufacturing technology used in research regarding fibre reinforced composites (FRC). To incorporate composite reinforcement within the stereolithography process, photopolymer materials are

mixed with particulates or fibres to enhance their properties. These fibre combinations include fibre mats, continuous fibres and short fibres. The most effective variation being glass fibres, which still allow most of the emitted UV light to be absorbed into the resin because of their opacity [133]. Continuous reinforcement fibres provide the best mechanical property enhancements, though a trade-off between the fibre volume and effective layer formation must be made due to several procedural complications. For example, 1) the addition of reinforcements increases the viscosity of the polymer thwarting the layer coating process; 2) there may be a non-homogeneous distribution of particles; 3) crack propagation origins may increase due to particulates that form bubbles in the layers; 4) The thicker liquid absorbs less laser energy during manufacturing, which calls for longer exposure time and in turn a longer process duration [134].

To remedy these anomalies several process adaptations have been employed. For instance, the Optoform process arose, a variation of SL technology that utilizes a photo-curable multi material paste instead of the photopolymer liquid resin. Optoform has been well adapted to a wide choice of materials and applications for shells, parts and investment casting cores.
Alternatively, coated fibres have been proven to mitigate the clumping effects of the reinforcements phase and results in a uniform distribution throughout. These fibres assist in forming bonds between layers, where they are partially settled in previous laminate [53]. Lastly, specialized polymer mixtures may also be developed to facilitate thermal curing energy instead of photo-curing [53].

Laminated Object Manufacturing

LOM utilizes pre-produced laminates as input material, these laminates first must be reinforced with particulates or fibres prior to production. Despite this additional value adding component in the process chain LOM of composite materials provides a unique advantage over other AM methods, due to the possibility of applying laminates with different compositions into a single part. This characteristic has been exploited to produce functionally graded materials (FGM) and experiment with several laminar composite structures [135].

FRC sheets have been produced via LOM by merging fibre prepregs with ceramic tape. Fibre prepregs are often produced by impregnating a unidirectional continuous fibre fabric with a thermosetting resin system that already includes the necessary curing agent; this eliminates additional resin requirements before heat treatment. In another intriguing case, LOM parts were created through cellulose fibre based filter paper that has been pyrolysed and bound to adhesive tape comprising of phenolic resin, benzyl butyl phthalate, ethanol and polyvinyl butyral. This composition is then pyrolysed again at roughly 800ºC. The phenolic resin is then converted into carbon leaving the sample parts porous and suitable for post-production vacuum infiltration with silicon (Si) at 1500 ºC [53].

Fused Deposition Modelling

FDM incorporates a feedstock composite as filament material that is melted and extruded in layers which adhere together. Within this branch of AM the critical component in terms of composite production is the development of feedstock material. Its unique composition should allow for high strength and low viscosity when melted to aid extrusion. Feedstocks conventionally consist of metals, polymers or ceramics that are mixed with a tackifier, plasticizer and surfactant contained within a base polymer material. Surfactant allows the metal/ceramic phase to be dispersed evenly throughout the solution, the plasticiser improves the flow of the molten material, while the tackifier provides adhesion and flexibility when cooled, and lastly the base polymer provides strength. The quantities of each ingredient are varied depending on the desired properties of the final material [53], [136].

In fibre reinforced FDM composites the thermoplastic has an increased stiffness, and the heated material experiences less swelling when extruded from the printing nozzle. However, these composites tend to be more brittle when dry; making it difficult to wind the filament feedstock onto easily transported cylindrical drums. For this reason, the mixture is supplemented with an additional linear polymer material to increase its ductility and flexibility overall. By introducing thermotropic liquid crystalline polymers (TLCP), the extrusion of high aspect ratio fibres results in fewer fracture-related complications when moving through the small diameter printing nozzle. This relates to fibres with a length over diameter ratio greater than 100 (L/D > 100). The processing temperatures of TLCP is higher than that of the base thermoplastic within the feedstock, thus they have to be heated and mixed separately to mitigate the degradation of the base material [53], [137].

Ultrasonic Consolidation

This metallic foil based technique is most often used to produce metal composites or metal-matrix composites. Foils are welded together ultrasonically and conventionally consist of Al, Fe, Cu and Ni. This process provides advantages such as meticulous precision in placing fibre structures and mitigated damage to fragile fibres due to less intensive temperature changes during production. Experimentation with UC to study the bond ability of materials has yielded composite materials such as SiC fibres bonded successfully with shape memory alloy fibre, and the production of a commercially available composite foil, MetPreg, which consists of alumina fibre embedded over an Al foil [53].

COMPOSITES MANUFACTURED WITH POWDER BASED AM

When manufacturing composites with powder bed laser technology, the reinforcement phase is in the form of particulates and not fibres. This aids the development of a smooth powder bed and is beneficial to aggregated final part strength and density. Particle reinforced composites consist of a hard particulate phase that is engulfed in a

binding matrix phase[53]. The particulate phase reinforces the material by restricting movement of the matrix phase within their vicinity, thereby hindering the motion of dislocations. This restricts plastic deformation and increases tensile strength and hardness of the material. [45]. This review will place emphasis on SLS/SLM methods for producing composite materials, which comprises of integrated processes utilizing various powders, in-situ reactions, and furnace treatments [53]. Lastly, additional powder based AM processes such as 3D printing and LENS will also be discussed.

Table 2: Powder based methods for producing composites, their descriptions and examples of materials produced sourced from [53].

Manufacturing method	Description	Examples
Powder Based (PMCs)	Largely created by means of liquid phase sintering. The preferred material combination consists of polymer powders mixed with ceramic reinforcement particles. The matrix constituent may be coated with polymer resins to promote adhesion and improve material strength. Alternatively, the reinforcement particulate and polymer mixture may be substituted with a single composite powder to ease powder mixing and even spread of the particulates throughout the final part.	• Hydroxypatite (HA) added to polycapralactone (PCL) and sintered together to form a material that is stronger and more biocompatible than its constituents. • PEEK (Polyether ether ketone) sintered with HA has shown significant improvements in the biocompatibility of implants [138]. • HA powder coated with Polymethyl mathacrelate (PMMA) have also been successfully sintered into composites, which strengthens the final component, however at the expense of biocompatibility.
Powder Based (MMCs)	The most widely produced composite utilizing powder based laser technologies. Part densities of laser sintered ceramics and metals are often subordinate to that of PMCs. Though densities may be improved significantly by post production infiltration, or adding more material phases to reduce the melt's surface tension and increase the sinter-ability of the material.	• A variety of Tungsten Carbide alloys. • Fe, Ni and TiC • Iron (Fe) with graphite reinforcement particles. • Virtually any material combinations that can be produced in powder form of small enough particle size.
Powder Based (CMC)	Ceramic matrix composites are not a popular choice in SLS/SLM production, though the composites that have been produced may be used as electrical insulators and wear resistant coatings.	• SiSiC • Alumina-Zirconium ceramics [139]

Selective Laser Sintering & Selective Laser Melting

Composites are produced by SLS/SLM for two primary applications: 1) to facilitate use of liquid phase sintering (LPS) in the SLS process, and 2) to combine several constituents to achieve properties otherwise unattainable by a single material. The first may be described via an example of the Fe-Cu composite. The Cu serves as a binding fluid to adhere the Fe-particles together and does not enhance the properties of the final product. It is only utilized to consolidate the Fe-powder into its net shape with ease [53].

The latter application, however, emulates the conventional production of fibre-, or particle-reinforced composites and replaces the technology in the process chain with SLS/SLM. Here all the constituent materials interact to produce a final part with improved or specialized chemical and physical properties. An example includes the production of tungsten-carbide-nickel metal matrix composites; wherein the tungsten carbide particulate phase increases material durability and hardness, while the nickel phase both binds the particles and provides good corrosion resistance [36].

The most distinct advangtages of powder based AM technology is the versatility of compatible materials, which has resulted in multiple new metallic powders being developed for use in SLM, SLS, 3DP and LENS machinery within recent years. They allow for part production without any tools, whereas conventional manufacturing methods require dedicated toolling such as moulds and dies. The technology may open up new avenues for innovative manufacturing methods and material composites to satisfy niche requirement markets [34].

Technology has developed rapidly in recent years, especially since SLM and SLS has become a common solution to mainstream manufacturing requirements. Due to SLS/SLM's capability produce parts of complex geometries from

virtually any material that can be crushed into a powdered particulate state, it may be the most effective solution in many niche industries including that of composite materials [34].

In situ Reactions

In situ reactions are laser-induced chemical reactions that are utilized to create in-situ particles during sintering. There are two ways wherein the laser beam's energy is converted, namely 1) to surpass the reactants' activation energies as to form chemical compounds, and 2) prompt a chemical reaction that both forms a compound and engenders sufficient thermal energy to allow chemical reactions to propagate autonomously. This is also referred to as self-propagating High-Temperature Synthesis (SHS). The in-situ formation of compound materials are advantageous due to their uniform spreading of compounds throughout, superior wetting characteristics, and promotion of binding reactions from the release of exothermic energy [53].

In the laser processing of SiC, the disintegration of SiC and its reaction with O2 results in the formation of SiO2, which acts as a binder matrix, encompassing silicon carbide (SiC) particulates. Though an intriguing phenomenon, the manufacturing technique does not result in strong enough parts to be of interest in real world applications [53]. Table 3 below includes examples of chemical compounds formed by both methods mentioned above.

Table 3: Chemical compounds produced by overcoming reactant activation energies or by self propagating high-temperature synthesis (SHS)

Classification	Example	Constituents
Overcoming of reactant activation energies	Includes the production of MMCs that are reinforced with Titanium diboride (TiB_2) or titanium carbide (TiC).	The composites originate from a compound powder mixture of copper (Cu) Titanium (Ti) and Boron Carbide (B_4C)
SHS	TiC-Al_2O_3	Titanium oxide (TiO_2) Aluminum (Al) and Carbon (C).
SHS	Al_2O_3-Cu	Cupric oxide (CuO) and Al
SHS	NiTi-HA	Ni, Ti, HA.

Post production Furnace treatment.

Laser sintered materials do not consistently yield parts with desirable densities, which calls for the use of post-production furnace treatments. These treatments are traditionally performed in one of two ways, 1) by debinding the porous material constituents, which may result in phase changes and changes in material structures, and does not necessarily involve the addition of infiltration material. Secondly, 2) applying the furnace to facilitate chemical reactions within the material during infiltration of the part [140].

3D printing

In this powder based AM process, powder layers are bound together with a polymer binder that is extruded onto it via one or more pressurized printing nozzles. Provided that the binder does not chemically react with or dissolve the powder, several compositions may be utilized to form composite materials. An advantage of 3D printing includes the possibility of altering material properties such as electrical and thermal conductivity, magnetism, and reflectivity. Furthermore, FGM can be achieved with the use of multiple nozzles, which can be applied to vary material hardness throughout the part [141].

Porous ceramic or metal parts produced with 3D printing may be infiltrated post production for composite reinforcement. Examples of such parts include a 60% stainless steel green part infiltrated with 40% reinforcement, either consisting of copper, starch and polyurethane, or starch and surgical wax. Though fibre-reinforced composites cause complications during powder based processes, porous parts may be injected with carbon nano-fibres within an epoxy resin to enhance strength and electrical conductivity [53].

Laser Engineered Net Shaping

LENS utilizes a similar production technique to SLS. It is powder based and it utilizes similar laser power interaction. The key difference lies in the manner which powder is deposited. A variant of the technology, CMB, includes an option to use wire feedstock material, which opens possibilities of developing metallic composites with AM that are not powder based [32]. Laser Engineered Net Shaping is capable of utilizing several powders for production of materials with chemical composition gradients. For composite materials, varying degrees of reinforcement phases may be incorporated into FGM by combining powders from separate nozzles pressurized by non-reactive gasses [53].

NANO COMPOSITE DEVELOPMENTS

This branch of composite materials is still only emerging and has only experienced innovation boom in recent years. Nanocomposites are made up of nanoparticles entrenched in a matrix material, much like particle or fibre reinforced composites. Although an interesting observation that convoys with a decrease in particle size is that the chemical and physical properties also experience a dramatic change. The materials can be designed to accommodate improved mechanical, magnetic, thermal, optical, electrical, transport, and biological properties [45].

The significance of these effects relies on the size of the particles and the ratio of particle surface area compared to bulk volume; as atoms at the surface of a material have differing properties to that of the bulk material. When the particles become smaller, the surface atoms and their phenomena begin to dominate. Nanocomposite properties depend on both the matrix material and the nanoparticle characteristics, in tandem with the shape of the particles and their interfacial bonding with the matrix material [45].

As stated, nanotechnology is still a novel field, production setbacks still occur, especially regarding homogeneous and uniform distribution of Nano-reinforcements within the binder matrix [45]. By combining AM and nanotechnology, specialized materials characterized by optimized properties and multifunctionality can be produced, and their relevant research avenues exploited. This may result in greater functionality of produced parts, such as improved conductivity and high temperature strength. It also bears the potential to improve the printability of certain feedstock [3].

There are various challenges to be addressed before the full potential of nanocomposites can be unlocked. For instance, the addition of nanoparticles may increase the viscosity of resins, clog printing nozzles, and complicate the aggregation of reinforcement particles throughout the material [3]. In powder based AM techniques, nanoparticles may decrease the tap density and process-ability of the material, yet this may be resolved by using micron-sized nanostructure powder alternatives, which exhibit nano-effects post production [53].

Polymer matrix nanocomposites are currently in vogue, with less prominent work being conducted regarding metal matrix composites. Without diminishing impact resistance, nanoparticles included into polymer based resins improve tensile strengths by inhibiting the movement of polymer macromolecules. High concentrations of nanoparticles may decrease the final density of parts, which calls for a trade-off to optimize the desired properties [142]. The addition of minute volumes of nanoparticles has shown positive transformation in the mechanical, thermal, optical and electrical properties of parts produced with SL and FDM. Small volume fraction additions allow for the enhancement of the matrix polymer without major increases in the viscosity of the resin. With recent advances in AM technology and its integration with nanocomposites, new materials with functionalities beyond that of standard printing feedstocks are being developed. These new-age nanofiller materials facilitate the fabrication of parts with unique structural reinforcement, -sensing, -magnetic, -heating, -and conductive properties [3]. These advancements expand the reach of AM technology and aid accelerating its adoption. For example, in SL a unique nano-ceramic material, named Bluestone, has been developed that produces parts suitable for housing electrical components [53].

Nanofillers are property enhancing doping agents incorporated into the matrix phase of composites. Various hydrogels, polymer matrices, thermoplastics and thermosetting resins incorporate nanofillers to create materials capable of producing multifunctional structures, such as nanoclay, carbonaceous nanofillers and metallic nanofillers. Metallic nanofillers, consisting of silver nanoparticles or nanowires, carbon nanofibers, graphene, or carbon nanotubes improve the conductive properties of materials significantly. Nanofillers are incorporated into insulating polymers to fabricate composites with unique electrical properties for applications in sensing devices and electromagnetic shielding (especially popular in aerospace industries) [3].

Various strategies for nanocomposite material mixing have recently been made available throughout literature as researchers aim to identify trends which obtain an optimal blend of desired properties. In a particularly interesting study by Yugang et al. [53] the viscous and mechanical properties of a TiO_2 -nanoparticle reinforced photopolymer were considered. A 0.25 wt% nanofiller addition resulted in the following improvements compared to parts produced with pure resin: 1) 89% tensile strength increase, 2) an 18% rise in elasticity modulus, and 3) 6% improvement in the flexural strength of the material. An increase in the viscosity of the nanocomposite was observed in all cases, with a sharper increase noted during the use of functionalised nanofillers. These filler materials are ‘functionalised’ by addition of silane coupling agents like KH 570, which forms hydroxyl groups at their surface and increases interfacial interactions between the filler and matrix [3].

There are various microfabrication techniques utilized to produce nanocomposite parts with AM, however, this article will not be able to address them in full. Table 4 includes a summary of the most popular AM processes used to produce nanocomposites, including their relevant nomenclature, a description of the process, materials used, and potential applications thereof.

Table 4: A summary of popular microfabrication techniques that can produce nanocomposite parts adapted from [3].

Name	Description	Common Nanocomposite Materials	Potential Applications
Inkjet printing	The deposition of ink materials in small drops onto a substrate via a pressure jet.	• Photopolymer solution encompassing Ti-nanoparticles. • Graphene sheets adorned with silver nanoparticles. • Graphene hydrogels.	• Electronic devices with flexible physical features. • Input sensors. • Data storage. • Supercapacitors. • Anti-counterfeiting.
Powder-bed technology (Binding-based inkjet printing)	Similar to 3D printing, where layers of an adhesive resin with low viscosity is deposited onto a powder bed, binding adjacent powder grains together.	• Carbon nanofiber epoxy. • Hydroxyapatite or graphene oxide nanoparticles.	• Bio-applications. • Supercapacitors. • Optics. • Water purification.
Micro-stereolithography (MSL)	This technique produces 3D microstructures by imitating the SL process of curing photopolymer resins with a precision UV laser on a micro-meter scale.	• TiO_2 nanoparticle reinforced photopolymers.	• Beam steering and focusing. • Electromagnetic absorption or shielding.
Dynamic optical projection stereolithography (DOPsL)	DOPsL is based on the same principle as MSL, but incrorporates the use of a digital mirror array device (DMD) capable of producing dynamic virtual photo masks for each layer of the print.	• Polydiacetylene-nanoparticle reinforced hydrogels.	• Flow sensing and biomedical detoxification.
Direct-wire assembly (DW)	This technique relies largely on the deposition of continuous ink filaments via a computer-controlled robot. It offers a wide variety of compatible materials such as rheologically customized ink filaments consisting of nanoparticles, colloid or organic material.	• Nano platelet filled epoxy. • Silver nanoparticle filled conductive ink. • Nanotube filled epoxy. • Self-healing materials.	• Photovoltaics. • Opto-electronics. • LEDs. • Self-healing materials.
Fused Deposition Modelling	A modified form of the FDM technique discussed in Table 1, with the addition of nanoparticle materials into the feedstock material.	• ABS or PLA thermoplastics reinforced with nanoclay or nanocrystalline hydroxyapatite.	• Noise reduction materials. • Tissue engineering. • Electronic sensors.
Solvent-cast 3DP (SC-3DP) or Liquid Deposition Modelling (LDM	A recent development in AM technologies which relies on direct deposition of nanocomposite or polymer solutions.	• Nanotubes encompassed by thermoplastics, specifically PLA.	• Microelectronics. • Liquid sensing.

Conformal 3DP (C-3DP)	**An extrusion based printing technique capable of extruding ink filaments onto curved (conformal) surfaces, which enables fabrication of complex geometries.**	• **Nanotubes encompassed by photopolymers.** • **Silver nanoparticle filled conductive ink.**	• **Multiple layered tactile piezoelectric sensors.** • **Microelectronics.** • **Antennas.**
UV-Assisted 3DP (UV-3DP)	**Based on the DW process, UV-3DP is utilized to produce features by the deposition of ink filament that cures upon exposure to sunlight. The nozzle is movable in three dimensions and is used to produce both freeform and supported structures.**	• **Nanotube filled photopolymers.**	• **Sensors.** • **Field-effect transistors.** • **Microelectronics.**

CONCLUSION: OPPORTUNITIES, CHALLENGES AND FUTURE FOCUS

Though still in their early stages, research avenues regarding composite materials by AM are currently trending within the advanced materials industry and academia. Thus far the majority of AM composite applications were surrounding mechanical and structural reinforcement applications, however, the field shows great potential for other inter-disciplinary uses that have yet to be thoroughly researched. There is an apparent need to develop current AM technologies, or investigate entirely new processes and materials that will enrich the field of applications. Promising opportunities regarding the integration of these technologies include [9, 24 , 25]:

- Developments which enable the optimization of a material's microstructure without affecting its physical properties.
- SL and LOM processes that facilitate the effective production of continuous fibre reinforced structural composites. Albeit at the lack of time efficient and precise reproducibility, the potential for future applications is prevalent, and will come with maturity in these processes.
- Another area for further research is SLS and LENS processes for producing ceramic composites by in-situ reactions. Most importantly, in the case of powder based AM processes, the research and development of specialized powders for composite production should be encouraged as it will provide the capability of producing composite parts without the additional cost of upgrading machinery.
- AM provides a distinct advantage over traditional manufacturing techniques in terms of time, cost, waste and labour requirements, especially in novel industries that require specialized small batch manufacturing.

Some difficulties regarding technological maturity and material development are still present, including the following [24, 27, 28]:

- Technological adoption of AM processes by manufacturing companies that resist drastic changes in their operations.
- Due to layered addition of materials, the surface quality of parts produced with AM is not refined and requires post processing treatments.
- Although efficient, many direct manufacturing techniques produce metallic composite parts with undesirable densities.
- AM machinery includes a higher initial system cost.
- Challenges persist regarding optimal mixing strategies that mitigate the effects of nanofiller additions on the viscosity, flow-ability and transparency of printing materials for the fabrication of nanocomposite parts.

Lastly, AM, composites and nanocomposite technologies have made impressive progress within recent years and are on a fast track to revolutionizing several industries. Future developments provided by current research within these fields include the following predictions [24, 28].

- The recent boom in the popularity of AM systems will extrapolate to increase the number of potential users. This increased demand may likely decrease the cost of AM machinery, which will coincide with greater research and development efforts within novel AM fields such as composites and nanocomposites.
- AM systems will evolve to incorporate multiple material feeds, which allow for the production functionally graded multi material compositions within produced parts.
- The multi-functionality associated with nanoparticle-reinforced composites will fuel the development of newer AM machinery and feedstock materials to produce nanocomposites more effectively.

By combining the advantages of both technologies, the integration of nanotechnology with AM will bring several improvements in the production of multifunctional devices on both a macro, - and micro scale. AM provides the means to produce materials with greater freedom and dimensional accuracy, while the addition of nanotechnology adds broader functionality to printed parts [147]. The following years will be crucial in advancing these industries enough

to facilitate a synergy that will shape the future of material sciences and additive manufacturing for generations to come.

REFERENCES

[1] P. C. Pandey, "Engineering Applications of Composites Materials," in *Module 11: Engineering Applications of Composite Materials*, 2011, pp. 1–89.

[2] R. D. Matthews, F. L. Rawlings, *Composite materials : engineering and science*. Cambridge: Woodhead publishing ltd., 1994.

[3] R. D. Farahani, M. Dubé, and D. Therriault, "Three-Dimensional Printing of Multifunctional Nanocomposites: Manufacturing Techniques and Applications."

[4] D. J. De Beer, "Establishment of rapid prototyping / additive manufacturing in South Africa," *J. South. African Inst. Min. Metal.*, vol. 111, no. MARCH, pp. 211–215, 2011.

[5] V. A. Tracey, "Nickel in hardmetals," *Int. J. Refract. Met. Hard Mater.*, vol. 11, no. 3, pp. 137–149, 1992.

[6] R. Boyer, G. Welsch, and E. W. Collings, *Materials properties handbook : titanium alloys*. ASM International, 1994.

[7] C. Guo *et al.*, "Effects of WC-Ni content on microstructure and wear resistance of laser cladding Ni-based alloys coating," *Surf. Coatings Technol.*, vol. 206, no. 8–9, pp. 2064–2071, 2012.

[8] A. C. van Staden, "A Fundamental Analysis on Additive Manufacturing of a Cemented Tungsten Carbide," no. December, 2015.

[9] L. Thijs, F. Verhaeghe, T. Craeghs, J. Van Humbeeck, and J. P. Kruth, "A study of the microstructural evolution during selective laser melting of Ti-6Al-4V," *Acta Mater.*, vol. 58, no. 9, pp. 3303–3312, 2010.

[10] D. . Pham and R. . Gault, "A comparison of rapid prototyping technologies," *Int. J. Mach. Tools Manuf.*, vol. 38, no. 10–11, pp. 1257–1287, Oct. 1998.

[11] J.-P. Kruth, M. C. Leu, and T. Nakagawa, "Progress in Additive Manufacturing and Rapid Prototyping," *CIRP Ann. - Manuf. Technol.*, vol. 47, no. 2, pp. 525–540, 1998.

[12] A. C. Van Staden, "A Fundamental Analysis on Additive Manufacturing," no. December, 2015.

[13] D. Hagedorn-Hansen, R. Cichon, M. B. Bezuidenhout, P. A. Hugo, and G. A. Oosthuizen, "Geometric Deviation of Hybrid Parts Produced by Selective Laser Melting," *Rapid Prod. Dev. Assoc. South Africa*, pp. 1–9, 2015.

[14] R. I. Campbell, D. J. De Bee, and E. Pei, "Additive manufacturing in South Africa: building on the foundation," vol. 17. pp. 156–162, 2011.

[15] Statista, "Value of the Additive Manufacturing (3D printing) Market worldwide from 2011 to 2021," 2014. [Online]. Available: http://www.statista.com/statistics/261693/3d-printing-market-value-forecast/. [Accessed: 20-Jun-2016].

[16] E. Campbell, R.I. De Beer, D.J. Pei, "Additive manufacturing in South Africa: building on the foundations," *Rapid Prototyp. J.*, vol. 17, no. 2, pp. 156–162, 2011.

[17] S. Van Der Berg, "Current poverty and income distribution in the context of South African history," *Work. Pap. Dep. Econ. Bur. Econ. Res. Univ. Stellenbosch*, pp. 1–23, 2010.

[18] S. Wild, "SA joins 3D printing revolution," *Mail & Guardian*. [Online]. Available: http://mg.co.za/article/2014-09-26-sa-joins-3d-printing-revolution. [Accessed: 16-Mar-2016].

[19] F. Authors, "Rapid prototyping in South Africa : past , present and future." 2012.

[20] R. I. Campbell and D. J. De Beer, "Rapid prototyping in South Africa: past, present and future," *Rapid Prototyp. J.*, vol. 11, no. 4, pp. 260–265, 2005.

[21] B. Berman, "3-D printing: The new industrial revolution," *Bus. Horiz.*, vol. 55, no. 2, pp. 155–162, 2012.

[22] C. Aligner, I. Transcribed, S. Dna, S. Nucleotide, P. Snp, and S. N. P. Ssr, "IMPROVEMENTS IN THE CAPABILITY PROFILE OF 3-D PRINTING: AN UPDATE," vol. 16, no. 2, pp. 295–300, 2014.

[23] D. Dimitrov, K. Schreve, N. de Beer, and P. Chritiane, "Three dimensional printing in the South African industrial environment," *South African Journal …*, vol. 19, no. May 2008. pp. 195–213, 2008.

[24] C. Tuck, R. J. M. Hague, and N. D. Burns, "Rapid manufacturing impact on supply chain methodologies and practice," *Int. J. Serv. Oper. Manag.*, vol. 3, no. 1, pp. 1–22, 2007.

[25] S. H. Huang, P. Liu, A. Mokasdar, and L. Hou, "Additive manufacturing and its societal impact: A literature review," *International Journal of Advanced Manufacturing Technology*, vol. 67, no. 5–8. pp. 1191–1203, 2013.

[26] Y. Luo, Z. Ji, M. C. Leu, and R. Caudill, "Environmental Performance Analysis of Solid Freeform Fabrication Processes," *Int. Symp. Electron. Environ.*, pp. 1–6, 1999.

[27] ATKINS, "Manufacturing a low carbon footprint," 2007.

[28] A. Drizo and J. Pegna, "Environmental impacts of rapid prototyping: an overview of research to date," *Rapid Prototyp. J.*, vol. 12, no. 2, pp. 64–71, Mar. 2006.

[29] G. Janaki Ram, C. Robinson, Y. Yang, and B. Stucker, "Rapid Prototyping Journal Use of ultrasonic consolidation for fabrication of multi-material structures) "Use of ultrasonic consolidation for fabrication of multi-material"Integrating stereolithography and direct print technologies for 3D structu," *Rapid Prototyp. J. Rapid Prototyp. J. Iss Rapid Prototyp. J.*, vol. 13, no. 03, 2010.

[30] S. L. Campanelli, N. Contuzzi, A. Angelastro, and A. D. Ludovico, "Capabilities and Performances of the Selective Laser Melting Process," *ew Trends Technol. Devices, Comput. Commun. Ind. Syst.*, p. Chapter 13, 2010.

[31] D. . Pham and R. . Gault, "A comparison of rapid prototyping technologies," *Int. J. Mach. Tools Manuf.*, vol. 38, no. 10–11, pp. 1257–1287, 1998.

[32] A. Bandyopadhyay, B. V. Krishna, W. Xue, and S. Bose, "Application of Laser Engineered Net Shaping (LENS) to manufacture porous and functionally graded structures for load bearing implants," in *Journal of Materials Science: Materials in Medicine*, 2009, vol. 20, no. SUPPL. 1.

[33] F. Weng, C. Chen, and H. Yu, "Research status of laser cladding on titanium and its alloys: A review," *Mater. Des.*, vol. 58, no. November, pp. 412–425, 2014.

[34] K. Maeda and T. H. C. Childs, “Laser sintering (SLS) of hard metal powders for abrasion resistant coatings,” *J. Mater. Process. Technol.*, vol. 149, no. 1–3, pp. 609–615, 2004.

[35] S. Bremen, W. Meiners, and A. Diatlov, “Selective Laser Melting. A manufacturing technology for the future?,” *Laser Tech. J.*, vol. 9, pp. 33–38, 2012.

[36] J. Kruth and P. Mercelis, “Binding mechanisms in selective laser sintering and selective laser melting,” *Rapid Prototyping Journal*, vol. 11, no. 1. pp. 44–59, 2005.

[37] D. D. Gu, W. Meiners, K. Wissenbach, and R. Poprawe, “Laser additive manufacturing of metallic components: materials, processes and mechanisms,” *Int. Mater. Rev.*, vol. 57, no. 3, pp. 133–164, 2012.

[38] C. Hauser, T. H. . Childs, C. Taylor, and M. Badrossamay, “Direct Selective Laser Sintering of Tool Steel Powders to High Density. Part A: Effects of Lasr Beam Width and Scan Strategy,” *14th Proc. Solid Free. Fabr. Symp.*, p. 12, 2003.

[39] E. Toyserkani, A. Khajepour, and S. Corbin, *Laser Cladding*, vol. 119. CRC Press, 2004.

[40] S. Nowotny, A. Richter, and K. Tangermann, “Surface Protection of Light Metals by One-Step Laser Cladding with Oxide Ceramics.”

[41] C. Leyens, F. Brückner, E. Lopez, and M. Riede, “Successes and Challenges of SLM and LMD for Industrial Production,” vol. 49, no. Il, 2017.

[42] I. Gurrappa, “Characterization of titanium alloy Ti-6Al-4V for chemical, marine and industrial applications,” *Mater. Charact.*, vol. 51, no. 2, pp. 131–139, 2003.

[43] M. J. Donachie, *Titanium : a technical guide*. ASM International, 2000.

[44] D. Hagedorn-Hansen, “The Effects of Developed Selective Laser Melting Strategies on Titanium Hybrid Parts by,” no. March, pp. 1–117, 2017.

[45] W. D. Callister and D. G. Rethwisch, *Materials Science and Engineering Materials Science and Engineering*, 9th Editio. Wiley, 2013.

[46] G. Lütjering, J. C. Williams, and A. Gysler, “MICROSTRUCTURE AND MECHANICAL PROPERTIES OF TITANIUM ALLOYS,” in *Microstructure and Properties of Materials*, WORLD SCIENTIFIC, 2000, pp. 1–77.

[47] Y. C. Lin, B. H. Yan, and Y. S. Chang, “Machining characteristics of titanium alloy (Ti–6Al–4V) using a combination process of EDM with USM,” *J. Mater. Process. Technol.*, vol. 104, no. 3, pp. 171–177, 2000.

[48] J. H. Zuo, Z. G. Wang, and E. H. Han, “Effect of microstructure on ultra-high cycle fatigue behavior of Ti–6Al–4V,” *Mater. Sci. Eng. A*, vol. 473, no. 1, pp. 147–152, 2008.

[49] A. Hasçalık and U. Çaydaş, “Electrical discharge machining of titanium alloy (Ti–6Al–4V),” *Appl. Surf. Sci.*, vol. 253, no. 22, pp. 9007–9016, 2007.

[50] H. Nortjé, “An Investigation of Fretting Wear in Aerospace Applications by,” no. December, 2011.

[51] E. Labban, H. F, E. R. I, and A. Wadai, “Laser cladding of Ti - 6Al - 4V alloy with vanadium carbide particles,” pp. 159–167, 2014.

[52] S. Yang, N. Chen, W. Liu, M. Zhong, Z. Wang, and H. Kokawa, “Fabrication of nickel composite coatings reinforced with TiC particles by laser cladding,” *Surf. Coatings Technol.*, vol. 183, no. 2, pp. 254–260, 2004.

[53] S. Kumar and J.-P. Kruth, “Composites by Rapid Prototyping Technology,” *Mater. Des.*, vol. 31, no. 2, pp. 850–856, 2010.

[54] C. M. Fernandes and A. M. R. Senos, “Cemented carbide phase diagrams: A review,” *Int. J. Refract. Met. Hard Mater.*, vol. 29, no. 4, pp. 405–418, 2011.

[55] Z. Yao, J. Stiglich, and T. S. Sudarshan, “WC-Co enjoys proud history and bright future,” *Met. Powder Rep.*, vol. 53, no. 2, pp. 32–36, 1998.

[56] N. Magnusson and Schmidt, “Understanding cemented carbides,” *Sandvik*, p. 20, 2008.

[57] N. M. PARIKH and M. HUMENIK, “Cermets: II, Wettability and Microstructure Studies in Liquid???Phase Sintering,” *J. Am. Ceram. Soc.*, vol. 40, no. 9, pp. 315–320, 1957.

[58] V. A. Tracey, “Nickel in hardmetals,” *Int. J. Refract. Met. Hard Mater.*, vol. 11, no. 3, pp. 137–149, Jan. 1992.

[59] “Engineering ToolBox,” 2001. [Online]. Available: https://www.engineeringtoolbox.com. [Accessed: 12-Jun-2018].

[60] A. Fernández Guillermet, “The Co-Fe-Ni-W-C Phase Diagram: A Thermodynamic Description and Calculated Sections for (Co-Fe-Ni) Bonded Cemented WC Tools,” *Zeitschrift für Met.*, vol. 80, no. 2, pp. 83–94, 1989.

[61] T. O. F. Contents, “International journal of refractory metals and hard materials,” *International Journal of Refractory Metals and Hard Materials*. pp. 1–11, 2011.

[62] D. Q. Zhang, Z. H. Liu, Q. Z. Cai, J. H. Liu, and C. K. Chua, “Influence of Ni content on microstructure of W-Ni alloy produced by selective laser melting,” *Int. J. Refract. Met. Hard Mater.*, vol. 45, pp. 15–22, Jul. 2014.

[63] D. Q. Zhang, Z. H. Liu, Q. Z. Cai, J. H. Liu, and C. K. Chua, “Influence of Ni content on microstructure of W-Ni alloy produced by selective laser melting,” *Int. J. Refract. Met. Hard Mater.*, vol. 45, pp. 15–22, 2014.

[64] J. Beddoes and M. J. Bibby, *Principles of Metal Manufacturing Processes*. Arnold, 1999.

[65] R. Asthana, A. Kumar, and N. Dahotre, *Materials Processing and Manufacturing Science*. 2006.

[66] B. Wittmann, W. D. Schubert, and B. Lux, “WC grain growth and grain growth inhibition in nickel and iron binder hardmetals,” *Int. J. Refract. Met. Hard Mater.*, vol. 20, no. 1, pp. 51–60, 2002.

[67] Federal Carbide Company, “Tungsten Carbide and Tungsten Carbide Components by Federal Carbide.” [Online]. Available: https://www.federalcarbide.com/tungsten_carbide.html. [Accessed: 27-Jul-2018].

[68] S. Sharafat, A. Kobayashi, S. Chen, and N. M. Ghoniem, “Production of high-density Ni-bonded tungsten carbide coatings using an axially fed DC-plasmatron,” *Surf. Coatings Technol.*, vol. 130, no. 2–3, pp. 164–172, 2000.

[69] J. Verwimp, M. Rombouts, E. Geerinckx, and F. Motmans, “Applications of laser cladded WC-based wear resistant coatings,” in *Physics Procedia*, 2011, vol. 12, no. PART 1, pp. 330–337.

[70] S. D. Guest, A. P. Gerlich, and P. F. Mendez, “Depositing Ni-WC wear resistant coatings with hot-wire assisted Oil Sands and Wear,” pp. 1–15, 2011.

[71] S. Y. Ahn, S. W. Kim, and S. Kang, “Microstructure of Ti(CN)-WC-NbC-Ni Cermets,” *J. Am. Ceram. Soc.*, vol. 84, no. 4, pp.

843–849, 2001.

[72] N. Eliaz, T. M. Sridhar, and E. Gileadi, “Synthesis and characterization of nickel tungsten alloys by electrodeposition,” *Electrochim. Acta*, vol. 50, no. 14, pp. 2893–2904, May 2005.

[73] R. Li, Y. Shi, J. Liu, Z. Xie, and Z. Wang, “Selective laser melting W-10 wt.% Cu composite powders,” *Int. J. Adv. Manuf. Technol.*, vol. 48, no. 5–8, pp. 597–605, 2010.

[74] I. Yadroitsev and I. Smurov, “Selective laser melting technology: From the single laser melted track stability to 3D parts of complex shape,” *Phys. Procedia*, vol. 5, no. PART 2, pp. 551–560, 2010.

[75] M. F. Zaeh and M. Ott, “Investigations on heat regulation of additive manufacturing processes for metal structures,” *CIRP Ann. - Manuf. Technol.*, vol. 60, no. 1, pp. 259–262, 2011.

[76] D. Zhang, Q. Cai, J. Liu, J. He, and R. Li, “Microstructural evolvement and formation of selective laser melting W-Ni-Cu composite powder,” *Int. J. Adv. Manuf. Technol.*, vol. 67, no. 9–12, pp. 2233–2242, 2013.

[77] A. C. Van Staden, D. Hagedorn-Hansen, G. A. Oosthuizen, and N. Sacks, “Characteristics of single layer Selective Laser Melted tool grade cemented tungsten carbide,” *Int. Conf. Compet. Manuf. COMA ’16*, pp. 141–146, 2016.

[78] H. Exner *et al.*, “Laser micro sintering: A new method to generate metal and ceramic parts of high resolution with sub-micrometer powder,” *Virtual Phys. Prototyp.*, vol. 3, no. 1, pp. 3–11, 2008.

[79] L. E. Murr *et al.*, “Metal Fabrication by Additive Manufacturing Using Laser and Electron Beam Melting Technologies,” *J. Mater. Sci. Technol.*, vol. 28, no. 281, pp. 1–14, 2012.

[80] D. Gu, Y. Shen, P. Dai, and M. Yang, “Microstructure and property of sub-micro WC-10 %Co particulate reinforced Cu matrix composites prepared by selective laser sintering,” *Trans. Nonferrous Met. Soc. China*, vol. 16, no. 2, pp. 357–362, 2006.

[81] D. Zhang, Q. Cai, and J. Liu, “Formation of nanocrystalline tungsten by selective laser melting of tungsten powder,” *Mater. Manuf. Process.*, vol. 27, no. 12, pp. 1267–1270, 2012.

[82] E. Yasa and J. Kruth, “Application of Laser Re-Melting on Selective Laser Melting Parts,” *Adv. Prod. Eng. Manag.*, vol. 6, no. 4, pp. 259–270, 2011.

[83] D. D. Gu, W. Meiners, K. Wissenbach, and R. Poprawe, “Laser additive manufacturing of metallic components: materials, processes and mechanisms,” *Int. Mater. Rev.*, vol. 57, no. 3, pp. 133–164, May 2012.

[84] R. Glardonl, N. Karapatisl, and V. Romanoz, “Influence of Nd : YAG Parameters on the Selective Laser Sintering of Metallic Powders,” *Manuf. Technol. J.*, vol. 50, no. 1, pp. 133–136, 2001.

[85] A. Simchi, “Direct laser sintering of metal powders: Mechanism, kinetics and microstructural features,” *Mater. Sci. Eng. A*, vol. 428, no. 1–2, pp. 148–158, 2006.

[86] D. Gu and Y. Shen, “Balling phenomena in direct laser sintering of stainless steel powder: Metallurgical mechanisms and control methods,” *Mater. Des.*, vol. 30, no. 8, pp. 2903–2910, 2009.

[87] J. Jhabvala, E. Boillat, T. Antignac, and R. Glardon, “On the effect of scanning strategies in the selective laser melting process,” *Virtual Phys. Prototyp.*, vol. 5, no. 2, pp. 99–109, 2010.

[88] V. Manvatkar, A. De, and T. DebRoy, “Spatial variation of melt pool geometry, peak temperature and solidification parameters during laser assisted additive manufacturing process,” *Mater. Sci. Technol.*, vol. 31, no. 8, pp. 924–930, 2015.

[89] H. Hassanin, F. Modica, M. A. El-Sayed, J. Liu, and K. Essa, “Manufacturing of Ti-6Al-4V Micro-Implantable Parts Using Hybrid Selective Laser Melting and Micro-Electrical Discharge Machining,” *Adv. Eng. Mater.*, vol. 18, no. 9, pp. 1544–1549, 2016.

[90] J. Butler, “Using selective laser sintering for manufacturing,” *Assem. Autom.*, vol. 31, no. 3, pp. 212–219, 2011.

[91] I. Yadroitsev, A. Gusarov, I. Yadroitsava, and I. Smurov, “Single track formation in selective laser melting of metal powders,” *J. Mater. Process. Technol.*, vol. 210, no. 12, pp. 1624–1631, Sep. 2010.

[92] E. C. Santos, M. Shiomi, K. Osakada, and T. Laoui, “Rapid manufacturing of metal components by laser forming,” *Int. J. Mach. Tools Manuf.*, vol. 46, no. 12–13, pp. 1459–1468, 2006.

[93] S. Kumar, “Manufacturing of WC-Co moulds using SLS machine,” *J. Mater. Process. Technol.*, vol. 209, no. 8, pp. 3840–3848, 2009.

[94] C. P. Paul and A. Khajepour, “Automated laser fabrication of cemented carbide components,” *Opt. Laser Technol.*, vol. 40, no. 5, pp. 735–741, 2008.

[95] B. Vrancken, “Study of Residual Stresses in Selective Laser Melting,” *PhD Thesis; KU Leuven Arenb. Dr. Sch. Fac. Eng. Sci.*, no. June, pp. 1–253, 2016.

[96] M. F. Zaeh and G. Branner, “Investigations on residual stresses and deformations in selective laser melting,” *Prod. Eng.*, vol. 4, no. 1, pp. 35–45, Feb. 2010.

[97] X. Wang, K. S. Hwang, M. Koopman, Z. Z. Fang, and L. Zhang, “Mechanical properties and wear resistance of functionally graded WC-Co,” *Int. J. Refract. Met. Hard Mater.*, vol. 36, pp. 46–51, 2013.

[98] D. Wang, Y. Yang, X. Su, and Y. Chen, “Study on energy input and its influences on single-track,multi-track, and multi-layer in SLM,” *Int. J. Adv. Manuf. Technol.*, vol. 58, no. 9–12, pp. 1189–1199, 2012.

[99] M. Rombouts, J. P. Kruth, L. Froyen, and P. Mercelis, “Fundamentals of selective laser melting of alloyed steel powders,” *CIRP Ann. - Manuf. Technol.*, vol. 55, no. 1, pp. 187–192, 2006.

[100] W. T. Kwon, J. S. Park, S. W. Kim, and S. Kang, “Effect of WC and group IV carbides on the cutting performance of Ti(C,N) cermet tools,” *Int. J. Mach. Tools Manuf.*, vol. 44, no. 4, pp. 341–346, 2004.

[101] H.-O. Andrén, “Microstructures of cemented carbides,” *Mater. Des.*, vol. 22, no. 6, pp. 491–498, 2001.

[102] I. Yadroitsev, L. Thivillon, P. Bertrand, and I. Smurov, “Strategy of manufacturing components with designed internal structure by selective laser melting of metallic powder,” *Appl. Surf. Sci.*, vol. 254, no. 4, pp. 980–983, 2007.

[103] N. K. Tolochko *et al.*, “Balling processes during selective laser treatment of powders,” *Rapid Prototyp. J.*, vol. 10, no. 2, pp. 78–87, 2004.

[104] W. E. King *et al.*, “Observation of keyhole-mode laser melting in laser powder-bed fusion additive manufacturing,” *J. Mater. Process. Tech.*, vol. 214, pp. 2915–2925, 2014.

[105] S. Ločs and I. Boiko, “Quality assessment of laser cladded HSS coatings with deep penetration into base material to obtain a

smooth gradient of properties in coating-substrate interface," *Agron. Res.*, vol. 16, no. Special Issue 1, pp. 1095–1109, 2018.

[106] K. G. Prashanth, S. Scudino, T. Maity, J. Das, and J. Eckert, "Is the energy density a reliable parameter for materials synthesis by selective laser melting?," *Mater. Res. Lett.*, vol. 5, no. 6, pp. 386–390, 2017.

[107] O. Eso, Z. Fang, and A. Griffo, "Liquid phase sintering of functionally graded WC-Co composites," in *International Journal of Refractory Metals and Hard Materials*, 2005, vol. 23, no. 4–6 SPEC. ISS., pp. 233–241.

[108] C. H. Allibert, "Sintering features of cemented carbides WC ± Co processed from ® ne powders," *Int. J. Refract. Metals Hard Mater.*, vol. 19, pp. 53–61, 2001.

[109] L. N. Carter, C. Martin, P. J. Withers, and M. M. Attallah, "The influence of the laser scan strategy on grain structure and cracking behaviour in SLM powder-bed fabricated nickel superalloy," *J. Alloys Compd.*, vol. 615, pp. 338–347, Dec. 2014.

[110] J.-P. Kruth, J. Deckers, E. Yasa, and R. Wauthle, "Assessing and comparing influencing factors of residual stresses in selective laser melting using a novel analysis method," *Proc. Inst. Mech. Eng. Part B J. Eng. Manuf.*, vol. 226, no. 6, pp. 980–991, 2012.

[111] M. Agarwala, D. Bourell, J. Beaman, H. Marcus, and J. Barlow, "Direct selective laser sintering of metals," *Rapid Prototyp. J.*, vol. 1, no. 1, pp. 26–36, 1995.

[112] K. A. Mumtaz, P. Erasenthiran, and N. Hopkinson, "High density selective laser melting of Waspaloy?," *J. Mater. Process. Technol.*, vol. 195, no. 1–3, 2008.

[113] M. Shiomi, K. Osakada, K. Nakamura, T. Yamashita, and F. Abe, "Residual Stress within Metallic Model Made by Selective Laser Melting Process," *CIRP Ann. - Manuf. Technol.*, vol. 53, no. 1, pp. 195–198, 2004.

[114] M. C. Sinirlioglu, "Rapid Manufacturing of Dental and Medical Parts via LaserCUSING Technology using Titanium and CoCr Powder Materials," *US-Turkey Work. Rapid Technol.*, pp. 89–92, 2009.

[115] D. Q. Zhang, Q. Z. Cai, J. H. Liu, L. Zhang, and R. D. Li, "Select laser melting of W-Ni-Fe powders: Simulation and experimental study," *Int. J. Adv. Manuf. Technol.*, vol. 51, no. 5–8, pp. 649–658, 2010.

[116] D. S. Rickerby, "A review of the methods for the measurement of coating-substrate adhesion," *Surf. Coatings Technol.*, vol. 36, no. 1–2, pp. 541–557, 1988.

[117] M. Eosint, "Technical Description EOSINT M 280 Technical description Technical Description EOSINT M 280," *Eos (Washington. DC).*, no. December, pp. 1–33, 2010.

[118] "Laser sintering system EOSINT M 280 for the production of tooling inserts , prototype parts and end products directly in metal The Technology : Laser sintering - the Key to e-Manufacturing."

[119] EOS, "Eosint M 280," *Web page*, pp. 1–3, 2014.

[120] "PST_Powders_Solutions_Catalog_2014 (1).pdf." .

[121] L. J. Prakash, "Application of fine grained tungsten carbide based cemented carbides," *Int. J. Refract. Met. Hard Mater.*, vol. 13, no. 5, pp. 257–264, 1995.

[122] B. Liu, R. Wildman, C. Tuck, I. Ashcroft, and R. Hague, "Investigation the Effect of Particle Size Distribution on Processing Parameters Optimisation in Selective Laser Melting Process," *Sff*, no. mm, pp. 227–238, 2011.

[123] N. SEMATECH, *NIST Engineering statistics handbook*. 2003.

[124] J. Antony, *Design of Experiments for Engineers and Scientists*, no. October. 2003.

[125] M. Cavazzuti, *Optimization methods: From theory to design scientific and technological aspects in mechanics*. 2013.

[126] R. H.Myers, D. C.Montgomery, and C. Anderson-Cook, M, *Response Surface Methodology: Process and Product Optimization Using Designed Experiments*. 2016.

[127] R. M. De Baun, S. Technometrics, and N. Feb, "American Society for Quality Response Surface Designs for Three Factors at Three Levels American Society for Quality Stable URL : http://www.jstor.org/stable/1266305 Linked references are available on JSTOR for this article : Response Surface Designs for ," vol. 1, no. 1, pp. 1–8, 2018.

[128] "Pickling and Descaling - ASM International." [Online]. Available: https://www.asminternational.org/news/-/journal_content/56/10192/ASMHBA0001229/BOOK-ARTICLE. [Accessed: 19-Aug-2018].

[129] J. P. Kruth, B. Van der Schueren, J. E. Bonse, and B. Morren, "Basic Powder Metallurgical Aspects in Selective Metal Powder Sintering," *CIRP Ann. - Manuf. Technol.*, vol. 45, no. 1, pp. 183–186, 1996.

[130] D. Tang, "Effect of substrate preheating temperature and coating thickness on residual stress in plasma sprayed hydroxyapatite coating," *IOP Conf. Ser. Mater. Sci. Eng.*, vol. 87, no. 1, 2015.

[131] P. Yuan and D. Gu, "Molten pool behaviour and its physical mechanism during selective laser melting of TiC/AlSi10Mg nanocomposites: Simulation and experiments," *J. Phys. D. Appl. Phys.*, vol. 48, no. 3, 2015.

[132] T. A. Campbell and O. S. Ivanova, "3D printing of multifunctional nanocomposites," *Nano Today*, vol. 8, pp. 119–120, 2013.

[133] L. Lu, J. Fuh, and Y. S. Wong, *Laser-induced materials and processes for rapid prototyping*. Massachusetts 02061: Kluwer Academic Publishers, 2001.

[134] Karalekas D and Antoniou K., "Composite rapid prototyping: overcoming the drawback of poor mechanical properties," *J Mat Pro Techno*, pp. 526–30, 2004.

[135] D. Klosterman, R. Chartoff, G. G., O. N., and P. B., "Interfacial characteristics of composites fabricated by laminated object manufacturing," in *Composites Part A*, 1998, no. 29, pp. 1165–74.

[136] S. Onagoruwa, S. Bose, and A. Bandyopadhyay, "Fused deposition of ceramics (FDC) and composites," in *Proceedings of Solid Freeform Fabrication Symposium*, 2001, pp. 224–231.

[137] R. W. Gray IV, D. G. Baird, and J. H. Bohn, "Effects of processing conditions on short TLCP fiber reinforced FDM parts," *Rapid Proto J*, vol. 4, no. 1, pp. 14–25, 1998.

[138] P. Johansson, R. Jimbo, Y. Naito, P. Kjellin, F. Currie, and A. Wennerberg, "Polyether ether ketone implants achieve increased bone fusion when coated with nano-sized hydroxyapatite: a histomorphometric study in rabbit bone.," *Int. J. Nanomedicine*, vol. 11, pp. 1435–42, 2016.

[139] I. Shishkovsky, I. Yadroitsev, P. Bertrand, and I. Smurov, "Alumina-zirconium ceramics synthesis by selective laser sintering/melting," *Appl. Surf. Sci.*, vol. 254, no. 4, pp. 966–970, Dec. 2007.

[140] T. Alexandre, J. Giovanola, S. Vaucher, O. Beffort, and U. Vogt, "Layered manufacturing of porous ceramic parts from

ceramic powders and preceramic polymers.," pp. 497–504, 2004.

[141] D. Dimitrov, K. Schreve, and N. de Beer, "Advances in three dimensional printing – state of the art and future perspectives," *Rapid Prototyp. J.*, vol. 12, no. 3, pp. 136–147, 2006.

[142] L. J. Wozniak, Graulet, Hazany, Kata D, "Highly loaded UV curable nanosilica dispersions for rapid prototyping applications.," *J Euro Ceram. Soc*, vol. 29, no. 11, p. 2259–65., 2009.

[143] D. Hotza, C. M. Gomes, and J. G??nster, "Advances in additive manufacturing processes and materials," *Adv. Mech. Eng.*, vol. 2014, 2014.

[144] S. K. Jing, G. H. Song, J. H. Liu, J. T. Zhou, and H. Zhang, "A Review of Product Design for Additive Manufacturing," in *Applied Mechanics and Materials*, vol. 635–637, Trans Tech Publ, 2014, pp. 97–100.

[145] T. Grim, *Users Guide to Rapid Prototyping*. Society of Manufacturing Engineeers, 2004.

[146] I. Campbell, D. Bourell, and I. Gibson, "Additive manufacturing: rapid prototyping comes of age," *Rapid Prototyp. J.*, vol. 18, no. 4, pp. 255–258, Jun. 2012.

[147] H. A. Hegab, "Design for additive manufacturing of composite materials and potential alloys: a review," *Manuf. Rev.*, vol. 3, p. 11, 2016.